Stress Tensor Estimates Derived from Focal Mechanism Solutions of Sparse Data Sets: Applications to Seismic Zones in Virginia and Eastern Tennessee

by

Frederick C. Davison, Jr.

Dissertation submitted to the Faculty of the
Virginia Polytechnic Institute and State University
in partial fulfillment of the requirements for the degree of
Doctor of Philosophy
in
Geophysics

APPROVED:

G. A. Bollinger, Chairman

Cahit Çoruh

John K. Costain

Edwin S. Robinson

J. Arthur Snoke

September 30, 1988

Blacksburg, Virginia

Stress Tensor Estimates Derived from Focal Mechanism Solutions of Sparse Data Sets: Applications to Seismic Zones in Virginia and Eastern Tennessee

by

Frederick C. Davison, Jr.

G. A. Bollinger, Chairman

Geophysics

(ABSTRACT)

A technique has been developed to estimate the directions of principal stresses from focal mechanism solutions, under the assumption that the stress is homogeneous throughout the seismic zone. That method is called the Multiple Solution per Earthquake Technique (MSET), and utilizes each member of multiple focal mechanism solution set as a possible solution. The MSET is useful when applied to small data sets, and differs from existing techniques in that (1) the use of multiple focal mechanisms for individual earthquakes allows for a range in the possible orientation of the fault geometry, while preserving fit to the original polarity and amplitude ratio data, and (2) the differences between the observed and theoretical fault slip is used as a weighting scheme for the results of the tensor estimation. Other methods, which rotate the single observed focal mechanism solution from its original configuration to estimate misfit, do not take into consideration the fit of that final solution to the original input data but assume that a minimization of errors between the theoretical stress model and the focal mechanism solution indicates a reasonable fit. For large data sets that assumption is likely to be met.

The MSET was applied to a set of 32 earthquakes to estimate the principal stress orientations for seismically active zones in the Southeastern United States, using focal mechanism solution sets derived by the program **FOCMEC**. Eight events were studied for the Giles County Seismic Zone, 13 for the Central Virginia Seismic Zone, and 11 for the Eastern Tennessee Seismic Zone. After testing against approximately 25000 theoretical solutions, an average of sixteen focal mechanism solutions fit the input polarity and $(SV/P)_z$ amplitude ratio data for each earthquake. The **P**-axes of the multiple focal mechanism solutions were averaged to determine a provisional single **P**-axis

direction for each earthquake. **P**-axes for the Giles County and Eastern Tennessee Seismic Zones trended generally NE-SW, while those of the Central Virginia Zone varied with depth, with the **P**-axes of events above approximately 8 km trending NE-SW, and those below trending NW-SE.

Application of the MSET resulted in consistent principal stress orientations for the Giles County and Eastern Tennessee Zones, with the horizontal component of the maximum compressive stress direction ($\overline{\sigma}_1$) trending about N40°E and N50°E, respectively. Results for the Central Virginia Zone also suggested differently oriented stress regimes above and below a depth of 8 km. The direction of the $\overline{\sigma}_1$ axis above that boundary was N70°E, while below it was east-west, with a shallow plunge to the west. While those results were not as pronounced as suggested initially by the **P**-axis data alone, the hypothesis of two stress tensors produced better MSET results than for a single stress tensor for the combined data set.

The technique developed for this study produces comparable results to other methods when applied to identical data sets. Estimation of error is based on subjective criteria, and includes the fit of the original seismic polarity and amplitude ratio data with the focal mechanism solutions. The error associated with each step in the process (e. g. distribution and reliability of the polarity and ratio data, calculation of focal mechanism solutions and estimation for the stress field) is very difficult to parameterize, and thus, no formal statistical analyses were undertaken.

After the estimate of the homogeneous stress field was made for each zone, a single best focal mechanism solution for each earthquake could be objectively chosen by constraining the slip associated with each mechanism to be aligned with the resolved stress derived from the principal stress directions. In that manner, focal mechanism solutions could be identified which fit the sparse input polarity and amplitude ratio data, but which were not compatible with the calculated stresses. Also, in that same procedure, the fault plane was chosen from the set of two nodal planes for each focal mechanism solution by examination of the theoretical slip on each of those planes. The faults within the Giles County Seismic Zone matched the direction found in previous seismic reflection surveys, with an average strike of N25°E. In the Eastern Tennessee Seismic Zone, faulting also occurred on planes oriented predominantly NE-SW. For the five shallow Central Virginia events, faults trended NW-SE, while for the deeper events there was no consistent trend.

A comparison was made between the **P**-axis and $\bar{\sigma}_1$ axis derived for each earthquake. Although in 81% of the cases $\bar{\sigma}_1$ was within 35° of at least one **P**-axis of the focal mechanism solution set, no further empirical relationship was found.

The MSET has proven itself useful in two ways when applied to sparse data sets. First of all, the primary seismic data (polarities and amplitude ratios) are not overlooked when deriving the orientation of a stress tensor associated with local faulting. Secondly, the MSET is an objective method for defining the best fitting solution among a family of focal mechanism solutions by requiring compatibility with the regional stresses. In the future, after integration with a program such as **FOCMEC**, regional stress tensors may be derived by the MSET which incorporate reasonable statistical parameters based on the fit of that primary data.

Acknowledgements

This research was completed with the help of many individuals who deserve special thanks for their contributions.

Dr. G. A. Bollinger provided financial support, but, above all, contributed greatly to the original concept of this work. He was willing to offer comments and encouragement along the way, and was particularly helpful in the critique of the several drafts which preceded the final copy of this dissertation.

Dr. J. A. Snoke wrote the program for the generation of focal mechanism data, as well as many subroutines which were utilized in the main program reported herein. He was most helpful in discussions of the theoretical aspects of this research and, in particular, his insightful review of the technical portions of this report was invaluable.

Drs. C. Çoruh, J. K. Costain, and E. S. Robinson reviewed the manuscript and offered suggestions to correct mistakes and make the text more readable. I am indebted to them for their helpful comment.

The comparison with other methods was accomplished with the help of of the USGS and of Cornell University, who were willing to share their computer programs and to analyze data which I provided. helped to recover that data from diskettes.

Most of all, I would like to thank my family for financial support, encouragement, and patience. This work is dedicated to them: my wife ., son , and my parents, and ..

Table of Contents

List of Illustrations

List of Tables

Introduction

The Southeastern United States (SEUS) is characterized by an overall low level of seismicity, with several imbedded zones of greater activity. That activity is shown on Figure 1, with both historic (1698 - 1976) and instrumental (1977 - 1986) earthquake epicenters plotted. Since the SEUS encompasses a tectonically stable intraplate region with no evidence of recent surface rupture, seismogenic structures responsible for the activity are poorly defined. Focal depths of earthquakes are generally upper crustal (less than 20 kilometers), but vary somewhat between seismic zones, probably indicating control by the brittle to ductile transition (Bollinger and others, 1985a; Sibson, 1982). Overall studies of crustal stress have only been made in a regional sense (e.g. Richardson and others, 1979; Zoback and Zoback, 1980, 1985), with most interpretations based on widely scattered data. More detailed resolution of current stress directions is necessary to interpret the nature of faulting within individual seismic zones.

During the past decade significant advances have been made relating crustal stresses with the resulting seismicity of highly active regions. Some experiments have involved direct measurements made in relatively shallow boreholes, while others have made interpretations based upon data recorded during the rupture process. In particular, much information has been obtained from calculated focal mechanism solutions. In the seismic regions of the Southeastern United States, there currently exists an excellent opportunity to capitalize on recent studies of instrumentally

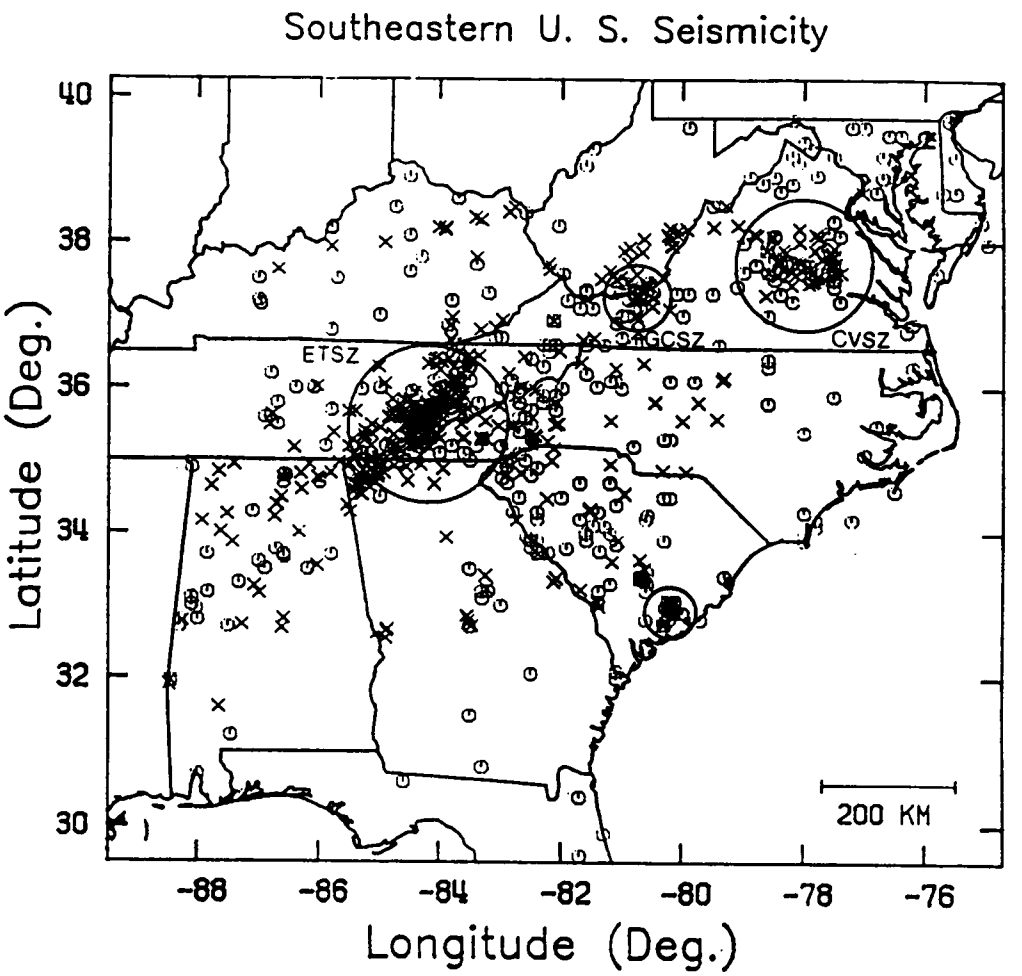

Figure 1. **Southeastern United States (SEUS):** Historic earthquakes occurring from 1698 - 1976 are shown as small circles; events recorded instrumentally since 1977 are shown as x's. Larger circles delineate the imbedded seismic zones near Charleston, South Carolina, Giles County, Virginia (GCSZ), Central Virginia (CVSZ) and Eastern Tennessee (ETSZ).

recorded earthquakes and to use those data to infer regional stress directions. Seismic networks installed in the area since 1977 have produced high quality location, first motion, and amplitude data. Use of those data with the computer program **FOCMEC** (Snoke and others, 1985) has generated an important collection of focal mechanism solutions, most of which have been reported previously by Teague (1984) and Munsey (1984). The program **FOCMEC** does not produce a single 'best' focal mechanism for input phase polarities and $(Sv/P)_z$ amplitude ratios, but calculates a set of 'acceptable' solutions. The number of set members is directly related to search and error parameters chosen by the operator. For example, the operator may choose to allow a larger number of polarity errors for a particular set of input data, thereby increasing the number of solutions deemed acceptable by the program.

The research reported herein will be divided into three interrelated phases. The first of those will estimate stress tensors for three of the four most active zones in the SEUS, where local seismic networks have provided a well constrained, albeit small, data set. Each of those stress tensors will then be used, in turn, to choose a single best focal mechanism solution for each earthquake. That high-graded data set will be the basis for discussion of the modes of faulting in each of the seismic zones under study. Finally, the focal mechanism solution sets from individual earthquakes will be examined a second time to indicate how much information may be gleaned from a single earthquake.

Seismic Setting

Importance of the SEUS in Studies of Seismic Stress

The Southeastern United States is an appropriate locale for studies of intraplate crustal stress. Located in that region are four important seismogenic zones, each with unique characteristics (Figure 1). The Giles County Seismic Zone in southwestern Virginia and the Eastern Tennessee Seismic Zone are both located in the Valley and Ridge and Blue Ridge physiographic provinces and are part of a more diffuse band of seismicity extending from the Virginia - West Virginia border to north-central Alabama (Bollinger, 1973; Johnston and others, 1985). The Central Virginia Seismic Zone is contained entirely within the Piedmont province and includes the city of Richmond near its eastern edge. The last of the four zones, in the Coastal Plain surrounding Charleston, South Carolina is the most well known, as it was the site of the largest historic earthquake in the region. Although earthquakes in the SEUS are infrequent relative to interplate regions of the western United States, the potential for damage is not small, since the seismic wave attenuation within the crust in the eastern portion of the continent is substantially smaller than in the west (e.g. Nuttli, 1973; Bollinger, 1973). In fact, the felt areas of eastern earthquakes may be as much as ten or more times greater than felt areas for similarly sized west coast events.

A second reason for basing this study in the SEUS is the high quality data set that has become available over the past decade. During that period local networks of seismic instruments were installed in all of the major seismogenic zones, allowing for accurate hypocentral determinations. New data, especially those in digital format, have facilitated construction of the regional velocity models which, along with the more accurate depth measurements, have been fundamental in the calculation of the sets of well constrained focal mechanism solutions used in this study.

Seismic Zones Involved in this Study

Prior to this study, Teague (1984) and Munsey (1984) derived focal mechanism solutions for earthquakes located within three of the four seismic zones of the Southeastern United States. The historic and on-going seismicity of those three zones will be reviewed briefly. Figure 2 shows the locations of those zones with reference to the entire SEUS, as well as the thirty-two earthquakes for which the focal mechanisms used in this study have been determined. Focal mechanism solutions and local stress regimes will be discussed later. Hypocentral locations and error estimates are listed in Appendix A. Uncertainties in location were calculated in terms of the horizontal and vertical errors (ERH and ERZ, respectively; see Lahr, 1980). Average ERH and ERZ were found to be 1.0 $\pm$ 0.2 km and 2.1 $\pm$ 0.8 km for the Giles County Seismic Zone; 1.4 $\pm$ 0.7 km and 3.1 $\pm$ 2.4 km for the Central Virginia Seismic Zone; and 0.5 $\pm$ 0.1 km and 1.2 $\pm$ 0.4 km for the Eastern Tennessee Seismic Zone.

Giles County, Virginia. The Giles County, Virginia, Seismic Zone (GCSZ) is located in the Valley and Ridge and Blue Ridge physiographic provinces and straddles the border with West Virginia (see Figure 1 and Figure 3). The largest event in the Southern Appalachians during the historic era occurred in the GCSZ in 1897. That event, which caused intensity VIII (MMI) level damage effects in and near the town of Pearisburg, had an estimated equivalent body wave magnitude of 5.8 (Bollinger and Wheeler, 1988).

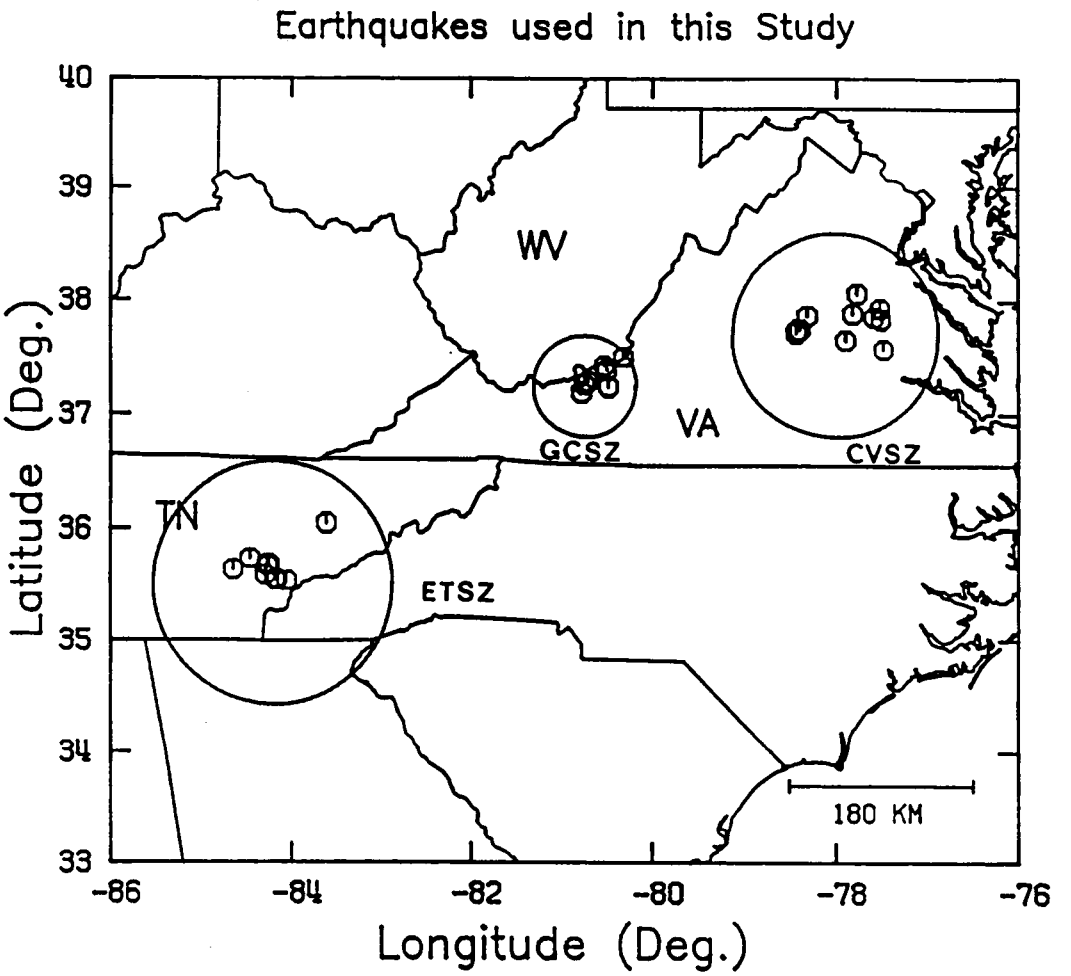

Figure 2. **Earthquakes used in this study:** All epicenters are shown as small circles. Seismic zones studied are shown as larger circular regions, and are, from west to east, Eastern Tennessee, Giles County, VA, and Central Virginia.

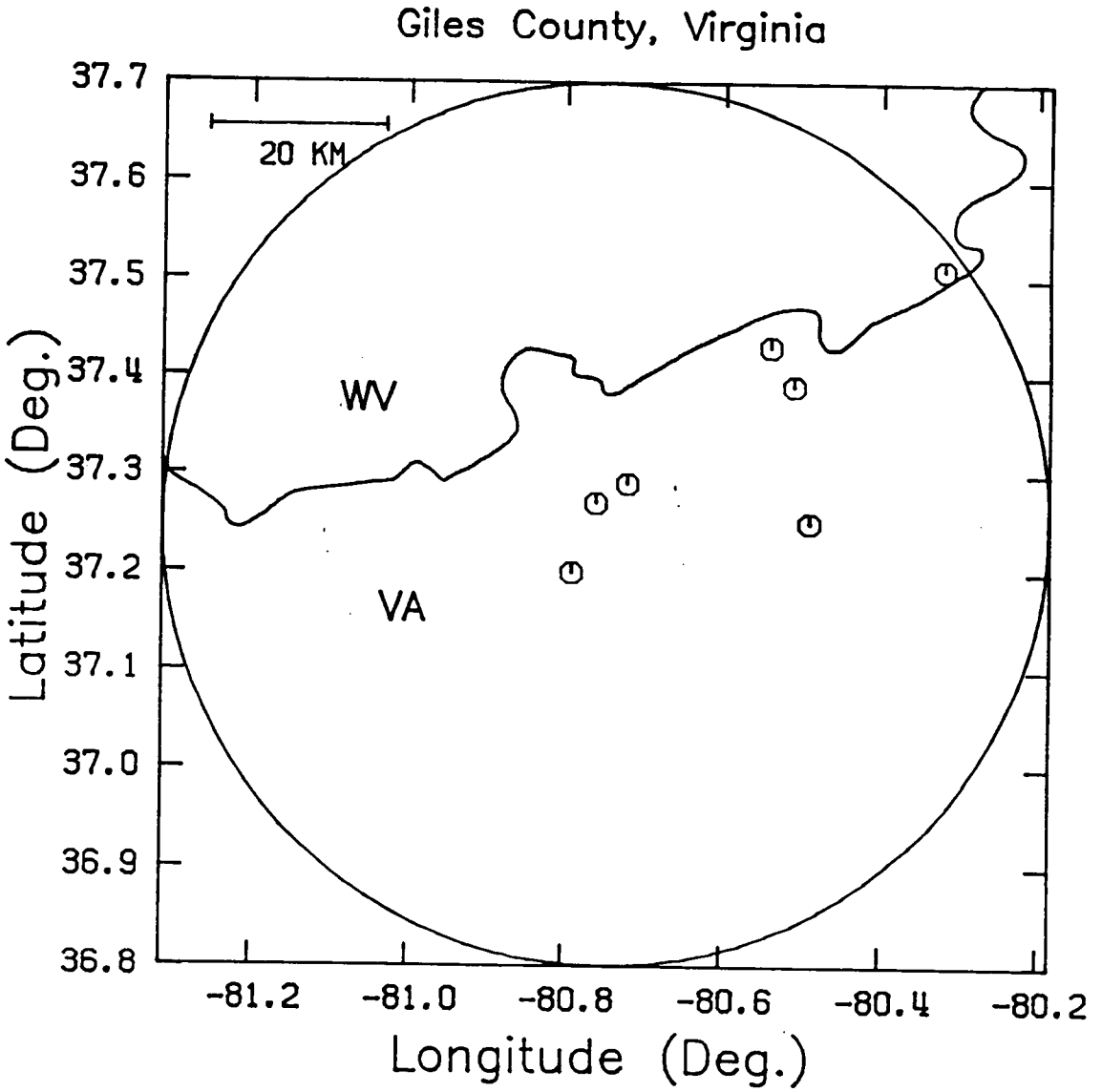

Figure 3. **Giles County, Virginia, Seismic Zone (GCSZ):** Epicenters of the eight events used in this study are shown. Refer to Figure 1 for location of the zone.

The Virginia Tech Seismological Observatory (VTSO) has operated seismic stations in the Giles County vicinity since 1977. That network has produced high quality location data, including accurate depth determinations. A total of 27 earthqakes, the largest of which was an m_b = 2.9 event near Blacksburg, have been recorded since the installation of the network. All earthquakes have been located with the program **HYPOELLIPSE** (Lahr, 1980) using the velocity model developed by Moore (1979). Spatially, the hypocenters define a near-vertical tabular zone trending approximately N45°E at depths generally underlying the detachment surface, which is at 5 - 6 km. The presence of such a lineation is unique among seismic zones in the SEUS.

Gresko (1985) examined the crustal structure of Giles County using reflection data derived from vibrator sources producing both P- and SH- waves. Dominant structures in the shallow crust were interpreted as thrust sheets with bordering faults trending N60-65°E. An important feature pertaining to the seismicity of the region was found below the allochthonous uppermost crust at a depth of 7 - 10 km, where an apparent thickening was interpreted as a series of steeply dipping faults trending N20-27°E. Those structures were assumed to be remanent of normal faulting associated with the opening of the Proto-Atlantic Ocean during the Eocambrian. Current seismicity, which has concentrated around those depths, may be due to reactivation of those faults by appropriately oriented stresses. Another significant result of the reflection study of Gresko (1985) was the similarity of the derived velocity model to that constructed earlier by Moore (1979).

The combination of continuing seismicity and steep topography within the GCSZ has created a potential hazard from strong shaking as well as earthquake triggered debris slides. Miller (1985) used graphical and digital mapping methods to estimate slope stability for Giles County. The data set was synthesized from studies of topography, surficial deposits, geologic structure, and seismic slope response. The county was divided into twelve slope stability categories from which slope movement caused by seismic shaking (among other factors) could be estimated. Areas of highest risk were found to be the obsequent slopes in the central portion of the county and dip slopes on linear ridges in the western part. Although population centers were generally located in areas of low to moderate risk, major highways and rail lines passed through high risk regions. A detailed analysis based on the possible occurrence of a magnitude 7, MMI IX, earthquake in Giles County found

that such an event would severely damage public buildings, electrical power facilities and railroads (Bollinger and others, 1985b).

Central Virginia Seismic Zone. The Central Virginia Seismic Zone is a roughly circular region within the Piedmont physiographic province which exhibits persistent, although scattered, earthquake activity (Bollinger and Sibol, 1985; see Figure 1 and Figure 4). Sequences of events of nearly identical magnitude occurring within a short time span (minutes to months) are common, including a recent swarm of three events (m_b = 3.4, 3.2, and 2.9) near Scottsville in 1981, whose origin times were within an 8 minute period (Sibol and Bollinger, 1981). Other recent felt earthquakes have included a magnitude 4.0 event that occurred during August 1984 near Charlottesville, on the western side of the zone (Davison and others, 1984). On the eastern edge of the zone a series of up to a dozen small (m_b < 2.5), felt earthquakes in Richmond were recorded from December, 1986 through January, 1987 (Davison and Bodé, 1987). Although those small events are typical, larger magnitudes are not unknown; in 1875 the portion of the zone west of Richmond in Goochland County was the site of an earthquake of estimated m_b = 5 (Oaks and Bollinger, 1986).

Seismic data have been collected by instruments installed and maintained by the VTSO during the period since 1978. In the first 10 years of operation, approximately 50 earthquakes have been located. Hypocenters calculated with the velocity model developed by Chapman (1979) generally have depth estimates accurate enough to define events relative to an observed boundary at a depth of about 8 km in the region. That surface was discussed by Pratt (1986), and has been described more recently as a broad, antiformal structure extending from a depth of 18 km on the east near Richmond, shallowing westward to an extreme of 3 - 4 km before deepening to 10.5 km toward the western part of the CVSZ (Çoruh and others, 1988a; 1988b). Seven earthquakes with well-constrained depth estimates (ERZ < 5 km) have been recorded within 5 km of a seismic reflection line which was run through Central Virginia. All of those events correlated with either the major reflector or with associated splay faults above it (Bollinger and others, 1983; Çoruh and

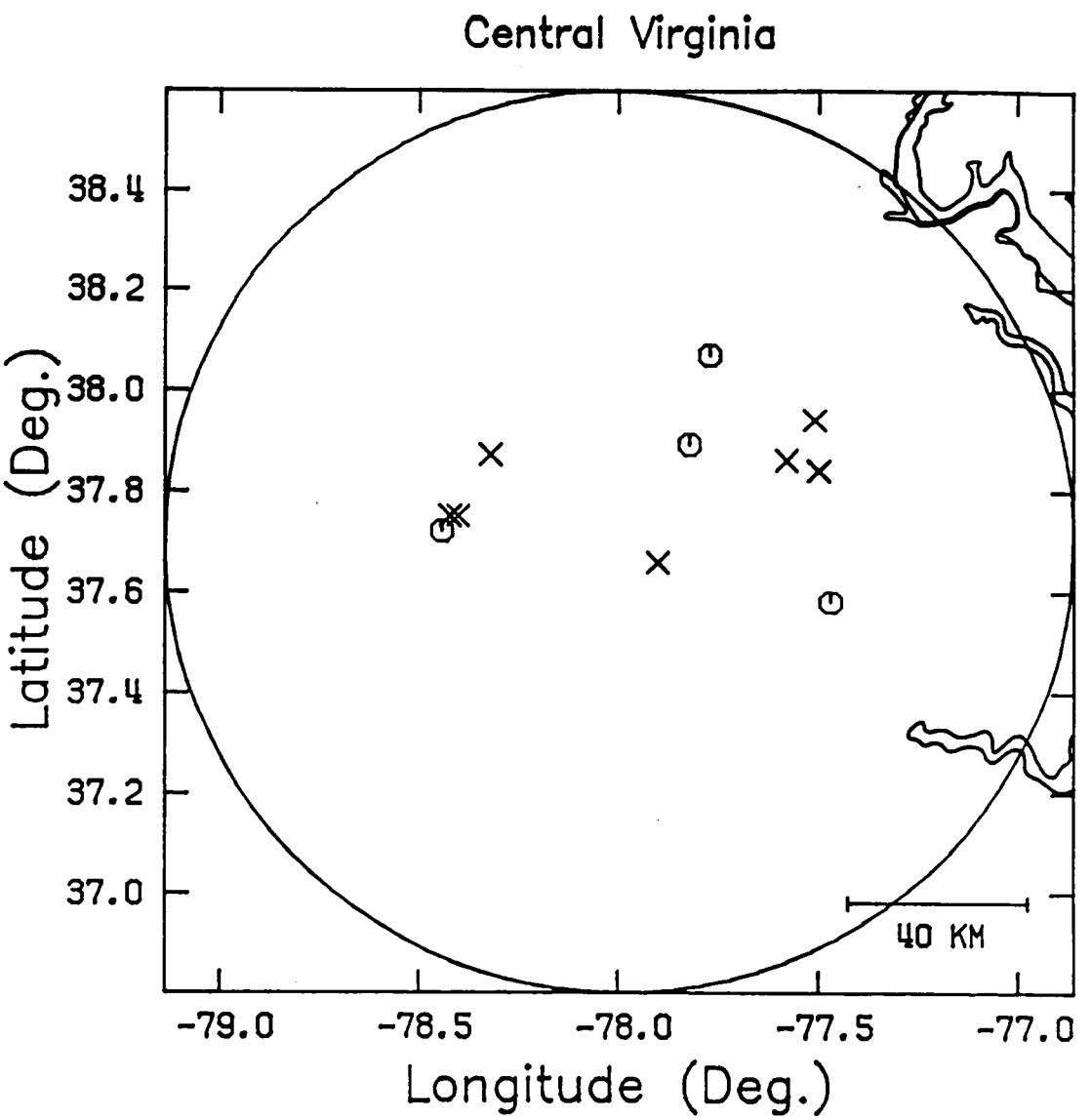

Figure 4. **Central Virginia Seismic Zone (CVSZ):** The 13 epicenters shown indicate those earthquakes for which focal mechanisms were calculated. Circles indicate events interpreted as being above the decollement, x's are for events below that surface. Refer to Figure 1 for location of the zone.

others, 1988b). The CVSZ implies potential earthquake damage for the suburban area surrounding Richmond as well as for nuclear power plants at North Anna on the northern periphery of the zone.

Eastern Tennessee Seismic Zone. The Eastern Tennessee Seismic Zone (ETSZ), located within the Valley and Ridge physiographic province, is presently the most active area in the SEUS (Sibol and others, 1986) and also comprises the largest seismogenic volume of the three study zones. The ETSZ was the site of an MMI VII earthquake in 1913. In addition, three earthquakes with magnitudes greater than 4.0 have been reported since 1925, including a magnitude 4.6 in 1973, near Maryville, Tennessee. That event and its more than 30 aftershocks were studied by Bollinger and others (1976). It was believed that the main shock was caused by reverse movement on a northwest striking fault.

Figure 1 and Figure 5 show instrumental data collected in the ETSZ by instruments installed by the Tennessee Valley Authority and the Tennessee Earthquake Information Center during the period 1981 - 1983. Events have been located using the same velocity model as that developed by Moore (1979) for Giles County, Virginia.

Primary analysis of seismicity in the ETSZ by Johnston and others (1985) was based on more than 100 events obtained during the first thirty months of operation of the 16 station Southern Appalachian Regional Seismic Network. Depths of 58 of those earthquakes were determined as reliable (ERZ < 2 km), based on the distance to the nearest station and the stability of the location calculations. Hypocenters indicated that while events ranged in depth from 3 to 29 km, they were concentrated from 9 - 15 km deep, which is well below the Appalachian overthrust surface. That surface had been defined by seismic reflection profiling as being at a depth of 5 to 6.5 km in the region (Cook and others, 1979). Earthquakes were found to concentrate within the Valley and Ridge Province to a greater extent than suggested by earlier historic data. Most events were situated in an 'Ocoee Block', which was defined as that region bounded on the northwest by the New York - Alabama lineament and on the southeast by the Clingman and Ocoee lineaments. Although those lineations are based on magnetic anomalies interpreted to be caused by structures within the basement, no continuous seismogenic features were inferred from the analysis of the earthquake

data. As with the Giles County Seismic Zone, the northeast-southwest structural trend of the Appalachians in the ETSZ was not found to be colinear with seismogenic features (focal plane solutions, isoseismal contours), which trend more north-south.

Depths of earthquakes in each of the three seismic zones have been found to differ systematically (Bollinger and others; 1985a). Focal depths from the Valley and Ridge and Blue Ridge Provinces (of which the ETSZ and the GCSZ are a part) are significantly deeper than those in the Coastal Plain and Piedmont (containing the CVSZ). The 90% depths within the provinces are 20 km (Valley and Ridge and Blue Ridge) and 13 km (Piedmont and Coastal Plain). For the events used in this study, the average depth for the Valley and Ridge and Blue Ridge Provinces was 13.3 $\pm$ 3.3 km, while the average for the Piedmont and Coastal Plain was 8.5 $\pm$ 4.0 km. The average of each group was thus at least one standard deviation from the depth of the other. Reconciliation of those depths with models based on crustal rheology and heat flow appear to be complex as several unknown quantities must be estimated, including strain rate and crustal composition. Two hypotheses proposed by Bollinger and others (1985a) were that the Valley and Ridge and Blue Ridge Provinces may have much larger strain rates than the Piedmont, or that they contain a higher proportion of quartz-poor rocks in the mid-to-lower crust.

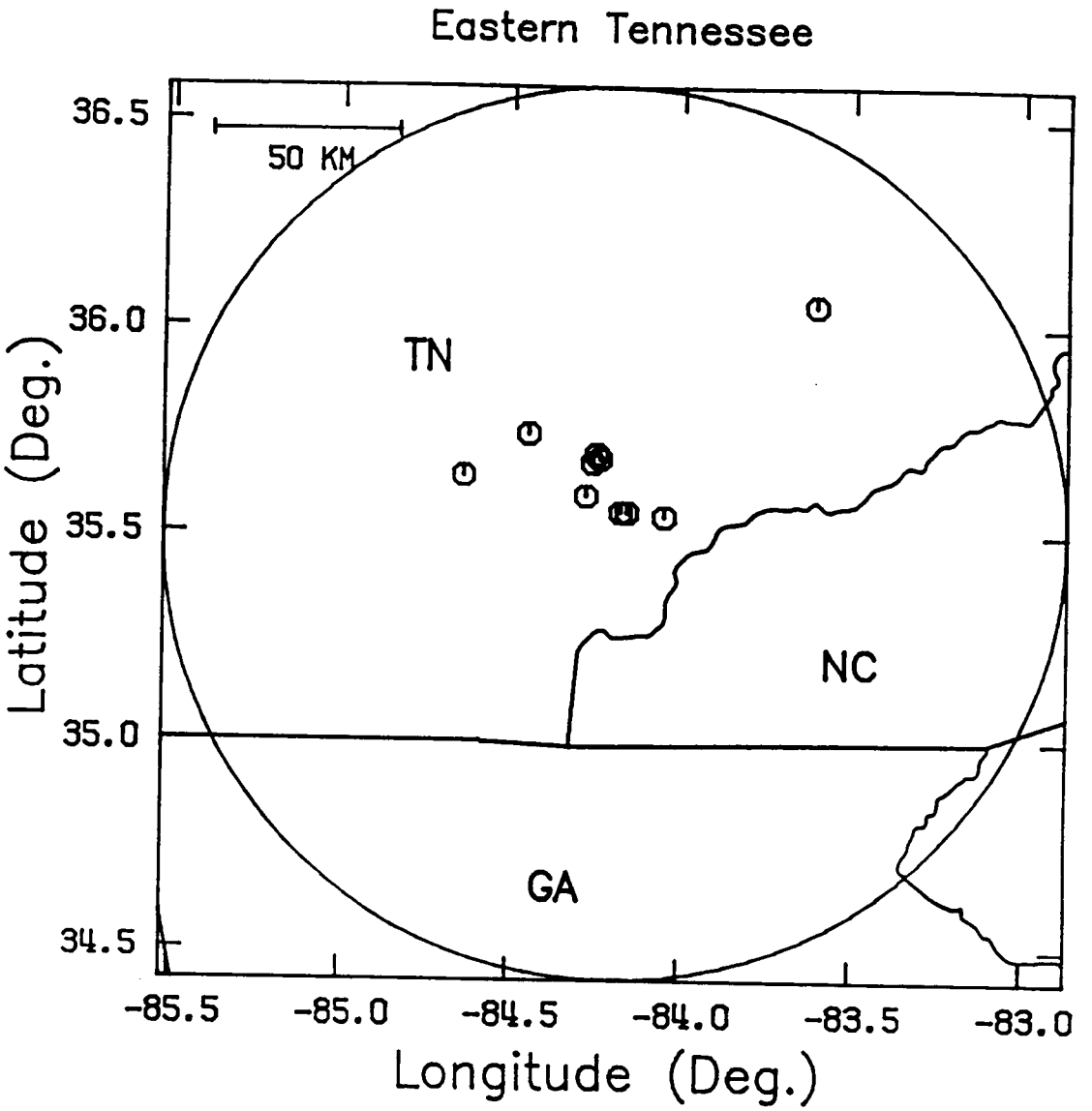

Figure 5. Eastern Tennessee Seismic Zone (ETSZ): Eleven events were used in this study. Refer to Figure 1 for location of the zone.

Previous Research: Failure Criteria, Mode of Faulting, and P-Axis

Failure Criteria

Failure criteria relating causal stresses to movement along a new or pre-existing fracture have been studied to understand faulting and the earthquake process. Stresses responsible for initiating fault motion can be expressed in terms of a tensor, σ_{ij} . A common way to quantify stress is to specify the magnitudes of the principal stresses related to a particular stress tensor. Those values are derived by finding the appropriate coordinate system in which the off-diagonal elements of the given tensor (the shear components) equal zero. The diagonal members of the matrix, σ_{11}, σ_{22}, and σ_{33}, are the values of tension (negative) or compression (positive) acting upon the principal planes, which are perpendicular to the new coordinate axes. Those components are redefined as the principal stresses σ_1, σ_2, and σ_3, such that;

$$\sigma_1 > \sigma_2 > \sigma_3.$$

The orientation of the principal stresses can be related to a geographic coordinate set (e. g. north, east, down) by a rotation matrix. For basic derivations of the stress matrix and discussion of tensor notation and rotation, see Means (1976). In the following discussion the magnitude and direction of the maximum principal stress ($\overline{\sigma}_1$) and minimum principal stress ($\overline{\sigma}_3$) will be considered. The orientation of those vectors will be used to describe the normal stress ($\overline{\sigma}_n$) and the shear stress ($\overline{\sigma}_s$) along any arbitrary planar surface in a three-dimensional, homogeneous medium. In addition, we will deal only in the plane within such a medium which includes both the $\overline{\sigma}_1$ and $\overline{\sigma}_3$ vectors.

The use of a two-dimensional model has been justified by Jaeger and Cook (1969; p.99). Figure 6 shows a three-dimensional Mohr diagram for a material subjected to a stress with principal values of σ_1, σ_2, and σ_3. By convention, σ_n is plotted on the abscissa and σ_s on the ordinate. A - B is the graphical representation of an experimentally derived failure curve, specific examples of which will be given later in this discussion. In general, when the failure curve touches the perimeter of the largest circle (related to σ_1 and σ_3 magnitudes), failure will occur. Two conclusions are obtained from such a relationship. First, the intermediate magnitude principal stress (σ_2) does not affect the initiation of failure; rather it is the stress deviator (σ_1 - σ_3), which is the critical factor (Blès and Feuga, 1986; p. 24; also called the differential stress; e. g. Sibson, 1974). Secondly, the plane of failure must be perpendicular to the $\overline{\sigma}_1$ - $\overline{\sigma}_3$ plane, and thereby passes through the $\overline{\sigma}_2$ vector.

From the previous discussion it becomes evident that the mechanism most often associated with earthquake faulting is shear failure in which the fault plane is oblique to the principal planes of the stress tensor. Actually, rock is weakest under tension. However, except in cases such as downwarping due to lithostatic loading or bending of plates at subducting margins, large-scale tension is much less common than compression. Therefore we will consider only the case of shear failure of rocks under general compression ($\sigma_1 \neq \sigma_2 \neq \sigma_3$; all values positive), a condition which is common in the Earth (Means, 1976; p. 80).

For the case of stress in two dimensions, the magnitudes of the normal and shear stresses across any plane perpendicular to the $\overline{\sigma}_1$ - $\overline{\sigma}_3$ plane can be written,

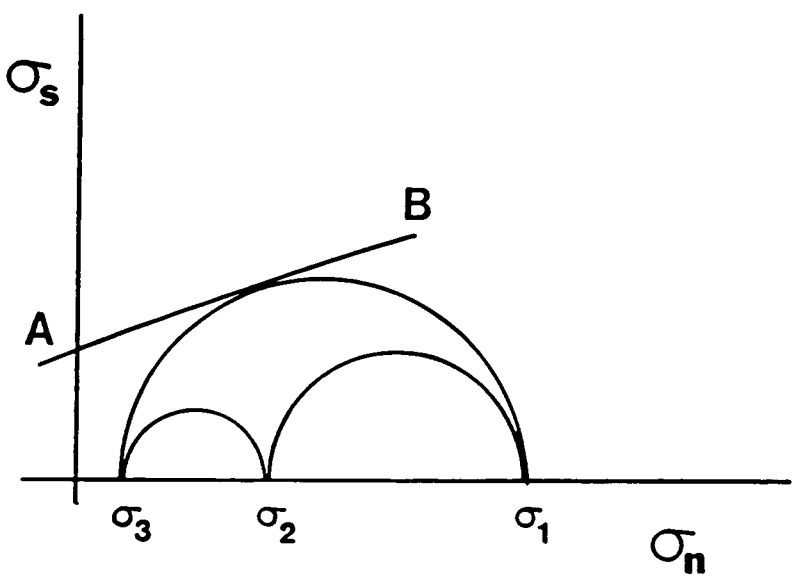

Figure 6. **Mohr's circle for three-dimensional stress:** Magnitudes of principal stresses are shown along the horizontal (σ_n) axis. The ordinate gives the value of shear stress (σ_s). The curve A - B represents an experimentally derived failure criterion relating σ_n to σ_s. Failure is controlled by the values of σ_1 and σ_3 , since the relative location of σ_2 does not affect the radius of the largest semi-circle. Figure adapted from Jaeger and Cook (1969; p. 99).

$$\sigma_n = \sigma_{11} \cos^2\theta + 2\sigma_{13} \sin\theta \cos\theta + \sigma_{33} \sin^2\theta$$

and

$$\sigma_s = \frac{\sigma_{33} - \sigma_{11}}{2} \sin 2\theta + \sigma_{13} \cos 2\theta,$$

following Jaeger and Cook (1969; pages 12 - 14). In those equations, θ represents the angle between maximum compressive stress and the normal to the plane under consideration. In this analysis, compressions are considered positive.

If we then rotate the coordinate system so that it coincides with the principal stress directions ($\overline{\sigma}_1$ and $\overline{\sigma}_3$), the two equations reduce to;

$$\sigma_n = \frac{\sigma_1 + \sigma_3}{2} + \frac{\sigma_1 - \sigma_3}{2} \cos 2\theta$$

and

$$\sigma_s = -\frac{\sigma_1 - \sigma_3}{2} \sin 2\theta.$$

It is thus implied that the maximum shear stress is on the planes represented by θ = 45° and 135°. Although this is a satisfactory starting point, it disagrees with observations. In laboratory experiments the angle of fresh cracks generated in homogeneous rock is approximately 30°.

The first rigorous analysis of rock fracture resulted in what has become known as the Coulomb failure criterion (Coulomb, 1773; see Hobbs and others, 1976; p. 316). In that early work the following relationship was derived:

$$\sigma_s = C + \mu\sigma_n,$$

where C represented a rock property known as the cohesion or shear strength and the proportionality constant μ was called the coefficient of internal friction. In this form, μ affects the orientation of the new fault plane and C dictates the magnitudes of σ_1 and σ_3 at which failure will

occur. The value of μ has been found experimentally to be approximately 0.6 over a wide range rock types, which corresponds to an angle of about 29.5° between $\bar{\sigma}_1$ and the plane of faulting.

If fractures exist in a rock body, another important factor, the friction on the fault plane, becomes important. The coefficient of friction is analogous to the parameter μ introduced in the Coulomb criteria, and is frequently represented by the same symbol. However, confusion is often associated with the type of friction being discussed. Three types are common in the literature, and are often not defined specifically, but are referred to only by the general term, coefficient of friction (Byerlee, 1978). Assume two rock masses in contact with one another along a smooth surface. When a force parallel to the fault surface is applied to the materials on one side of the contact, the value of friction when sliding originates is the *initial* friction. This value increases until an upper limit, the *maximum* friction, is reached. Sliding then proceeds, either in a stick-slip or smooth fashion. The value of the coefficient of friction associated with stable sliding is known as the *residual* friction. For studies of movement associated with earthquakes, we most often are concerned with the maximum friction.

In large-scale tectonic movement, such as that associated with regional thrust faulting, early calculations indicated that friction was large enough to preclude any fault movement whatsoever. Therefore, it became necessary to introduce the role of fluid pore pressure into the faulting process. This was first studied in detail by Hubbert and Rubey (1959) and became known the law of effective stress. In that research σ_n was redefined as

$$\sigma_n \equiv \sigma_n' = \sigma_n - p,$$

where σ_n' was known as the effective normal stress and p was a measure of the pore fluid pressure. In other words, the liquid within a porous material could effectively reduce the normal pressure across a pre-existing fault. Since the frictional force is a function of the normal pressure across the fault plane, a reduction of sliding resistance would accompany any increase of pore pressure. In terms of a Mohr's circle analysis, the introduction of pore pressure effectively moves the values on the normal stress axis closer to an intersection with the failure curve by reducing the values of the normal stresses plotted along the abscissa.

A dramatic example of seismicity induced by high pore pressure was observed for the Rocky Mountain arsenal near Denver, Colorado (Evans, 1966; Healy and others, 1968). A high-pressure injection well began operation at the arsenal in March, 1962. In the next 30 months, the Denver area, which had been seismically quiet since 1882, experienced 710 earthquakes, of which 21 were magnitude 3 or larger. The rate of those seismic events correlated with the periods of well operation. It was determined that the increased pore pressure at the bottom of the well was lowering the effective normal stress across pre-existing fractures in Precambrian gneiss, allowing slippage to occur. A subsequent controlled experiment in earthquake generation was undertaken by Raleigh and others (1972) in an oil field near Rangely, Colorado. Fluids injected under pressure at depth in wells was also found to influence the normal pressure and lead to increased seismic activity.

The pore fluid pressure has been described to occur naturally in the crust as:

$$p = \lambda \sigma_v,$$

where σ_v is the vertical stress. In that relationship, λ is the pore fluid factor relating the normal stress across a surface both with and without the presence of a fluid;

$$\sigma_f = \lambda \sigma,$$

where σ_f is the normal stress with the fluid, and σ , without. The value of λ has been calculated to be 0.46 under normal conditions (see Ramsay, 1967; p. 287), but has been observed to be as large as 0.9 under abnormally high pressure situations (Hubbert and Rubey, 1959). If lithostatic conditions are assumed and fluid is present, the vertical stress may be approximated by

$$\sigma_v = \rho g z(1 - \lambda),$$

in which ρ is the crustal density, g is the acceleration due to gravity, and z is the depth. For some cases as discussed later, an increase in depth could relate to a change in the nature of faulting due to both the increased pore pressure and larger vertical stress.

The work of Byerlee (1978), known as the law of rock friction, examined the relationship of σ_n and σ_t at high pressures such as those which exist down to mid-crustal depths. The following relationship was found to hold:

$$\sigma_s = \mu' \sigma_n',$$

in which μ' was the coefficient of maximum friction. For shallow depths (σ_n < 2kbar = $2 \times 10^2 MPa$), the value of μ' was found observationally to be equal to 0.85. In deeper crust, an additional term was needed to make an empirical fit to the observed data. At those depths;

$$\sigma_s = 0.5kbar + 0.6\sigma_n',$$

where $0.5kbar = 50MPa$. The additional constant term added to that equation may be interpreted as the shear strength of the rock which may be enhanced in the high pressure regime. The depth of transition from the first equation to the second corresponded to about 6.5 - 8 km, based on an average lithostat (Spencer, 1972; p. 123). On the average over both depth ranges, the relationship between shear stress and normal stress was found to closely follow

$$\sigma_s = 0.75\sigma_n',$$

and was virtually independent of rock type. Although the results of Byerlee (1978) were valid for initially finely-ground interlocked surfaces as well as for new irregular faults produced in intact rock, they have been found to fail in cases where large thicknesses of low-friction gouge separate the fault surfaces.

Mode of Faulting

In the above discussions, we have dealt with general observations regarding rock failure. The relationship of crustal stresses to the mode of faulting was first discussed quantitatively by Anderson

(1951). All faulting was assumed to be the result of new fractures occurring in homogeneous rock. Planes of maximum shear (and thereby faulting) were shown to be 45° from the maximum compressive stress, but the actual attitude of the fault plane was found subsequently to be controlled by the value of μ, as described earlier. When applied to brittle fracture in the crust, it was shown that the orientation of the principal stresses was responsible for the mode of faulting:

1) Reverse faulting - $\overline{\sigma}_1$ horizontal, $\overline{\sigma}_3$ vertical;

2) Normal faulting - $\overline{\sigma}_1$ vertical, $\overline{\sigma}_3$ horizontal; and,

3) Strike-slip faulting - $\overline{\sigma}_1$ and $\overline{\sigma}_3$ horizontal.

In all cases the fault was perpendicular to the plane containing the maximum and minimum principal stresses. If a principal stress was vertically oriented, an increase in depth would give it a greater magnitude. That could lead to a transition from, for example, a shallower zone characterized by reverse faulting to a deeper one dominated by normal faulting.

Bott (1959) discussed the various types of faulting in relation to the vertical and horizontal stresses, which he defined as σ_z, σ_x, and σ_y (σ_z vertical; σ_x and σ_y horizontal). The degree of oblique faulting (i. e. other than pure strike-slip or pure dip-slip) was shown to depend on the relative magnitudes of those stresses, thereby allowing movement on a fault in any direction. That direction was shown to be controlled by the maximum shear stress resolved on the fault. Thus, the occurrence of different modes of faulting along pre-existing fractures does not imply an inhomogeneous stress field but simply slippage on the weakest fault subjected to the greatest shear stress. That factor has become the most important assumption when inverting fault or slip data to derive the stress tensor.

Sibson (1974) examined the mode of faulting as a function of depth and the differential stress, which was defined as $\sigma_3 - \sigma_1$. Curves were constructed which indicated the minimum value of the differential stress necessary to cause sliding on different types of faults. Density, gravity, and μ were fixed (values of 2.8 gm/cm^3; 980 cm/s^2; 0.75; respectively) and the faults were assumed to be ideally oriented, i.e., following the discussion of Anderson (1951). Predictably, the differential stresses increased linearly with depth, with the largest values required to initiate slippage on reverse faults,

and the smallest values for normal faults. This result reflects the general observation that, for reverse faulting, σ_v equals σ_3, while for normal faulting, $\sigma_v = \sigma_1$.

Since brittle faulting has been observed only to mid-crustal depths in typical continental crust, Sibson (1982) also examined the nature of the brittle-ductile transition as it affects normal, reverse, and strike-slip faulting. Shear resistance of the crust was found to increase with depth, until heat flow effects forced the rock to behave in a ductile manner. That depth corresponds to the base of the earthquake zone. One implication of Sibson's (1982) study was that larger earthquakes would nucleate at depth, where shear resistance was the largest, allowing the greatest accumulation of strain energy. A more general discussion relating to fault geometry and dependency on rock type can be found in Sibson (1983).

P-axis

The **P**-axis of a focal mechanism solution has often been used to infer the maximum compressive stress direction. This has been in spite of the fact that the **P**-axis itself is defined by the double-couple source model always to be 45° from the fault plane (Aki and Richards, 1980; p. 82). McKenzie (1969) showed that focal mechanism data were not sufficient to determine the orientation of the maximum compressive stress for an earthquake, unless that event represented rupture of a previously homogeneous, unfaulted material. The only constraints found were that the $\bar{\sigma}_1$ direction must be confined to a dilitational quadrant of the focal sphere, though it could be up to 90° from the actual fault plane. In other words, the error between a true $\bar{\sigma}_1$ direction and the computed **P**-axis could be as large as 45°. Sbar and Sykes (1973) tried to reconcile the difference between the theoretical and observed relationship of $\bar{\sigma}_1$ and the **P**-axis by making the additional assumption that $\bar{\sigma}_1$ was 30° from the slip vector in the direction of the **P**-axis, based on rock fracture experiments. The assumption was made that one had *a priori* knowledge to distinguish the fault plane from the auxiliary plane. Raleigh and others (1972) used physical measurements to document that the $\bar{\sigma}_1$ direction and the trend of the **P**-axis were within $\pm 35°$ from one another.

An interesting relationship between stress orientation and the mode of faulting was observed recently by Zoback and others (1987), who showed that the compression associated with the San Andreas fault in California was nearly perpendicular to the strike of the fault. Their data consisted of focal mechanism solutions, wellbore breakouts, hydraulic fracturing experiments, and volcanic alignments. Those results were significant because they indicated that the San Andreas fault zone was quite weak, and therefore should not produce high heat flow values due to frictional heating. That helped to explain the earlier work of Lachenbruch and Sass (1980), who found no heat flow anomalies associated with the large amount of slip along the San Andreas. The results were also significant because they demonstrated the reorientation of a regional *in situ* stress field produced by a very weak fault zone. Such reorientations are not observed in seismic zones of the central and eastern United States, implying that the intraplate seismic faults are not 'weak' in the same sense as the major San Andreas transform fault and/or that they are simply not large enough to significantly alter the regional stress orientation.

Previous Research: Regional Stress Regime

Sbar and Sykes (1973) examined the relationship between compressive stress and seismicity in eastern North America. Overall, their results suggested an east to northeast trend of the maximum compressive stress. In the southern Appalachians, however, results were not so simple. Because *in situ* stress measurements of varying directions were made in igneous and metamorphic rocks in that region, the authors proposed that remnant stresses were contaminating any regional trends. In a later study, Haimson (1977b) used all available hydrofracturing data to calculate the mean direction for the horizontal compressive stress in the Southern Appalachians, and found it to be N65°E $\pm$ 15°.

Zoback and Zoback (1980) used data from several sources to estimate the state of stress in the crust of the conterminous United States. They postulated a northeastward directed compressive stress within most of the midplate region, with the possible exception of an anomalous zone of northwestward stress along the Atlantic seaboard. Further investigations (Zoback and Zoback, 1985; Zoback and others, 1985), were based on more highly constrained data and indicated that the northeastward trend was characteristic of the entire intraplate region. Data in all studies were derived from hydraulic fracture and overcoring of drill holes and from focal mechanism solutions, including measurements from the Charleston Seismic Zone (Zoback and Healy, 1977; Talwani, 1982).

Shallow *in situ* horizontal stress measurements have been made using the overcoring technique in several mining districts of the SEUS (see Table 1). In the Appalachian Piedmont north of the CVSZ (near Rapidan, Virginia), Hooker and Johnson (1969) derived a maximum horizontal stress of 1678 psi ($1.1 \times 10^3 MPa$) and a minimum of 1385 psi ($9.5 \times 10^2 MPa$) with orientations of N6°E and S84°E, respectively. Data were collected on the near-surface in competent diabase. Other measurements were reported by Hooker and Johnson (1969) west of the ETSZ in the Mount Airy Granite at a depth of 33 ft (10 m) and indicated a maximum compressive stress direction of N87°E with a magnitude of 2464 psi ($1.7 \times 10^3 MPa$). Two additional values of horizontal stress were reported by Aggson (1978) close to the GCSZ and ETSZ, and at greater depths. In the Beckley No. 1 Mine near Bolt, West Virginia, southwest of the GCSZ, the horizontal direction of the maximum compressive stress was N69°E, and had an approximate value of 3000 psi ($2.0 \times 10^3 MPa$). Measurements were made in the mine at a depth of 700 feet (213 m). Within the ETSZ, near Knoxville, Tennessee, horizontal stress was calculated in the Immel mine at the 925 foot (282 m) level. Orientation of the 3007 psi ($2.1 \times 10^3 MPa$) maximum horizontal stress was found to be N58°E. A single hydrofracturing measurement has been reported by Haimson (1977b) for a vertical borehole near Wayne, West Virginia, west of the GCSZ. That measurement, made at a depth of 840 meters, showed the orientation of the maximum horizontal stress to be oriented N50°E.

Bollinger and Wheeler (1988) compiled a list of *in situ* stress measurements for the region surrounding the Giles County Seismic Zone, most of which were not included in the above discussion. Those measurements were made by two techniques; hydrofracturing and petal-centerline fractures. The petal-centerline method involved the measurement of the orientation of vertical cracks induced during drilling. The combined data were analyzed and high-graded using criteria based upon factors including depth and location of the measurement. All data were chosen which were likely to be representative of the stress regime at seismogenic depths. The horizontal orientations of the 8 best measurements had a median value of N64°E. Combination of those results with focal mechanism solutions led Bollinger and Wheeler (1988) to argue that the

maximum compressive stress is likely to plunge to the southwest, even though that value was poorly constrained.

Table 1 shows the directions of the maximum horizontal compressive stress for the zones of this study and surrounding regions. Note that while each azimuth is within the northeast quadrant, the directions vary significantly, averaging 56 $\pm$ 25° for the entire region. However, as those measurements were made at different depths, such a variation is not surprising. Also, most of the deeper measurements were taken very near to mine tunnels, which themselves may have altered the local stress field.

Observations of regional stresses have been made recently for specific seismic zones of the SEUS using earthquake data. In the Giles County Seismic Zone a limited number of focal mechanism solutions were available prior to network installation. One solution, derived by Herrmann (1979) from surface wave data, was constructed for the Elgood, WV, earthquake of November 20, 1969. The **P**-axis of that solution was horizontal, and had an orientation of S14°E. However, a later study of that event, combined with considerations of fault zone geometry and borehole fractures, postulated east to northeast trending compressive stress (Wheeler and Bollinger, 1981). Munsey (1984) studied 11 Giles County earthquakes and also concluded that the horizontal compressive stress trended northeast-southwest. That orientation was nearly the same as that for the ETSZ further to the southwest, but was significantly different from events located further northeast along the trend of the Appalachians in Bath County, VA. In that area Todd (1982) used sparse data to construct a focal mechanism solution with one well-constrained nodal plane, which had an east-west strike and dipped to the south.

Detailed examination of 16 earthquake mechanisms (11 single event, 5 composite) by Munsey (1984) implied that different modes of faulting occurred on either side of the 8 km boundary within the Central Virginia Seismic Zone. Focal mechanisms were predominantly dip-slip for the shallower events and strike-slip for deeper earthquakes. In addition, **P**-axes in the uppermost crust exhibited clustering in the northeast and southwest quadrants, while those below the decollement were grouped to the northwest and southeast. In the majority of cases the **P**-axes were subhorizontal regardless of depth. When plotted against depth, the azimuths of the **P**-axes were

Table 1. *In situ* Maximum Horizontal Stress Measurements.

Location	Azimuth (°)	Depth(m)	Magnitude MPA x 1000	Authority
Rapidan, Virginia	6	Near-surface	1.1	Hooker and Johnson,1969 *
Mt. Airy Granite, TN	87	10	1.7	Hooker and Johnson, 1969 *
Bolt, WV	69	213	2.0	Aggson, 1978 *
Knoxville, TN	58	282	2.1	Aggson, 1978 *
Wayne, WV	50	840	---	Haimson, 1977b **
Surrounding GCSZ	64	---	---	Bollinger and Wheeler, 1988 ***

* - Overcoring technique
** - Hydrofracturing
*** - Composite of hydrofracturing and petal-centerline fractures

found to be about N30°E close to the surface, then varied systematically to nearly S60°E at a depth of 15 km.

The viewpoint of Munsey (1984) was later opposed by Nelson and Talwani (1985). In that work, a total of twelve earthquakes were incorporated into five composite fault plane solutions with one additional single event solution. Although the events were identical to those used by Munsey (1984), compositing of the P-wave polarity data was based on different criteria, with earthquakes grouped according to depth considerations as well as similarity of solution type. Amplitude ratio data utilized by Munsey (1984) were ignored. In spite of the fact that the total range of **P**-axis trends spanned from N38°E to S25°E, the preferred solutions were limited from N60°E to N75°E.

Teague (1984) examined 18 focal mechanism solutions (11 single event solutions; 7 composite solutions) for Eastern Tennessee and determined that the trend of the maximum compressive stress (based on the **P**-axis) averaged about N50°E. That agreed closely with focal mechanisms reported earlier by Bollinger and others (1976), and Herrmann (1979) and was consistent with the trend obtained by Munsey (1984) for the Giles County Seismic Zone. Although Teague (1984) did not observe a substantial change of stress orientation with depth in the ETSZ, he did show that with an increase of focal depth, the **P**-axes became more closely restricted to follow a trend of 40 - 50 degrees and a plunge of 5 - 10 degrees. Both the work by Munsey (1984) and Teague (1984) were based only on the **P**-axes of the *single* preferred focal mechanism solution from each earthquake selected from the family of acceptable solutions produced by **FOCMEC**.

Johnston and others (1985) analyzed four new focal mechanism solutions for earthquakes in the ETSZ. Three of those were for instrumentally recorded main shock - aftershock sequences, while the fourth was a composite of 47 events within the Valley and Ridge Province. **P**-axis orientation suggested a horizontal southwest-northeast compressive stress on faults with north-south orientation. Those results were significantly different from most previous studies and demonstrated the importance of well-constrained, instrumental data collected by a small aperture network.

In summary, estimates of the maximum compressive stress have been made for the seismic zones of the Southeastern United States, based on scattered focal mechanisms and *in situ*

measurements. The borehole data generally trended northeast for the Giles County and Eastern Tennessee Seismic Zones, agreeing with the results based on either the **P**-axis direction of focal mechanism solutions or on the superposition of the **P**-axis quadrants. The single borehole measurement near the Central Virginia Seismic Zone was made at shallow depth in competent diabase (Hooker and Johnson, 1969). That measurement will be discounted as it represented neither the depth nor probable lithology of the seismogenic region. Focal mechanism solutions in the CVSZ indicated a change in **P**-axis orientation with depth, varying from northeast above 8 km to northwest for events below that depth. All stress estimates will be compared later with the results of this study.

Data

Data Collection and Quality Control

Most of the first motion and amplitude data for the three seismic zones of interest were originially collected and published in the theses of Munsey (1984) and Teague (1984). Data for earthquakes from the Central Virginia and Giles County Seismic Zones subsequent to those studies have been added. Seismic data from those zones have been recorded digitally since April, 1985, and thus are of superior quality. A total of 32 earthquakes from both sources were used in this study.

To insure consistent results of focal mechanism calculations, emphasis was directed towards quality control of the input data, which were recorded by local networks operated by Virginia Tech (Giles County and Central Virginia Zones) or by the Center for Earthquake Research and Information (formerly the Tennessee Earthquake Information Center) and the Tennessee Valley Authority (Eastern Tennessee Seismic Zone). Additional data at regional distances were obtained from the New York Network operated by Woodward-Clyde Consultants. All stations used in the collection of first motion and amplitude data are shown on Figure 7. P-wave polarities and amplitudes of both P- and S-waves were read within the first cycle and a half of phase arrival. Station polarities were checked periodically for proper orientation by comparing with impulsive teleseismic arrivals. Only those events less than 100 km from each station were used for amplitude

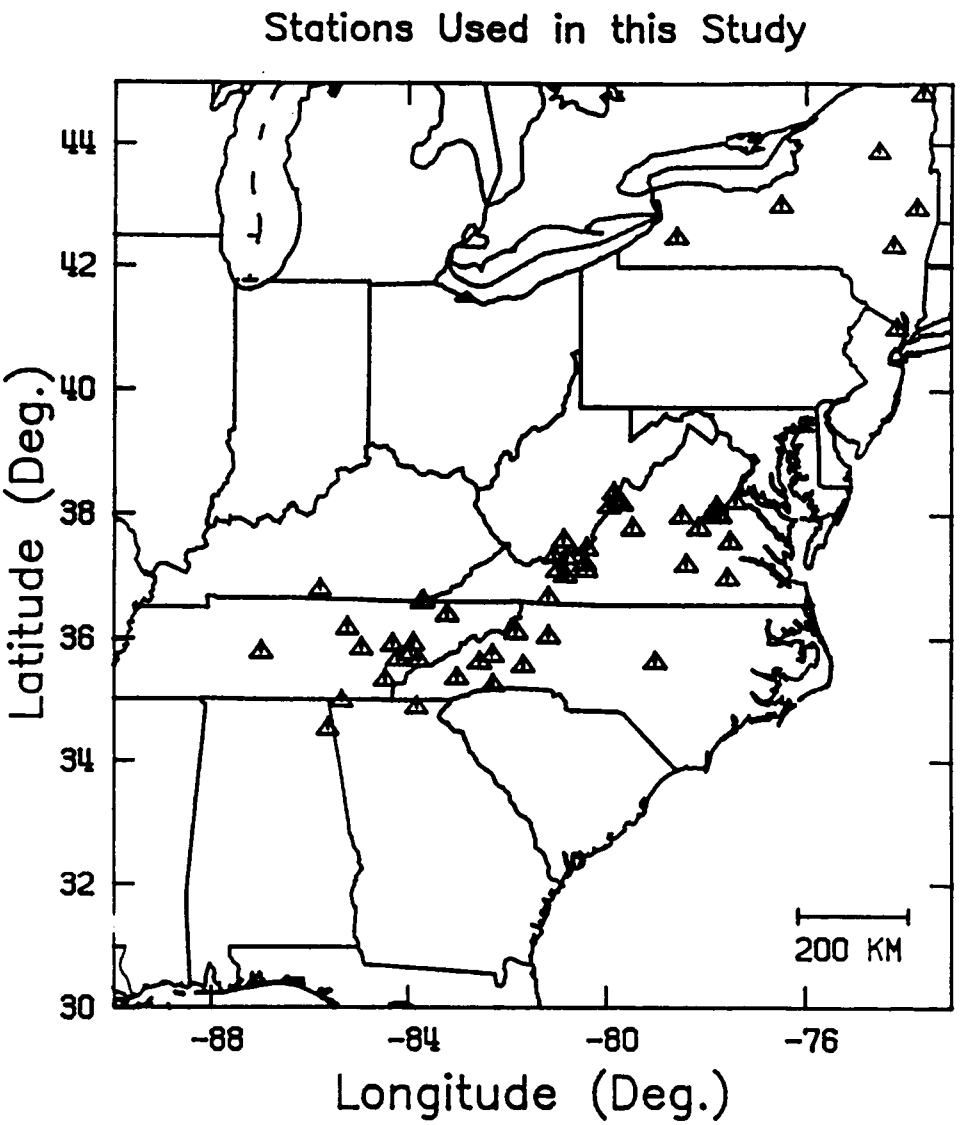

Figure 7. **Seismic Stations used for collection of data:** The stations shown (small triangles) were used to collect first motion and/or amplitude ratio data for calculation of focal mechanism solutions.

data to eliminate possible head wave interference and minimize the effects of differences in attenuation. Finally, all records were read by at least two independent observers, with any inconsistent data being deleted.

Preliminary Data Reduction

As local and regional earthquakes occurred, epicenters and depths were routinely calculated at the VTSO using the program **HYPOELLIPSE** (Lahr, 1980). Azimuths and take-off angles from the hypocenter to the regional recording stations were then computed by the program **RAYFIND**, which allowed a choice of crustal velocity models. It was determined at that stage which data were not to be used in the calculation of focal mechanisms. Raypaths with shallow ($< 2°$) emergence angles were not considered. Rays with emergence angles from 27 to 40 degrees were also eliminated because of the rapid variation of free surface effects within that range (Kisslinger and others, 1981; 1982).

Two types of data were necessary for calculation of focal mechanism solutions; the polarity of the P-wave arrival and the ratio of the amplitude of the vertical components of the P-wave to the SV-wave. After the data were high-graded, an average of 6 polarity readings and 5 amplitude ratios were available for each earthquake. Only one event (Event 111 in the CVSZ) had no relible ratio measurements. The limited data set for each earthquake required an objective approach in the determination of reliable focal mechanism solutions. As previously mentioned, rather than a single solution for each earthquake, a range of possible solutions was calculated.

Program FOCMEC

Program **FOCMEC** (Snoke and others, 1985) was the primary tool used to determine focal mechanism solutions for seismic events. Input data were compared with a large number of test

solutions to identify possible nodal planes and the associated **P** (pressure), **T** (tension), and **B** (null) axes. That search was made by uniformly sampling the focal sphere in such a manner that more than 25,000 hypothetical solutions were tested for each earthquake. In addition to polarity and amplitude ratio, the azimuth and take-off angle of the ray from the hypocenter to the station were necessary input data. The program required the researcher to choose the number of errors allowed before a theoretical solution was judged a misfit. **FOCMEC** allows different raypaths for P- and S-waves.

Polarity data involved only the vertical component of the P-wave, and thus constrained the raypath to be in either a compressional or dilitational quadrant of the focal mechanism solution. If a polarity did not correspond to the correct quadrant of the tested solution, an error was declared. No degree of fit could be calculated, as a polarity would either fit the solution, or it would not. An option does exist within the program to weight any polarity error according to its relationship with the assumed nodal plane, however, that option was not routinely used.

The second type of input data was the ratio between the vertical component of the amplitudes of the SV-arrival and the P-arrival. That ratio varies within each of the quadrants of the focal mechanism solution. At close distances (< 100 km) the ratios are independent of magnitude. Ratios are more stable to use in calculations than the amplitudes themselves because they do not require that the seismograph be acurately calibrated (Kisslinger,1980). The solution was considered a match if the ratio was within a certain predetermined range of the theoretical value. Values of the subjectively determined allowed difference between the measured and theoretical amplitude ratios are given in Table 2 through Table 4 for each of the seismic zones. Those differences range in value from 0.15 to 0.26. Both ratios and ratio error allowances were expressed in terms of logarithms. Root-mean-square (RMS) values could then be calculated by taking the square root of the squares of the difference between known and theoretical ratio values. Two RMS calculations were made in **FOCMEC**. The first calculated the error associated with only the accepted ratio measurements, while the second indicated the error for all ratio data. Often these two values were compared when choosing a best single solution (Munsey, 1984). Amplitude ratios required the most intensive calculations within the program, as corrections must be made as waves propagated

through the assumed velocity structure, then were converted to vertical motion at the surface (Kisslinger and others, 1982). The addition of $(SV/P)_z$ ratios has been very instrumental in allowing the researcher to reduce the number of possible solutions based only on polarity data. However, amplitude ratio data themselves do not fully constrain the problem, as the sense of slip on the fault surface cannot be resolved. There are also some fault plane orientations (i. e. strike-slip motion on a near vertical fault) which are not well resolved (Kissingler, 1980). In most cases, however, those ambiguities are removed by the addition of polarity data.

Output from **FOCMEC** was in the form of a set, or 'family', of acceptable solutions for each group of input data. Use of that full set of solutions was the most appropriate manner for displaying focal mechanisms, as the distribution of possible solutions was directly related to the constraints provided by the original polarities and amplitude ratios. Due to the symmetry of solutions about the two nodal planes, **FOCMEC** cannot distinquish between the fault plane and auxiliary plane. At the VTSO, the fault plane was chosen as that nodal plane on which the rake of the slip (measured counterclockwise from horizontal) was between the values of -90° and 90°, since no geologic constraints were possible. In Figure 8 are shown examples of both a well-constrained and a poorly-constrained **FOCMEC** solution to demonstrate the difficulty of picking a single best solution from a solution set. As a solution to that difficulty, error statistics generated by the program were used in previous studies to choose a preferred solution. However, we propose to use the **entire family of solutions** produced for each single event to constrain the stress tensor, with each member of the solution set subjectively weighted according to the quality of fit between the original input data and each hypothetical solution.

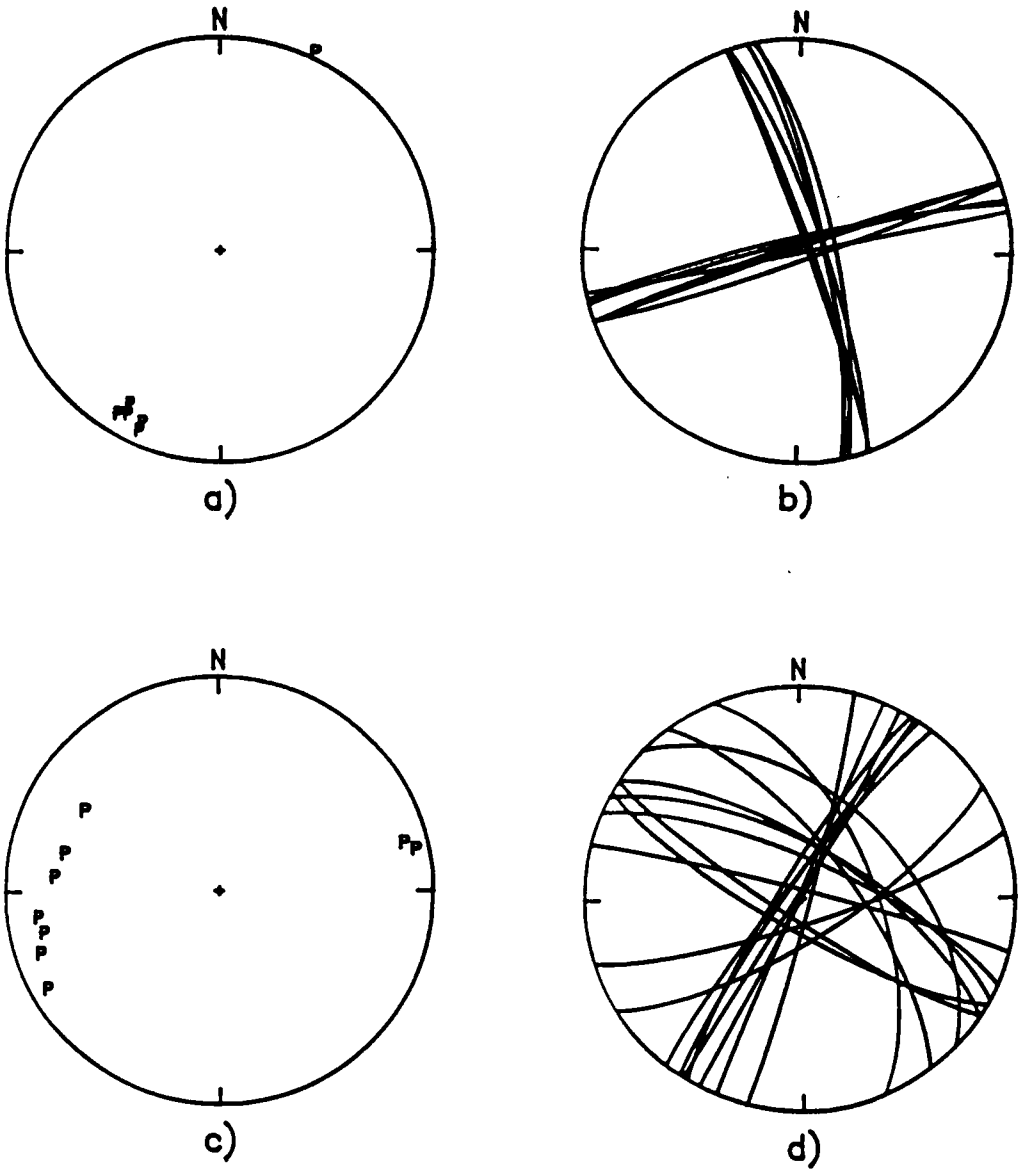

Figure 8. **Well-constrained and poorly-constrained FOCMEC solutions:** a) P-axes of well-constrained Event 63; b) Nodal planes of Event 63; c) P-axes of poorly-constrained Event 97; d) Nodal planes of Event 97.

Preliminary analysis of P-Axis Data

The input data of Teague (1984) and Munsey (1984) were used to redetermine focal mechanism solutions for this study, using an updated version the program **FOCMEC** which searched on an equal area, rather than an equal angle, grid. Hypocentral locations of those earthquakes are given in Appendix A. Eight events from Giles County were studied, as well as 13 from Central Virginia and 11 from Eastern Tennessee. There were 511 solutions deemed acceptable by the program for the 32 focal mechanism solutions, using the input criteria listed in Table 2 through Table 4. Solutions and errors are documented in Table 5. Numbers of solutions in each set ranged from 1 (1/18/83 and 1/27/83) to 47 (5/6/82) with an approximate average of 16. In calculating the final data set of focal mechanism solutions, 96% of the polarity data were correct and 76% of the ratio data were within the pre-selected error limits shown in Table 5. Output data were represented as plots of nodal planes and of **P**-, **T**-, and **B**-axes. Examples of representative **FOCMEC** output are shown in Figure 9 through Figure 11.

As a first-order analysis of regional stress, the orientations of the **P**-axes of the individual focal mechanism solution sets were estimated. Those results will be compared with later calculations of stress tensor orientations, as well as to earlier studies of focal mechanism solutions. Two methods were used to estimate the orientation of the pressure axis associated with each earthquake. Those

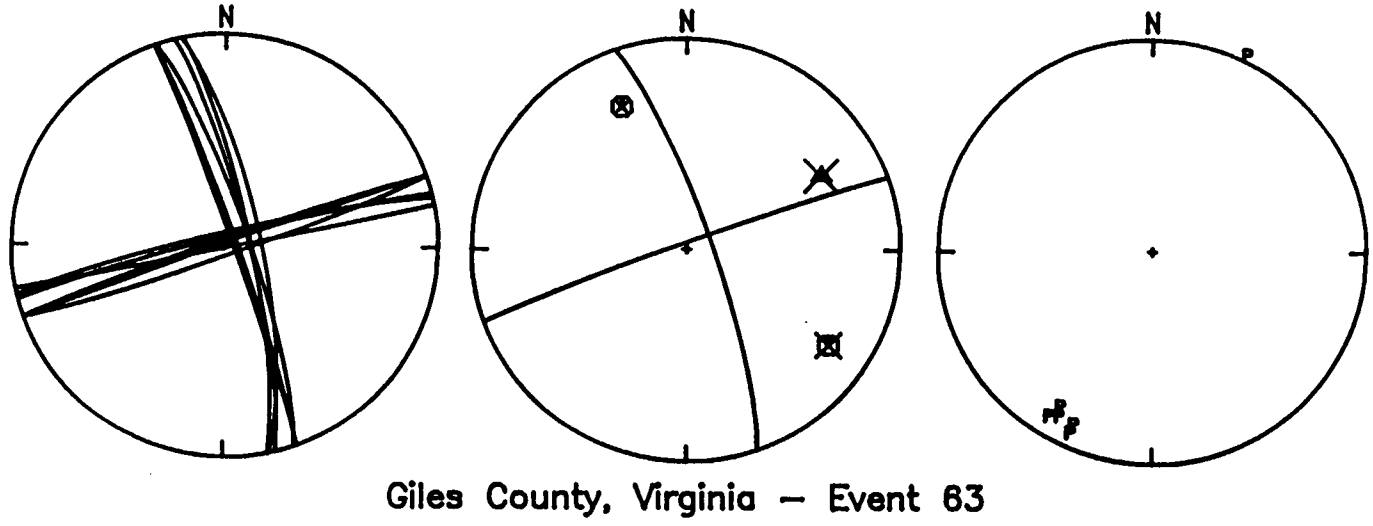

Figure 9. Example FOCMEC output for GCSZ: These plots show focal mechanism solutions for Event 63. Plot in center shows 'best solution' and input data (circles represent compressions, triangles are dilitations, and the size of the x's correspond to the log of the corrected SV/P amplitude ratios). Left-hand plot shows the family of nodal plane solutions. The plot on the right shows P-axes for all solutions.

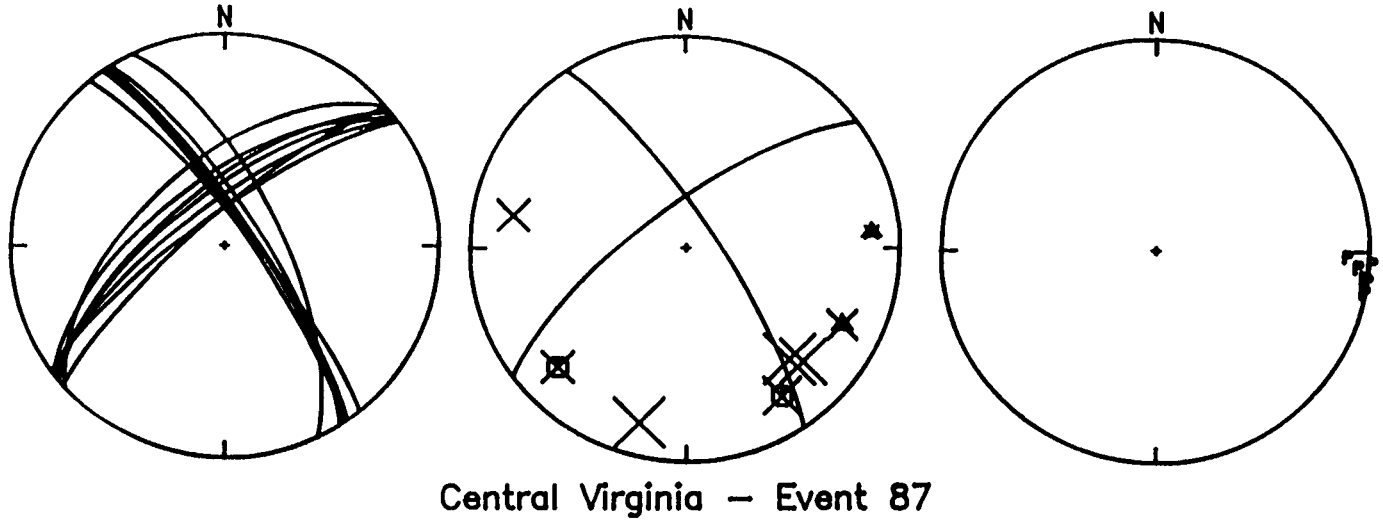

Figure 10. Example FOCMEC output for CVSZ: Event 87 is shown. Figure format and symbols are the same as for Figure 9.

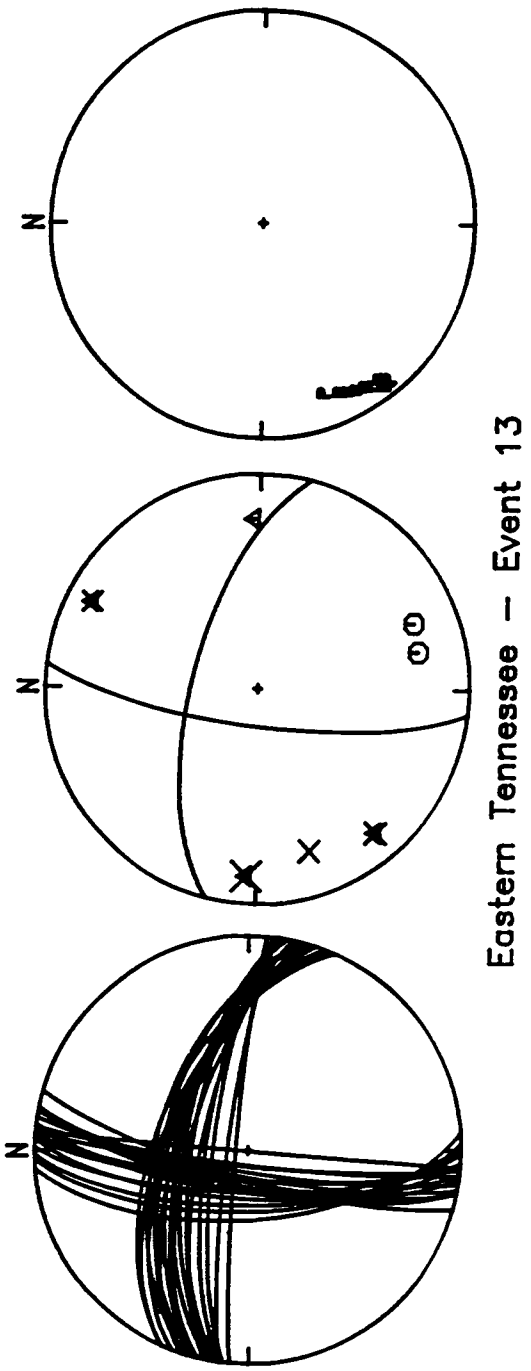

Figure 11. Example FOCMEC output for ETSZ: Event 13 is shown. Figure format and symbols are the same as for Figure 9.

techniques are the best overall solution from the **FOCMEC** output, and an average solution based upon all members of the solution set.

Best Single Solution

In this comparison, the **P**-axis solution with the lowest RMS error was chosen as the 'best' solution, following the work of Teague (1984) and Munsey (1984). Uncertainties were introduced by this method, as it was common for two or more solutions with quite different orientations to have similar errors. In approximately 40% of the cases, a slight increase (+ .02 or less) in the RMS error would include solutions with more than 10° difference in strike or dip from the 'best' solution. It was also occasionally necessary to choose between a solution with a small RMS error and another solution with a larger RMS value, but with one less amplitude ratio error. In the one solution calculated with polarity data only, no RMS values were calculated, so an additional procedure was necessary to choose the 'best' solution. In that case, the nodal planes were grouped tightly enough that it was reasonable to pick the median solution, but if more scatter had been present among the acceptable solutions, choosing the single most representative focal mechanism would have been difficult. For solutions with both polarity and ratio data, use of the RMS value as a discriminant could be misleading, as that procedure only made use of the error introduced by the amplitude ratio data, which were inherently less reliable than the polarities of the first motions, in part due to the difficulty in picking SV-wave amplitudes. Because **FOCMEC** generates a *set* of acceptable solutions, each should be considered when calculating any single **P**-axis trend to represent the solution as a whole and the variability of that estimate. It should be noted that the 'best' solutions shown on Table 6 through Table 8 do not agree exactly with those determined by Teague (1984) and Munsey (1984). Due to a change in the search algorithm of **FOCMEC** (equal area rather than equal angle search), solution sets in this research vary somewhat from the earlier sets, even with identical input data and search parameters.

Table 2. Variables used in FOCMEC - Giles County Seismic Zone.

Date	Event	Polarities/ Allowed Errors	Ratios/ Allowed Errors	Log Ratio Difference*	Vp/Vs	Number of Solutions
12/02/80	63	3/0	3/0	0.25	1.700	6
1/25/83	90	12/1	10/6	0.25	1.700	23
5/26/83	94	5/0	9/1	0.25	1.720	36
7/10/83	97	4/1	6/2	0.15	1.720	9
12/09/83	104	5/1	5/1	0.15	1.720	23
7/02/84	110	5/0	4/1	0.25	1.720	35
6/10/85	118	6/0	5/1	0.23	1.720	3
3/26/86	127	7/0	6/3	0.23	1.720	3

* - Represents the acceptable difference between the logs of the theoretical and actual amplitude ratios.

Table 3. Variables used in FOCMEC - Central Virginia Seismic Zone.

Date	Event	Polarities/ Allowed Errors	Ratios/ Allowed Errors	Log Ratio Difference*	Vp/Vs	Number of Solutions
8/04/80	53	5/1	7/2	0.20	1.730	13
9/26/80	57	5/0	2/0	0.14	1.730	35
2/11/81	64A	9/0	3/0	0.25	1.730	15
2/11/81	64B	7/1	5/2	0.25	1.730	22
1/18/82	78	3/0	4/0	0.17	1.730	16
5/06/82	82	5/0	6/1	0.25	1.730	47
6/25/82	86	7/0	6/2	0.25	1.730	14
9/20/82	87	4/0	8/2	0.25	1.730	7
8/10/83	100	3/0	3/1	0.17	1.730	39
8/17/84	111	24/2	0/-	-	-	5
10/17/84	113	6/0	5/1	0.20	1.730	15
12/10/86	133	6/0	6/3	0.23	1.730	12
4/11/87	138	6/0	7/5	0.23	1.732	4

* - Represents the acceptable difference between the logs of the theoretical and actual amplitude ratios.

Table 4. Variables used in FOCMEC - Eastern Tennessee Seismic Zone.

Date	Event	Polarities/ Allowed Errors	Ratios/ Allowed Errors	Log Ratio Difference*	Vp/Vs	Number of Solutions
11/25/81	2	5/0	4/1	0.17	1.720	22
9/24/82	13	6/0	4/0	0.20	1.720	18
9/24/82	14	9/0	4/0	0.23	1.720	2
1/18/83	22	9/1	6/2	0.23	1.720	1
1/27/83	23	10/1	6/1	0.23	1.720	1
4/05/83	28	4/0	6/1	0.23	1.720	16
5/16/83	29	3/0	5/1	0.15	1.700	17
5/25/83	30	2/0	5/0	0.20	1.700	18
5/26/83	31	5/0	6/2	0.20	1.640	25
7/08/83	34	11/0	4/0	0.23	1.720	7
7/15/83	36	2/0	5/0	0.26	1.720	2

* - Represents the acceptable difference between the logs of the theoretical and actual amplitude ratios.

Table 5. Error Synopsis for Solutions from Program FOCMEC.

Date	Event	Number of Solutions	Total Polarities	Total Polarity Errors	Total Ratios	Total Ratio Errors
12/02/80	63	6	18	0	18	0
1/25/83	90	23	276	23	230	136
5/26/83	94	36	180	0	324	31
7/10/83	97	9	36	9	54	18
12/09/83	104	23	115	23	115	23
7/02/84	110	35	175	0	140	35
6/10/85	118	3	18	0	15	3
3/26/86	127	3	21	0	18	9
8/04/80	53	13	65	13	91	25
9/26/80	57	35	175	0	70	0
2/11/81	64A	15	135	0	45	0
2/11/81	64B	22	154	22	110	44
1/18/82	78	16	48	0	64	0
5/06/82	82	47	235	0	282	41
6/25/82	86	14	98	0	84	28
9/20/82	87	7	28	0	48	12
8/10/83	100	39	117	0	117	39
8/17/84	111	5	120	10	-	-
10/17/84	113	15	90	0	75	15
12/10/86	133	12	72	0	72	36
4/11/87	138	4	24	0	28	20
11/25/81	2	22	110	0	88	22
9/24/82	13	18	108	0	72	0
9/24/82	14	2	18	0	8	0
1/18/83	22	1	9	1	6	2
1/27/83	23	1	10	1	6	1
4/05/83	28	16	64	0	96	15
5/16/83	29	17	51	0	85	17
5/25/83	30	18	36	0	90	0
5/26/83	31	25	125	0	150	50
7/08/83	34	7	77	0	28	0
7/15/83	36	2	4	0	10	0

Total Polarities	2812
Total Polarity Errors	102
Percentage of Consistent Polarities	96
Total Ratios	2639
Total Ratio Errors	622
Percentage of Consistent Ratios	76

Average Trends Based on All Solutions

A single average **P**-axis direction representing each **FOCMEC** family was calculated using the method described by Fisher (1953). That procedure has been used successfully in other geophysical applications; for example, it has been applied to paleomagnetic data to determine average pole positions (see McElhinny, 1979, pp 78 - 79, for a description of the method). Recent work by Frohlich and Willemann (1987) indicated that a more robust statistical technique would be the use of the Anderson-Darling test for clustering. The Fisher test was used in this work simply as a preliminary analytical tool.

In the initial treatment of **P**-axis averages, all solutions within a set were given an equal weight by assuming a vector length of unity. A more rigorous application of this method was then employed using a subjective weighting scheme based upon the RMS error of the ratio measurements. Each vector was adjusted in length by comparing its associated RMS error with the best solution within the set, which was given a weight of 1.0. It was also possible to weight the ratio data as a whole in comparison to the polarity data. In all cases it was chosen to give only half as much value to an amplitude ratio error as to a single polarity error. Averages based upon those weighted solutions, however, were not significantly better than those calculated using unweighted data, as shown on Tables 8 - 10.

Finally, a slightly different procedure was applied to those six **FOCMEC** solution sets which included one or more polarity errors. The amplitude (and thus the reliability) of the first motion of the P-wave increases as a function of distance away from the nodal planes. For each solution which included a polarity error, the theoretical amplitude for the first motion *in error* was calculated using the assumed solution, along with the azimuth and take-off angle of the ray. Each solution in the set was then weighted in relation to the inverse of the amplitude of the polarity in error. For example, if the theoretical amplitude of an incorrect first motion was determined to be only 0.3 (out of a possible 1.0), this solution was weighted greater than an erroneous solution with a theoretical amplitude of 0.8. This final weighting scheme followed the equation:

$$TotalWeight = \frac{\frac{PAMP(Smallest)}{PAMP(Solution)} + \left[\frac{RERR(Smallest)}{RERR(Solution)} \times RFAC\right]}{(1.0 + RFAC)},$$

where:

Total Weight was the weight of the individual solution set member,

PAMP(Smallest) was the smallest theoretical first motion amplitude within the solution set,

PAMP(Solution) was the theoretical first motion amplitude of the individual solution set member,

RERR(Smallest) was the smallest RMS ratio error within the solution set,

RERR(Solution) was the RMS ratio error of the individual set member, and

RFAC was the weighting factor relating the reliability of the ratio data to the polarity data (the factor used in this study was 0.5).

A comparison of weighted and unweighted P-axis trends and plunges, along with the 'best' solution as described above, is given in Table 6 through Table 8.

One drawback of the averaging technique was that the average solution obtained may not, itself, be viable when compared to the original polarities and amplitude ratios. For vectors which are either clustered or distributed in a solid band, that should not be an important consideration. However, if the solutions define two or more separate clusters, then any average direction would likely fall between the acceptable groups, and be inappropriate. Care was taken in this study to avoid such a case by carefully screening the data. In addition, since **FOCMEC** solutions were given only in terms of the lower hemisphere projection of the **P**-axis, it was often necessary to examine both the given vector and its projection in the opposite direction (the back azimuth) to ensure proper clustering. As an example, if the azimuths of two vectors were 0° and 180°, they would be considered nearly colinear if both had shallow plunges. For poorly clustered vector sets with several outlying members, a number of iterations using different azimuth - back azimuth combinations were necessary to determine the average direction with the best statistical parameters.

Table 6. P-Axis Orientations - Giles County Seismic Zone.

Date	Event	'Best Solution' P(Trend,Plunge)	Average P(Trd,Plng,Std Dev*)	Weighted Avg. P(Trd,Plng,Std Dev*)
12/02/80	63	205,09	208,07,06	208,07,06
1/25/83	90	59,33	62,33,18	62,34,17 **
5/26/83	94	49,28	46 33,18	46,33,18
7/10/83	97	298,27	263,11,22	265,12,23 **
12/09/83	104	76,06	269,06,22	269,05,22 **
7/02/84	110	67,45	62,51,31	62,51,31
6/10/85	118	14,35	10,35,03	10,35,03
3/26/86	127	00,29	03,29,07	3,29,07

* - Standard deviation about the mean orientation.
** - Includes both polarity and ratio weighting.

Table 7. P-Axis Orientations - Central Virginia Seismic Zone.

Date	Event	'Best Solution' P(Trend,Plunge)	Average P(Trd,Plng,Std Dev*)	Weighted Avg. P(Trd,Plng,Std Dev*)
9/04/80	53	90,12	244,00,34	237,05,38 **
8/26/80	57	254,14	263,03,12	262,03,12
2/11/81	64A	56,18	31,08,24	31,08,24
2/11/81	64B	189,10	207,04,31	201,05,29 **
1/18/82	78	43,21	48,22,13	48,22,13
5/06/82	82	108,17	115,21,12	115,21,12
6/25/82	86	200,38	192,36,19	193,36,19
9/20/82	87	99,03	98,05,06	98,05,05
8/10/83	100	295,35	307,51,23	307,50,23
8/17/84	111	286,19	288,17,04	288,16,04 **
10/17/84	113	323,14	315,07,11	315,08,11
12/10/86	133	69,15	68,02,15	68,02,15
4/11/87	138	291,28	284,25,05	284,25,06

* - Standard deviation about the mean orientation.
** - Includes both polarity and ratio weighting.

Table 8. P-Axis Orientations - Eastern Tennessee Seismic Zone.

Date	Event	'Best Solution' P(Trend,Plunge)	Average P(Trd,Plng,Std Dev*)	Weighted Avg. P(Trd,Plng,Std Dev*)
11/25/81	2	34,15	212,29,29	213,28,29
9/24/82	13	237,07	236,07,07	236,07,07
9/24/82	14	54,03	53,05,03	53,05,04
1/18/83	22	36,25	36,25,*	36,25,**
1/27/83	23	16,26	16,26,*	16,26,**
4/05/83	28	88,10	87,03,18	87,03,18
5/16/83	29	284,14	53,06,27	53,06,27
5/25/83	30	218,46	244,42,16	244,42,16
5/26/83	31	44,39	236,29,33	236,29,33
7/08/83	34	59,00	56,01,10	56,01,10
7/15/83	36	82,03	261,09,18	261,08,18

* - Standard devation about the mean orientation.
** - Only a single solution exists in these cases. A standard deviation is therefore meaningless.

Interpretation of Preliminary P-Axis Trends

The trends and plunges of the **P**-axes calculated using the procedures described in the previous section will be examined for each seismic zone. Plots show the calculated *average* trends and plunges with the associated standard deviations calculated using the method of Fisher (1953). Although **P**-axes have been used to infer regional stresses, it should be remembered that they are related to the orientation of the moment tensor of the source, and not the stress tensor itself. Therefore the figures introduced here should not be used to support any final interpretations concerning the state of stress in the crust; instead, they simply provide a starting point for the more detailed analysis which forms the bulk of the research reported herein. They will also be used for comparison with prior studies of focal mechanism solutions, as well as derived stress tensor orientations. It should be reiterated that there is no simple one-to-one relationship between the directions of the **P**-axis derived from individual focal mechanisms and the orientation of the largest regional compressive stress.

Giles County Seismic Zone. Horizontal trends of the mean direction calculated from the set of **FOCMEC** solutions varied an average of 8° from the 'best' solution based on error parameters (Figure 12). **P**-axes trended in a general east-northeastward direction, with 6 of the 8 solutions overlapping the azimuth of N45°E $\pm$ 24° postulated by Munsey and Bollinger (1985). Plunges varied from slightly negative to as much as 50°. Events 118 and 127 (both located near Blacksburg, VA) showed the greatest deviation from the general orientation. Those earthquakes occurred about 20 km southeast of the tabular seismic zone described earlier, and may reflect a somewhat different stress regime. No events had solutions similar to that obtained by Herrmann (1979) for the November 20, 1969, Elgood, WV, earthquake, but that event was not within the zone itself. **P**-axes were also examined as a function of depth and epicentral position, with no correlations found.

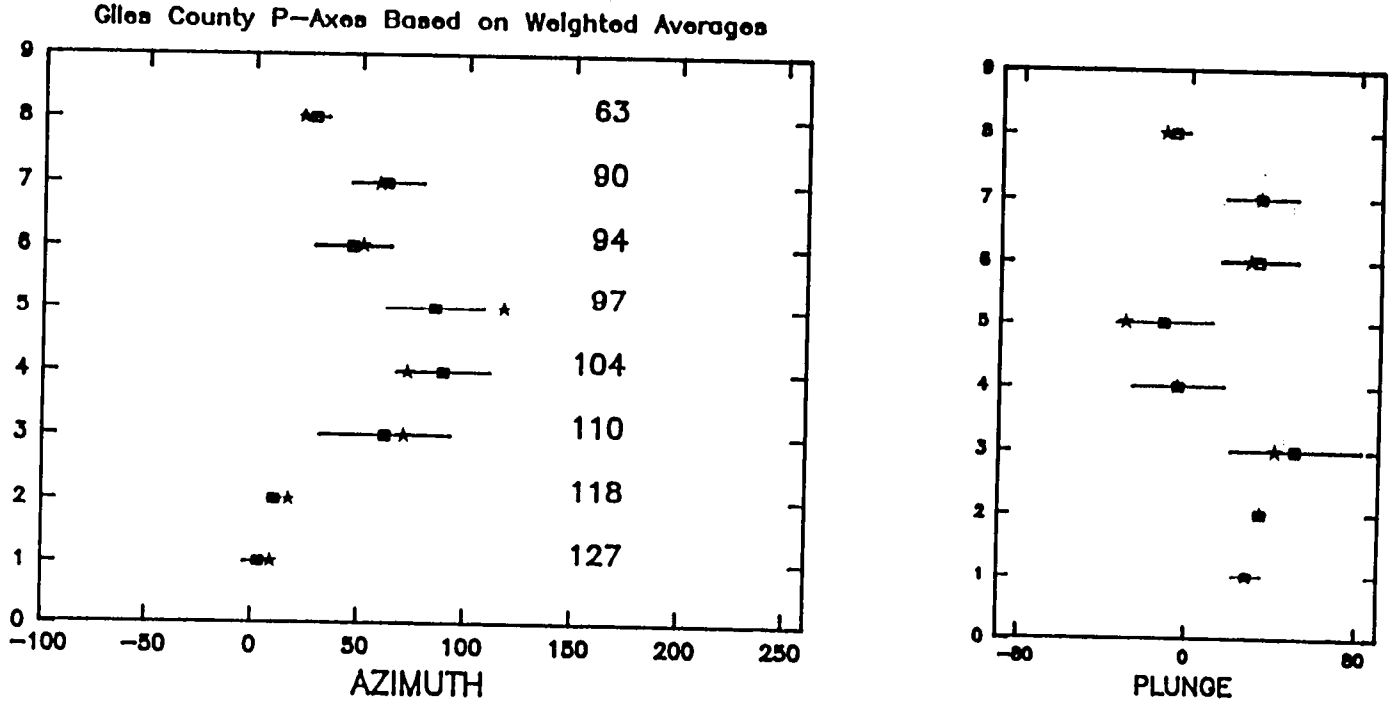

Figure 12. Average P-axis trends for the Giles County Seismic Zone: Azimuths are shown along the abscissa and event number along the ordinate. Horizontal lines indicate the associated standard deviation. ★s represent 'best' solutions, based on RMS error.

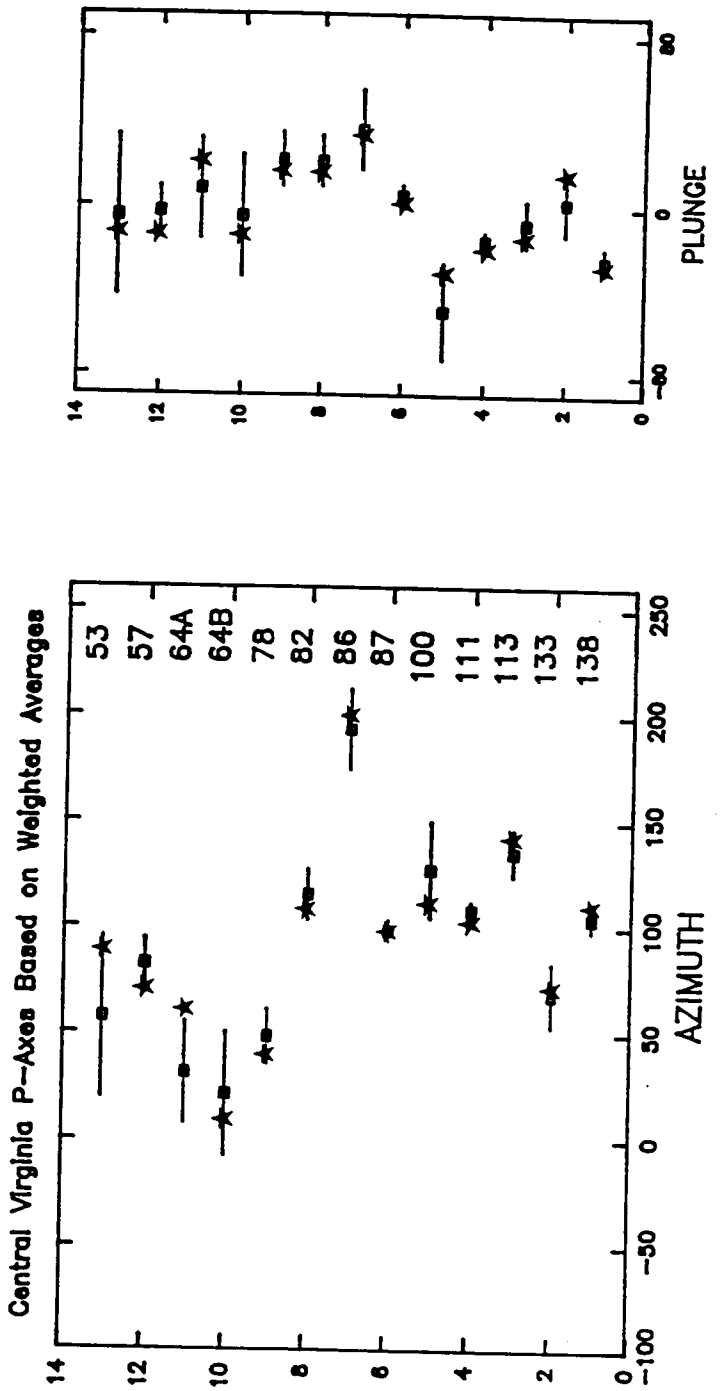

Figure 13. Average P-axis trends for the Central Virginia Seismic Zone: Azimuths are shown along the abscissa and event number along the ordinate. Horizontal lines indicate the associated standard deviation. ★s represent 'best' solutions, based on RMS error.

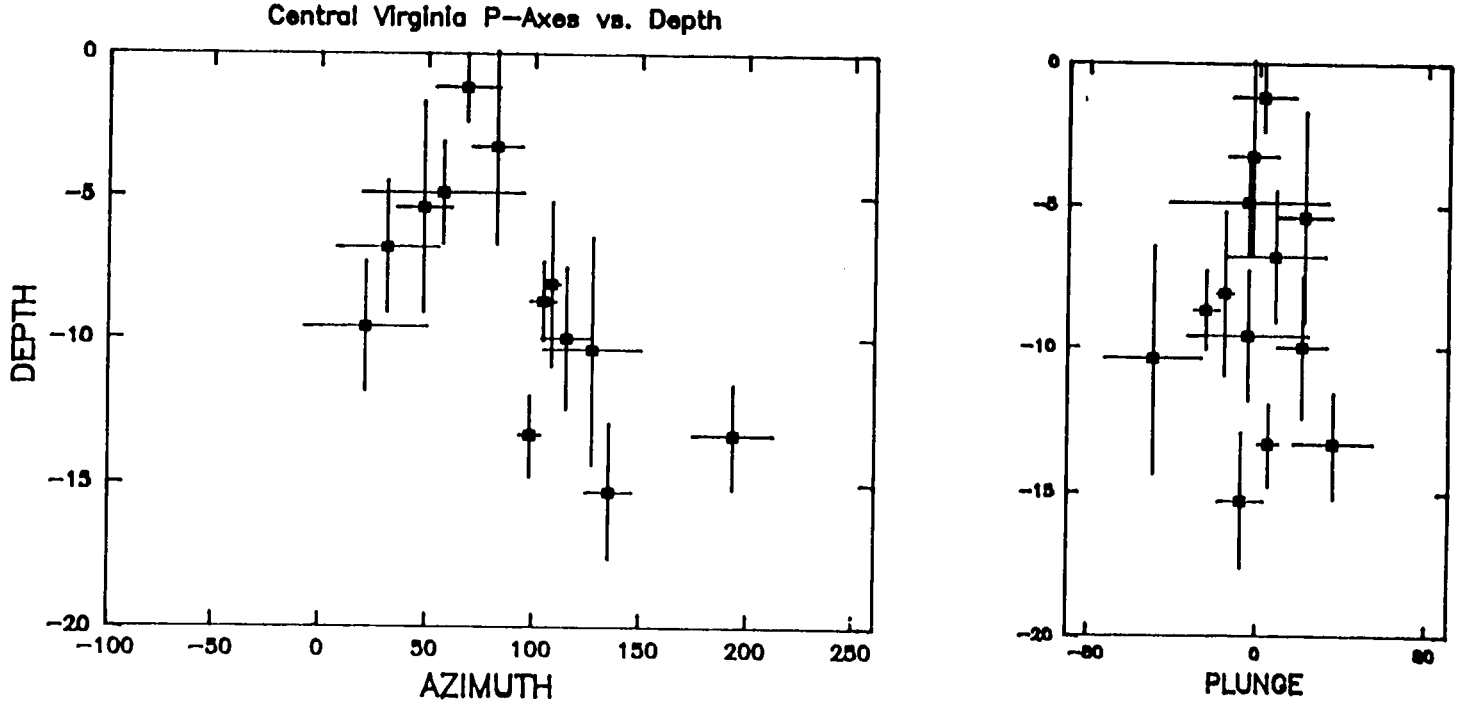

Figure 14. Average P-axis trends versus depth for the CVSZ: Azimuths are shown along the abscissa and depth along the ordinate. Horizontal lines indicate the associated standard deviation of the azimuth measurement; vertical lines show the ERZ. Note the shift of azimuth with depth.

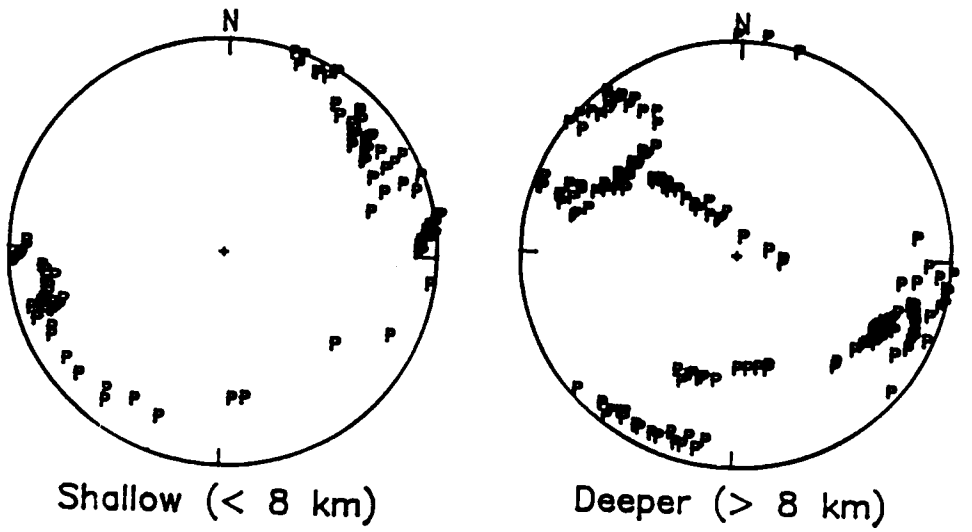

Figure 15. P-axes for all CVSZ events, plotted against depth: Note the general change of orientation above and below the depth of the suspected decollement (8 km).

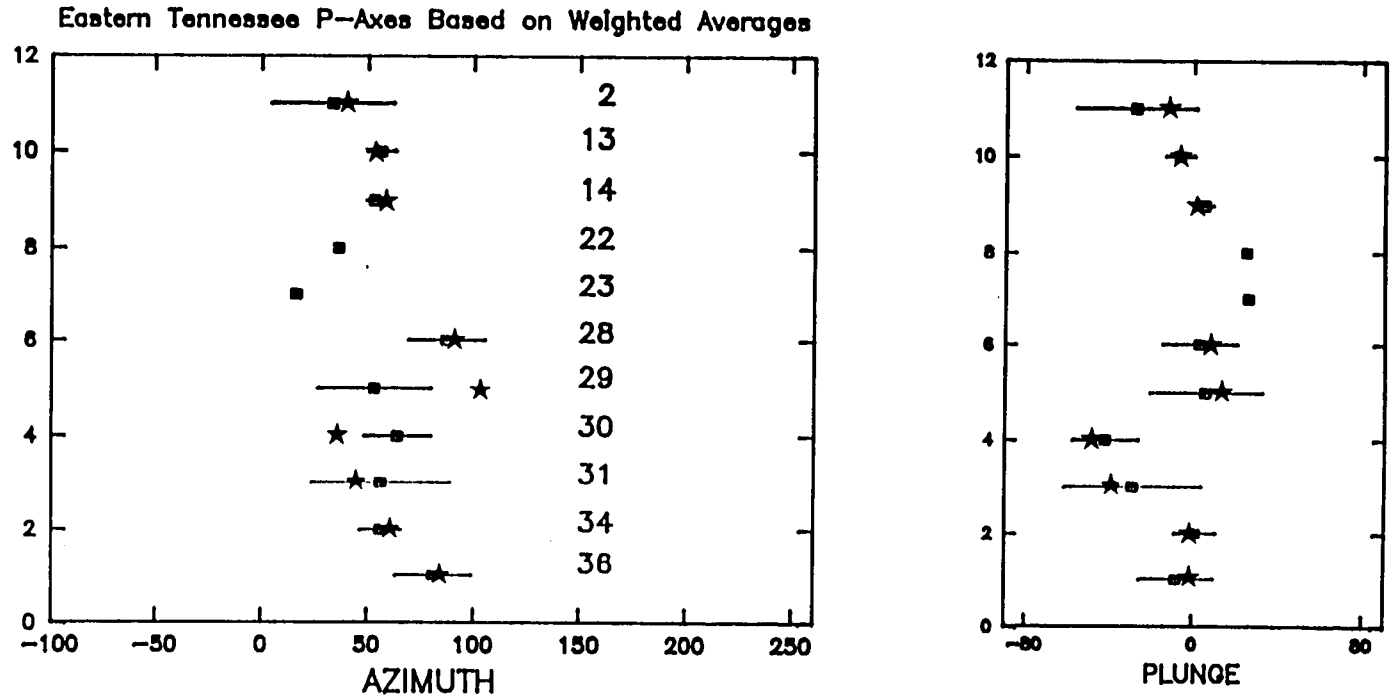

Figure 16. Average P-axis trends for the Eastern Tennessee Seismic Zone: Azimuths are shown along the abscissa and event number along the ordinate. Horizontal lines indicate the associated standard deviation. ★s represent 'best' solutions, based on RMS error.

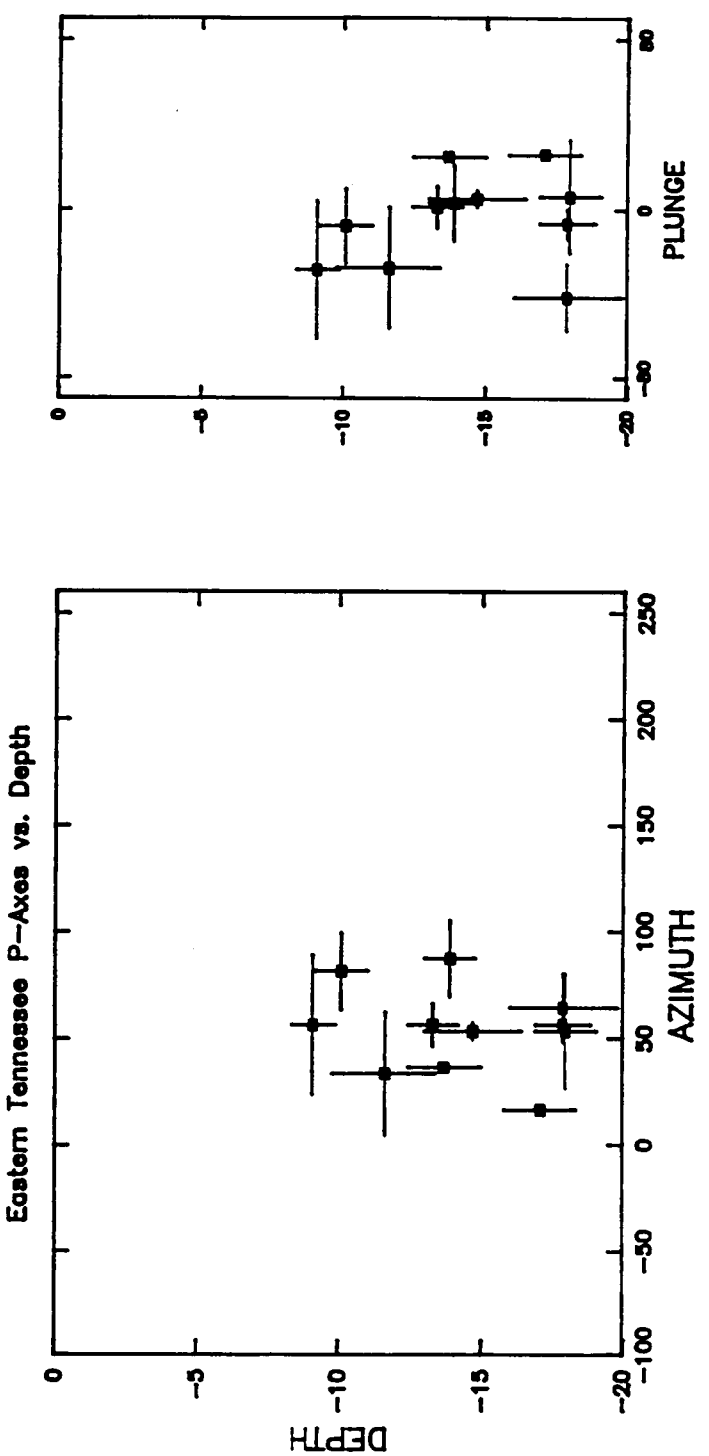

Figure 17. Average P-axis trends versus depth for the ETSZ. Azimuths are shown along the abscissa and depths along the ordinate. Horizontal lines indicate the associated standard deviation of the azimuth measurement; vertical lines show the ERZ. There is no clustering of directions with depth.

Central Virginia Seismic Zone. In Central Virginia, the mean difference between the average P-axis trend and the single solution with the lowest RMS value was almost 10°. Although most P-axes were subhorizontal, more deviation in the horizontal trends was apparent than for any other zone (Figure 13). However, when the trends were plotted against depth as shown in Figure 14, two distinct orientations became evident, as described by Munsey (1984). The observed boundary, assumed as being at a depth of between 8 and 10 km, separated general northeastward trending stresses above from southeastward trends at greater depths. No gradual change in orientation was postulated, as there appear to be two distinct P-axis clusters. The uncertainty in depth shown on Figure 14 was based on the ERZ of the **HYPOELLIPSE** solutions, with the exception of Event 133. That earthquake, which was part of the 1986-1987 swarm within Richmond, was constrained by several independent procedures (e. g. relation of magnitude to intensities; recordings from a portable instrument) to be very shallow (Davison and Bodé; 1987). Figure 15 shows a composite of all P-axes for focal mechanism solutions above and below 8 km. The data with the largest deviation from the above discussion was derived from Event 86.

Eastern Tennessee Seismic Zone. The Eastern Tennessee Seismic Zone was the most consistent in terms of P-axis trends, with values averaging around N54°E (Figure 16). The mean difference between average P-axis trend and that of the best single solution was about 9°, though that figure was dominated by two extreme readings. With Events 29 and 30 excluded, the average difference was only 2°. That stability was indicative of the relative tight clustering of 8 of the 11 **FOCMEC** solution sets. The average horizontal trend agreed well with the values published by Johnston and others (1985) and by Teague and others (1986). Ten of the eleven events were within the range N48°E $\pm$ 23° obtained from single event focal mechanism solutions by Teague and others (1986). However, their research indicated that with increasing hypocentral depths, axes tended to cluster with trends near 40° and with plunges of 5 - 10°. That was not indicated by the data shown in Figure 17, which was based upon weighted averages of the individual sets of solutions. Instead, the maximum horizontal compressive stress at all depths was characterized by a band of values

centered at approximately N50°E. That is not surprising, as all events were substantially below the Appalachian overthrust surface (Johnston and others, 1982).

Previous Research: Determination of Stress Tensor

In the following, two second-order tensors will be discussed, a **moment** tensor and a **stress** tensor. The moment tensor depends on the strength and orientation of the seismic source. We will be interested primarily in the moment tensor as a model for the focal mechanism of earthquakes. The second tensor of interest is the stress tensor, which defines the state of stress in the crust at the initiation of seismic rupture. We will invert for the stress tensor from data collected from sets of focal mechanism solutions.

Assuming a double couple mechanism for an earthquake, two perpendicular nodal planes of zero P-wave amplitude result from the P-wave radiation pattern. Those planes divide the focal sphere into quadrants, each characterized by either compressional (outgoing) or dilatational (inwardly directly) motions for the initial P-wave. One nodal surface is the model fault plane; the other is termed the auxiliary plane. In the center of the compressional quadrant is the **T**-axis; the **P**-axis is in the center of the dilitational quadrant. (It should be remembered that the **P**- and **T**-axes refer to pressure and tension, respectively, at the focus, while the compression and dilitation quadrants refer to the motion at the receiver.) Orthogonal to those axes is the **B**-axis, which is along the intersection of the nodal planes. The **P**-, **T**-, and **B**-axes are in the same direction as the principal axes of the moment tensor. In the case in which the actual fault plane is also a plane of maximum shear, the **P**-axis corresponds to the direction of the stress tensor with the greatest

magnitude (σ_1) and the T-axis to the direction of the smallest (σ_3). However, since breakage in crustal rocks occurs most frequently on zones of weakness that are not coplanar with the plane of maximum shear, there is no simple relationship between the orientation of the moment tensor and the stress tensor beyond the fact that $\overline{\sigma}_1$ is in the dilitational quadrant (McKenzie, 1969).

Research procedures that use focal mechanism solutions (FMSs) to invert for a regional stress tensor have generally employed similar assumptions. A single focal mechanism solution would be derived for each earthquake. For sparse data, often a composite mechanism solution was calculated by pooling input data so that a single focal mechanism was obtained from the data of several earthquakes. Further information concerning regional stress patterns could then be made by combining results from a collection of such individual and composite solutions under the assumption of a homogeneous stress regime. For the following discussion it will be important to distinguish between composite focal mechanism solutions (CFMSs) and multiple focal mechanism solutions (MFMSs). As just described, a CFMS would produce one focal mechanism using data from several events. On the other hand, a MFMS would simply be the combination of several single event or CFMSs that would then be used to derive an estimate of stress. Since several solutions are necessary to make one stress tensor determination, the use of MFMSs requires a large number of well-recorded earthquakes to provide input data.

Etchecopar and others (1981) studied the striations measured on actual fault surfaces and subsequently employed inversion techniques to determine the paleostress environment which produced the observed slips. Included in that report was a brief introduction to their stress tensor analysis, which will be outlined below for our use herein. Double overlined quantities (e. g. $\overline{\overline{T}}$) are second order tensors, vectors are represented by a single overline (e. g. $\overline{n}$), and magnitudes of vectors have no overlines.

There always exists a coordinate frame in which the stress tensor $\overline{\overline{T}}$ may be written;

$$\begin{bmatrix} \sigma_1 & 0 & 0 \\ 0 & \sigma_2 & 0 \\ 0 & 0 & \sigma_3 \end{bmatrix}$$

where σ_1, σ_2, and σ_3 are the stresses associated with the principal directions of the stress tensor. That tensor may be totally described by those values, along with the three Euler angles ψ, θ, and ϕ , which represent the orientation of the tensor with respect to some known coordinate system. Resolved forces in a plane defined by a normal vector $\bar{n}$ can be calculated by

$$\bar{f}_t = \bar{\bar{T}} \cdot \bar{n} - (\bar{n} \cdot \bar{\bar{T}} \cdot \bar{n}) \bar{n} \ .$$

The stress tensor itself may be expressed as the sum of two parts, the deviatoric part $\bar{\bar{D}}$ and the isostatic pressure part $\bar{\bar{P}}$ ($= P\bar{\bar{I}}$, where $\bar{\bar{I}}$ is the identity dyad). Of those two, only $\bar{\bar{D}}$ contributes to the force resolved onto the fault plane since $\bar{\bar{P}}$ always contributes to a normal force. The orientation of $\bar{f}_t$ remains unchanged when $\bar{\bar{T}}$ is multiplied by any positive constant.

Because the values of the magnitudes of the principal stresses are often difficult to obtain individually, Etchecopar and others (1981) describe the ratio;

$$R = \frac{\sigma_2 - \sigma_3}{\sigma_1 - \sigma_3} \ .$$

A value of **R** is not representative of a single stress tensor, but defines a set of tensors, which may be represented by four arbitrary components; the Euler angles ψ, θ , and ϕ, and the value of **R**.

Angelier and Mechler (1977; see also Angelier, 1984, for a description in English) described stress determination using MFMSs, which they referred to as the Method of Right Dihedra. The ambiguity of fault and auxiliary planes was explicitly ignored by assuming that the regional compression must be in a dilitational quadrant of the focal mechanism solution. The Method of Right Dihedra used only the orientation of the **P**- and **T**-quadrants, and no values for the magnitudes of the principal axes were obtained or assumed. Test positions located as a grid on the lower hemisphere of a stereographic projection of an individual focal mechanism solution were given either a value of 100 or 0, depending upon whether that location was included in the compressional or dilatational quadrant, respectively. Data from several focal mechanism solutions were then combined numerically into a single plot, and the average value for each test position was found. That average value, which ranged from 0 to 100, was referred to as the areal frequency.

Portions of the plot with the highest and lowest frequencies were interpreted as the positions of the $\bar{\sigma}_3$ axis and $\bar{\sigma}_1$ axis, respectively. No weighting based on either the quality of focal mechanism data or the orientation with respect to the slip directions of the MFMS set was attempted. Angelier (1979) pointed out that the method allowed the relative magnitudes of the principal stresses to vary among all members of the MFMS set. If the principal stress magnitudes and their orientations were assumed constant throughout the study region, then there would be no such variation in the magnitude ratio.

Ellsworth and Zhonghuai (1980) and Ellsworth (1982) produced a minimization technique as a generalization of Angelier (1979). In those studies, the stress was maximized in the direction of slip and minimized in the direction of the **B**-axis. The assumption was made that the slip produced by an earthquake on a physical fault was parallel to the shear traction found by resolving the estimated stress tensor onto that same fault plane. Under that condition, both the orientation and relative magnitudes of the principal stresses could be determined by an iterative process. The root-mean-square component of the shear traction acting on planes perpendicular to each slip direction of a MFMS set was minimized, with the constraint that the traction parallel to each slip direction must always be positive. Random errors in the method were associated with the uncertainties of the orientations of the slip vector, the null vector, and the vector normal to the fault plane. The distinction between the fault and auxiliary planes was not always known prior to the inversion and, in such cases, all combinations of possible fault planes were considered. In addition to the above geometric considerations, the Coulomb failure criteria was also incorporated in the form;

$$|\tau| - \mu\sigma_n \geq 0,$$

where τ was the shear stress, μ the coefficient of initial friction, and σ_n the normal stress. That inequality had to be met or exceeded for slip to occur. When applied to focal mechanisms from the Rangely oil field experiment (Raleigh and others, 1972), the uncertainty of the derived stress tensor was large, indicating either errors in the focal mechanism solutions or a true spatial variation of stress within the region.

In later work, Angelier (1984) discussed the derivation of paleostress tensors by using slickenside lineations measured on fault surfaces. The nonlinear inversion that he described was also useful for analysis of focal mechanism solutions with results agreeing well with the method of right dihedra. In the mathematical method of Angelier (1984), assumptions were made concerning the shape of the stress ellipsoid as described in the following.

Angelier (1984) reduced the number of unknowns in the stress tensor from six to four by assigning particular values to the parameters m and n, which represented the degree of sphericity of the stress ellipsoid and a scaling factor, respectively. Since the choice of those parameters would affect only the shape of the stress ellipsoid and not the orientation of the principal stresses, they were picked so as to make calculations easier. Angelier (1984) defined the stress tensor in such a way so that it could be written:

$$\overline{\overline{T}} = \begin{bmatrix} x_1 & x_2 & x_3 \\ y_1 & y_2 & y_3 \\ z_1 & z_2 & z_3 \end{bmatrix} \begin{bmatrix} 1 & 0 & 0 \\ 0 & R & 0 \\ 0 & 0 & 0 \end{bmatrix} \begin{bmatrix} x_1 & y_1 & z_1 \\ x_2 & y_2 & z_2 \\ x_3 & y_3 & z_3 \end{bmatrix}$$

where x_i, y_i, and z_i were the direction cosines of the principal axes. Therefore, there were four unknowns in the inversion; the orientation of the principal axes, and the value of **R**. Prior to the inversion, values of 1, **R**, and 0 were given to the principal stresses σ_1, σ_2, and σ_3, respectively. That was done by assigning the following relationships;

$$m = \frac{1}{\sigma_1 - \sigma_3}$$

and,

$$n = m\sigma_3.$$

In other words, the shape of the stress ellipsoid was defined.

A procedure was then undertaken to minimize the angle between the model shear stress and the observed unit slip vector on the fault surface. Since the inversion about the entire focal sphere was not well-behaved (i. e. there could be a number of minima), a grid search was made by

systematically changing the orientation of the principal stresses and varying the value of **R** between 0 and 1. That grid search tested all stress orientations and was not affected by small local minima. An advantage of the work of Angelier (1984) was that the algorithm did not need to know which nodal plane was the fault plane. As with other methods, only the orientation, but not the shape of the stress ellipsoid could be found. Angelier's (1984) approach was not based on physical measurements of the fault orientation, and would work only if the regional stress field was uniaxial ($\sigma_3 = \sigma_2$). Angelier (1984) believed that condition was usually the case (i. e. **R** was small), though other authors (see Michael, 1987a), found that **R** could vary throughout the full range 0 to 1.

Vasseur and others (1983) used MFMSs to interpret the state of stress associated with the 1980 El Asnam, Algeria, earthquake and eighty-one of its aftershocks. Multiple solution sets were chosen based on epicentral positions of the aftershocks in relation to the fault so as to group similar focal mechanism types. The stress field was assumed homogeneous for each multiple-event set. Hypothetical stress tensors were compared to all focal mechanisms within each group, using a Monte Carlo technique to choose the test tensors. Four parameters were sought in the inversion, the three angles associated with the orientation of the stress tensor, and the ratio **R**, as described earlier. The ambiguity between the fault plane and auxiliary plane was removed by resolving the shear stress onto each plane. For only one nodal plane would the resolved shear stress and the slip vector be parallel. That plane was subsequently chosen as the fault plane. For a tensor to be accepted, the calculated slip had to be parallel to the known slip on the fault plane of each focal mechanism solution. That slip was 'known' only in the sense of its geometrical relationship to the focal mechanism solution. Since most focal mechanism solutions in the study were based on 20 - 25 polarity readings, the authors believed that the attitude of the fault surface was correct to within $\pm 15°$. The value of **R** also had to be consistent for each member of the MFMS set. The results of the inversion for the stress tensor were similar to those calculated from eight measurements of striations on exposed fault surfaces. For the $\bar{\sigma}_1$ axis, the difference between the two methods was less than 20°; for the $\bar{\sigma}_3$ axis, it was less than 10°.

Gephart and Forsyth (1984) developed another inversion for the determination of stress fields from focal mechanism data. Two sets of orthogonal coordinate axes were identified. The first of

those, labeled $\bar{x}_1$, $\bar{x}_2$, and $\bar{x}_3$ were defined by the directions of the principal stresses. The second orthogonal set was based upon descriptive parameters of a single focal mechanism. The normal to the fault plane was defined as $\bar{x}'_1$, the **B**-axis as $\bar{x}'_2$ and the normal to the auxiliary plane as $\bar{x}'_3$. In this formulation the absolute magnitude of the individual principal stresses could not be calculated, but acceptable orientations of the principal stress directions could be determined by the relationship between the two coordinate frames, as discussed in the following paragraphs.

The rotation matrix which relates the principal stresses to each focal mechanism solution is composed of the nine members β_{ij}. The first subscript represents the focal mechanism coordinate system and the second relates to the stress system. For example, β_{23} would be the cosine of the angle between the **B**-axis of the focal mechanism solution and the $\bar{\sigma}_3$ direction of the assumed stress field. The β matrix is fundamental in the calculation which eliminates certain stress orientations as possible causal fields for a given focal mechanism solution.

Orthogonality of a coordinate system before and after rotation required that the following general condition be met:

$$0 = \beta_{11}\beta_{21} + \beta_{12}\beta_{22} + \beta_{13}\beta_{23} \,. \quad (1)$$

As previously discussed, it was assumed that the slip on the fault plane was parallel to the direction found by resolving the stress tensor onto that same surface. That was equivalent to the observation that there was no shear stress on the fault plane in the direction normal to the slip, which may be stated as;

$$\sigma_{12}' = 0 = \sigma_1\beta_{11}\beta_{21} + \sigma_2\beta_{12}\beta_{22} + \sigma_3\beta_{13}\beta_{23} \,, \quad (2)$$

where σ_{12}' represents the shear stress in the **B**-axis direction. This last equation results from the general tensor transformation law (see, e. g. Frederick and Chang, 1972; p. 11);

$$\bar{\bar{A}}_{ij}' = \beta_{ik}\beta_{jl}\bar{\bar{A}}_{kl};$$

using the stress tensor;

$$\overline{\overline{A}}_{kl} = \begin{bmatrix} \sigma_1 & 0 & 0 \\ 0 & \sigma_2 & 0 \\ 0 & 0 & \sigma_3 \end{bmatrix}.$$

Equations (1) and (2) above were combined to find;

$$\frac{\sigma_2 - \sigma_1}{\sigma_3 - \sigma_1} = \frac{-\beta_{13}\beta_{23}}{\beta_{12}\beta_{22}},$$

which was equivalent to the parameter **R** introduced by Etchecopar and others (1981). Since by definition,

$$\sigma_1 > \sigma_2 > \sigma_3,$$

the value of **R** must be in the range $0.0 \leq \mathbf{R} \leq 1.0$. Therefore, if an orientation of the principal stress axes was arbitrarily chosen, it could be tested against a focal mechanism solution to determine if such a stress field could cause the known slip. If the calculated values of **R** were found to be less than 0.0 or greater than 1.0, the chosen stress conditions would not be valid under the assumption that there was no shear stress perpendicular to the slip direction.

Gephart and Forsyth (1984) found that the above test was a necessary condition for fault slippage, but was not sufficient for the total analysis, since the sense of faulting (e. g. normal vs. reverse) was not taken into consideration. Therefore, the stress was resolved onto the fault surface to determine if the known and calculated slips were in the same direction. When applied to a large data set, the search routine was broken down into two phases. Initially a rough search was made of the focal sphere to obtain an approximate range for the orientation of the stress tensor. That approximation determined the smallest angle **about any single** $\bar{x}_i'$ axis of the focal mechanism solution which would bring the slip direction on the fault into conformance with the tested tensor. An exact inversion was then utilized to find the best-fit tensor. To minimize the number of calculations, that secondary phase was limited to the region surrounding that direction indicated by the first-order search. The exact inversion constructed a matrix which represented the minimum rotation of the focal mechanism needed to bring the observed and theoretical slip into alignment

(i. e. a rotation about all three $\bar{x}_i'$ axes, rather than a single axis, as in the approximate method). Errors were calculated based on the minimum rotation necessary to reconcile the known slip and the direction of maximum shear.

An advantage of the method of Gephart and Forsyth (1984) was that the computer algorithm made an objective determination of one fault plane from the set of two nodal surfaces defined by the focal mechanism solution. The fault plane was that nodal surface which required the minimum rotation necessary to bring the direction of the observed slip direction into colinearity with the model shear stress. Both nodal planes would not be compatible with a given stress tensor, unless that stress tensor was axially symmetric ($\sigma_2 = \sigma_3 < \sigma_1$), which would produce an **R** value of 0.

The method of Gephart and Forsyth (1984) has been used advantageously to examine the stress fields of specific locales. In the original study, the method was applied to MFMSs of the San Fernando earthquake sequence, where it was found that a hypothesized homogeneous stress field would produce well-behaved results. This was also the case for a subsequent study of New England (Gephart and Forsyth, 1985). In a more recent work, Ma and others (1988) investigated events in the western portion of the state of Washington using the Gephart and Forsyth (1984) technique. That study used focal mechanisms from 189 earthquakes from both crustal and subcrustal focal regions on the interplate boundary. The results indicated poorly constrained stresses which were, in turn, interpreted to be an indication of a heterogeneous stress field.

Harmsen and Rogers (1986) expanded on the method of Gephart and Forsyth (1984) by defining a second set of tests for the compatibility between stress tensors and focal mechanism results. The work of Gephart and Forsyth (1984) was defined as Criterion I, and the additional tests, which were based on studies of rock mechanics, were incorporated as Criterion II. As previously discussed, the Coulomb criteria for fracture has been modified to account for the effect of pore pressure. Harmsen and Rogers (1986) used the form;

$$|\tau_{xy}| = S_0 \pm \mu\sigma_{eff},$$

where τ_{xy} was the tangential traction needed to overcome friction, S_0 was the cohesion, μ was the coefficient of friction, and σ_{eff} was the effective stress ($\sigma_n - P$; where P was the pore pressure;

previously defined herein as σ_n'). Criterion II stated that, when considering a pre-faulted material, slip would occur only if the spatial relationship between the fault and the stress field was such that the ratio of the traction needed to overcome friction on the fault and the effective stress reached the maximum value possible for a tested stress tensor (i. e. $|\tau_{xy}|/\sigma_{eff}$ was a maximum). Criterion II was used to find the best oriented planes for frictional sliding and Criterion I was then invoked to determine the direction of slip. The value of S_0 was assumed to be negligible because of pre-faulting and published values of μ were incorporated into the equation. A variety of generalized focal mechanism types based on those actually found in the Southern Great Basin of Nevada were examined to find the range of stress orientations allowed by the data. The application of the method was not applied to real data samples, and a joint minimization of errors based on the two criteria had not been undertaken.

Michael (1987a) evaluated different methods which utilized slickenside data or focal mechanism solutions to solve for the regional stress. Comparisons were made of the methods introduced by Angelier (1984) and Gephart and Forsyth (1984), as well as a linear inversion scheme (Michael, 1984) which he introduced to invert slickenside data. His method was an different from Angelier (1984) in that it assumed that the **magnitude of the traction on the fault plane was the same on all surfaces during rupture**. The stresses were also examined using assumed fracture criteria based on the ratio of the deviatoric and isotropic portions of the stress tensor. The methods of Angelier (1984) and Michael (1984), though they were designed primarily to invert slickenside data, could easily be modified to utilize focal mechanism data, with the primary problem that, while slickensides define the fault plane, focal mechanisms data do not.

Confidence limits were estimated by using a bootstrap resampling technique. A data subset was chosen at random from the master set and inverted for stress. This sampling process was then repeated as many times as necessary to determine empiracally the confidence limits required by the researcher. The method was dependent upon a great many calculations; to calculate an 80% confidence region, the data were resampled 500 times.

Since confidence limits estimated by the empirical bootstrap technique were based on resampling, rather than by theoretical calculations, it was an excellent tool for comparing various

error estimates for different models. Three data sets were considered by Michael (1987a) for such a comparison. Those data sets were chosen for their different ranges of fault orientations and conjugate faulting characteristics. It was found that the error estimates of both Gephart and Forsyth (1984) and Michael (1984) were incorrect. That analysis was made by plotting the errors associated with each of those methods and then graphically comparing them with the results from the bootstrap resampling technique. Methods to separate fault and auxiliary planes were also examined by converting known slickenside data into corresponding focal mechanism data. Expectably, the best results were found when the fault plane was known prior to inversion; algorithms which chose the fault planes lead to larger confidence regions.

Michael (1987b) also used the bootstrap technique to investigate stresses associated with the 1983 Coalinga, California, earthquake sequence. Fault planes were either known *a priori*, or were chosen by the program. The compressional axis ($\overline{\sigma}_1$) was found to rotate by 15° during the 500 days immediately following the mainshock. The bootstrap technique allowed a confidence level of 95% for this rotation. Stress axes were also found to vary spatially between the two primary aftershock zones.

Summary. Several methods of inverting focal mechanism data to determine the stress tensor have been developed. Some of those (e. g. Angelier, 1984; Michael 1984) were extensions of methods designed specifically for the inversion of slickensides data, where, by the nature of the data, the orientation of the fault plane was known. Choosing the fault plane from the two nodal surfaces of a focal mechanism solution was dealt with in different manners. Angelier (1984) eliminated that problem by developing a technique which was not dependent upon the choice of fault plane, but for which either plane could be appropriate. That assumption was nongeologic since movement would take place only on one of the planes during a single seismic episode. Vasseur and others (1983) and Gephart and Forsyth (1984) used an algorithm which determined which of the planes was most appropriate, and based their error analyses on the misfit of that plane to an 'ideally' oriented fault surface. The computation of error was accomplished in various ways; the most utilitarian was the bootstrap method of Michael (1987a) which used numerous subsets of the focal

mechanism solution set to produce a variety of MFMSs. Rock fracture criteria were dealt with in detail by Harmsen and Rogers (1986). However, results from actual focal mechanisms were not used as input data by them.

The input data for all of the methods reviewed depended solely on a set of single focal mechanism solutions, i. e. one focal mechanism for one earthquake. No weighting scheme was used that was based upon the error associated with each of those solutions. In particular, the fit and adequacy of the input data (in all cases P-wave polarities) to the chosen focal mechanism solution was not taken into consideration. In the method of Gephart and Forsyth (1984) the assumption was made that the FMS of an earthquake was in error. That error was calculated by a measure of the rotation necessary to bring the FMS into conformance with the stress tensor. However, no attempt was made to assure that the rotated FMS was compatible with the **original input polarity and/or amplitude ratio data.** Those data, while subject to errors associated with velocity model or location, are more fundamental than any single focal mechanism solution. Clearly, measures of the accuracy of the individual focal mechanism solutions used in any inversion must be utilized to allow the most objective determination of the *in situ* stress field.

In a region such as the Southeastern United States, where earthquakes are relatively infrequent, and station coverage for each event is poor, the uncertainty associated with a single focal mechanism for each earthquake is large. Whereas for data sets composed of tens to hundreds of earthquakes and seismic stations, any error would be reduced using standard minimization techniques (e. g. least squares fitting), such can not be assumed for data sets consisting of ten or fewer stations and earthquakes. Therefore, in the case of sparse data, all allowed **FOCMEC** solutions (for given search and error parameters) should be considered.

Outline of the Tensor Estimation

The stress regimes responsible for the activity in each seismic zone were estimated from their corresponding focal mechanism solutions using a modification of the procedures described in the previous section. No determination of a 'best' focal mechanism solution was attempted for each earthquake, as all members of the **FOCMEC** output family for each earthquake were used in the calculation, with weighting based upon the orientation of the observed resolved stress relative to the model slip direction and the fit of the original P-wave first motion and $(SV/P)_z$ amplitude ratio data. The use of a MFMS set for each earthquake accounted for the uncertainty of the focal mechanism solution itself.

A detailed discussion of the algorithms developed in this study and the procedures involved in their use can be found in Appendix C. An outline of the tensor estimation will be presented in the following paragraphs, and the procedure by which the methods were applied will be found in the next section. In each discussion, various parameters will be labeled as either observed or theoretical. Any factor associated with the focal mechanism output from **FOCMEC** will be referred to as *observed*. Of course, there are errors associated with each observed solution. Those errors are dependent upon the number as well as the fit of the input data to each FMS, and were dealt with as part of the weighting scheme applied to individual members of each set of focal mechanism solutions. Any *theoretical* parameters mentioned will be associated with a particular stress tensor

that was compared to the set of focal mechanism solutions. For example, the focal mechanism constrained the slip direction on the fault plane (an *observed* parameter), while the stress tensor defined a *theoretical* slip on the same surface.

The program written for the determination of the stress tensor was called **STRESS** and was written in Fortran on the MicroVax workstation of the VTSO. The tests made by that program on each member of a focal mechanism family were, in general, the same as those used by Gephart and Forsyth (1984), although the methodology differed. We will initially discuss the comparison of a single theoretical stress tensor with a focal mechanism solution, then will explain how a family of such test stress tensors was chosen.

In the first comparison of stress tensor and FMS, the value of **R** was calculated from the direction cosines for both the input fault plane and the auxiliary plane. If either plane was associated with an **R** value in the range $0 < \mathbf{R} < 1$, then that particular solution was passed on to the next test, which found the projection of the theoretical stress tensor on the plane of interest. If the stress tensor produced a slip on the plane with a component in the same direction as the observed slip (the slip required by the focal mechanism solution), then that theoretical stress tensor was judged to be compatible with the observed focal mechanism solution. At that stage the angular distance between the observed and theoretical slips was not considered. Often a theoretical stress tensor was capable of producing appropriate slip on both FMS nodal planes. In that case, the relationship between the observed slip and the theoretical slip were calculated for both nodal planes. The surface on which the two slips were most nearly colinear was chosen as the fault plane. As previously discussed, such a procedure was commonly used by other investigators; however, it is considered to be less reliable than the case in which the fault plane was known prior to calculations, based on geologic criteria. Expectably, the introduction of an algorithm to choose the fault plane has been found to expand the confidence regions about the best solution (Michael, 1987a), but was necessary for the data from the SEUS.

At this point in the program the following elements would be known. A single focal mechanism solution was either compatible with the orientation of the test stress tensor , or it had failed the **R** test and/or the slip direction test. If the solution was compatible (i. e. it had passed

both tests), then the relative orientations of the observed slip and the theoretical slip had been calculated. If necessary, the best-fit fault plane was chosen from the input nodal (fault and auxiliary) planes. For the first pass of data through the program, an important parameter found was the error count relating the FMS and the test tensor. If the focal mechanism had passed both tests, then the error count was zero. If either or both of the tests produced negative results, the error count was one.

Next, each additional solution within the **FOCMEC** solution set for an individual earthquake was compared with the same test stress tensor orientation, and the total number of errors was tabulated. For a set of **n** focal mechanism solutions, the error count would range anywhere between 0 and **n**. In addition, the angular difference between each acceptable theoretical slip direction and the observed slip direction was tabulated along with the average measurement of that angle for the entire solution set. Once all **FOCMEC** solutions for a single earthquake had been compared to a particular stress tensor orientation and the number of errors tabulated, a new orientation for the theoretical tensor was chosen and testing resumed.

The choice of test tensors was made using a grid search of the lower hemisphere of the focal sphere. This method is incremental and provides an excellent first-order estimate of the orientation of the principal axes. In addition, it was felt that the small number of earthquakes and the uncertainty associated with the input data were the limiting factors in this study, not the search routine. In the process of choosing the stress tensor to test against the focal mechanism solutions set, the orientations of of $\bar{\sigma}_1$ and $\bar{\sigma}_2$ were chosen as variables, with $\bar{\sigma}_3$ constrained by orthogonality. The direction of $\bar{\sigma}_1$ was specified first. The focal sphere was divided into 324 test positions, which represented a systematic 10° change in azimuth from 10° to 360°, followed by an increase in plunge. That procedure was repeated for 36 azimuthal values and plunges ranging from 0° to 80° in 10° increments. For the first test of each $\bar{\sigma}_1$ orientation, $\bar{\sigma}_2$ was considered horizontal. In subsequent tests, $\bar{\sigma}_2$ was varied by 10° increments from 10° to 170°. Because of symmetry considerations, that procedure represents a full search of the focal sphere. A total of 5,832 tensors were constructed by the program and compared to all members of each **FOCMEC** solution.

As described earlier in the **Data** section of this report, each member of the **FOCMEC** solution set was subjectively weighted based upon the fit of the input data to that particular focal mechanism solution. The total weight of a FMS was based upon two factors, the number of polarity errors and the match of the measured amplitude ratio to the theoretical value calculated within the **FOCMEC** program. The second, and most important, portion of the weighting scheme was based on the cosine of the angular difference between the theoretical slip directions calculated for the stress tensor, and those known from the focal mechanism solutions. That weighting factor was then multiplied by the relative quality of the focal mechanism data, also normalized to unity.

An example of the weighting based on the orientation of the resolved stress onto the fault plane is shown in Figure 18. The figures shown are lower hemisphere projections of the focal mechanism solution for a normal fault. That fault strikes east-west and dips 45° to the south. The circles superposed on the projection represent the $\bar{\sigma}_1$ directions of tested stress tensors which produce slip on the fault that has a vector component in the same direction as the observed slip. When all solutions are considered, regardless of their weight, any $\bar{\sigma}_1$ axis within the **P**-axis quadrant is an acceptable solution, as stated by McKenzie (1969). However, as the theoretical slip direction on the fault plane becomes more nearly colinear with the observed slip, the weighting factor increases.

Several options exist within the program framework. For the first pass through a **FOCMEC** solution set, all 324 $\bar{\sigma}_1$ test positions were considered. The operator could select the focal plane for each FMS, or let the program choose the best aligned nodal plane. Also, the number of allowed errors generated by the FMS set was permitted to vary before a test tensor was deemed unacceptable. In that manner, the investigator was allowed the option of specifying the number of misfit members of each MFMS set. As will be discussed later, that number was generally chosen to be **n** - 1, where **n** was the number of members of the **FOCMEC** set. The output data was written in such a format that it could by used as input into plotting routines (external to the program) to display those $\bar{\sigma}_1$ test orientations which were compatible with the FMS set.

A second pass through the data was then made by using a modification of the program **STRESS** (called **STRESS1**) which allowed the researcher to specify the particular test tensor

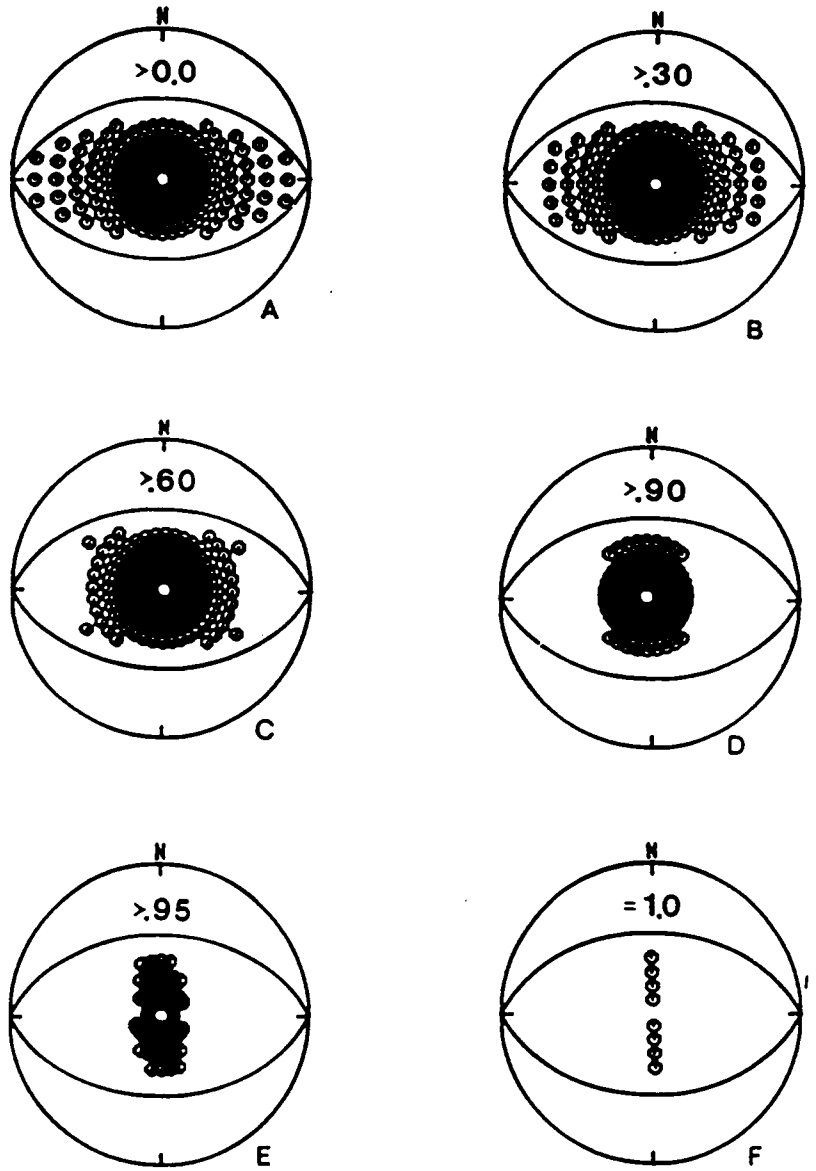

Figure 18. **Weighting Scheme based on Known and Theoretical Slip:** The first figure (A) represents all acceptable $\bar{\sigma}_1$ orientations for an east-west normal fault dipping 45° to the south. As observed and theoretical slips on the fault plane become more nearly colinear (B - F), the weighting factor increases to a maximum value of 1.00 and the number of acceptable $\bar{\sigma}_1$ orientations decreases.

orientation. A complete set of output was produced which included the value of **R** associated with each FMS, as well as the various components of the weighting scheme. That more detailed output data was then used to find those stress tensor orientations (the directions of $\overline{\sigma}_2$ and $\overline{\sigma}_3$ in addition to $\overline{\sigma}_1$ found earlier). which were compatible with at least one observed FMS from each earthquake.

The basic assumption in the procedure was that *any one* of the nodal planes generated by the program **FOCMEC** was capable of movement when a theoretical stress tensor was applied and that solution was not too much different from the actual movement on the fault. In truth, of course, physical slip only occurred on one plane. However, if that plane could not be determined unambiguously by geologic factors, then all solutions had to be considered. The weighting scheme helped to delineate the faults with the most favorable orientations, and those surfaces were used to estimate the principal stress directions. The fact that the answers were well behaved and that correct answers were produced for known input data indicated that estimates of fault planes were reasonable. Those results will be discussed in a later section.

Research Procedure

Any analysis of regional stress based on earthquake focal mechanism data generated for the Southeastern United States must allow for the uncertainties documented by the solution sets calculated by **FOCMEC**. In this research, each of those solutions were considered during the estimation of the stress tensor orientation for a particular seismic zone. Once that tensor was defined, a detailed study of the focal mechanisms for each earthquake could be made, and the most appropriate solution could be chosen, based on the assumption that the rupture was caused by a homogeneous stress field. Procedures used in this research are shown schematically in Figure 19 and are summarized below. Step numbers refer to the captions on the figure.

A) For the first step, focal mechanism solutions were found for each earthquake. The number of possible solutions depended upon the search parameters for the program **FOCMEC**, as well as the number of acceptable errors. A family of possible solutions was defined for each event.

B) The focal mechanism solution sets for all earthquakes within a zone were compared by the program **STRESS** against all 5,832 theoretical tensor orientations. Since a particular $\bar{\sigma}_1$ direction needed to be consistent with only one of the focal mechanisms contained within the set of **FOCMEC** solutions for each event, a maximum of **n** - 1 errors were allowed for any tested stress tensor orientation, where **n** was the number of solutions in the **FOCMEC** family. In most cases

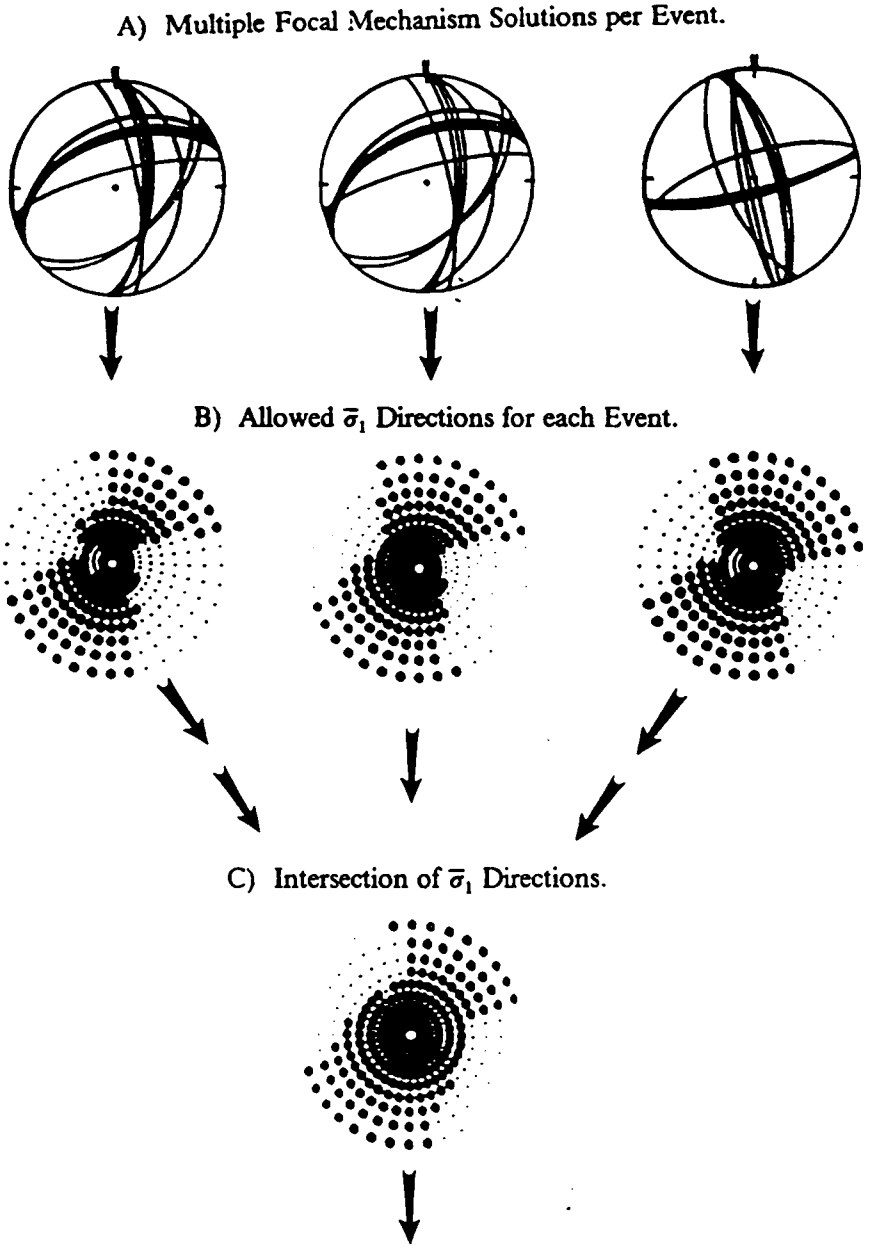

Figure 19. Schematic showing outline of methodology: All possible $\bar{\sigma}_1$ axes are found for each set of focal mechanism solutions. The intersection of those results are composited for each zone, then highgraded to determine the best-fitting stress tensor. The best focal mechanism solution from each set is then chosen.

From Previous Page

D) Tests made on the value of R.

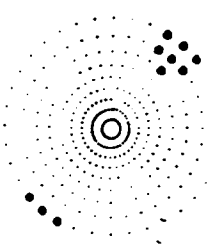

E) Best Stress Tensor Orientation.

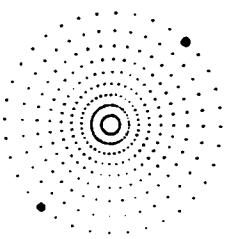

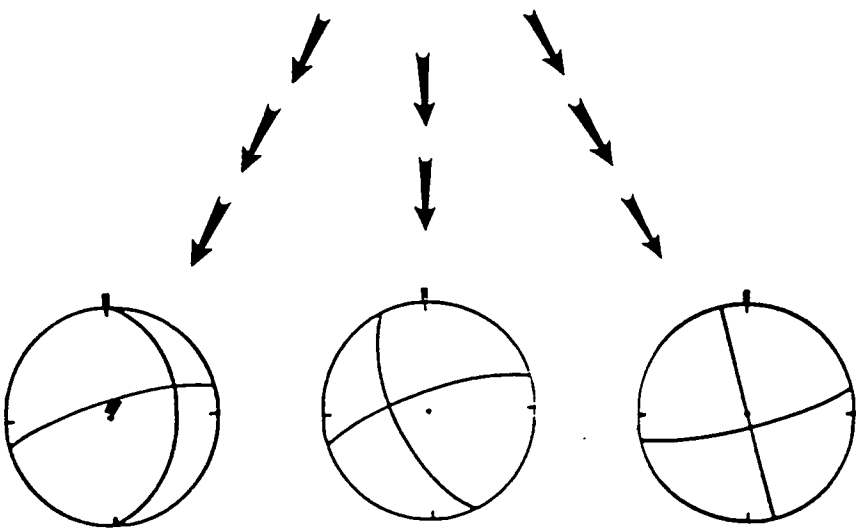

F) Best Focal Mechanisms.

Figure 19. (cont.)

only a relatively few $\overline{\sigma}_1$ trends were eliminated by this method, as shown in Figure 19 and by the plots for each event found in the Appendix D.

C) Results for all earthquakes within a specific zone were then compared, with the $\overline{\sigma}_1$ orientations common among all events being noted. The value of **R** was not considered at this stage, except that it must fall in the range between 0 and 1.

Acceptable $\overline{\sigma}_1$ directions were then compared in greater detail, considering possible rotations of $\overline{\sigma}_2$ and $\overline{\sigma}_3$ around $\overline{\sigma}_1$. Calculations were made using the program **STRESS1**, which allowed the operator to test individual tensor orientations, and which then printed a more complete set of output data than the program **STRESS**. Again, results for all earthquakes within an individual zone were compared to find the common stress tensor orientations allowed by at least one member of the **FOCMEC** solution set of each earthquake. Acceptable $\overline{\sigma}_1$ orientations could then be plotted to display any general trends.

D) For final selection of the theoretical best-fitting stress tensor, it was necessary to consider the value of the parameter **R** as calculated by **STRESS1**. The goal was to find that combination of stress tensor with one focal mechanism solution from each earthquake which exhibited a minimum variation about a single **R** value. Computer time restraints prohibited a complete search, so it was accomplished in two phases. In the first, approximate, phase, a search was made for ten values of **R** between 0.05 and 0.95, and an output 'bin' was established for each. Every **R** value representing a combination of stress tensor orientation and focal mechanism solution was assigned to the bin with the closest value. An average value of **R** and the standard deviation around that average were then calculated for the numbers in each bin. The best solution was considered as that set of fault planes, one from each earthquake, which produced the most well-constrained **R** value. For the best orientation (or set of orientations) found by the approximate method, a more exact calculation for **R** was then made. The best stress tensor orientation was used to produce a value of **R** for all members of each focal mechanism solution set. All possible combinations of **R** within a selected range of the approximate value were then processed to find the combination which had the smallest standard deviation, using one **R** value from each earthquake. Once that task was completed, both the orientation of the stress tensor and the value of **R** were known.

E) If more than one set of solutions had nearly identical standard deviations, an additional comparison was made, based on the weighting of the individual focal mechanism solutions, as described previously. In that case, the composite set of focal mechanisms with the smallest standard deviation and the greatest weight was identified as the best solution set.

After the best solution(s) for each zone was found, the directions of $\bar{\sigma}_1$, $\bar{\sigma}_2$, and $\bar{\sigma}_3$ were tabulated. Plots were made which indicated the orientation of both the full stress tensor and the horizontal component of the maximum compressive stress. Those figures were useful for comparing the results to earlier estimates of regional stress based on either borehole stress measurements and/or studies of focal mechanism solutions. The maximum compressive stress directions were compared directly with the average **P**-axis solutions discussed earlier, so that any relationship could be quantified, and the significance of the focal mechanism **P**-axis as an indicator of the *in situ* stress direction could be evaluated.

F) The focal mechanism solutions related to the best fitting regional stress tensor were identified as the most appropriate solutions for each respective earthquake. By plotting those focal mechanism solutions, both the mode of faulting and the fault orientations of earthquakes within a seismic zone could be studied. Since the program chose the fault plane from the two nodal surfaces, there was no ambiguity in the plotted fault plane orientations. Those solution sets were superior to earlier studies of FMSs for the study regions, as they were consistent with an assumed homogeneous stress field.

The final phase of research was an attempt to understand how much information about the stress tensor orientation (specifically the trend of $\bar{\sigma}_1$) could be obtained from a *single* earthquake, using the multiple solutions from the program **FOCMEC**. Following the work of McKenzie (1969), the **P**-axis quadrants of all focal mechanism solutions for a single event were combined into one plot. That union of all possible $\bar{\sigma}_1$ directions had a large probability of containing the correct answer, but was, of course, very poorly constrained. Then, as suggested by the work of Raleigh and others (1972), all orientations up to 35° from any of the solution set **P**-axes were merged, followed by smaller angles of 25° and 15°. As the angular measures became smaller, the probability of containing the $\bar{\sigma}_1$ direction also decreased, although the implied direction of $\bar{\sigma}_1$ became more

restricted. The graphical results of those restricted orientations were compared directly with the regional stress tensor found earlier to identify any possible empirical relationships.

Assumptions of the Methodology

The estimation of stress tensors described herein was an empirical technique, and, as such, required several assumptions. Some of those assumptions were absolutely critical to the effectiveness of the method, while others needed only to be met approximately. For the purpose of this discussion, assumptions are described which would affect the results of the procedure. The manner in which those uncertainties would alter the results will also be described. In most cases, relaxation of those criteria would only increase the scatter in the output data, rather than nullify the usefulness of the method entirely.

The FOCMEC program. The program used to derive the families of focal mechanism solutions depended upon several theoretical and physical assumptions. The source mechanism was based upon the double-couple model, which has been shown to be appropriate for most earthquakes (e.g. Aki and Richards, 1980; p. 43). Calculated ray paths depended upon the accuracy of the chosen velocity model and the minimal effect of velocity anisotropy. Those velocity models have been used with success in locating the earthquakes in all seismic zones of this study, and, in the case of the Giles County and Central Virginia Seismic Zones, have been confirmed independently (Gresko, 1985; Chapman and Bollinger, 1984 and Viret and others, 1984; respectively). Any inaccuracies included in the assumed velocity structure would introduce errors in the location of raypaths plotted

on the focal sphere. In the case of polarity data, that error would be significant only if it caused the data to be located in the incorrect quadrant of the FMS, which would only happen for polarities near a nodal surface. Since polarities near such a boundary would not, in most cases, be easily read, they were likely to be excluded by the quality control procedures discussed earlier. On the other hand, since $(SV/P)_z$ data change from point to point about the focal sphere, a poorly located data point would, in all cases, introduce a discrepancy between measured and calculated values. Seismic wave attenuation was not considered when dealing with amplitude ratio data, except by the elimination of longer ray paths. The use of 100 km as the distance for that maximum value followed the procedure used by Munsey (1984) and Teague (1984). Station distribution was also critical; related errors could only be minimized by the use of all possible stations for the determination of each focal mechanism solution set.

Choice of error and search parameters within **FOCMEC** is dependent upon the program operator. The experience gained within a short period of time was considered sufficient enough that results from the program would be stable and well within the range of appropriate solutions. In all cases the primary objective in high-grading the solution set from **FOCMEC** was to minimize the number of polarity errors. That step was followed by consideration of the amplitude ratio data. When dealing with a MFMS from the Richmond, Virginia, earthquake sequence of December 1986 through January, 1987, Davison and Bodé (1987) found that an increase in the allowed ratio errors would result in more allowed solutions from **FOCMEC**, but would not alter the general orientation of the solution set. In general, **FOCMEC** solution sets were considered complete and accurate enough so as not to be a limiting factor within the estimation technique, although robust statistical techniques have not been incorporated into the program.

Basic assumptions of the temsor estimation. The basic assumption for any regional stress determination scheme has been that the orientation and the magnitudes of the principal stresses were the same throughout the study region. The degree to which this assumption is true has been found to vary in different seismotectonic regions. Gephart and Forsyth (1984) found that focal mechanism data from the aftershock zone of the San Fernando earthquake were compatible with

a homogeneous stress field. In a later work (Gephart and Forsyth, 1985), they studied FMSs from New England, and determined that a homogeneous stress field was also appropriate for that much larger region. Other authors have had less consistent results. In studies of active regions, Ma and others (1988) found that a heterogeneous stress field must be used to describe the seismicity of the western portion of Washington, and Ellsworth (1982) determined that the induced seismicity near Rangely, Colorado could not be explained by a consistent stress orientation. Even for an individual earthquake sequence, the stress field has been found to change. Vasseur and others (1983), found it necessary to subdivide the aftershock zone of the 1980 El Asnam earthquake into geographical regions to produce well-behaved stress orientations, and Michael (1987b) found both spatial and temporal variations in the stress field were associated with the 1983 Coalinga, California, earthquake series. In the study of the seismicity of the Southeastern United States, the assumption of a homogeneous stress tensor for each seismic zone was necessary because of both the limited data set (about 10 earthquakes per zone) and the small areal extent of each zone, ranging from 7,850 km^2 for the GCSZ to 45,240 km^2 for the ETSZ. Finally, the **P**-axis of a focal mechanism solution and the $\bar{\sigma}_1$ orientation could not be considered colinear, though it appears to be reasonable to assume that they were within a given range of one another.

Continental crust in seismogenic regions is characterized by pervasive, pre-existing planes of weakness, so it was not appropriate to assume that the earthquakes were caused by new fracture of homogeneous rock, though that possibility could not be excluded. Since we inverted for both the directions of the principal axes and the value of the ratio **R**, the relative magnitudes of the principal stresses had to remain constant among earthquakes located in the same region. However, if the effect of the crust overlying the focus of an earthquake was only to change the vertical stress rather than simply to alter the confining pressure, then the stress tensor would change with depth. If one of the principal axes was near-vertical, then such a change in vertical load would primarily affect the shape of the ellipsoid (by altering the relative magnitudes of the principal stresses), rather than reorient the axis directions.

In the actual methodology, the slip direction was assumed to be colinear with the maximum shear vector found when the stress tensor was resolved onto the fault surface. In the set of FMSs

for each event, distribution of fault orientations had to be dense enough that at least one of the solutions was similar to the actual mechanism of the earthquake. Since an average of sixteen solutions for each earthquake were used, that condition was probably met. The cosine weighting scheme based on the angular separation between the known and theoretical slips was useful in only a few analyses, as will be shown later. However, that scheme was not so restrictive as to overly constrain the results, since only the poorest solutions were eliminated. The two parts of the subjective weight (based on the quality of fit with the original input data as well as the orientation of the theoretical slip) were each normalized to unity and multiplied together. That weighting scheme would perhaps be more indicative of the fit of the FMS solution if the previously mentioned additional statistical calculations were incorporated into **FOCMEC**.

Results

Results for the stress tensor orientations and the subsequent choices for the most appropriate set of focal mechanisms for each seismic zone are presented in this section. Also included is a newly derived data set which compares the **P**-axis direction of each earthquake with the $\bar{\sigma}_1$ orientation derived for the zone in which that event occurred. Most results are in graphical and tabular form, with interpretations of those results discussed in detail in the next portion of this report.

Stress Tensor Estimation

The estimation for the stress tensor was based upon the use of the one focal mechanism from each event which, when taken as a set, produced the most consistent **R** value for the seismic zone. The tensors produced in this manner were generally well-behaved. The horizontal components of the acceptable $\bar{\sigma}_1$ axes were tightly clustered (generally within $\pm$ 15°) and, in most cases, the orientation of the single best stress tensor was picked easily based on the error associated with **R**. Results of the stress tensor estimates are given in Table 9 and are shown graphically in Figure 20 through Figure 29. In each of those figures small crosses indicate the test position for the $\bar{\sigma}_1$ axis superposed on the lower hemisphere of a equal area projection. At each of those orientations, 18

Table 9. Stress Tensor Orientations.

Seismic Zone	σ_1 Trend	σ_1 Plunge	σ_2 Rotation *	R	Standard Deviation (+/-)
Giles County, Va	40	0	120	0.93	0.03
Central Virginia					
All	80	20	80	0.13	0.04
Deep	270	20	100	0.56	0.027
Shallow	70	10	60	0.46	0.004
Eastern Tennessee	50	0	110	0.66	0.04

* - clockwise from horizontal

positions of the $\overline{\sigma}_2$ axis were tested. If any of those $\overline{\sigma}_2$ trends produced an acceptable solution for at least one of the focal mechanism solutions of each earthquake in the seismic zone, then a small circle was plotted on the appropriate $\overline{\sigma}_1$ direction. As larger values of the standard deviation about **R** were eliminated, additional plots of acceptable $\overline{\sigma}_1$ orientations were made, which further restrained the $\overline{\sigma}_1$ direction. The best solution or set of solutions for each zone is shown as a separate figure, with the orientation of all axes indicated. The horizontal components of maximum compressive stress for each zone in the SEUS are shown on Figure 30. Each principal stress axis will be described in terms of its projection onto the lower hemisphere of a equal area projection. In all cases the initial test orientation of $\overline{\sigma}_2$ was horizontal and 90° in a clockwise direction from the horizontal projection of $\overline{\sigma}_1$.

Giles County Seismic Zone. (Figure 20). For the Giles County Seismic Zone, the general orientation of the $\overline{\sigma}_1$ axis was found to be approximately NE-SW, but was not as well constrained as that found later for Eastern Tennessee. In fact, two clusters of solutions seem to be present, one around N40°E with a shallow plunge, and another dipping steeply at a northerly azimuth. As solutions were confined to those with the smallest standard deviation about **R**, both clusters diminished in size, but neither was eliminated entirely. However, the orientation with the smallest variation about **R** was found to be that with a horizontal $\overline{\sigma}_1$ axis with a trend of N40°E. The orientation of the full tensor is shown on Figure 21. The trend of $\overline{\sigma}_2$ was N50°W with a plunge of 60°, while the $\overline{\sigma}_3$ axis plunged 30° from an azimuth of S50°E.

Central Virginia Seismic Zone. Events in the Central Virginia Seismic Zone were studied in two phases. Initially, all earthquakes were combined into a single data set and inverted for the stress tensor. Although results of that estimation were acceptable, an additional study was made, as suggested by the variation of **P**-axis orientation with depth described earlier. Events from the zone were split into two subsets based on depth; a shallow set for events less than 8 km deep (5 events), and a second group of deeper events (8 events). Stress estimates were made for those data, and

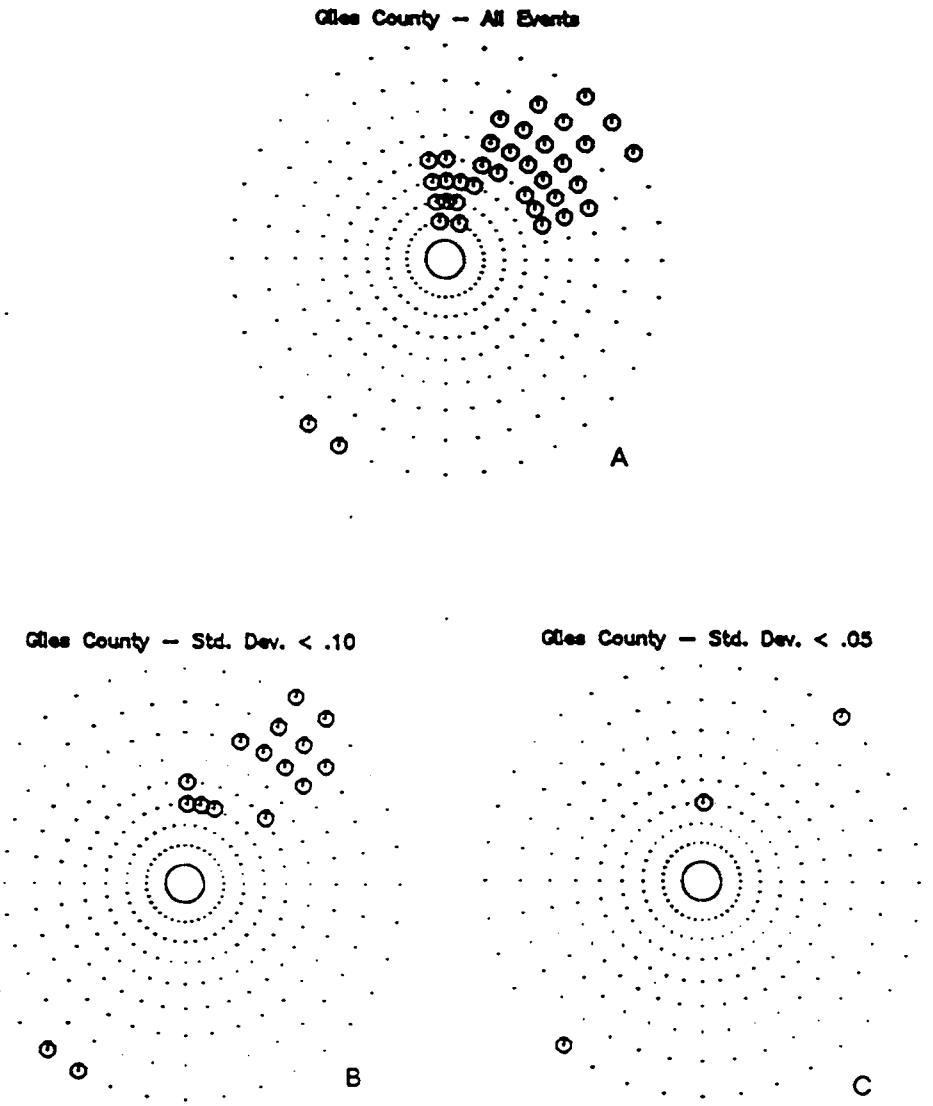

Figure 20. **Stress tensor results for the Giles County Seismic Zone:** Lower hemisphere plot showing orientation of $\bar{\sigma}_1$ for which there was at least one acceptable solution. A) All results, B) solutions for which R had a standard deviation of less than 0.10, C) standard deviation less than 0.05.

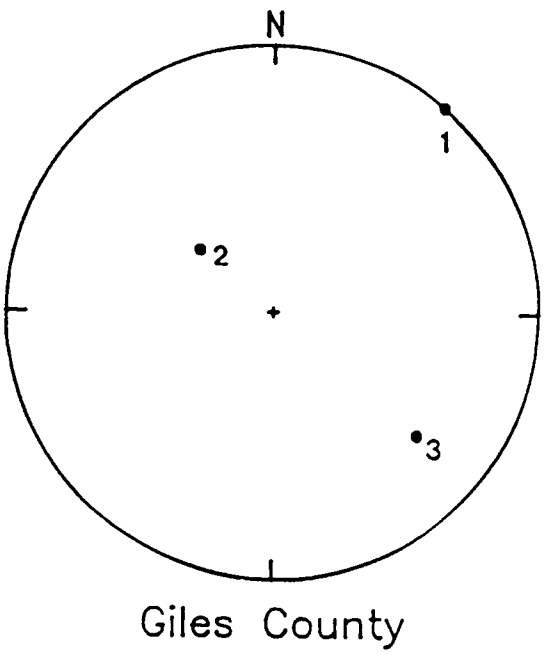

Figure 21. **Best stress tensor result for the Giles County Seismic Zone:** Lower hemisphere equal area projection showing the orientation of $\bar{\sigma}_1$, $\bar{\sigma}_2$, and $\bar{\sigma}_3$ (labeled 1, 2, 3, respectively). The value of R was 0.93 with a standard deviation of 0.03.

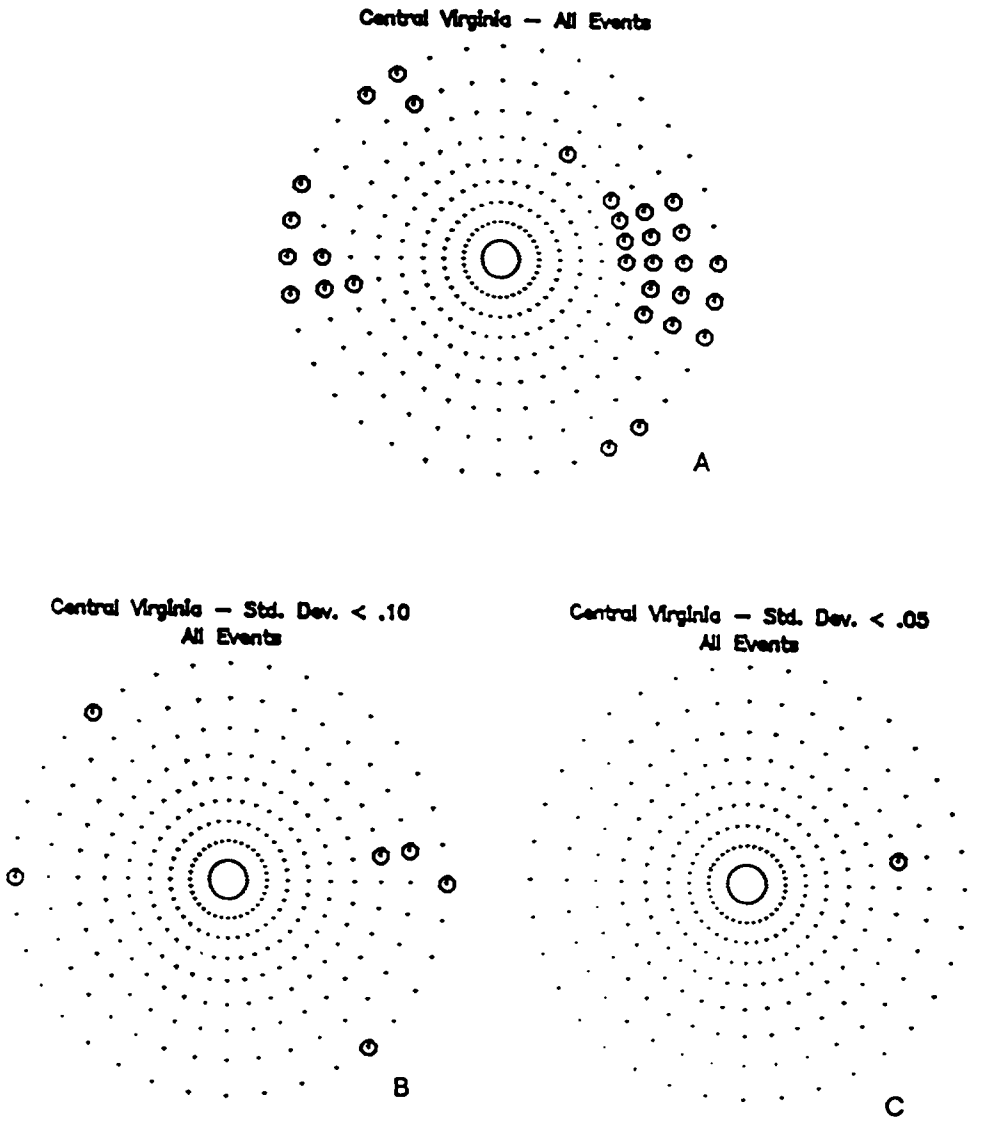

Figure 22. **Stress tensor results for all events in the CVSZ:** Lower hemisphere plot showing orientation of $\overline{\sigma}_1$ for which there was at least one acceptable solution. A) All results, B) solutions for which R had a standard deviation of less than 0.10, C) standard deviation less than 0.05.

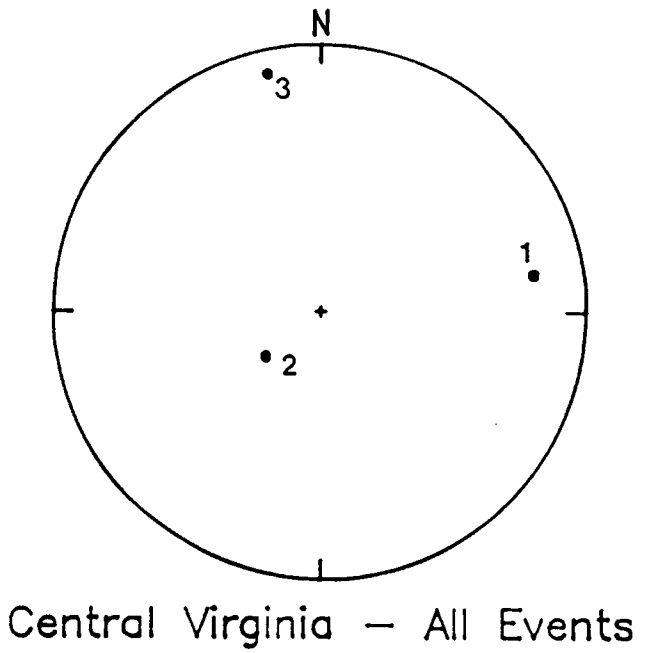

Figure 23. **Best stress tensor result for all events in the CVSZ:** Lower hemisphere equal area projection showing the orientation of $\bar{\sigma}_1$, $\bar{\sigma}_2$, and $\bar{\sigma}_3$ (labeled 1, 2, 3, respectively). The value of R was 0.13 with a standard deviation of 0.04.

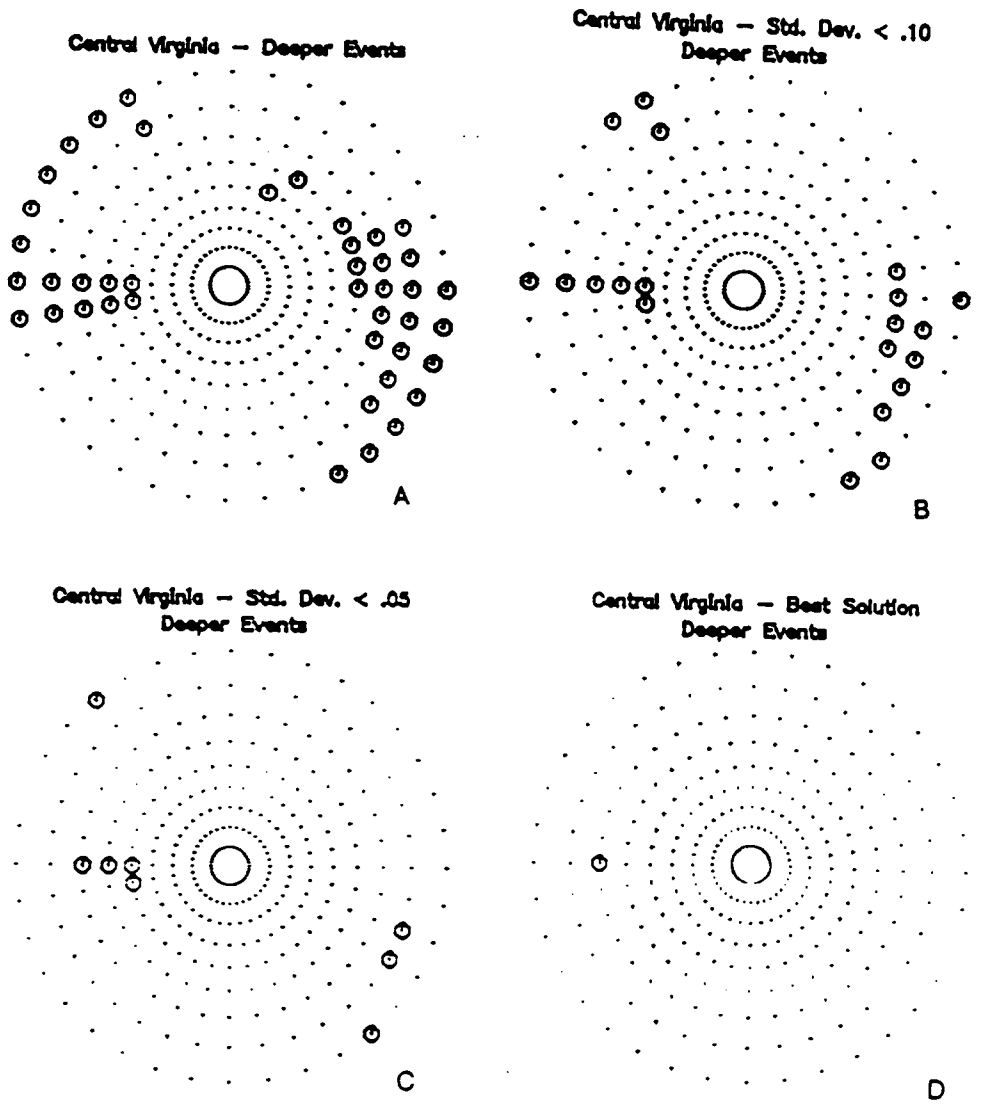

Figure 24. Stress tensor results for deeper (> 8 km) events in the CVSZ: Lower hemisphere plot showing orientation of $\bar{\sigma}_1$ for which there was at least one acceptable solution. A) All results, B) solutions for which R had a standard deviation of less than 0.10, C) standard deviation less than 0.05, D) preferred solution. Events in this depth range are assumed to be below the observed boundary.

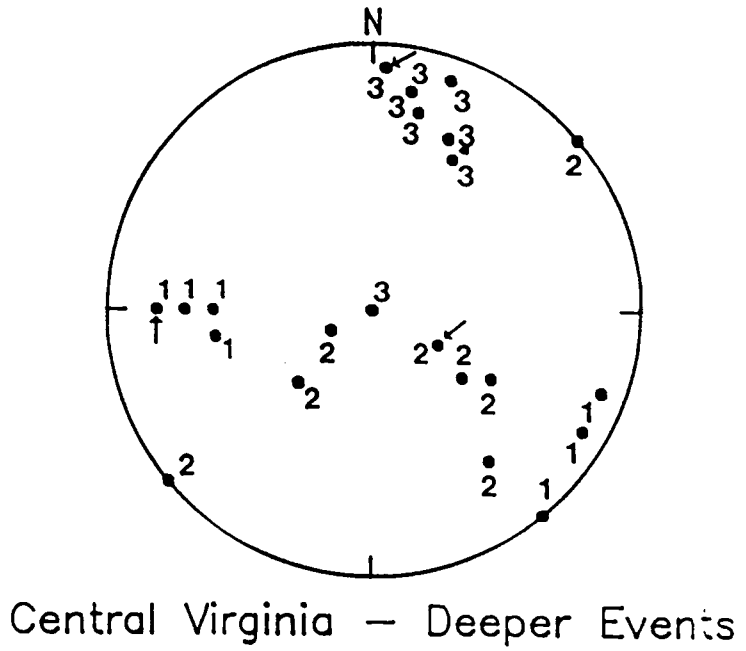

Figure 25. **Best stress tensor results for deeper (> 8 km) CVSZ events:** Lower hemisphere equal area projection showing the orientation of $\bar{\sigma}_1$, $\bar{\sigma}_2$, and $\bar{\sigma}_3$ (labeled 1, 2, 3, respectively) for the set of 8 best-fitting stress tensors. The preferred solution is arrowed. The value of R was 0.56 with a standard deviation of 0.027.

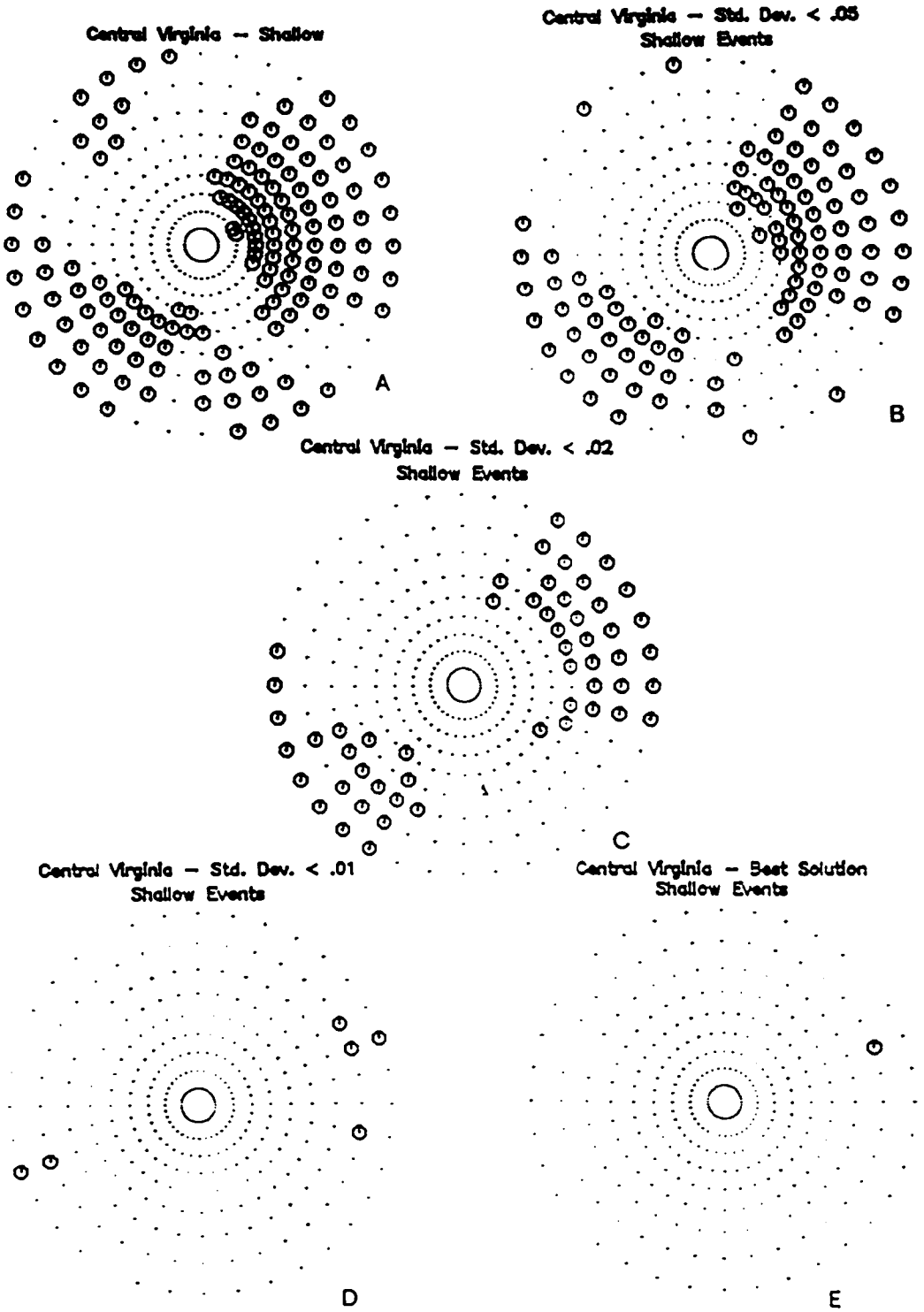

Figure 26. **Stress tensor results for shallow (< 8 km) events in the CVSZ:** Lower hemisphere plot showing orientation of $\bar{\sigma}_1$ for which there was at least one acceptable solution. A) All results, B) solutions for which R had a standard deviation of less than 0.05, C) standard deviation less than 0.02, D) standard deviation less than 0.01, E) preferred solution. Events in this depth range are assumed to be above the observed boundary.

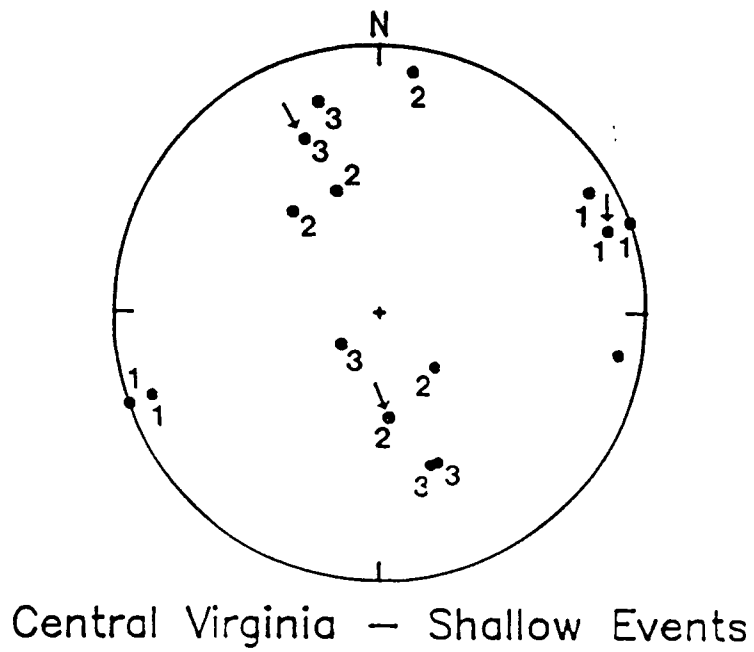

Figure 27. **Best stress tensor results for shallow (< 8 km) CVSZ events:** Lower hemisphere equal area projection showing the orientation of $\bar{\sigma}_1$, $\bar{\sigma}_2$, and $\bar{\sigma}_3$ (labeled 1, 2, 3, respectively) for the set of 6 best-fitting stress tensors. The preferred solution is arrowed. The value of **R** was 0.46 with a standard deviation of 0.004.

results plotted. It was found that the errors associated with those subsets were significantly smaller than for the entire data assemblage (see Table 9).

When estimating the stress tensor for the entire zone, the orientation of $\bar{\sigma}_1$ was found to be trending N80°E with a plunge of 20° (see Figure 22 and Figure 23). Corresponding azimuth and plunge of the other axes were approximately S52°W and 68° for $\bar{\sigma}_2$, and N15°W and 10° for $\bar{\sigma}_3$. The associated value of **R** was about 0.13 with a standard deviation of 0.04. Note, however, that a plot of all acceptable $\bar{\sigma}_1$ orientations, and particularly those solutions which have **R** values with a standard deviation of < 0.10 (Figure 25 and Figure 27) suggests two dominant trends for the horizontal component of $\bar{\sigma}_1$, one east-northeasterly and the other east-southeasterly. Therefore, further examination of the CVSZ was warranted.

The focal mechanism data associated with shallow and deeper Central Virginia earthquakes produced two *sets* of appropriate tensors rather than an easily distinguished *single* best result. Therefore, choice of that best solution was based on the weighting scheme described earlier. Each best-fitting FMS for an event was weighted according to its relationship to the theoretical stress tensor. Those values were multiplied together to produce one weight for comparison with results obtained from other tensor orientations. Both the orientation of the best tensor chosen in this manner, and the general characteristics of the set of appropriate stress tensors, will be described.

Events whose foci were greater than 8 km deep were only slightly better constrained than the set of all Central Virginia earthquakes, with an **R** value of 0.56 and a standard deviation of 0.027 (Figure 24). The trend and plunge of $\bar{\sigma}_1$ were due west and 20°; $\bar{\sigma}_2$ was best represented by a rotation of 100° from the horizontal. Seven additional tensors were found to fit the data nearly as well (Figure 25). In general, $\bar{\sigma}_1$ axes were constrained to be nearly east-west with only a slight plunge. The set of $\bar{\sigma}_3$ axes was also subhorizontal, but with an azimuth of north-northeast. Finally, the $\bar{\sigma}_2$ axes showed more variation, being arranged in a band ranging from horizontal to near vertical. The axes of the best solution were similar to the general characteristics of each cluster. A more tightly constrained grouping may have been obtained had depth control allowed more accurate division of the data set. The weighting of the best group was equal to 0.45.

The shallow events in Central Virginia produced six stress tensors with similar error parameters (Figure 26 and Figure 27). Nearly all $\bar{\sigma}_1$ axes were horizontal with an east-northeast azimuth. Both $\bar{\sigma}_2$ and $\bar{\sigma}_3$ axes were poorly constrained, following a band trending north-northwest and dipping from around 10° to 75°. The best solution was associated with a stress tensor with $\bar{\sigma}_1$ trending N70°E and plunging 10°; the $\bar{\sigma}_2$ axis was rotated 60° from the initial horizontal position. For the best solution, the standard deviation about an **R** value of 0.46 was only 0.004, the smallest of any group tested. Again, as with the deeper events, the best solution was chosen using the incorporated weighting scheme which, in this instance, was equal to 0.53. In both the sets of shallow and deeper events, the $\bar{\sigma}_1$ axes of the best fitting tensors were clustered, indicating that a comparison of that orientation with previous estimates of the direction of the maximum compressive stress was appropriate.

Eastern Tennessee Seismic Zone. Results are shown graphically in Figure 28. All acceptable $\bar{\sigma}_1$ orientations, regardless of the value of **R**, are shown on the left-hand plot. Note the strong lineation of $\bar{\sigma}_1$ trends whose horizontal components strike from N40°E to N60°E. As the allowed standard deviation was reduced progressively to less than .10 (center plot), then to .05 or less (right-hand plot), the number of solutions decreased to a single tested orientation. A full representation of the best tensor orientation is shown on Figure 29. The $\bar{\sigma}_1$ axis was horizontal and trended N50°E, while the $\bar{\sigma}_2$ axis had a trend of N40°W with a plunge of 70°. The corresponding $\bar{\sigma}_3$ axis had a trend and plunge of S40°E and 20°, respectively. The value of **R** was 0.66 with a standard deviation of 0.04. Note the nearly identical results for the best stress tensors from both the Eastern Tennessee and Giles County Seismic Zones (compare Figure 21 and Figure 29).

Focal Mechanism Solutions

Once stress tensor estimates were made for Giles County, Eastern Tennessee and the two Central Virginia subsets, the most appropriate focal mechanism solution could be chosen for each

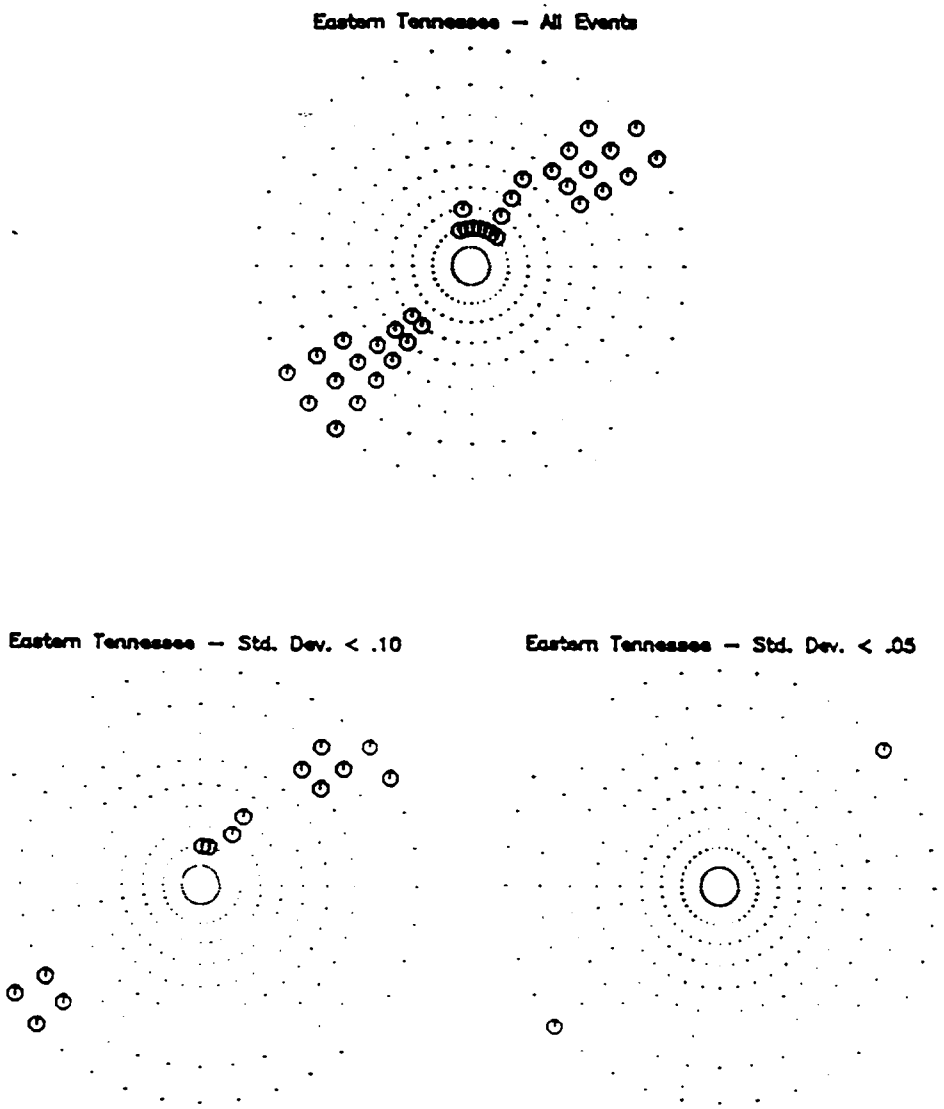

Figure 28. Stress tensor results for the Eastern Tennessee Seismic Zone: Lower hemisphere plot showing orientation of $\bar{\sigma}_1$ positions for which there was at least one acceptable solution. A) All results, B) solutions for which R had a standard deviation less than 0.10, C) standard deviation less than 0.05.

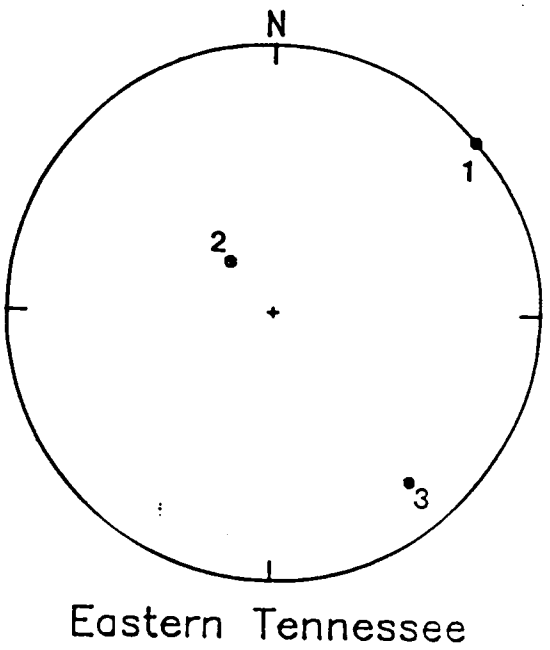

Figure 29. **Best stress tensor result for the Eastern Tennessee Seismic Zone:** Lower hemisphere equal area projection showing the orientation of $\bar{\sigma}_1$, $\bar{\sigma}_2$, and $\bar{\sigma}_3$ (labeled 1, 2, 3, respectively). The value of R was 0.66 with a standard deviation of 0.04.

Table 10. Fault Plane Attitude of the Best FMS for Each Earthquake.

Zone	Event No. *	Dip Degrees	Strike Degrees	Rake Degrees
Giles County	63	87	340	176
	90	55	215	-177
	94	21	173	136
	97	86	15	-176
	104	66	219	154
	110	42	219	-113
	118	35	44	0
	127	14	62	45
Central Virginia (> 8 km Deep)	64B	42	178	67
	82	76	253	-153
	86	85	94	70
	87	79	229	170
	100	51	330	8
	111	44	332	22
	113	66	356	26
	138	35	329	31
Central Virginia (< 8 km Deep)	53	45	349	135
	57	69	309	22
	64A	69	344	122
	78	83	349	135
	133	65	328	84
Eastern Tennessee	2	50	244	-23
	13	66	279	18
	14	90	277	10
	22	73	78	-18
	23	83	63	-29
	28	76	224	159
	29	76	84	-4
	30	18	40	147
	31	60	35	-145
	34	58	173	154
	36	81	217	176

* - see listing in Appendix A

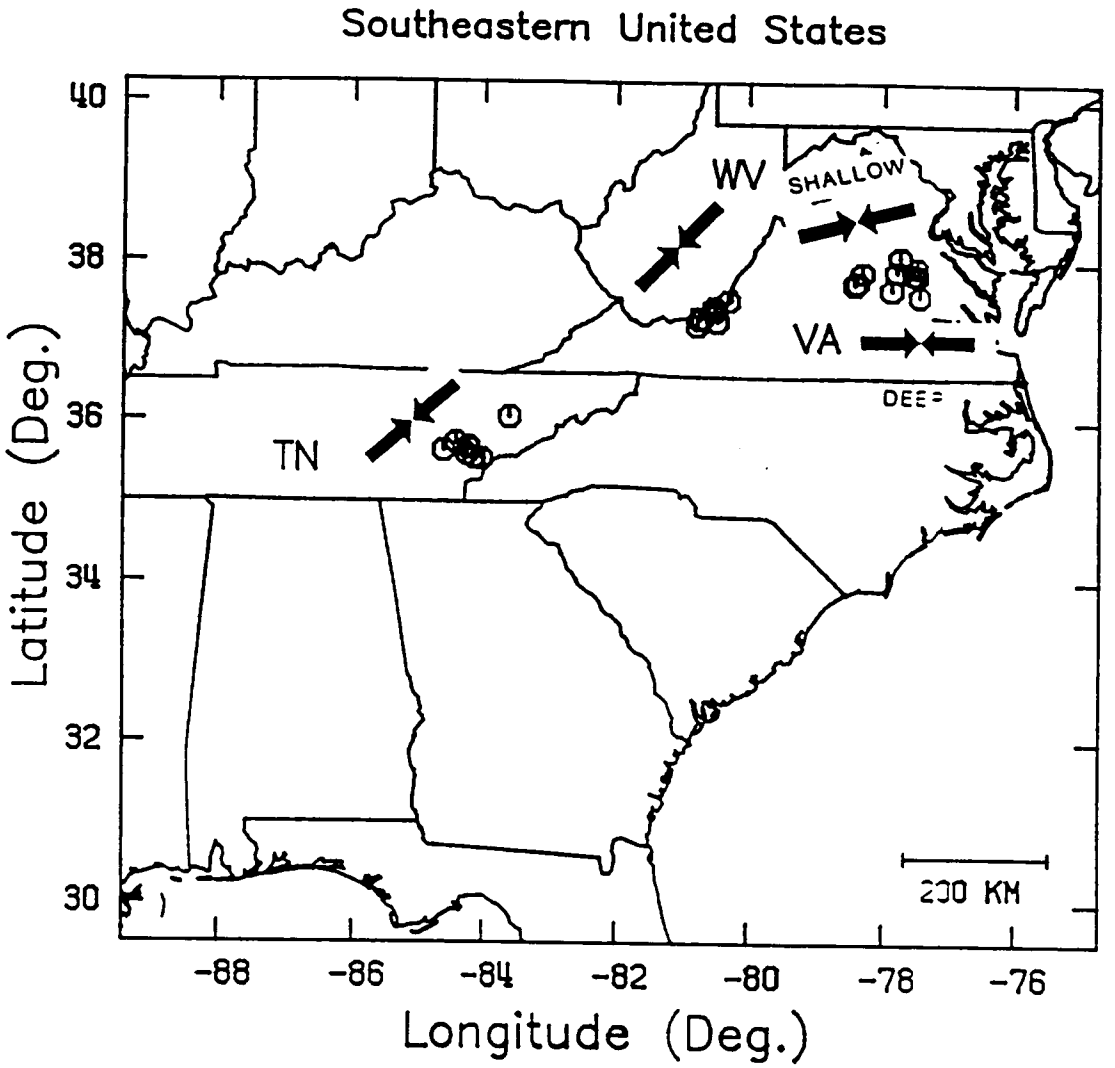

Figure 30. **Zonal stress estimates based on composited data:** The horizontal component of the maximum compressive stress is shown as a heavy arrow for each zone. Circles designate the epicenters of the events used in this study. All data from the Giles County Seismic Zone and the Eastern Tennessee Seismic Zone were used for their respective estimates. Central Virginia data were divided by depth at 8 km.

earthquake. Those solutions are plotted in Figure 31 through Figure 34. In each case the shaded quadrants indicate compression and the small marks along the circumference of the lower hemisphere plots indicate the fault plane as chosen by the program. Table 10 gives the attitude of the fault plane for each FMS chosen as the best solution for each earthquake.

Giles County Seismic Zone. See Figure 31. Most fault planes were oriented north to northeast, with the exception of two events (63 and 94), in which the planes trended slightly west of north. Focal mechanisms varied from right-lateral strike-slip (Events 63 and 97), to almost pure normal (Event 110), with most events showing oblique mechanisms. Fault planes ranged in attitude from near horizontal to near vertical.

Central Virginia Seismic Zone. Results are plotted for the data subsets as divided by depth (Figure 32, Figure 33). All shallow events indicate oblique faulting on planes trending north to northwest. Mechanisms of three of the five events (Events 53, 64A and 78) were very similar. Deeper events showed more variation of the orientation of the fault surfaces, though six of the eight events occurred along faults striking within 45° of north. A variety of focal mechanism types were represented, from strike-slip (Event 87) to reverse (Event 138). Dips of the fault planes ranged from about 30° to near vertical for events in both subsets of Central Virginia earthquakes.

Eastern Tennessee Seismic Zone. With the exception of Event 34, all fault planes were contained in the quadrant between 10° and 100°, with most in the range 30° to 70° (see Figure 34). Although all faulting was oblique, the most significant component was strike-slip on a steeply dipping surface. Only a single focal mechanism solution (Event 30) indicated slippage on a plane with a dip of less than 30°. The set of fault planes from the ETSZ were the most self-consistent of any of the zones studied.

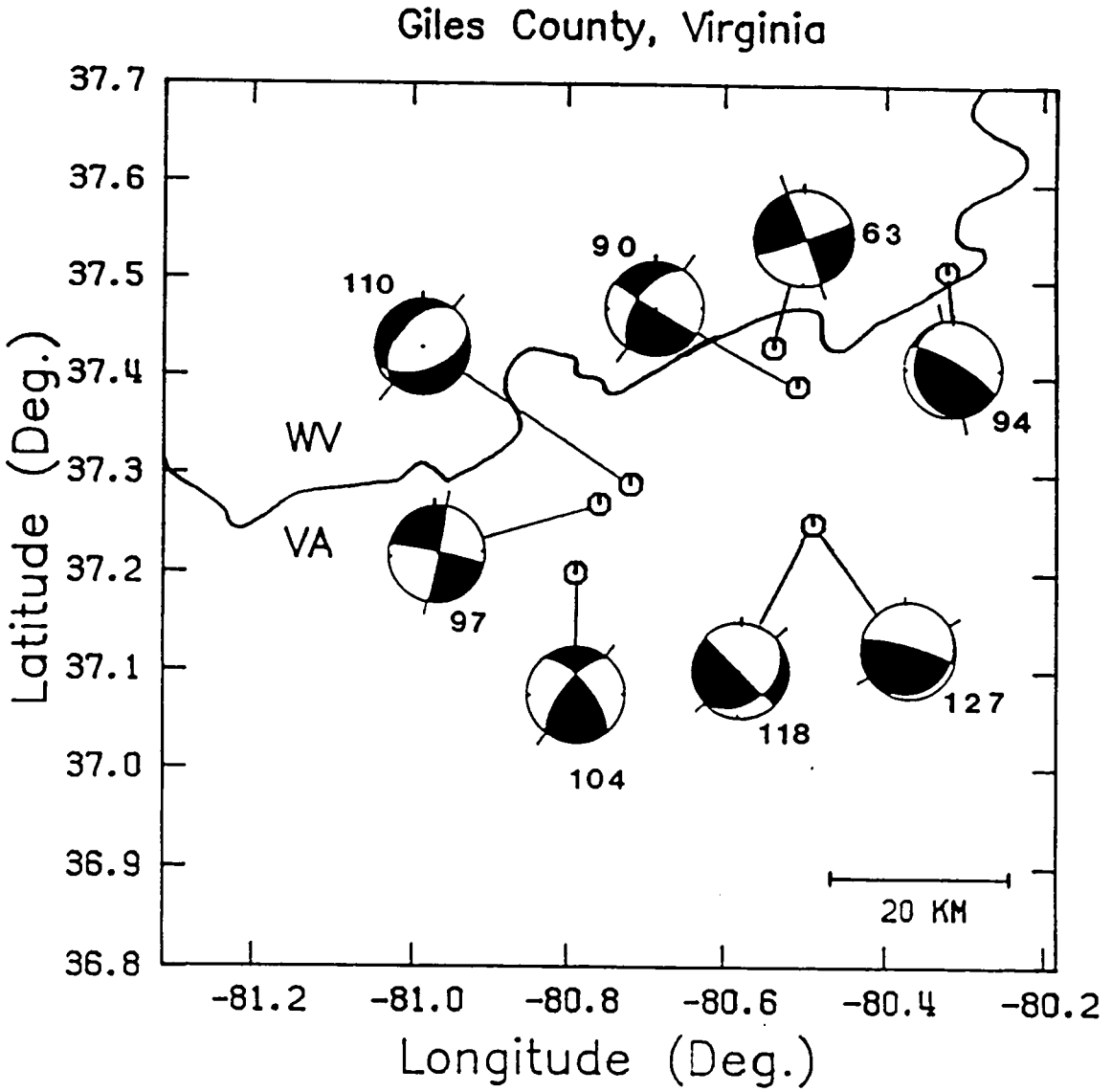

Figure 31. **Focal mechanism results for the Giles County Seismic Zone:** Focal mechanisms shown for each earthquake are those most compatible with the calculated regional stress. Equal area, lower hemisphere projections are used with compressional quadrants shaded. Event numbers refer to Table 10. Marks on the edge of each mechanism denote the chosen fault plane.

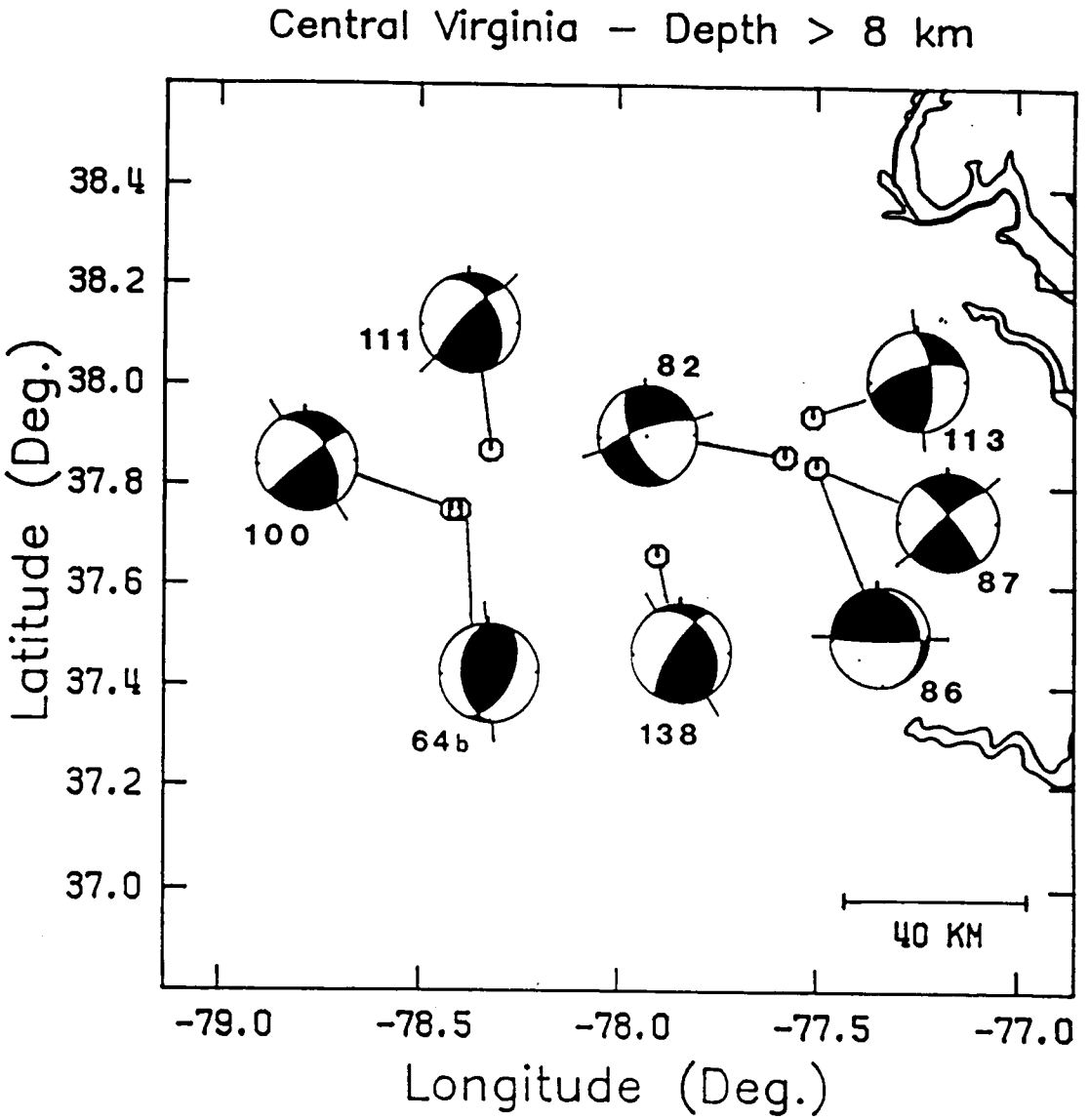

Figure 32. Focal mechanism results for deeper (> 8 km) events in the CVSZ: Focal mechanisms shown for each earthquake are those most compatible with the calculated regional stress. Equal area, lower hemisphere projections are used with compressional quadrants shaded. Event numbers refer to Table 10. Marks on the edge of each mechanism denote the chosen fault plane.

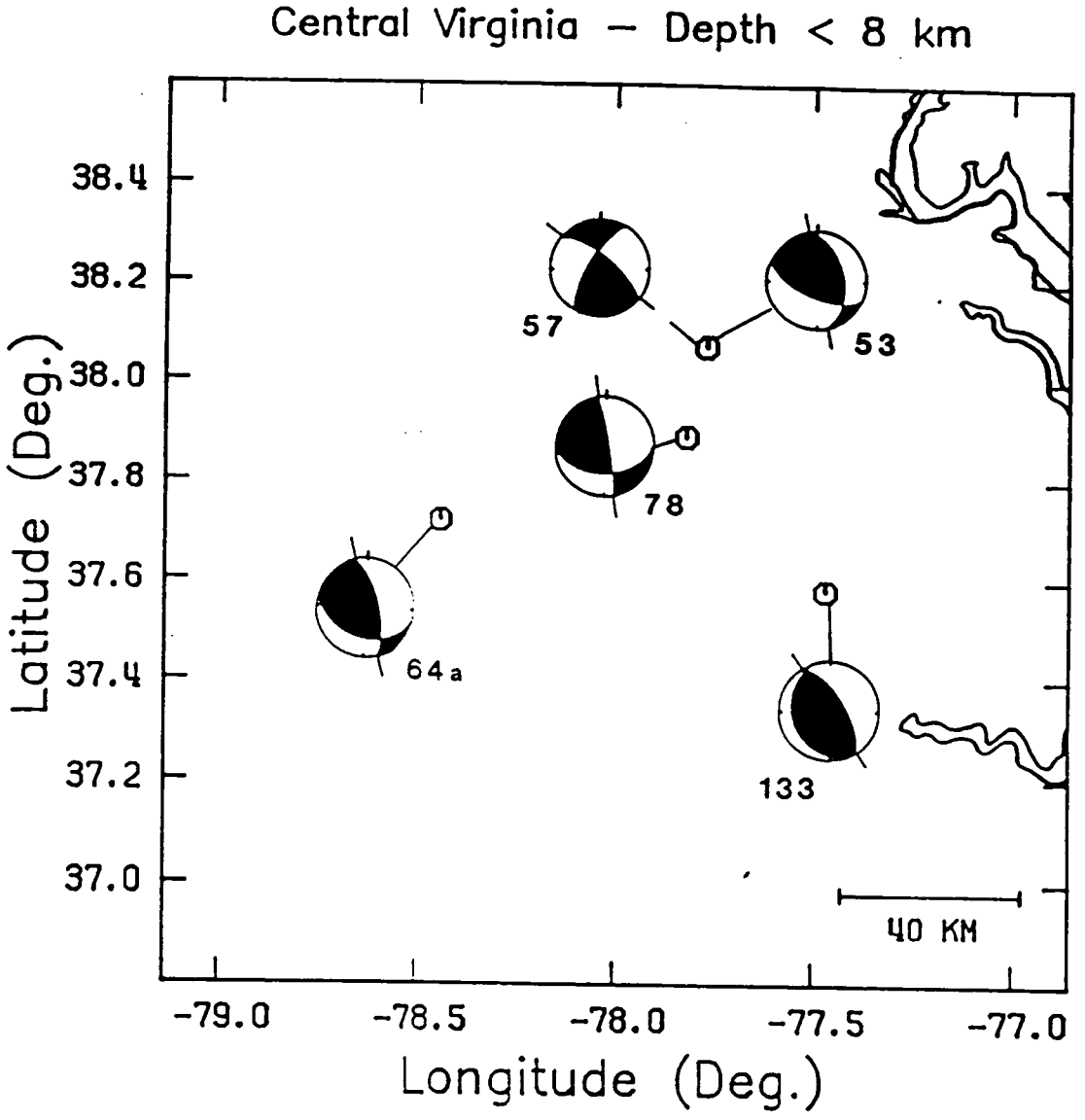

Figure 33. Focal mechanism results for shallow (< 8 km) events in the CVSZ: Focal mechanisms shown for each earthquake are those most compatible with the calculated regional stress. Equal area, lower hemisphere projections are used with compressional quadrants shaded. Event numbers refer to Table 10. Marks on the edge of each mechanism denote the chosen fault plane.

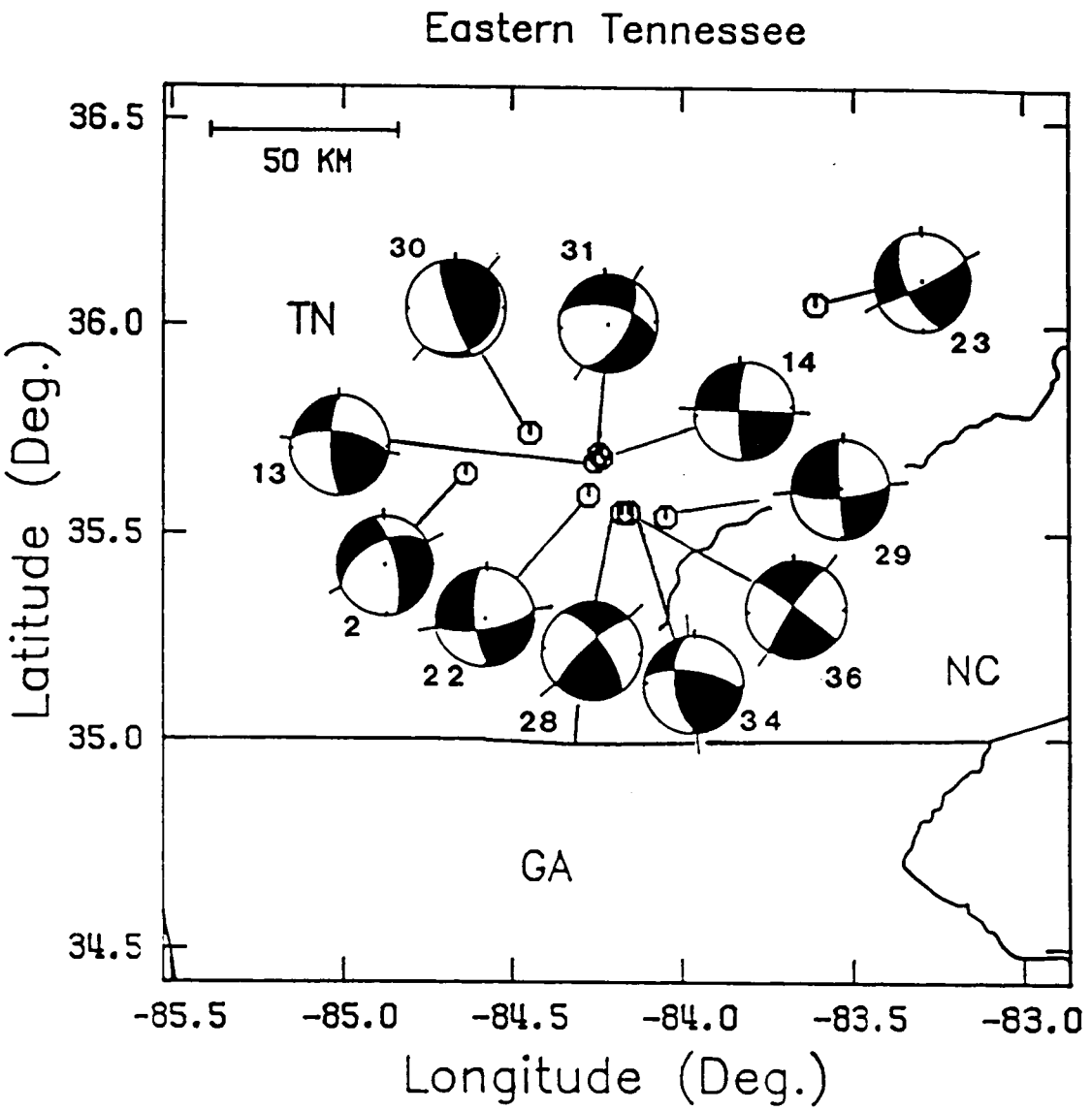

Figure 34. Focal mechanism results for the Eastern Tennessee Seismic Zone: Focal mechanisms shown for each earthquake are those most compatible with the calculated regional stress. Equal area, lower hemisphere projections are used with compressional quadrants shaded. Event numbers refer to Table 10. Marks on the edge of each mechanism denote the chosen fault plane.

Single Event Solutions

Once estimates of the stress tensor orientations were found, individual earthquakes were examined to study relationships between the estimate of the direction of maximum compressive stress and the individual **P**-axes of the focal mechanism solutions within each seismic zone. Those results are shown in Table 11 and Table 12, and figures showing the comparison are located in the appendices. For each earthquake, regions of the focal sphere within a chosen number of degrees from any of the **P**-axes were plotted. Values of that angular distance were picked to be 35, 25, and 15 degrees. For the entire set of 32 earthquakes, broken down into the Giles County Seismic Zone, the Eastern Tennessee Seismic Zone, and the two subsets of the Central Virginia Seismic Zone, 81% of the zonal $\bar{\sigma}_1$ axes were within 35° of at least one of the **P**-axes of the **FOCMEC** solution set for each earthquake. For the smaller angular distances of 25° and 15°, that percentage dropped to only 56% and 31%, respectively.

Table 11. Comparison of Estimated Maximum Compressive Stress and P-axes.

Zone	Event	35 Degrees	25 Degrees	15 Degrees
Giles County	63	X	X	X
	90	X		
	94	X		
	97	X	X	
	104	X		
	110	X		
	118			
	127			
Central Virginia (All)	53	X	X	X
	57	X	X	X
	64A	X	X	
	64B	X		
	78	X	X	X
	82	X	X	X
	86			
	87	X	X	X
	100			
	111			
	113			
	133	X	X	X
	138			
Central Virginia (> 8 km Deep)	64B	X		
	82	X	X	
	86			
	87	X	X	
	100	X	X	X
	111	X	X	
	113			
	138	X	X	X
Central Virginia (< 8 km Deep)	53	X	X	X
	57	X	X	X
	64A	X	X	
	78	X	X	
	133	X	X	X
Eastern Tennessee	2	X	X	
	13	X	X	X
	14	X	X	X
	22	X		
	23			
	28	X		
	29	X	X	X
	30			
	31	X	X	
	34	X	X	X
	36	X		

X - indicates maximum compressive stress direction within this angle from the P-axis.

Table 12. Angular Distance between Maximum Compressive Stress and P-axes.

Zone	35 Degrees	25 Degrees	15 Degrees
Giles County	75	25	12.5
Central Virginia (All)	61.5	53.8	46.2
Central Virginia (> 8 km Deep)	75	62.5	25
Central Virginia (< 8 km Deep)	100	100	60
Eastern Tennessee	81.8	54.5	36.4
All	81	56	31

Numbers in columns represent percentage of P-axes within this angle of maximum compressive stress.

Comparison with Other Methods

To specify the similarities and differences of the method developed for this study with similar techniques already published, an intercomparison was made. The techniques compared were the Method of Right Dihedra (MRD) of Angelier (1979), an updated version of the algorithm developed by Gephart and Forsyth (1984), which will be referred to as the Rotation of Misfit FMSs Inversion (RMI), and the inversion of Michael (1984) which made use of the bootstrap resampling technique for estimation of confidence regions (Michael, 1987a). Input data for all of those programs were the best focal mechanism solutions for the eleven events in the Eastern Tennessee Seismic Zone, chosen from each MFMS based on the lowest RMS ratio error. Results from each method will be briefly discussed, with solutions compared to one another as well as to the results from this study. Orientations of the principal axes calculated by each method are given in Table 13.

The Method of Right Dihedra. A computer program was written for this study which superposed the best focal mechanism solution from each event onto a single figure. Numerical values of 100 were given to all points in the **P**- axis quadrant, while a value of 0 was assigned to points included in the **T**-axis quadrant. Summations were made for 324 test points on the lower half of the focal sphere, and the results were plotted on a single figure. The data on the resulting figure, termed the

Table 13. Principal Stress Orientations Calculated by Different Methods.

Method	σ_1 Degrees Trend	Plunge	σ_2 Degrees Trend	Plunge	σ_3 Degrees Trend	Plunge
Right Dihedra Angelier (1979)	55	0	327	70	146	20
Rotation of Misfit FMSs Gephart and Forsyth(1984)	51	1	140 (320)	69	320 (140)	20
Bootstrap Resampling Michael (1987a)	57	6	302	76	149	12
MFMSs per Earthquake (This Study)	50	0	320	70	140	20

Values in parentheses indicate possible correct solution as discussed in the text.

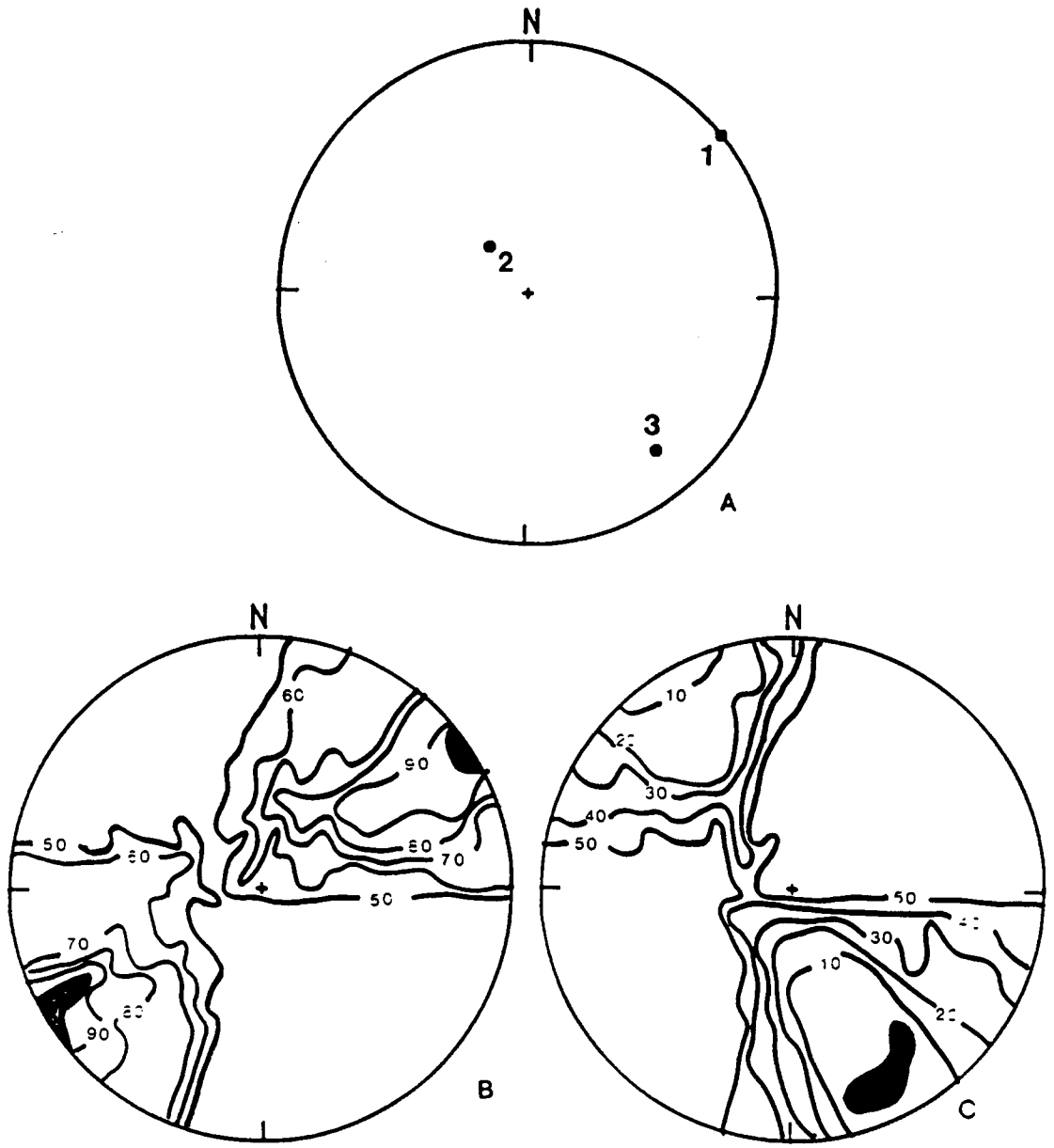

Figure 35. Comparison with the Method of Right Dihedra: All results are for 11 selected events in the Eastern Tennessee Seismic Zone. A) Results of this study; 1, 2, 3, refer to the $\bar{\sigma}_1$, $\bar{\sigma}_2$, and $\bar{\sigma}_3$ axes, respectively. B) and C) Results from the Method of Right Dihedra. B) Contours defining the $\bar{\sigma}_1$ axis for the regional stress, and C) Contours defining the $\bar{\sigma}_3$ axis.

areal frequencies, produced maximum and minimum values corresponding to the orientations of the $\bar{\sigma}_1$ and $\bar{\sigma}_3$ axes, respectively. That contoured data is shown on Figure 35 for both the $\bar{\sigma}_1$ and $\bar{\sigma}_3$ axes. The results of the MSET are also shown for comparison. Note the similarity of the results from the two methods. A median value of 55° and 0° was assigned to the trend and plunge, respectively, of the $\bar{\sigma}_1$ axis determined by the MRD. That orientation represented the center of the contoured region with the largest value. For the ETSZ, that contour value was 100, indicating the area of the focal sphere which was common to the P-axis quadrants of each solution. There was only a 5° misfit between the orientation of the $\bar{\sigma}_1$ axis found by this method and that found using the MSET. The orientation of $\bar{\sigma}_3$ also matched well, with only a 6° difference in the trends of the two results. The $\bar{\sigma}_2$ axis, which was not defined graphically, was constrained by the condition of orthogonality among the three principal stress axes.

Gephart and Forsyth (1984). The $\bar{\sigma}_1$ orientation found using an updated version of the program described in Gephart and Forsyth (1984) was similar to the orientation found in this study, with less than one degree of difference. The results of that method were kindly provided by J. W. Gephart and are shown in Figure 36. However, there is a discrepancy between the orientations of $\bar{\sigma}_2$ and $\bar{\sigma}_3$ from those of this study. That misfit corresponds to about a 40° rotation about the $\bar{\sigma}_1$ axis. No reason for that difference is known at this time, although it is probably an error in data handling, since a change of orientation of 180 degrees would bring the results of the two methods into alignment.

Bootstrap resampling. The inversion method described by Michael (1987a) was utilized to produce a third comparison with the results of this study. That method included the empirical bootstrap resampling technique for calculation of confidence regions. Results are shown in Figure 37 for the 95%, 75% and 50% confidence regions. Since none of the fault planes were specified prior to the inversion, each nodal plane of a single solution was given a 50% probability of breakage. Two thousand sample subsets were computed to derive the confidence regions. No measure of the best results were easily obtained because of the uncertainty associated with the fault planes (Michael,

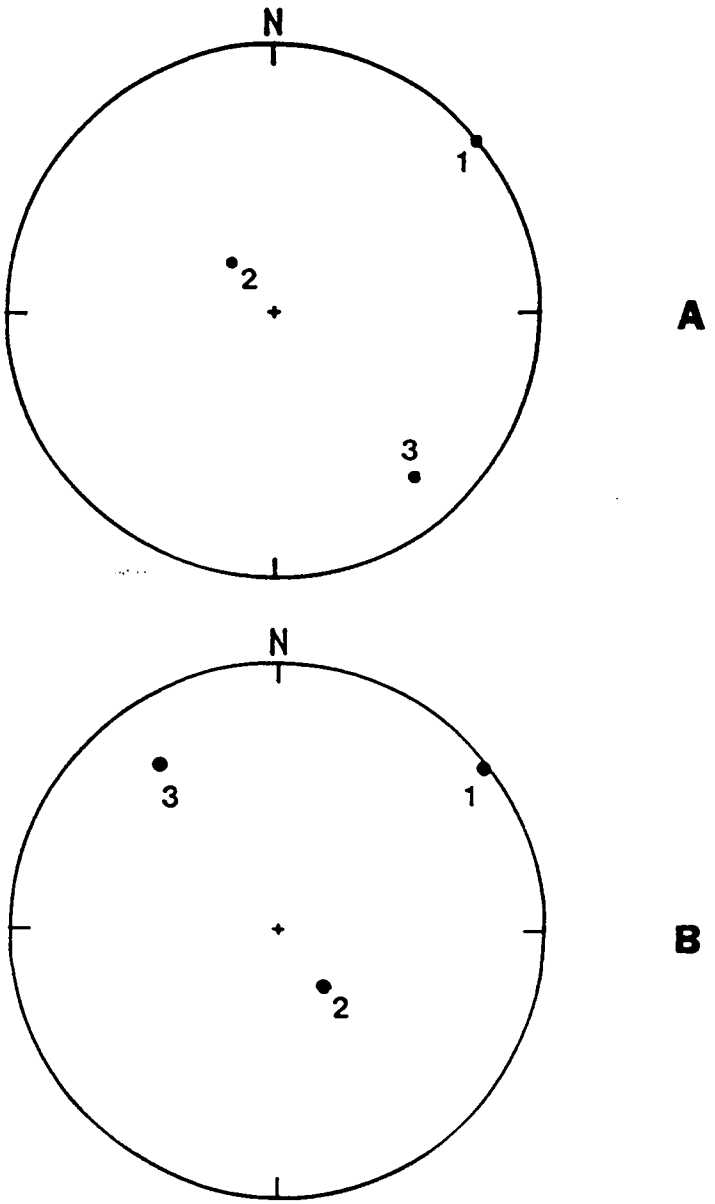

Figure 36. Comparison with the method of Gephart and Forsyth (1984): All results are for 11 selected events in the Eastern Tennessee Seismic Zone. A) Results of this study; 1, 2, 3, refer to the $\overline{\sigma}_1$, $\overline{\sigma}_2$, and $\overline{\sigma}_3$ axes, respectively. B) Results of the method of Gephart and Forsyth (1984). Although the $\overline{\sigma}_1$ axes are well matched, there is a rotation of about 40° between the results of the RMI and those of the MSET for both the $\overline{\sigma}_2$ and $\overline{\sigma}_3$ axes. That is interpreted as a mistake in data handling, as a change in orientation of exactly 180° would reconcile the results.

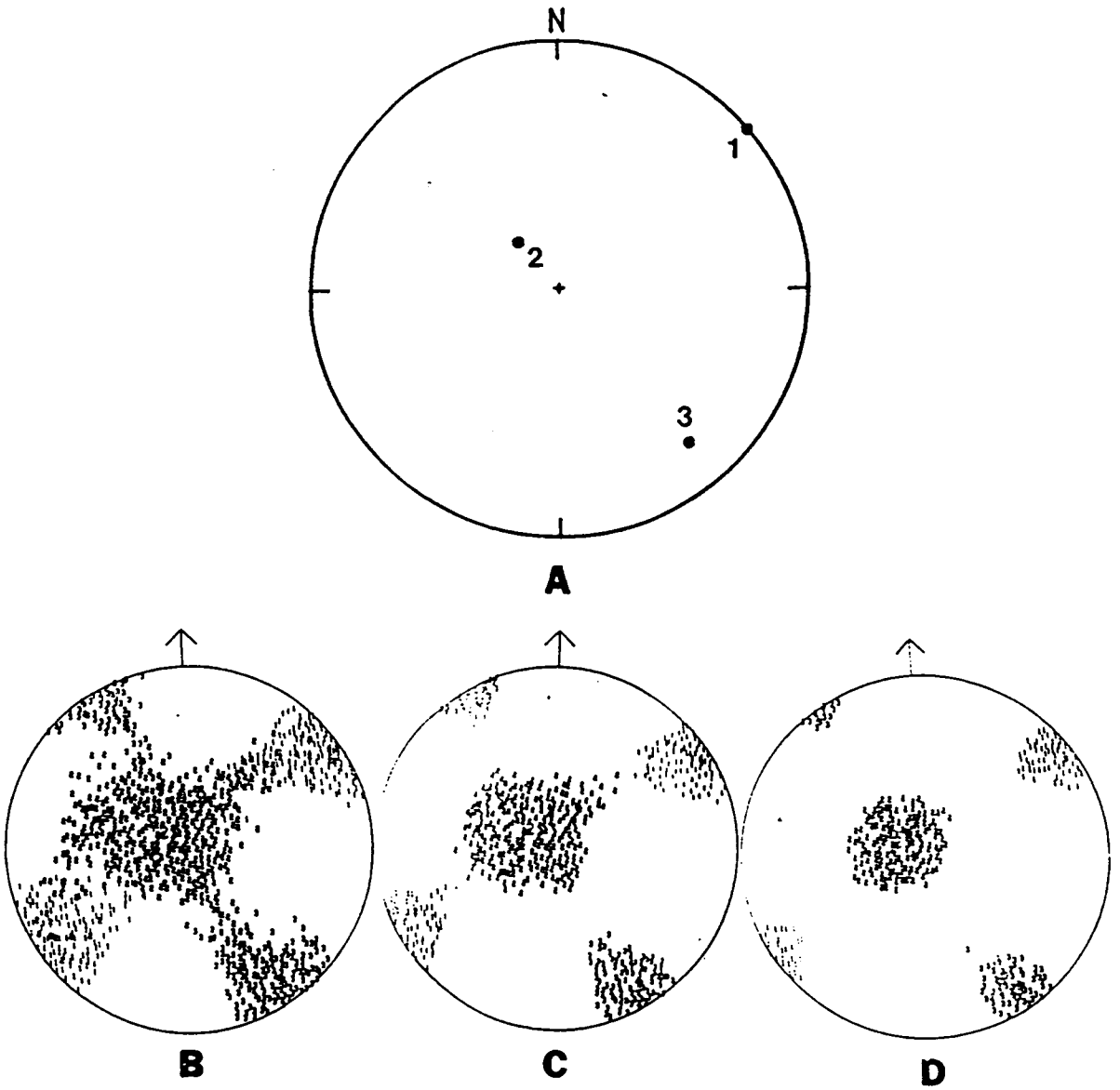

Figure 37. Comparison with the Bootstrap Technique: All results are for 11 selected events in the Eastern Tennessee Seismic Zone. A) Results of this study; 1, 2, 3, refer to the $\bar{\sigma}_1$, $\bar{\sigma}_2$, and $\bar{\sigma}_3$ axes, respectively. B - D) Results of the method of Michael (1987a) using the bootstrap resampling technique for confidence regions of 95%, 75% and 50%, respectively.

1988; personal communication). The average of those 2000 bootstrap results were used to obtain the orientations shown on Table 13, and compare well with the results of this study.

Summary. All four methods used for the derivation of the stress tensor orientation of the ETSZ produced similar results. The only exceptions were the trends of the $\bar{\sigma}_2$ and $\bar{\sigma}_3$ axes calculated by the method of Gephart and Forsyth (1984). That discrepancy most probably is an error in data handling rather than one of methodology. All results match particularly well for the orientation of the $\bar{\sigma}_1$ axis. Based on those comparisons, the estimates made using the MFMS sets of **FOCMEC** were found to produce a reliable measure of the orientations of the principal axes for the seismic zones of the Southeastern U. S.

Discussion

The discussion of the results contained herein will be divided into two segments. The first will be a review of the methodology. Included in that portion will be suggestions for further improvements of the procedure, including integration with the **FOCMEC** program. The second segment of the discussion will review the results as they pertain to the Southeastern U. S. and to the individual seismic zones, focusing on a comparison of the maximum compressive stresses determined by this study and how they relate to earlier work. The significance of the modes of faulting in each zone will also be discussed.

Methodology

This study developed a new technique (the MSET) for the estimation of a regional stress tensor from focal mechanism solutions. That technique is an improvement over earlier methods in several ways, particularly with the use of sparse data; 1) the fit of the input polarity (and in our case $(SV/P)_a$ amplitude ratios) with the selected best FMS for each earthquake is assured (it is not in other methods), 2) those selected best FMSs are chosen so as to be compatible with a homogeneous stress regime, and 3) the difference between the observed slip and theoretical slip

directions is used as a weighting scheme. Thus, no judgements of the quality of a best FMS for each earthquake was necessary prior to the stress estimation. Weighting was also based in part on how well true ground motion polarities and $(SV/P)_z$ amplitude ratios matched theoretical values of the focal mechanism itself. Each member of the focal mechanism solution set was given appropriate weight prior to derivation of an acceptable stress tensor. That weight was used in the choice of the most appropriate tensor orientation associated with the **FOCMEC** output data.

The MSET was also unique in that once the best-fitting stress tensor for a zone was found, it could, in turn, be used as a determining factor in the choice of the best focal mechanism solution from each **FOCMEC** set, under the assumption of a homogeneous stress tensor in each seismic zone. In past work, FMSs were determined for earthquakes primarily using polarity data. Those data were used to determine a single focal mechanism solution for each event. The error of each FMS could only be assessed by the number of misfit data points. When amplitude ratio data were introduced, the misfit could be more quantitatively calculated. However, amplitude data are neither as well recorded (e. g. often other phases interfere with the primary shear energy) nor as easily interpreted as the polarity of the first arriving P-wave. Therefore, the choice of a single best solution is often a subjective decision, especially in the case (as in the SEUS) where instrumentally recorded data sets are small, events are in the lower magnitude range (generally $m_b < 2.5$) and station coverage is limited. The assumption of a homogeneous stress tensor as another constraint on the orientation of a single FMS for each event is a useful addition. The important result is that the solution is compatible with the homogeneous stress assumption and, especially, solutions which are probably incorrect due to poor data constraint are eliminated.

The choice of FMSs to be composited was based simply on the location of each event. All earthquakes within a seismic zone for which a FMS had been determined were used in the computation. That decision was based primarily on the limited number of events in each zone. If more data had been available, then it may have been prudent to eliminate several earthquakes from this study. Those would include the events in the GCSZ southeast of the well-defined lineation (the earthquakes near Blacksburg), and those events in the CVSZ for which depth control was so poor that it could not be determined whether they were above or below the 8 km boundary.

At this stage any decrease in the size of the data set would limit the the usefulness of the technique. We must assume that the principal stresses associated with those events mentioned do not differ significantly from the general trend in each zone. The results of Zoback and Zoback (1985) indicate that such an assumption is reasonable.

The assumption of a homogeneous stress field worked well for the seismic zones. Each data set resulted in well-defined tensor orientations (as indicated by the figures in the **Results** section), and the standard deviation about **R** decreased in a well-behaved manner toward the single best solution. This was not surprising, as there are no known features associated with localized variations in the stress field, with the exception of the depth boundary in Central Virginia. That surface was taken into account by the division of the CVSZ data set into sets of events above and below 8 km.

As a part of the calculations, the computer program was allowed to choose the best-fitting nodal plane and consider it as the fault plane. Although a similar approach was taken by Gephart (1985), Michael (1987a) has pointed out that fault planes should be selected using other criteria. In the case of the SEUS, there are few constraints which may be placed on the sense of faulting (e.g. surface rupture, large scale seismic trends, aftershock sequences). Even in the case of the lineation of epicenters within the GCSZ there was enough variability in the individual FMSs that the choice of the fault plane for each event would be difficult. The method of Vasseur and others (1983) does not depend on the choice of one nodal surface as the fault plane, but is only effective for stress tensors with a small value of **R**. That condition was not met in this study, as **R** values associated with the derived stress tensors varied throughout the range from 0 to 1. Therefore, the approach judged to be best was to let the program determine the fault plane, although, for other data sets, the option does exist to make pre-determined selections of the fault planes which will not be altered by the program during analysis.

Error analysis would become very complex if attempted in a more rigorous manner than that of this study. Uncertainties that would be difficult to parameterize were involved not only with the estimation itself, but also with the choice of input data and the calculations of the MFMSs. Both the data used to determine the multiple focal mechanism solution sets and the parameters used in

the **FOCMEC** program must be considered as a source of potential error. However, a major practical consideration was the assumption that, in most cases, the first motion and amplitude ratio data do not allow only a single focal mechanism solution to best represent the dynamics of faulting of an earthquake. Rather, all possible focal mechanism solutions, calculated within constraints placed upon the fit of the input data, must be considered. If precise calculations of the error associated with each stress tensor were to be made, then a more rigorous analysis of the input data must be undertaken, with a correspondingly larger number of allowed **FOCMEC** solutions. Such an analysis would not be warranted by the quantity of most suites of input data in the SEUS.

A logical extension of the research reported herein would be a closer integration of the stress tensor estimation with the **FOCMEC** program. Advantage could be taken of the ability to vary the search routine within **FOCMEC** so that more FMSs could be tested, especially in the vicinity of solutions found to be nearly compatible with the theoretical stress tensor. In that manner, a FMS which has only a small amount of misfit could be reoriented, and yet its fit with the original input data (polarities and $(SV/P)_z$ data) would be maintained.

Additional future research using an integrated **FOCMEC/STRESS** program would best be performed in the following manner. A region with a well-determined, homogeneous stress field and adequate data (on the order of hundreds, rather than tens, of earthquakes) with good station coverage would be chosen. Focal mechanism solution sets would be determined with **FOCMEC** using original polarity and $(SV/P)_z$ amplitude ratio data. The best solution within each MFMS set would be determined using *a priori* knowledge of the local stress field, using *in situ* measurements and/or estimates based on previous well-constrained studies of focal mechanism solutions. As a second step, the full process would be utilized, solving jointly for both the best focal mechanism solution for each event and for the orientation of the principal stress axes. The well studied, highly instrumented seismic zones of the Western U. S. would be an ideal location for such research, as long as care was taken to avoid local reorientations of the stress field caused by large, weak fault systems (Zoback and others, 1987).

Stress tensor estimates made using composited data for each of the zones were constrained well enough to be compared directly with the results of previous studies. Except as noted, the

horizontal component of the maximum compressive stress ($\bar{\sigma}_1$) will be used in the following comparisons, as it relates directly to earlier work based on *in situ* measurements and/or studies of P-axes.

General Comparison with P-axes Solutions

As shown in the **Results** section, the relationship between the P-axes of the MFMSs and the direction of the maximum compressive stress derived in this study is not closely constrained. For the region, in 81% of the cases the P-axis is within $\pm 35°$ of $\bar{\sigma}_1$, which has been documented by Raleigh and others (1972) to be a reasonable distance. However, as smaller angular distances were tested, that correspondence dropped to 56% for $\pm 25°$ and only 31% for $\pm 15°$. An additional study of the orientation of the horizontal component of $\bar{\sigma}_1$ in relation to the average P-axis is shown for each seismic zone in Figure 38 through Figure 40. The vertical lines represent the values of strike of the $\bar{\sigma}_1$ axis for each of the seismic zones as derived in this study, with both shallow and deeper estimates shown on Figure 39 for Central Virginia. The best correspondence is shown for the ETSZ, where 64% (7 of 11) of the average P-axis measurements are within one standard deviation of the $\bar{\sigma}_1$ direction of the best-fitting stress tensor. For the other zones, that percentage is 25% for the GCSZ, 60% for the shallow events in the CVSZ, and 12% for the deeper events. Therefore it is likely that any estimate of the $\bar{\sigma}_1$ orientation based on a single earthquake would not be representative of the zonal average.

Regional Stress Field

In general, all results, except those from the deeper events in Central Virginia, agree with the estimates made by Zoback and Zoback (1980, 1985; also Zoback and others, 1985) for the Eastern United States. Those studies noted the pervasive northeasterly trending maximum horizontal

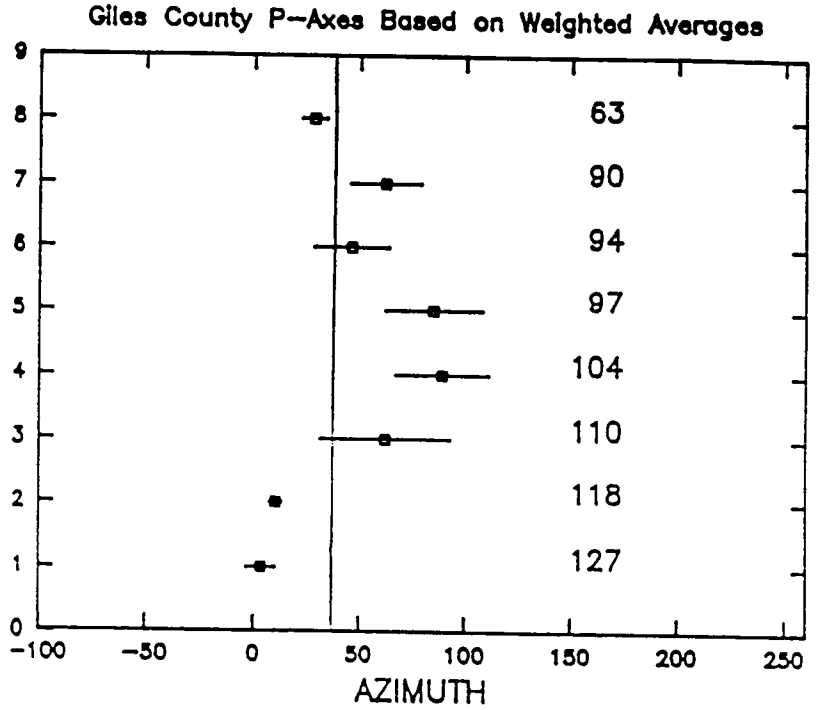

Figure 38. Comparison of Maximum Compressive Stress to P-axis for GCSZ: Standard deviations about a single 'average' P-axis of the MFMS output of FOCMEC are shown as horizontal lines for each event. Vertical line shows $\bar{\sigma}_1$ estimate of this study. For 25% of the events $\bar{\sigma}_1$ is within one standard deviation of the average P-axis. Event numbers refer to Appendix A.

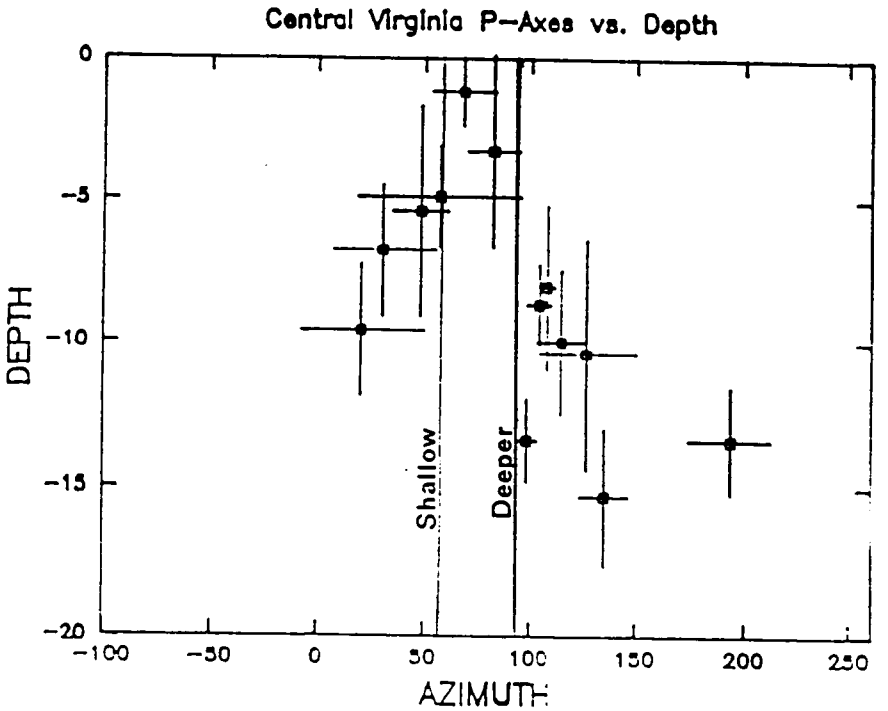

Figure 39. **Comparison of Maximum Compressive Stress to P-axis for CVSZ:** Standard deviations about a single 'average' P-axis of the MFMS output of FOCMEC are shown as horizontal lines for each event. Vertical lines show $\bar{\sigma}_1$ estimates of this study for shallow and deep data sets. For 60% of the shallow events, and 12% of the deeper events, $\bar{\sigma}_1$ is within one standard deviation of the average P-axis. Event numbers refer to Appendix A.

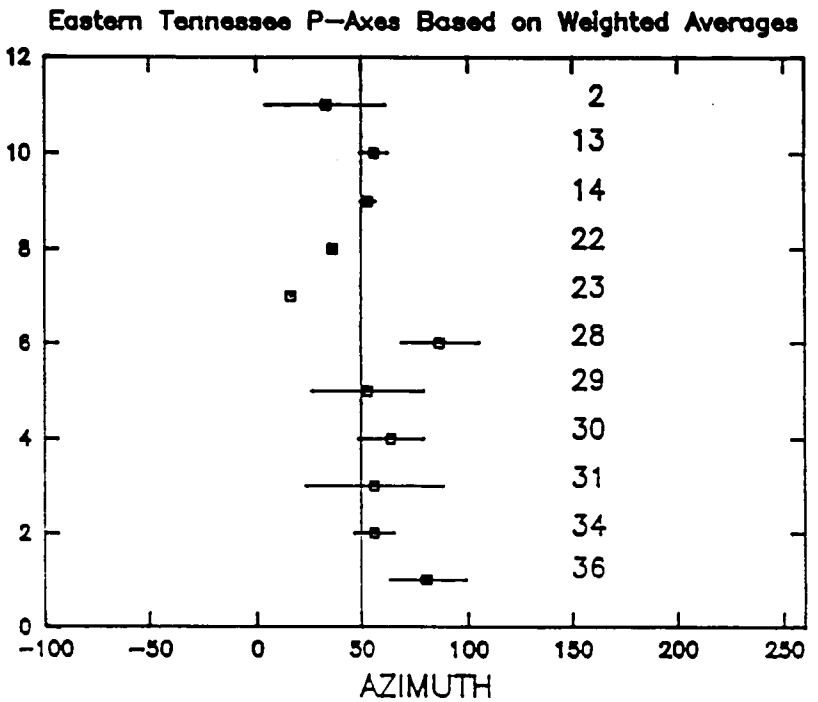

Figure 40. Comparison of Maximum Compressive Stress to P-axis for ETSZ: Standard deviations about a single 'average' P-axis of the MFMS output of FOCMEC are shown as horizontal lines for each event. Vertical line shows $\bar{\sigma}_1$ estimate of this study. For 64% of the events $\bar{\sigma}_1$ is within one standard deviation of the average P-axis. Event numbers refer to Appendix A.

compressive stress. Interpretations of that general trend have also been made to understand the tectonic forces responsible for the particular stress orientation. Richardson and others (1979) made a comprehensive study of stress in the plates and the fit of the stress orientations to numerical models incorporating various driving forces, including ridge push, gravitational sliding, and drag along the base of the plate. They concluded that boundary forces (e. g. ridge push at spreading centers, sinking at subduction zones, collisions at continent-continent boundaries) and forces acting along the base of the slab are both necessary to best describe the global crustal stress pattern. In particular, forces acting along the base of the lithosphere appear to be most complex, and are directed such that they are neither uniformly opposing nor augmenting the absolute plate motion.

Local Seismic Zones.

The following discussions center on both the stress tensors derived in this study and related focal mechanism solutions as they apply to the seismic zones studied herein.

Giles County Seismic Zone. The horizontal component of maximum compressive stress for the GCSZ follows a trend of 40°, which is similar to the estimate of N46°E found by Munsey and Bollinger (1985) using **P**-axes from 6 single event focal mechanism solutions and 2 composite solutions. It also compares well with the hydrofracturing measurement reported by Haimson (1977b) from Wayne, West Virginia, for which the maximum compressive stress was found to be oriented N50°E. The compressive stress found in this study, however, was in poorer agreement with the *in situ* measurements of N69°E made by Aggson (1978) in Bolt, West Virginia, using the overcoring technique. Any comparison with *in situ* measurements must be qualified by recognizing the difference in depth between the location of those measurements and the seismic zone.

When all acceptable orientations of the $\overline{\sigma}_1$ axes were plotted in Figure 20, there were two clusters of solutions, one horizontal and striking N40°E, and the second with a steep dip and a trend of approximately north. That second cluster was nearly coincident with the best-fitting $\overline{\sigma}_2$ direction,

indicating a possible shift of principal stress directions with depth such that the $\bar{\sigma}_2$ axis for shallow events became the $\bar{\sigma}_1$ axis of deeper events. The data set was too small, and errors in depth measurements were too large, to split the data by depth to verify that hypothesis. Examination of the focal mechanism solutions associated with the best-fitting stress tensor revealed several interesting facts. The average strike of the fault planes was 25°, which compared well with the assumed seismic structure, defined by Gresko (1985) as deeply dipping faults striking N20-27°E. Only one event (Event 110) showed predominantly normal faulting. This was the only such focal mechanism observed in this region. Two events with nearly identical foci (Events 118 and 127) have very similar mechanisms. There was no systematic change in either the mode of faulting or orientation of the fault plane with depth or epicenter. The argument that faulting is generally on planes striking N20-27°E (e. g. Gresko, 1985; Munsey and Bollinger,1985) is well founded.

Central Virginia Seismic Zone. The data presented in this study confirm the dependence of stress with depth in the Central Virginia Seismic Zone as first discussed by Munsey (1984). Shallower earthquakes have a subhorizontal compressive stress oriented N70°E, while the deeper data set was associated with a westerly azimuth. Although the difference between those two sets was not as pronounced as that reported by Munsey and Bollinger (1985) (where trends were NE and SE), the data sets divided by depth fit the data better (i. e. the value of **R** was better constrained) than a single homogeneous zonal stress regime. That observation was particularly remarkable when the inherent error in depth determination was taken into account, since a misplaced solution would increase the scatter of the acceptable principal axis directions. One would expect shallow earthquakes to perhaps represent thin-skin local effects while deeper events would more closely follow regional trends. In Central Virginia, however, the opposite was found to be true. An explanation for the observed results cannot be made with any simple model, such as an exchange of principal stresses with the addition of a greater vertical load.

Since a single stress tensor for each the shallow and deeper Central Virginia events was not easily chosen except by consideration of the weighting scheme, those sets of the tensors with the best constrained **R** values were plotted in Figure 25 and Figure 27. Eight tensor solutions were

plotted for the deeper earthquakes, and six for the shallow events. Only the $\overline{\sigma}_1$ axes clustered for the shallow events, with a variety of orientations for both $\overline{\sigma}_2$ and $\overline{\sigma}_3$. Note, however, that the results for the deeper events showed a strong subhorizontal clustering of the $\overline{\sigma}_3$ axes, with less organization of the $\overline{\sigma}_2$ directions. That could be be explained by an increase of vertical load, the smallest principal compressive stress in that case would tend to be horizontal.

Deeper Central Virginia earthquakes had no consistent fault strike, but rather showed a wide range of attitudes, implying heterogeneous basement rocks with multiple planes of weakness. The poor constraint of those results was similar to those of Ma and others (1988) obtained for the Pacific Northwest. It was felt, however, that the $\overline{\sigma}_1$ orientations of deeper events were well enough constrained so that the fundamental difference with the stress field in the overlying crust was justified.

In the shallow crust (< 8 km), fault planes were oriented in the range from north-south to approximately northwest-southeast. That trend did not follow any known large-scale geologic features, but was consistent among the five events.

Eastern Tennessee Seismic Zone. The direction of the maximum compressive stress agrees well with regional observations made by other researchers (e. g. Teague, 1984; Johnston and others, 1985). The overall composited trend was an excellent fit for a compressive stress oriented N50°E. Note that this trend was nearly identical to that derived for the Giles County Seismic Zone for the orientation of not only $\overline{\sigma}_1$, but for $\overline{\sigma}_2$ and $\overline{\sigma}_3$ as well. In fact, the ETSZ and GCSZ have been previously studied and found to be similar in many other respects (Johnston and others, 1985). Data presented here compare quite well with deeper overcoring stress measurements. Aggson (1978) reported that the maximum stress within the Immel mine (in the ETSZ near Knoxville) had an azimuth of 58°.

As with the Giles County Seismic Zone, events in the ETSZ occured predominantly along steeply dipping planes striking northeast-southwest. Most of the events in Eastern Tennessee showed mainly strike-slip movement, while those in Giles County indicated a larger component of dip-slip. However, the overall similarity of the two regions is remarkable.

In both Eastern Tennessee and Giles County, the average angular distance between the maximum compressive stress and the fault plane was approximately 18°. Geologically, that indicates one of two possible scenerios. If a variety of fault orientations are present in the two zones, then those which exhibited movement must be weak, as they are not aligned at the most favorable angle in relation to the $\overline{\sigma}_1$ direction. Most likely, however, the fault populations in each of the zones are predominantly aligned within the northeast quadrant.

Summary

The results of this study may be summarized as follows:

1) The technique implemented for the derivation of the principal stress directions from sets of focal mechanism is an improvement over existing methods in that the fit of the best focal mechanism solution to the original polarity and $(SV/P)_z$ amplitude ratio data is assured particularly for use with limited data sets. Such is not the case with other methods, which require prior determination of a single FMS for each event, and in some cases, alter the orientation of that solution to best fit the stress tensor, without determining if that new orientation fits the original seismic data. Those techniques are most compatible with large data sets, where errors would average out with the application of minimization calculations.

2) The output from the **FOCMEC** program may be productively applied to studies of regional stresses. Errors associated with the focal mechanism solution of each event may, in part, be accounted for by the range of solutions allowed by **FOCMEC**. Thus, no determination of an arbitrary 'best' focal mechanism solution is necessary prior to calculations.

3) The orientations of stress tensors estimated by the technique used herein are similar with those derived by other methods (i. e. Angelier, 1979; Gephart and Forsyth, 1984; Michael, 1987a), but take into account a reasonable estimate of the error associated with the FMS. Error is dealt with by weighting the misfit of the observed and theoretical slip directions, rather than by a

reorientation of the focal mechanism solution, as is the case for the method of Gephart and Forsyth (1984).

4) Weighting schemes based upon primary data (first-motion direction and P-wave and SV-wave amplitudes) can be used to discern the best focal mechanism solution for a particular earthquake. The set of solutions for a seismic zone so chosen will be consistent with a homogeneous stress field.

5) Analysis of P-axis directions may be used for determination of stress directions only in a broad sense. The presence of a pre-faulted crustal material of various orientations and mechanical properties makes reconciliation of the P-axis to the $\bar{\sigma}_1$ direction approximate at best.

6) Stress tensor estimates for the seismic zones of this study were compatible with previous studies and presented an overview of regional stress directions. Most estimates of stresses within each seismic zone (with the exception of deeper events in Central Virginia) had a general east to northeast trend.

7) In the Giles County Seismic Zone the maximum compressive stress direction is horizontal and oriented N40°E, based on the best stress tensor estimate. Focal mechanisms indicate that rupture tends to occur on planes striking about N25°E.

8) In the Central Virginia Seismic Zone the observed boundary separates zones of different stress orientations. Stresses responsible for earthquakes trend S70°W above the detachment and due west in deeper crust. No explanation for these particular directions is presented at this time. Fault planes for shallow events had a general strike of north to northwest. No consistent faulting pattern was found for events deeper than 8 km.

9) In the Eastern Tennessee Seismic Zone the maximum compressive stress direction is oriented N50°E and is subhorizontal. The stress tensor orientation is nearly identical with that estimated for Giles County (varying by $< 10°$ of rotation). All but one of the faults of the best-fitting focal mechanism solutions were within the quadrant from 10° to 100°, with most striking in the range 30° to 70°. Faults tended to dip at angles greater than 30°. 10) Geologically it is probable that range of fault orientations differs among the zones. In Central Virginia, there seems to be a variety of fault attitudes. However, in Giles County and Eastern Tennessee, faults

are either predominantly aligned northeast-southwest, or are weak, since the resolved maximum compresseive stress direction is not aligned at the optimum 30° to the fault surface.

Bibliography

Aggson, James R. (1978). Coal mine floor heave in the Beckley Coalfield, *Bureau of Mines Report of Investigations 8274*, 32 pp.

Aki, Keiiti, and Paul G. Richards (1980). *Quantitative Seismology*, San Francisco, W. H. Freeman and Company, 932 pp.

Anderson, E. M. (1951). *The Dynamics of Faulting and Dyke Formation, with applications to Britain, 2nd Ed.*, Edinburgh, Oliver and Boyd, 206 pp.

Angelier, Jacques (1979). Determination of the mean principal directions of stresses for a given fault population, *Tectonophysics*, **56**, T17 - T26.

Angelier, Jacques (1984). Tectonic analysis of fault slip data sets, *Jour. Geophys. Res.*, **89**, 5835 - 5848.

Angelier, Jacques and Pierre Mechler (1977). Sur une méthode graphique de recherche des constraintes principales également utilisable en tectonique et en séismologie: la méthode des diédres droits, *Bull. Soc. Géol. France*, **XIX (7)**, 1309 - 1318.

Blès, G. L., and B. Feuga (1986). *The Fracture of Rocks*, London, North Oxford Academic Publishers, Ltd., 131 pp.

Bollinger, G. A. (1973). Seismicity of the southeastern United States, *Bull. Seis. Soc. Am.*, **63**, 1785 - 1808.

Bollinger, G. A. and Russell L. Wheeler (1988). The Giles County, Virginia, seismogenic zone - seismological results and geological interpretations, *U. S. Geological Survey Professional Paper 1355*, 85 p.

Bollinger, G. A. and M. S. Sibol (1985). Seismicity, seismic reflection studies, gravity and geology of the central Virginia seismic zone: Part I. Seismicity, *Geol. Soc. Am. Bull.*, **96**, 49 - 57.

Bollinger, G. A., C. J. Langer, and S. T. Harding (1976). The eastern Tennessee earthquake sequence of October through December, 1973, *Bull. Seism. Soc. Am.*, **66**, 525-547.

Bollinger, G. A., L. Glover III, J. K. Costain, and M. S. Sibol (1983). The Central Virginia Seismic Zone - seismicity and subsurface geology, *Earthquake Notes*,**54**, 83 - 84.

Bollinger, G. A., M. C. Chapman, M. S. Sibol, and J. K. Costain (1985a). An analysis of earthquake focal depths in the Southeastern U. S., *Geoph. Res. Let.*, **12**, 785-788.

Bollinger, G. A., E. G. Ehlers, Jr., Richard E. Marx and W. Christopher Alger (1985b). *Estimation of Earthquake Effects on Buildings, Lifelines and Residents in Giles County, Virginia*, Blacksburg, Virginia, Virginia Polytechnic Institute and State University Seismological Observatory, 99 pp.

Bott, M. H. P. (1959). The mechanics of oblique slip faulting, *Geol. Mag.*, **96**, 109 - 117.

Byerlee, J. (1978). Friction of rocks, *Pure and App. Geoph.*, **116**, 615 - 626.

Chapman, M. C. (1979). Seismic velocity structure of central Virginia, *M. S. Thesis*, Virginia Polytechnic Institute and State University, 146 pp.

Chapman, M. C. and G. A. Bollinger (1984). Reliability of focal depth estimates from a small network, *Earthquake Notes*, **55**, 16 - 25.

Cook, Frederick A., Dennis S. Albaugh, Larry D. Brown, Sidney Kaufman, Jack E. Oliver, and Robert D. Hatcher, Jr. (1979). Thin-skinned tectonics in the crystalline southern Appalachians; COCORP seismic-reflection profiling of the Blue Ridge and Piedmont, *Geology*,**7**, 563 - 567.

Çoruh, C., G. A. Bollinger, and J. K. Costain (1988a). Seismogenic structures interpreted from reflection seismic data in the Central Virginia Seismic Zone, *Seism. Res. Let.*, **59**, p. 50.

Çoruh, C., G. A. Bollinger, and J. K. Costain (1988b). Seismogenic structures in the central Virginia seismic zone, *Geology*, **16**, 748 - 751.

Coulomb, C. C. (1773). Sur une aplication des règles de maximus et minimis a quelques problèmes de statique relatifs à l'architecture. *Acad. Roy. des Sci., Memoires de Math. et de Physique par divers savans*, **7**, 343 - 382.

Davison, Frederick C., Martin C. Chapman, Jeffrey W. Munsey and G. A. Bollinger (1984). A note on the Cunningham, Virginia, earthquake of August 17, 1984, in the Central Virginia Seismic Zone, *Earthquake Notes*, **55**, 26 - 33.

Davison, Frederick C. and Melissa J. Bodé (1987). A note on the December 1986 - January 1987 Richmond, Virginia, felt earthquake sequence, *Seism. Res. Let.*, **58**, 73 - 80.

Ellsworth, W. L. (1982). A general theory for determining state of stress in the earth from fault slip measurements, *Terra cognita*, **2**, 170 - 171.

Ellsworth, W. L. and Xu Zhonghuai (1980). Determiation of the stress tensor from focal mechanism data, *EOS, Trans. Am. Geop. U.*, **61**, p. 1117.

Etchecopar, A., G. Vasseur, and M. Daignieres (1981). An inverse problem in microtectonics for the determination of stress tensors from fault striation analysis, *Jour. Struc. Geol.*, **3**, 51 - 65.

Evans, David M. (1966). The Denver area earthquakes and the Rocky Mountain Arsenal disposal well, *The Mountain Geologist*, **3**, 23 - 36.

Fisher, R. A. (1953). Dispersion on a sphere, *Proc. Roy. Soc. London*, **A217**, 295 - 305.

Frederick, Daniel and Tien Sun Chang (1972). *Continuum Mechanics*, Cambridge, Massachusetts, 218pp.

Frohlich, Cliff and Raymond J. Willemann (1987). Statistical methods for comparing directions to the orientations of focal mechanisms and Wadati-Benioff zones, *Bull. Seism. Soc. Am.*, **77**, 2135 - 2142.

Gephart, J. W. (1985).Principal stress directions and the ambiguity in fault plane identification from focal mechanisms, *Bull. Seism. Soc. Am.*,**75**, 621 - 626.

Gephart, J. W. and D. W. Forsyth (1984). An improved method for determining the regional stress tensor using earthquake focal mechanism data: application to the San Fernando earthquake sequence, *Jour. Geop. Res.*, **89**, 9305 - 2320.

Gephart, John W. and Donald D. Forsyth (1985). On the state of stress in New England as determined from earthquake focal mechanisms, *Geology*,**13**, 70 - 72.

Gresko, Mark J. (1985). Analysis and interpretation of compressional (P-wave) and shear (SH-wave) reflection seismic and geologic data over the Bane Dome, Giles County, Virginia, *Ph. D. Dissertation*, Virginia Polytechnic Institute and State University, 74 pp.

Haimson, B. C. (1977a). Crustal stress in the continental United States as derived from hydrofracturing tests, in *The Earths Crust, Geophys. Monogr. Ser.*, **20**, Washington, D. C., American Geophysical Union, 576 - 592.

Haimson, B. C. (1977b). A stress measurement in West Virginia and the state of stress in the Southern Appalachians, *EOS Trans. Am. Geophys. U.*, **58**, p. 493.

Harmsen, S. C. and A. M. Rogers (1986). Inferences about the local stress field from focal mechanisms: applications to earthquakes in the southern Great Basin of Nevada, *Bull. Seism. Soc. Am.*, **76**, 1560 - 1572.

Healy, H. C., W. W. Rubey, D. T. Griggs, and C. B. Raleigh (1968). The Denver earthquakes, *Science*, 1301 - 1310.

Herrmann, R. B. (1975). A student's guide to the uses of P and S wave data for focal mechanism determination, *Earthquake Notes*, **46**, 29 - 39.

Herrmann, Robert B. (1979). Surface wave focal mechanisms for Eastern North America with tectonic implications, *Jour. Geol. Res.*,**84**, 3543 - 3552.

Hobbs, Bruce E., Winthrop D. Means, and Paul F Williams (1976). *An Outline of Structural Geology*, New York, John Wiley & Sons, 571 pp.

Hooker, Verne E. and Charles F. Johnson (1969). Near-surface horizontal stresses including the effects of rock anisotropy, *Bureau of Mines Report of Investigations 7224*, 29pp.

Hubbert, M. K. and W. W. Rubey (1959). Role of fluid pressure in mechanics of overthrust faulting, *Geol. Soc. Am. Bull.*, **70**, 115 - 206.

Jaeger, J. C. and N. G. W. Cook (1969). *Fundamentals of Rock Mechanics*, New York, John Wiley and Sons, Inc., 585 pp.

Johnston, Arch C., Donald J. Reinbold, and Stephen I. Brewer (1985). Seismotectonics of the southern Appalachians, *Bull. Seism. Soc. Am.*, 291-312.

Kisslinger, Carl (1980). Evaluation of *S* to *P* amplitude ratios for determining focal mechanisms from regional network observations, *Bull. Seism. Soc. Am.*, **70**, 999 - 1014.

Kisslinger, Carl, J. Roger Bowman, and Karl Koch (1981). Procedures for computing focal mechanisms from local $(SV/P)_z$ data, *Bull. Seism. Soc. Am.*, **71**, 1719 - 1729.

Kisslinger, Carl, J. Roger Bowman, and Karl Koch (1982). Determination of focal mechanism from SV/P amplitude ratios at small distances, *Phys. Earth. Planet. Int.*, **30**, 172 - 176.

Lachenbruch, A. H. and J. H. Sass (1980). Heat flow and energetics of the San Andreas fault zone, *J. Geophys. Res.*, **85**, 6185 - 6222.

Lahr, J. C. (1980). **HYPOELLIPSE/MULTICS**: A computer program for determining local earthquakes hypocentral parameters, magnitude and first motion pattern, *U. S. Geological Survey Open-File Report 80-59, revised April 1980 for version II*, 59 pp.

Ma, L., R. S. Crosson, and R. Ludwin (1988). Regional tectonic stress in western Washington from focal mechanisms of crustal and subcrustal earthquakes, *Seism. Res. Let.*, **59**, p. 16.

McElhinny, M. W. (1979). *Palaeomagnetism and plate tectonics*, New York, Cambridge University Press, 358 pp.

McKenzie, Dan P. (1969). The relation between fault plane solutions for earthquakes and the directions of the principal stresses, *Bull. Seism. Soc. Am.*, **59**, 591 - 601.

Means, W. D. (1976). *Stress and Strain*, New York, Springer-Verlag, 339 pp.

Michael, Andrew J. (1984). Determination of stress from slip data: faults and folds, *J. Geoph. Res.*, **89**, 11,517 - 11,526.

Michael, Andrew Jay (1987a). Use of focal mechanisms to determine stress: a control study, *J. Geoph. Res.*,**92**, 357 - 368.

Michael, Andrew Jay (1987b). Stress rotation during the Coalinga aftershock sequence, *J. Geoph. Res.*, **92**, 7963 - 7979.

Miller, E. V. (1985). Graphical and digital slope stability analyses for Giles County, Virginia, *M. S. Thesis*, Virginia Polytechnic Institute and State University, 193 pp.

Moore, T. P. (1979). Crustal velocity structure in southwestern Virginia, *M. S. Thesis*, Virginia Polytechnic Institute and State University, 75 pp.

Munsey, Jeffrey W. (1984). Focal mechanism analysis for recent (1978 - 1984) Virginia earthquakes, *M. S. Thesis*, Virginia Polytechnic Institute and State University, 214 pp.

Munsey, Jeffrey W. and G. A. Bollinger (1985). Focal mechanism analyses for Virginia earthquakes (1978 - 1984), *Bull. Seis. Soc. Am.*, **75**, 1613 - 1636.

Nelson, K., and P. Talwani (1985). Reanalysis of focal mechanism data for the Central Virginia seismogenic zone, *Earthquake Notes*, **56**, p. 76.

Nuttli, Otto W. (1973). Seismic wave attenuation and magnitude relations for eastern North America, *Jour. Geophy. Res*, **78**, 876 - 885.

Oaks, S. D. and G. A. Bollinger (1986). The epicenter of the mb 5, December 22, 1875 Virginia earthquake: new findings from documentary sources, *Earthquake Notes*, **57**, 65 - 75.

Pratt, Thomas L. (1986). A geophysical study of the earth's crust in Central Virginia with implications for lower crustal reflections and Appalachian crustal structure, *PhD Dissertation*, Virginia Polytechnic Institute and State University, 69 pp.

Raleigh, C. B., J. H. Healy, and J. D. Bredehoeff (1972). Faulting and crustal stress at Rangely, Colorado: pp. 275-284 in Flow and Fracture of Rocks, H. C. Heard, I. Y. Borg, N. L. Carter, and C. B. Raleigh (eds), *Am. Geophys. Union, Geophys. Monograph 16*, 352pp.

Ramsay, John G. (1967). *Folding and Fracturing of Rocks*, New York, McGraw-Hill Book Company., 568 p.

Richardson, Randall M., Sean C. Soloman, and Norman H. Sleep (1979). Tectonic stress in the plates, *Rev. Geoph. Space Phys.*, **17**, 981 - 1019.

Sbar, Marc L. and Lynn R. Sykes (1973). Contemporary compressive stress and seismicity in eastern North America: an example of intra-plate tectonics, *Geol. Soc. Am. Bull.*,**84**, 1861 - 1882.

Sibol, M. S. and G. A. Bollinger (1981). A note on recent seismic activity in the Scottsville, Virginia, area, *Earthquake Notes*,**52**, 11 - 22.

Sibol, M. S., G. A. Bollinger and E. C. Mathena (1987). Seismicity of the Southeastern United States, July 1, 1986 - December 31, 1986, *SEUSSN Bulletin No. 19*, 64 pp.

Sibson, Richard H. (1974). Frictional constraints on thrust, wrench and normal faults, *Nature*, **249**, 542 - 544.

Sibson, Richard H. (1982). Fault zone models, heat flow, and the depth distribution of earthquakes in the continental crust of the United States, *Bull. Seism. Soc. Am.*, **72**, 151 - 163.

Sibson, Richard H. (1983). Continental fault structure and the shallow earthquake source. *J. Geol. Soc. London*, **140**, 741 - 767.

Snoke, J. A., J. W. Munsey, A. G. Teague and G. A. Bollinger (1985). A program for focal mechanism determination by combined use of polarity and Sv/P amplitude ratio data, *Earthquake Notes*, **55**, P. 15.

Spencer, Edgar Winston (1972). *The Dynamics of the Earth; an introduction to physical geology*, New York, Thomas Y. Crowell Company, 611 pp.

Talwani, Pradeep (1982). Internally consistent pattern of seismicity near Charleston, South Carolina, *Geology*,**10**, 654 - 658.

Teague, Alan G. (1984). Focal mechanisms for eastern Tennessee earthquakes, 1981 - 1983, *M. S. Thesis*, Virginia Polytechnic Institute and State University, 161 pp.

Teague, Alan G., G. A. Bollinger and Arch C. Johnston (1986). Focal mechanism analyses for eastern Tennessee earthquakes (1981 - 1983), *Bull. Seis. Soc. Am.*, **76**, 95 - 109.

Todd, Eric Donald (1982). Seismicity of the Bath County, Virginia, locale, *M. S. Thesis*, Virginia Polytechnic Institute and State University, 100 pp.

Vasseur, G., A. Etchecopar, and H. Philip (1983). Stress state inferred from multiple focal mechanisms, *Ann. Geophys.*, **1**, 291 - 297.

Viret, M., G. A. Bollinger, J. A. Snoke and J. W. Dewey (1984). Joint hypocenter relocation studies with sparse data sets - A case history: Virginia earthquakes, *Bull. Seis. Soc. Am.*, **74**, 2297 - 2312.

Wheeler, R. L. and G. A. Bollinger (1981). Stress orientations on the Giles County, Virginia, seismogenic zone, *Earthquake Notes*,**52**, 32 - 33.

Zoback, M. D. and J. H. Healy (1977). In-situ stress measurements near Charleston, South Carolina, *EOS Trans. Amer. Geophys. U.*, **58**, p. 493.

Zoback, Mark D., Mary Lou Zoback, Van S. Mount, John Suppe, Jerry P. Eaton, John H Healy, David Oppenheimer, Paul Reasenberg, Lucille Jones, C. Barry Raleigh, Ivan G. Wong, Oona Scotti, and Carl Wentworth (1987). New evidence on the state of stress of the San Andreas Fault System, *Science*, **238**, 1105 - 1111.

Zoback, M. L. and M. D. Zoback (1980). State of stress in the conterminous United States, *Jour. Geop. Res.*, **85**, 6113 - 6156.

Zoback, M. L. and M. D. Zoback (1985). Uniform NE to ENE maximum horizontal compressive stress throughout mid-plate North America, *EOS Trans. Am. Geophys. U.*, **66**, p. 1056.

Zoback, M. L., M. D. Zoback, and R. Dart (1985). Reassessment of the state of stress in the Atlantic Coast region, *Geological Society of America abstracts with Programs*, **17**, p. 759.

Appendix A

Hypocenters of Events used in this Study

The following tables document the location parameters for the events used in this study. The following abbreviations are used:

Mag - Earthquake magnitude, generally based on the amplitude of the Lg phase.

Gap - The largest angular range without instrument coverage.

DMIN - The distance to the closest station.

RMS - A measure of the average error between calculated and observed arrival times.

ERH - Horizontal error in the hypocentral location.

ERZ - Vertical error in the depth determination.

Table 14. Hypocenters of Earthquakes - Giles County Seismic Zone.

Event	Date (M/D/Y)	Time (UTC)	Lat (DEG N)	Long (DEG W)	Depth (KM)	Mag	Gap (DEG)	DMIN (KM)	RMS (SEC)	ERH (KM)	ERZ (KM)
63	12/02/80	07:47	37.43	80.54	18.0	0.4	113	25	0.16	1.2	3.8
90	1/25/83	20:38	37.39	80.51	15.8	1.8	81	14	0.24	0.8	1.5
94	5/26/83	01:04	37.51	80.32	9.0	2.2	103	8	0.24	0.8	1.4
97	7/10/83	14:05	37.27	80.76	7.1	1.0	89	6	0.26	1.1	2.9
104	12/09/83	00:11	37.20	80.79	12.2	1.1	98	13	0.22	0.7	1.1
110	7/02/84	19:51	37.29	80.72	10.8	1.4	89	8	0.19	1.0	2.0
118	6/10/85	12.22	37.25	80.49	11.1	2.8	99	6	0.28	0.9	2.0
127	3/26/86	16.36	37.25	80.49	11.9	2.9	110	7	0.29	1.1	2.4

Table 15. Hypocenters of Earthquakes - Central Virginia Seismic Zone.

Event	Date (M/D/Y)	Time (UTC)	Lat (DEG N)	Long (DEG W)	Depth (KM)	Mag	Gap (DEG)	DMIN (KM)	RMS (SEC)	ERH (KM)	ERZ (KM)
53	8/04/80	10:13	38.07	77.77	4.9	0.9	115	6	0.17	0.8	1.8
57	9/26/80	01:31	38.07	77.77	3.3	1.0	102	7	0.16	1.0	3.4
64A	2/11/81	13:44	37.72	78.44	6.8	3.4	123	29	0.16	1.1	2.3
64B	2/11/81	13:50	37.75	78.40	9.6	3.2	156	26	0.20	2.4	2.3
78	1/18/82	06:11	37.89	77.82	5.4	0.3	183	11	0.11	1.6	3.7
82	5/06/82	07:18	37.86	77.58	10.0	2.1	153	17	0.19	1.0	2.5
86	6/25/82	23:03	37.84	77.50	13.4	1.9	166	23	0.14	1.1	1.8
87	9/20/82	12:15	37.84	77.50	13.4	1.6	166	23	0.16	1.0	1.4
100	8/10/83	12:29	37.75	78.42	10.4	1.9	157	26	0.19	2.7	4.0
111	8/17/84	18:05	37.87	78.32	8.1	4.0	103	18	0.22	1.7	2.9
113	10/17/84	08:57	37.94	77.51	15.3	1.1	201	16	0.17	2.7	2.3
133	12/10/86	11:30	37.58	77.47	1.2	2.2	207	14	0.16	0.9	10.9
138	4/11/87	03:30	37.66	77.90	8.7	1.7	136	23	0.22	0.6	1.4

Table 16. Hypocenters of Earthquakes - Eastern Tennessee Seismic Zone.

Event	Date (M/D/Y)	Time (UTC)	Lat (DEG N)	Long (DEG W)	Depth (KM)	Mag	Gap (DEG)	DMIN (KM)	RMS (SEC)	ERH (KM)	ERZ (KM)
2	11/25/81	11:54	35.64	84.64	11.6	2.7	74	36	0.31	0.8	1.8
13	9/24/82	21:57	35.68	84.24	17.9	3.4	63	23	0.20	0.5	1.0
14	9/24/82	22:19	35.69	84.25	14.7	3.5	125	29	0.18	0.5	1.7
22	1/18/83	05:09	35.59	84.28	13.7	2.3	88	32	0.22	0.4	1.3
23	1/27/83	22:09	36.05	83.61	17.1	3.1	77	46	0.25	0.5	1.3
28	4/05/83	03:17	35.55	84.18	13.9	2.1	84	13	0.22	0.5	0.9
29	5/16/83	06:50	35.54	84.05	18.0	1.9	111	28	0.16	0.5	1.1
30	5/25/83	10:46	35.74	84.45	17.9	1.6	110	23	0.16	0.5	1.9
31	5/26/83	12:30	35.67	84.26	9.1	2.5	59	27	0.24	0.3	0.8
34	7/08/83	19:29	35.55	84.16	13.3	3.4	56	14	0.25	0.4	0.9
36	7/15/83	19:32	35.55	84.16	10.1	2.6	68	14	0.21	0.5	0.9

Appendix B

Best Focal Mechanism Solutions for Earthquakes used in this Study

The following tables document the parameters for the preferred focal mechanism solutions of the events used in this study.

Table 17. Characteristics of Best FMSs - Giles County Seismic Zone.

Event	Preferred Fault Plane Dip,Strike,Rake	Auxiliary Plane Dip,Strike,Rake	P-axis Trend,Plunge	T-axis Trend,Plunge	B-axis Trend, Plunge
63	87,340, 176	86, 70, 3	25, 0	295, 5	300,-85
90	55,215,-177	87,123, -35	73, 26	354,-22	299, 55
94	21,173, 136	76,305, 76	47, 29	14,-57	309, 15
97	86, 15,-176	86,285, -4	60, -5	330, 0	60, 85
104	66,219, 154	66,321, 26	90, 0	0,-35	0, 55
110	42,219,-113	52, 69, -71	38, 74	325, -5	57,-15
118	35, 44, 0	90,314, 125	14, 35	74,-35	314,-35
127	14, 62, 45	80,288, 100	10, 34	30,-54	286,-10

Table 18. Characteristics of Best FMSs - Central Virginia Seismic Zone.

Event	Preferred Fault Plane Dip,Strike,Rake	Auxiliary Plane Dip,Strike,Rake	P-axis Trend,Plunge	T-axis Trend,Plunge	B-axis Trend, Plunge
Deeper					
64B	42,178, 67	52, 28, 109	284, -5	357, 74	15,-15
82	76,253,-153	64,156, -16	297,-29	23, 7	280, 60
86	85, 94, 70	21,351, 167	21,-37	343, 46	275,-20
87	79,229, 170	80,321, 167	275, -1	5,-15	0, 75
100	51,330, 8	84,235, 140	289, 22	5,-32	47, 50
111	44,332, 22	75,226, 132	286, 19	357,-44	33, 40
113	66,356, 26	66,254, 154	305, 0	35,-35	35, 55
138	35,329, 31	73,214, 122	280, 21	340,-52	23, 30
Shallow					
53	45,349, 135	60,114, 55	49, -9	333, 59	314,-30
57	69,309, 22	69,211, 158	80, 0	350,-30	350, 60
64A	69,344, 122	38,104, 36	51, 17	295, 54	151, 30
78	83,349, 135	46, 86, 10	46, 24	298, 35	342,-45
133	65,328, 84	25,161, 102	62, 20	47,-69	330, -5

Table 19. Characteristics of Best FMSs - Eastern Tennessee Seismic Zone.

Event	Preferred Fault Plane Dip,Strike,Rake	Auxiliary Plane Dip,Strike,Rake	P-axis Trend,Plunge	T-axis Trend,Plunge	B-axis Trend, Plunge
2	50,244, -23	73,349,-138	34,-42	291,-14	7, 45
13	66,279, 18	73,181, 155	51, -5	318,-30	330, 60
14	90,277, 10	80,187,-180	51, 7	322, -7	277, 80
22	73, 78, -18	73,174,-162	36, 25	306, 0	36,-65
23	83, 63, -29	61,157,-172	16, 26	293,-14	50,-60
28	76,224, 159	70,320, 15	273, 4	1,-25	12, 65
29	76, 84, -4	86,175,-165	40, 13	309, 7	9,-75
30	18, 40, 147	80,162, 75	85,-34	54, 52	345,-15
31	60, 35,-145	60,286, -35	251, 45	341, 0	71, 45
34	58,173, 154	68,277, 35	43, 6	318,-39	305, 50
36	81,217, 176	86,308, 9	82, 3	353, -9	332, 80

Appendix C

Computer Routines

The computer program **STRESS**, which was used to determine the best fit stress field, was constructed of several modules, each contained in a separate subroutine. A general description of the program will be followed by more detailed explanations of each of the major subroutines.

The general format of the **STRESS** routine is to examine preselected directions for $\overline{\sigma}_1$, $\overline{\sigma}_2$, and $\overline{\sigma}_3$, and then to compute how well those orientations match the family of **FOCMEC** solutions which were used as program input. It was decided at an early stage to test 324 possible orientations of the $\overline{\sigma}_1$ axis. That represented varying the trend by 10° increments from 10 to 360 degrees, and then repeating for values of dip (also incremented by 10°) from 0 to 80 degrees. At each test point iterations were made for 18 possible variations of $\overline{\sigma}_2$ and $\overline{\sigma}_3$ associated with the $\overline{\sigma}_1$ under test, varying $\overline{\sigma}_2$ from 0 to 180 degrees by 10° increments (an additional test from 180 to 360 degrees was not necessary, as symmetry dictated that although the number of correct answers would double in such a case, the percentage of correct answers would not change). Additionally, at each orientation of $\overline{\sigma}_1$, $\overline{\sigma}_2$ and $\overline{\sigma}_3$, all members of the **FOCMEC** family were tested. It should be noted that the number of tests performed was 324 × 18 × **n**, where **n** was the number of **FOCMEC** solutions used as input. As an example, for a family of 20 solutions, 116,640 tests were made, each requiring 3 coordinate

transformations. In the following description, subroutines will be capitalized in **bold**, and those which are described in more detail later are followed by an asterisk.

Main Program. Two files are initially defined and opened. Unit 2 is the existing file containing the **FOCMEC** solutions to be used in the program, while unit 4 is the output file from program **STRESS**, which is automatically named **STRESS.OUT**. A heading for that file is obtained interactively, and is included in the first line of output.

Several queries are made to determine parameters used in the program run. The first of these asks for the number of allowable errors for a solution to be printed to the output file (and simultaneously to the screen). An error (to be described in detail later) is based upon whether a particular stress tensor orientation is applicable to any **single FOCMEC** solution included in the input file. The maximum number of errors equals the number of solutions in the family.

A second procedural question asks if the user wishes to use the fault plane, auxiliary plane or both in the testing procedure. The program assumes that the plane entered (defined in terms of strike, dip, and rake) is the fault plane. However, the auxiliary plane in most cases is as likely a solution (as there is little or no geological constraint in the Southeastern U. S.). One of the two nodal planes will more closely conform to the stress tensor tested. If the option is chosen, the program will use the plane which produces the best fit. For reasons of testing the program, it is useful to be able to choose whether to use the fault plane, auxiliary plane, or best fitting plane to compute results.

Once the initial questions are answered by the operator, the program proceeds without interuption. Subroutine **INDAT** reads the data from the input file and derives several variables to be used in the relative weighting of each **FOCMEC** solution. Weighting factors are calculated in the subroutine **WEIGHT**, and remain on hand for later calculations. In addition, **INDAT** finds the number of input solutions and uses them to define the integer value NUMSOL, which is necessary for several of the loops within the main program.

At this stage the iterative process begins. The first step is to position the $\bar{\sigma}_1$ axis in relation to the vectors associated with the fault plane (the normal to the fault plane, the normal to the

auxiliary plane, and the B axis). Subroutine **ROTATE1** calculates the trend and plunge of the $\bar{\sigma}_1$ axis to be tested. Those values are then passed to **TEST(*)** to calculate the appropriate rotation matrix. In all cases the new coordinate frame is based upon the orthogonal system $\bar{\sigma}_1$,$\bar{\sigma}_2$, and $\bar{\sigma}_3$; all tested vectors are rotated into proper orientation with respect to that frame.

The next loop involves the positioning of the $\bar{\sigma}_2$ and $\bar{\sigma}_3$ axes, keeping $\bar{\sigma}_1$ stationary. This rotation is performed by **ROTATE2(*)**. Finally, each solution of the **FOCMEC** family is tested to determine if it conforms to the calculated rotation. Before this is done, the trend, plunge and rake of the fault plane is translated by **FMREPS** to the corresponding representation using the following matrix:

$$\begin{bmatrix} A_{11} & A_{12} & A_{13} \\ A_{21} & A_{22} & A_{23} \\ A_{31} & A_{32} & A_{33} \end{bmatrix}$$

where the coefficients (A_{11},A_{12},A_{13})describe the normal to the fault plane, (A_{21},A_{22},A_{23}) is the normal to the auxiliary plane and (A_{31},A_{32},A_{33}) is the B axis.

At this point, all vectors have been defined in terms of the $\bar{\sigma}_1$, $\bar{\sigma}_2$, $\bar{\sigma}_3$ coordinate system, so that direct comparisons may be made between the directions of the principal stresses and the orientation of the focal mechanism. Those comparisons are the heart of the program and are performed within the subroutines **BMATRX(*)** and **TEST2(*)**. Two major variables are returned from those subroutines back to the main program. The first of those, **R**, must be in the range 0.0 $\leq$ **R** $\leq$ 1.0 or the solution is in error. A sign test is also performed. The variable **sign**, which represents the modulus of the dot product between the observed and predicted slip directions, must be positive. The program tallies the number of errors for each stress tensor orientation, and displays the following error criteria.

TEST - indicates the test number, from 1 to 324 as described earlier.

Least Errors - displays the number of errors for the particular $\bar{\sigma}_2$ and $\bar{\sigma}_3$ directions which, for the $\bar{\sigma}_1$ tested, produce the fewest errors.

PCT - represents the percent of correct answers for the tested orientation of $\overline{\sigma}_1$. The total number of correct solutions equals 18 × **n**, where **n** is the number of solutions in the **FOCMEC** family.

Best Group - indicates the weight of the best $\overline{\sigma}_2$ and $\overline{\sigma}_3$ orientations for the $\overline{\sigma}_1$ under test. The error criteria are output to the screen and file, and the program resets and begins computations for the next orientation of $\overline{\sigma}_1$.

As opposed to the work by others in the field, this program does not invert using **R** as a variable. Instead, **R** is calculated for all members of the **FOCMEC** family. In an ideal case, **R** should be a constant for all earthquake focal mechanism solutions in a seismic zone.

A second version of the **STRESS** program, named **STRESS1**, performs all of the tasks previously mentioned, but has two important features. The first of those is an interactive mode which allows the user to look at any particular $\overline{\sigma}_1$ test. After the test is chosen, the program will create a more complete error analysis. In that manner, the best orientation of $\overline{\sigma}_2$ and $\overline{\sigma}_3$ for a particular $\overline{\sigma}_1$ direction can be found.

The normal procedure for using the programs **STRESS** and **STRESS1** is as follows. The user will run the input data through **STRESS**, noting the $\overline{\sigma}_1$ orientations which have the smallest number of errors. These $\overline{\sigma}_1$ directions are subsequently passed through **STRESS1** for a more complete analysis, including weighting of individual solutions. The best orientation of $\overline{\sigma}_1$ is found (either a single solution of a set of solutions which pass user-determined criteria) and plotted using a lower hemisphere equal angle projection.

Subroutine TEST. Subroutine **TEST** is used to construct the rotation matrix which transforms the vectors describing the focal mechanism solution into the coordinate system defined by $\overline{\sigma}_1$, $\overline{\sigma}_2$, and $\overline{\sigma}_3$. Two variables are passed to the subroutine, **ROT1** and **ROT2**. **ROT1** represents the rotation about the z axis (i.e. a horizontal rotation) and **ROT2** corresponds to a dip, or rotation downward about the $\overline{\sigma}_2$ axis. Those rotations are in the form of 2 matrices which are multiplied together to give a single rotation matrix. That matrix can be calculated:

$$\begin{bmatrix} \cos(ROT2) & 0 & \cos(90-ROT2) \\ 0 & 1 & 0 \\ \cos(90+ROT2) & 0 & \cos(ROT2) \end{bmatrix} \times \begin{bmatrix} \cos(ROT1) & \cos(90-ROT1) & 0 \\ \cos(90+ROT1) & \cos(ROT1) & 0 \\ 0 & 0 & 1 \end{bmatrix}$$

$$= \begin{bmatrix} T_{11} & T_{12} & T_{13} \\ T_{21} & T_{22} & T_{23} \\ T_{31} & T_{32} & T_{33} \end{bmatrix}$$

From the above equations it is seen that:

$T_{11} = \cos(ROT1) \times \cos(ROT2)$

$T_{12} = \cos(ROT2) \times \cos(90 - ROT1)$

$T_{13} = \cos(90 - ROT2)$

$T_{21} = \cos(90 + ROT1)$

$T_{22} = \cos(ROT1)$

$T_{23} = 0.0$

$T_{31} = \cos(ROT1) \times \cos(90 + ROT2)$

$T_{32} = \cos(90 - ROT1) \times \cos(90 + ROT2)$

$T_{33} = \cos(ROT2).$

Rotation using this matrix will account for two of the three rotations needed to make the necessary tests.

Subroutine ROTATE2. Subroutine **ROTATE2** calculates the form of the rotation matrix needed to perform the third rotation, around the $\overline{\sigma}_1$ direction. The matrix is of the following form, where ANGLE is the amount of rotation (implicitly defined as 10°).

$$\begin{bmatrix} 1 & 0 & 0 \\ 0 & \cos(ANGLE) & \cos(90-ANGLE) \\ 0 & \cos(90+ANGLE) & \cos(ANGLE) \end{bmatrix} \times \begin{bmatrix} T_{11} & T_{12} & T_{13} \\ T_{21} & T_{22} & T_{23} \\ T_{31} & T_{32} & T_{33} \end{bmatrix}$$

$$= \begin{bmatrix} TT_{11} & TT_{12} & TT_{13} \\ TT_{21} & TT_{22} & TT_{23} \\ TT_{31} & TT_{32} & TT_{33} \end{bmatrix}$$

After completion, the rotation matrix is defined as folows;

$$TT_{11} = T_{11}$$

$$TT_{12} = T_{12}$$

$$TT_{13} = T_{13}$$

$$TT_{21} = T_{21}\cos(ANGLE) + T_{31}\cos(90 - ANGLE)$$

$$TT_{22} = T_{22}\cos(ANGLE) + T_{32}\cos(90 - ANGLE)$$

$$TT_{23} = T_{23}\cos(ANGLE) + T_{33}\cos(90 - ANGLE)$$

$$TT_{31} = T_{21}\cos(90 + ANGLE) + T_{31}\cos(ANGLE)$$

$$TT_{32} = T_{22}\cos(90 + ANGLE) + T_{32}\cos(ANGLE)$$

$$TT_{33} = T_{23}\cos(90 + ANGLE) + T_{33}\cos(ANGLE)$$

The transformation matrix is now complete and may be used to convert the focal mechanism solution from the **N**, **E**, **Z** coordinate system to one based entirely on the orientation of the $\bar{\sigma}_1$, $\bar{\sigma}_2$, $\bar{\sigma}_3$ frame.

Subroutine BMATRX. Subroutine **BMATRX** calculates the β matrix, whose components represent the cosines of the angles between the vectors describing the focal mechanism solution (the normal to the fault plane, the normal to the auxiliary plane, and the **B**-axis) and the principal directions of stress, $\bar{\sigma}_1$, $\bar{\sigma}_2$, and $\bar{\sigma}_3$. Each of those components is in the form β_{ij} where the following conventions are used:

Subscript i:

i = 1 - normal to fault plane,

i = 2 - **B** axis,

i = 3 - normal to auxiliary plane,

Subscript j:

j = 1 - $\bar{\sigma}_1$ direction,

j = 2 - $\bar{\sigma}_2$ direction,

j = 3 - $\bar{\sigma}_3$ direction.

Two values of **R** are calculated within the subroutine, one associated with the fault plane (**R1**) and the other with the auxiliary plane (**R2**). From the work of Gephart and Forsyth (1984) among others:

$$R = \frac{-(\beta_{13}\beta_{23})}{\beta_{12}\beta_{22}}$$

which we define as **R1**. **R2** is similarly described as:

$$R2 = \frac{-(\beta_{33}\beta_{23})}{\beta_{32}\beta_{22}}$$

The final calculation done within **BMATRX** is the calculation of the trace of the predicted slip on both the fault plane and auxiliary plane. It is assumed at this point that the slip will occur within the $\bar{\sigma}_1$ - $\bar{\sigma}_3$ plane (as described by Anderson, 1951). The trace of the slip is then simply the line defined by the intersection of the $\bar{\sigma}_1$ - $\bar{\sigma}_3$ plane with the fault plane (or auxiliary plane, as appropriate). At this stage, the direction of this line is undefined. The determination of direction as well as a sign test (the result of which must be positive) is next calculated by **TEST2(*)** and its result returned through subroutine **BMATRX** to the main program.

Subroutine TEST2. Subroutine **TEST2** contains several steps which, when complete, determine if the predicted slip on the fault (or auxiliary) plane is compatible with the known slip from the focal mechanism solution. The first of these tests tags the type of solution mandated by the calculation of **R1** and **R2**. If **R1** is in the range $0.0 \leq$ **R1** ≤ 1.0 and **R2** is not, the focal plane used as input is assumed to be correct. Conversely, if $0.0 \leq$ **R2** ≤ 1.0 and **R1** is outside this range, the program will test the auxiliary plane as if it were the focal plane. If both are outside the appropriate range, an error is declared. Finally, if both **R1** and **R2** are acceptable, an additional test is made to determine the most likely plane.

Next, the proper orientation of the vector normal to the fault plane must be determined. In all cases it is necessary that the normal is directed from the headwall to the footwall, or downward.

If the original vector points upward, then all components are multiplied by -1 to reverse the direction.

It is also important to examine the $\bar{\sigma}_1$ direction at this point. For the purpose of the tests made in this subroutine, it is appropriate to use the $\bar{\sigma}_1$ direction which most closely matches the direction of the normal to the headwall. In this case the dot product of $\bar{\sigma}_1$ and the normal to the headwall is calculated. If the product is positive, $\bar{\sigma}_1$ is not altered. However, if the dot product is negative, $\bar{\sigma}_1$ is reversed. This is appropriate because $\bar{\sigma}_1$ is represented by a pair of vectors of equal magnitude and opposite direction. The program only needs to choose the one which is correct based on the conventions used regarding direction of slip and description of the fault plane.

At this point the $\bar{\sigma}_1$ direction is compared to the theoretical slip calculated within **BMATRX**. As stated in the previous section, the absolute direction of this slip is not determined. However, this line may now be compared to the corrected $\bar{\sigma}_1$ direction. If the dot product is positive, no alterations are made. On the other hand, if the dot product is negative, the theoretical slip direction is reversed.

The above steps appear convoluted, but are necessary to find the correct sense of slip predicted by the stress tensor being tested within the program. Several important intermediate results have been found up to this point. They are:

1) the fault plane or auxiliary plane is defined as the plane on which the slip occurs;

2) the orientation of the fault plane is described in a consistent manner (with the normal pointing from the headwall into the footwall), and;

3) the slip on the fault plane caused by the stress tensor is found.

The final step of the subroutine, and its main function, can now be performed. The sense of predicted slip and the known slip must be in approximately the same direction, a result which is not accounted for by simply passing the $0.0 \leq \mathbf{R} \leq 1.0$ test. (This is due to the dichotomy between fault and auxiliary plane descriptions.) Now, the vector product of the known and predicted slip is found. If positive, the solution is acceptable; if negative an error is declared. The appropriate value of **R** is returned to the main program, as well as the cosine of the angle between the calculated and known slip directions.

Appendix D

Solutions For Individual Earthquakes

The following figures show results of this study for each earthquake relating the regional $\bar{\sigma}_1$ direction with the P-axis of the focal mechanism solution. The 324 $\bar{\sigma}_1$ test positions are shown as small + 's, superposed on the equal area projection. Acceptable solutions are drawn as circles on the appropriate test positions. In all cases the figure in the upper left-hand corner indicates the union of the P-axis quadrants of all acceptable solutions based on the search and error parameters used in FOCMEC. The regional $\bar{\sigma}_1$ orientation is shown by an open triangle. The remaining three figures on each plot show the regions on the focal sphere within 35, 25 and 15 degrees from any P-axis of the solution set. Events are arranged by seismic zone.

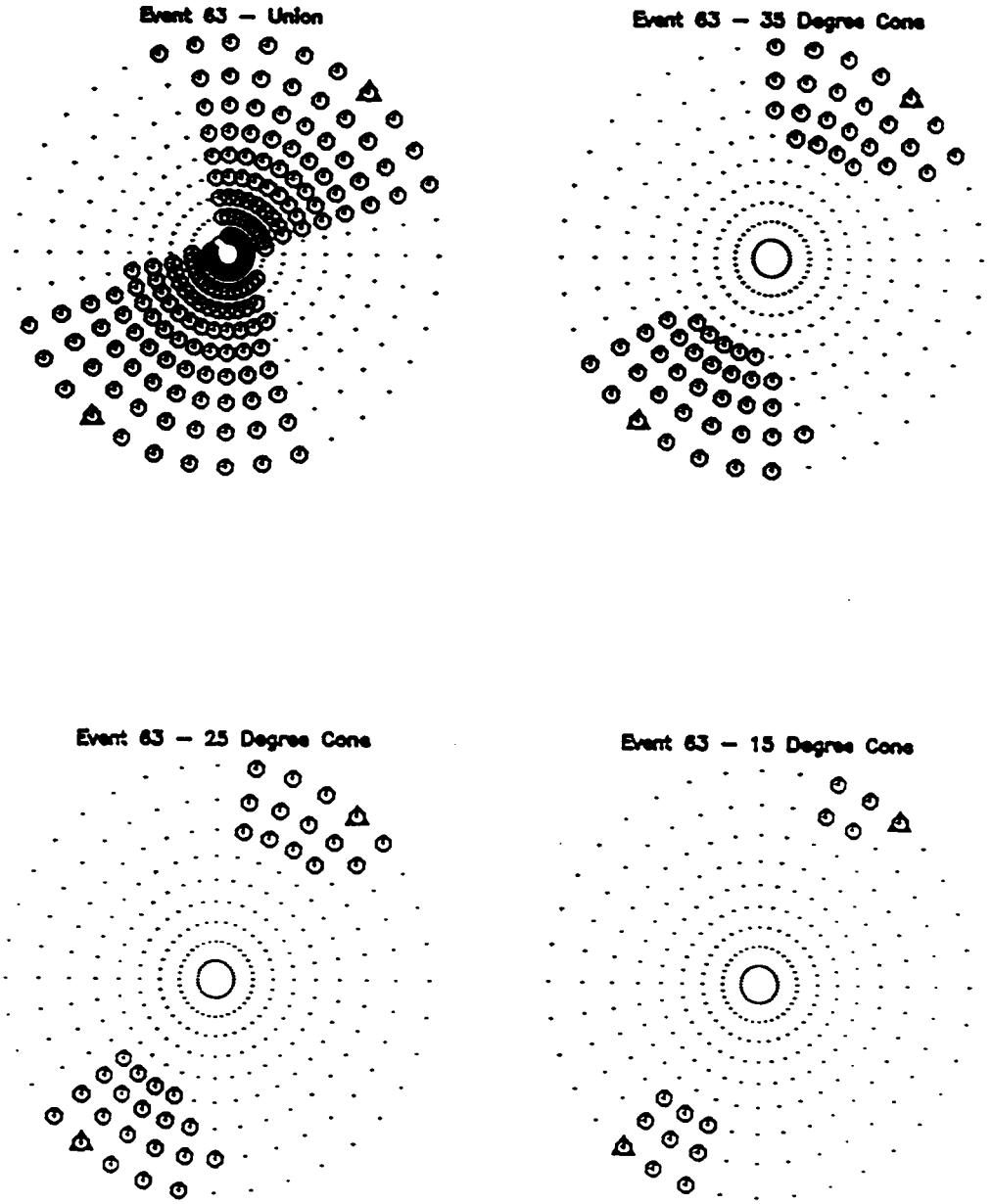

Figure 41. Event 63 - Giles County Seismic Zone

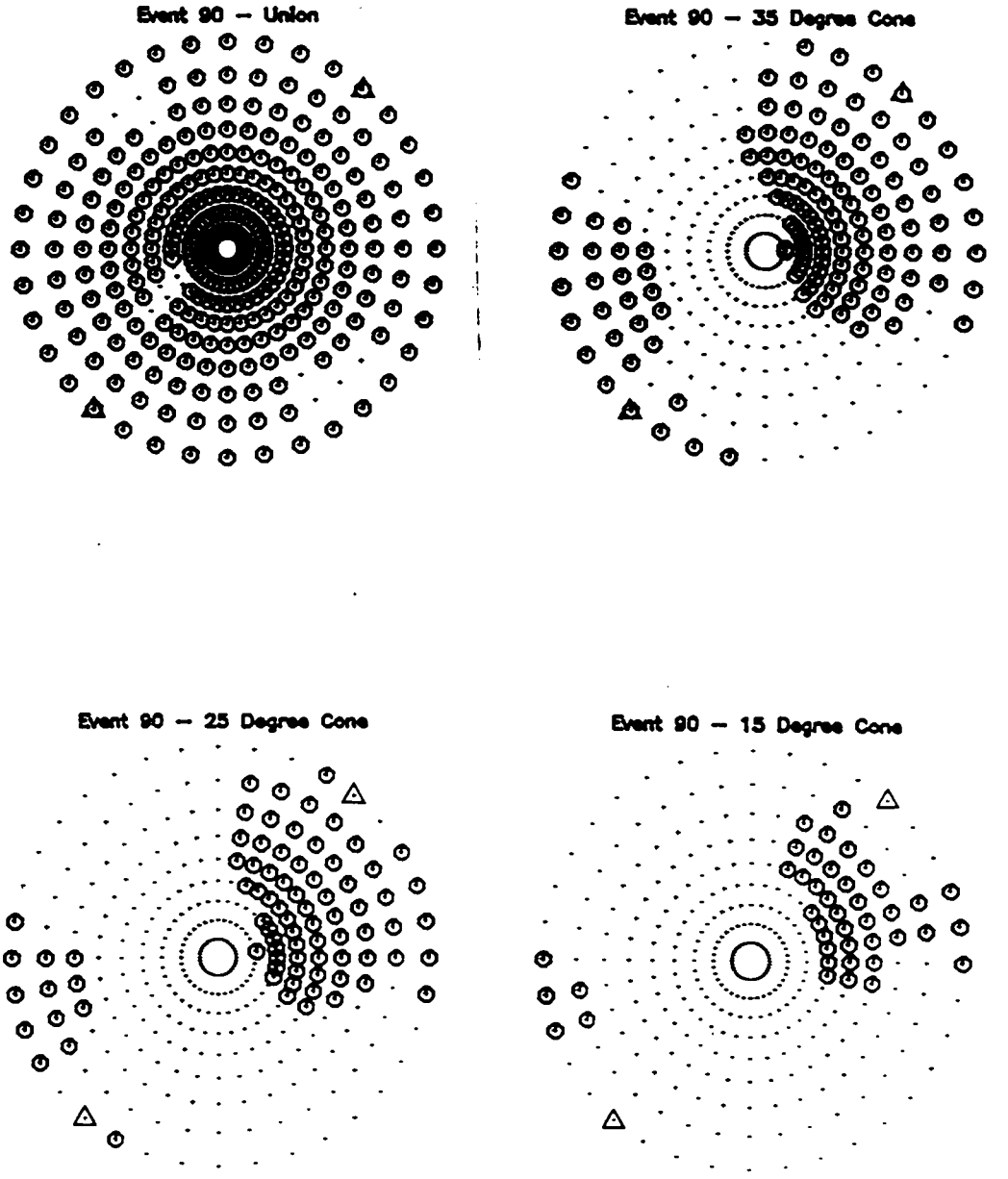

Figure 42. Event 90 - Giles County Seismic Zone

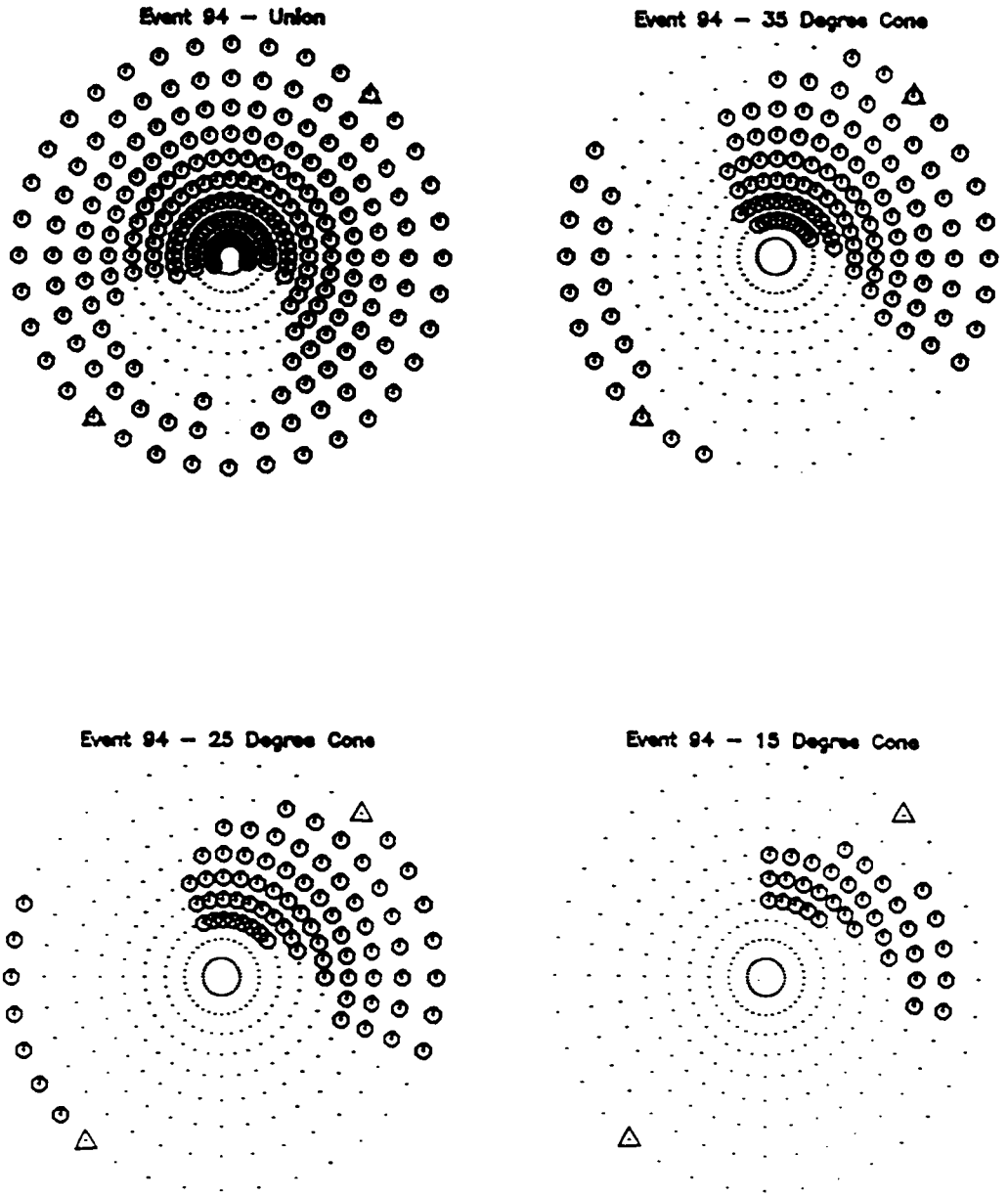

Figure 43. Event 94 - Giles County Seismic Zone

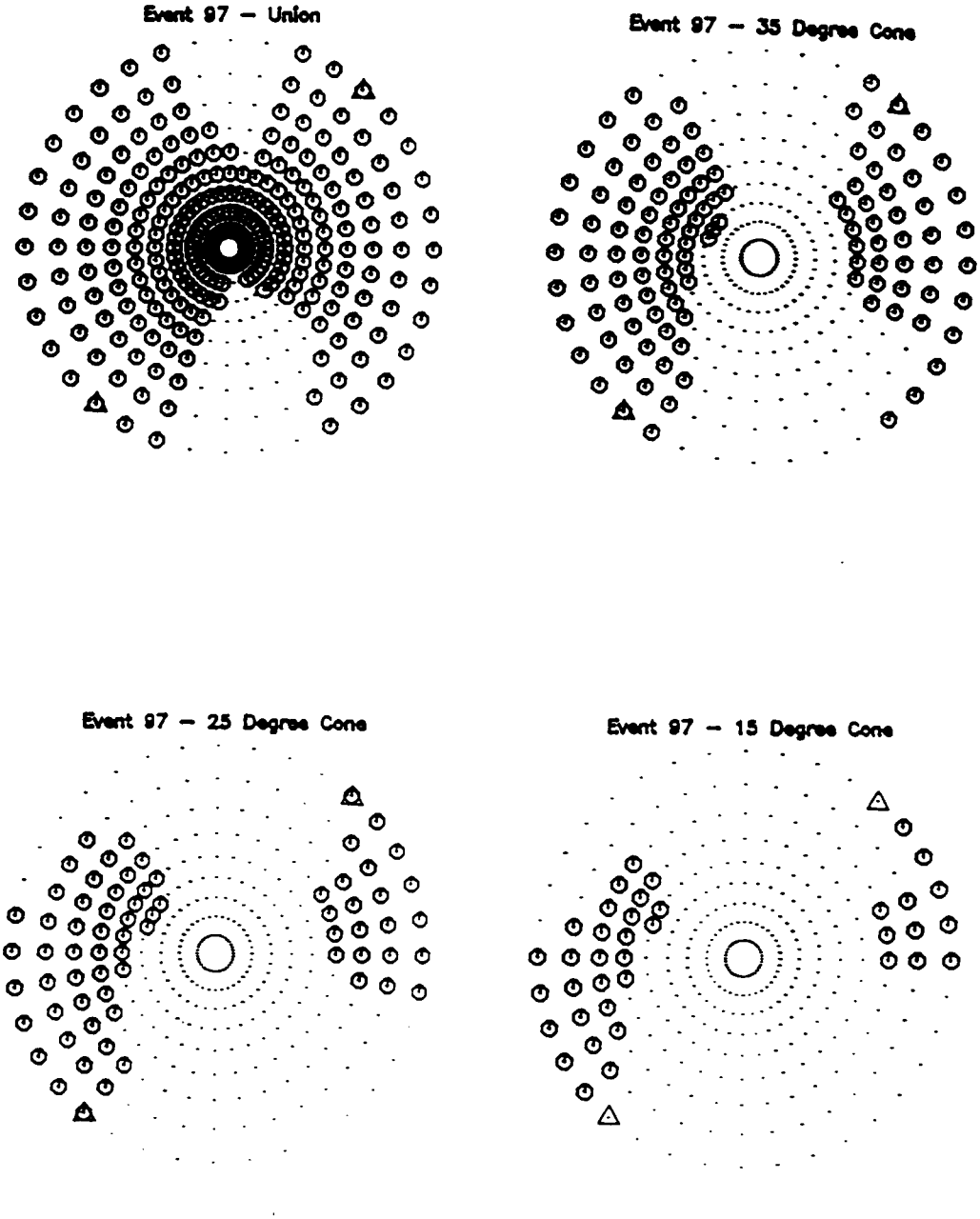

Figure 44. Event 97 - Giles County Seismic Zone

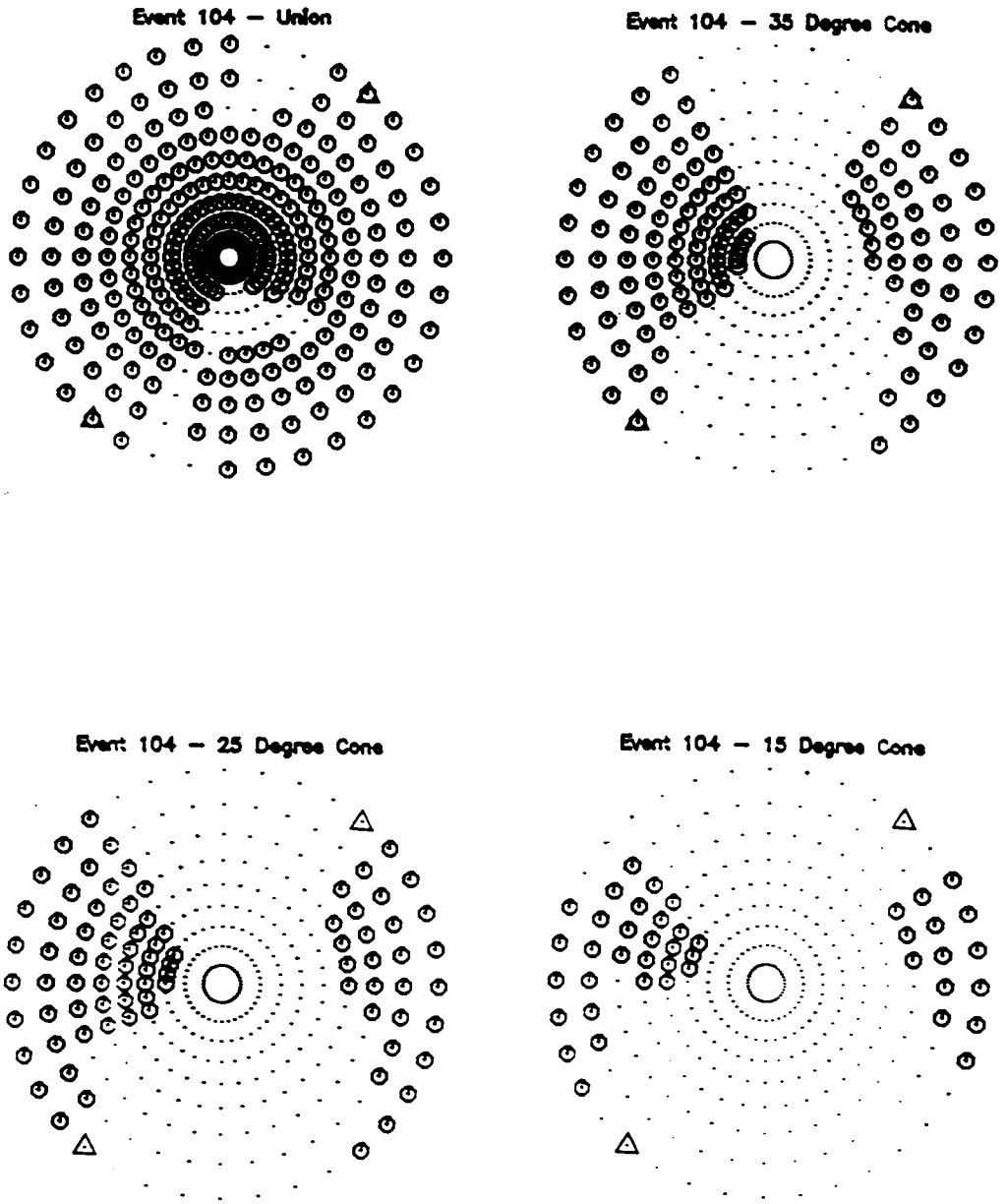

Figure 45. Event 104 - Giles County Seismic Zone

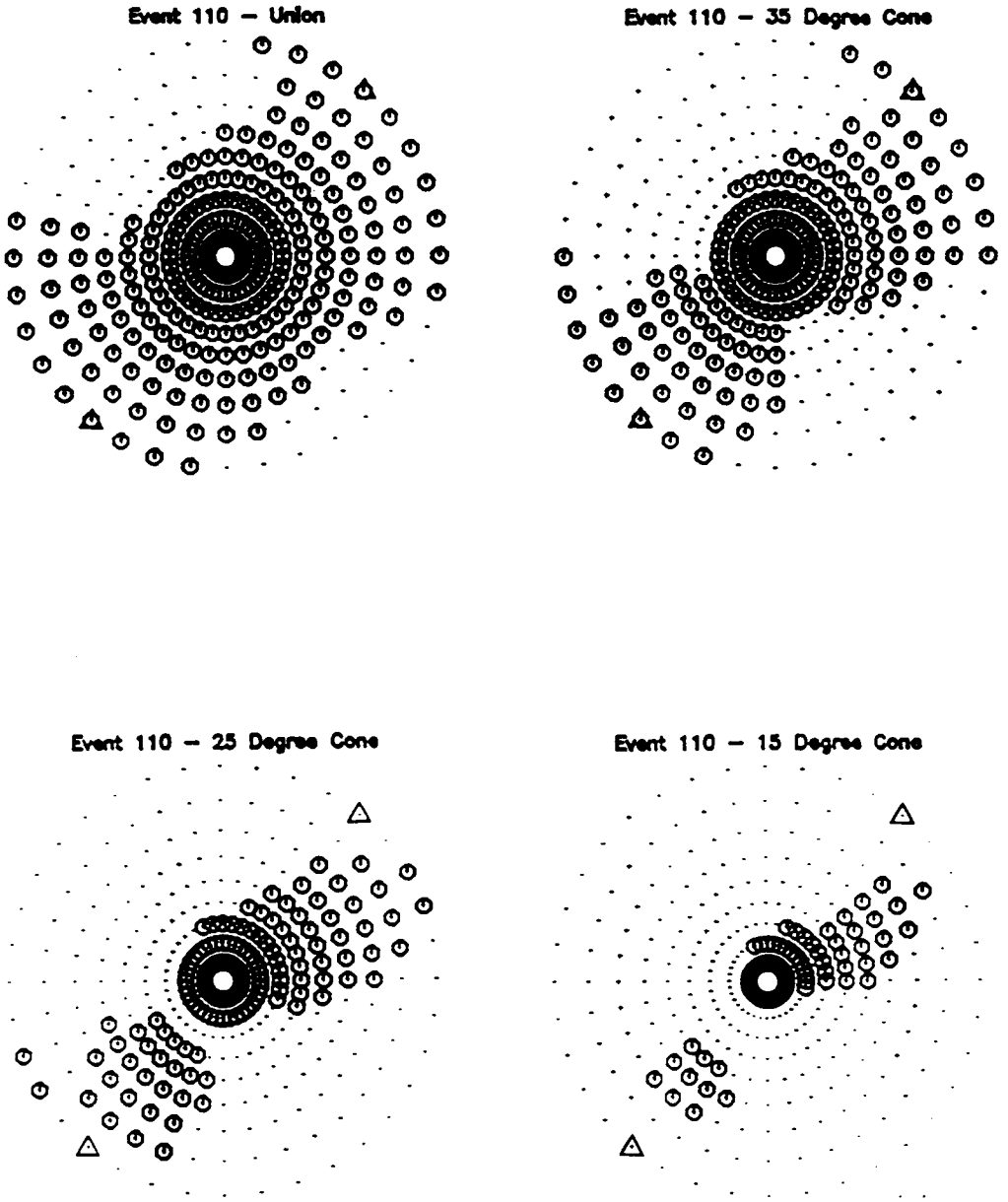

Figure 46. Event 110 - Giles County Seismic Zone

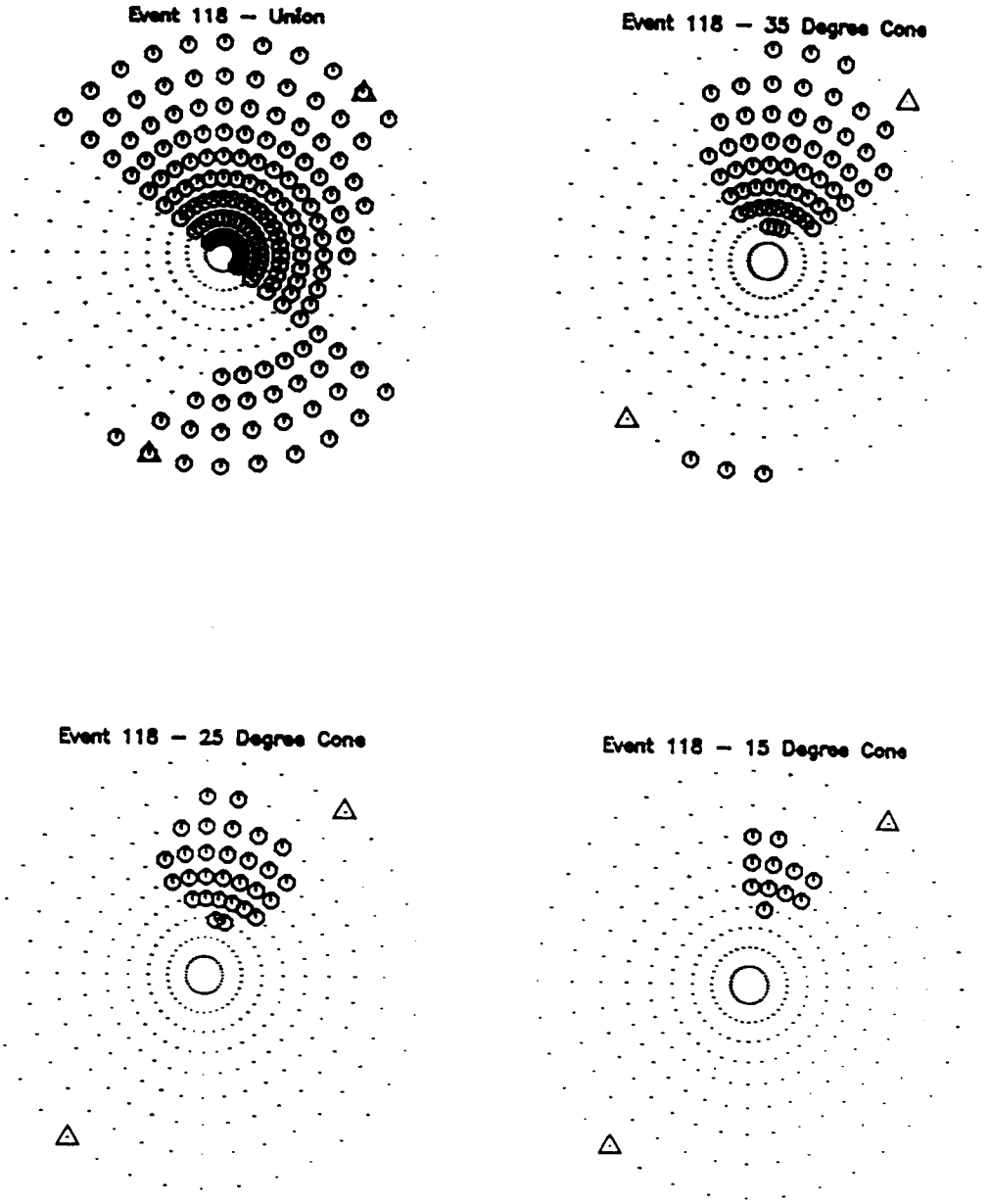

Figure 47. Event 118 - Giles County Seismic Zone

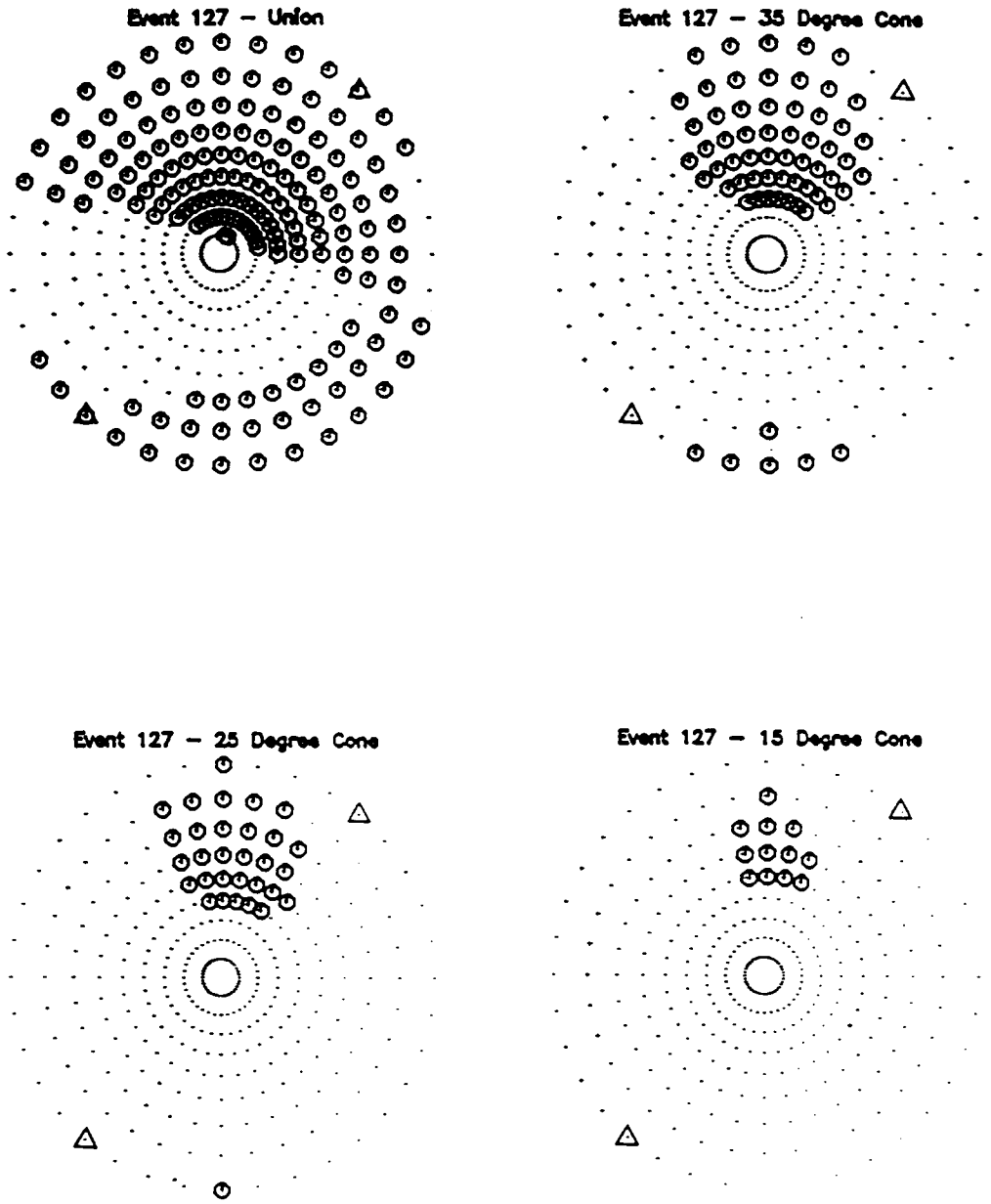

Figure 48. Event 127 - Giles County Seismic Zone

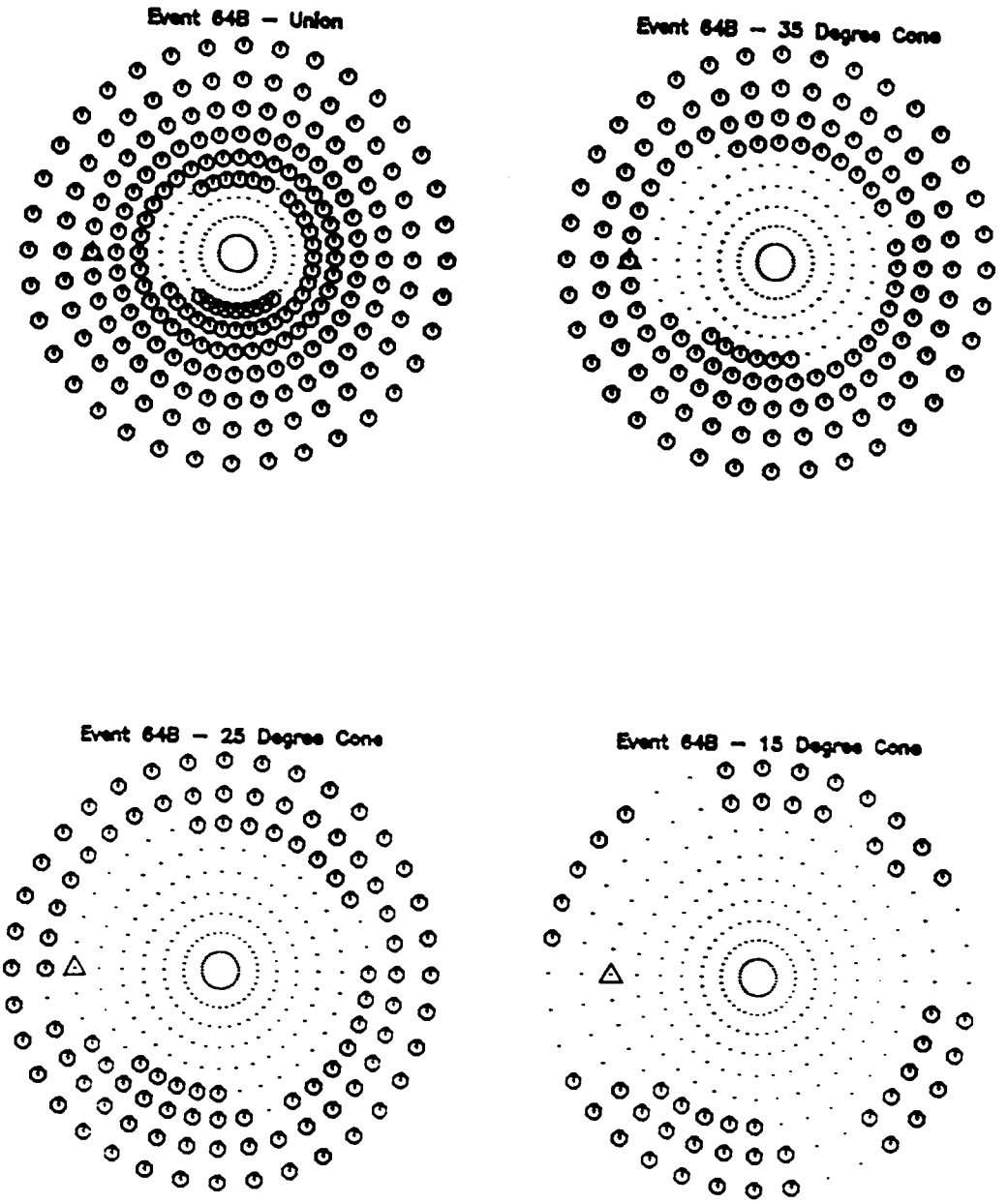

Figure 49. Event 64B - Central Virginia Seismic Zone (Deeper)

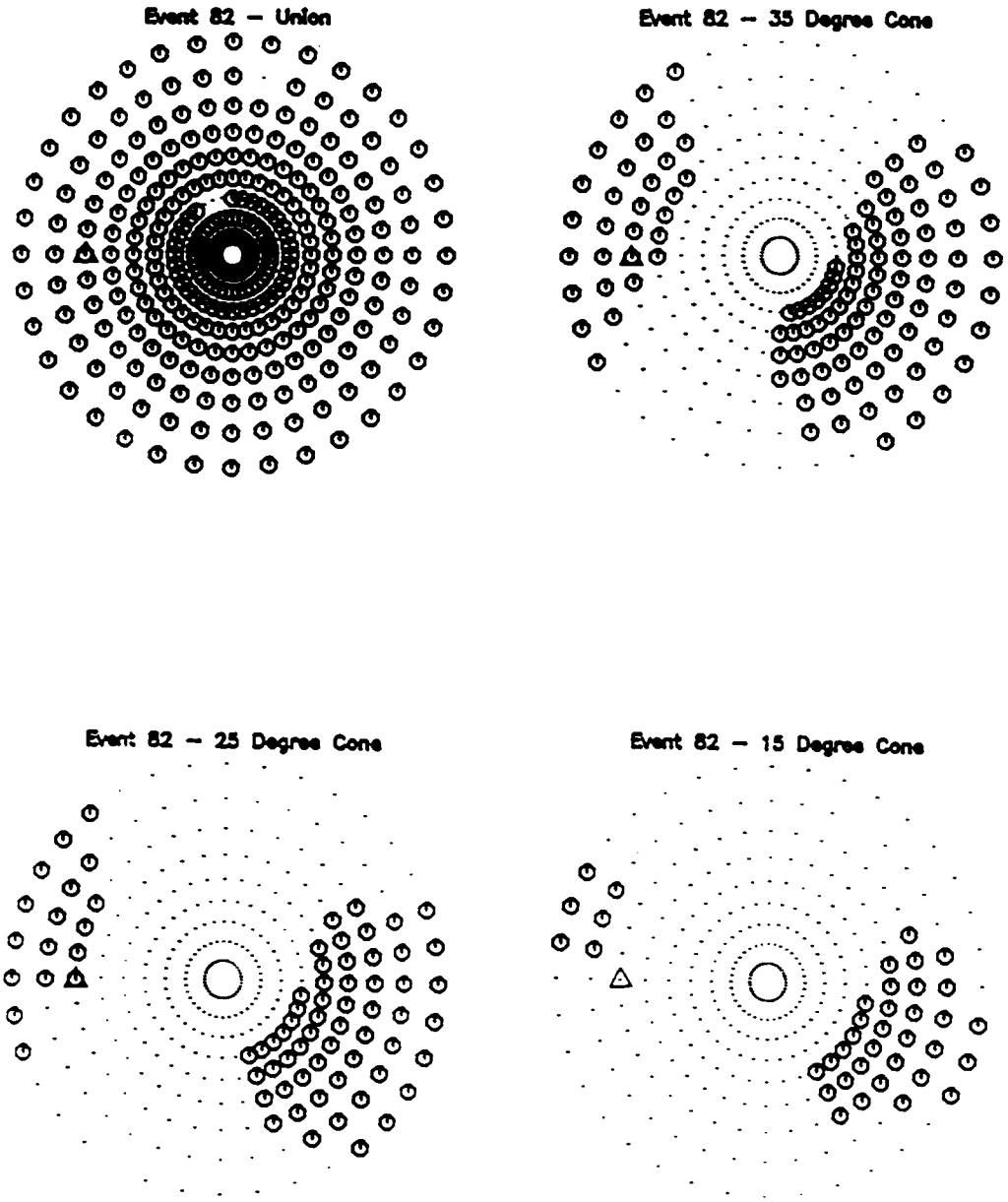

Figure 50. Event 82 - Central Virginia Seismic Zone (Deeper)

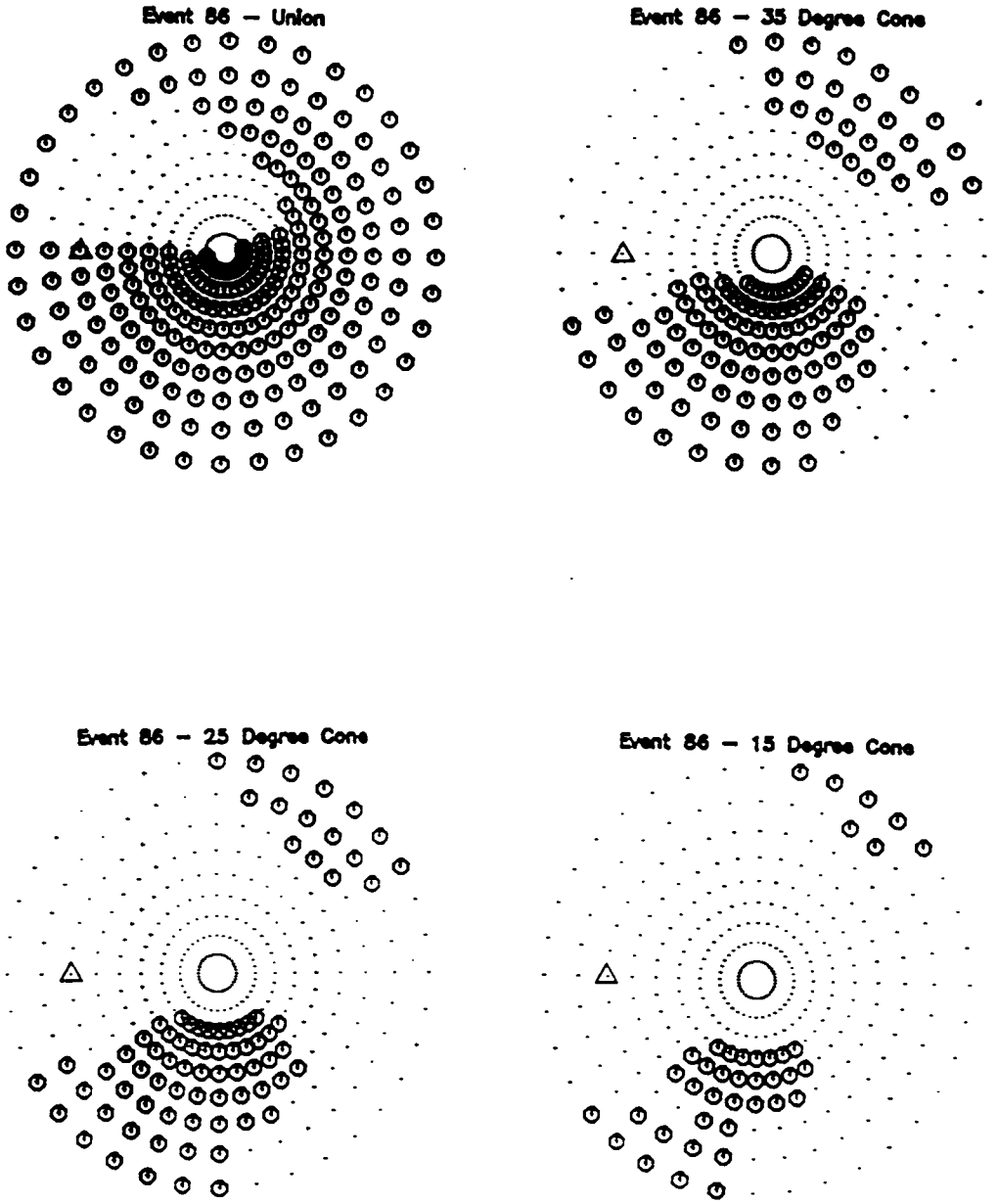

Figure 51. Event 86 - Central Virginia Seismic Zone (Deeper)

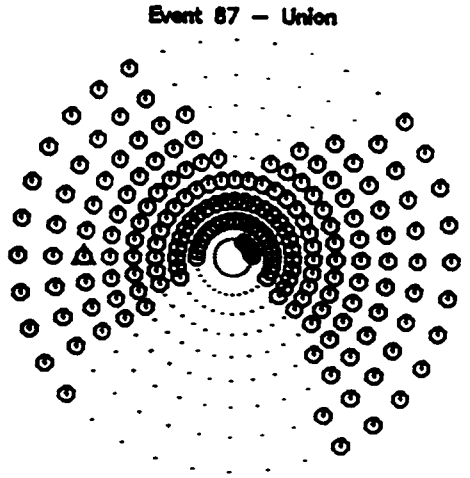

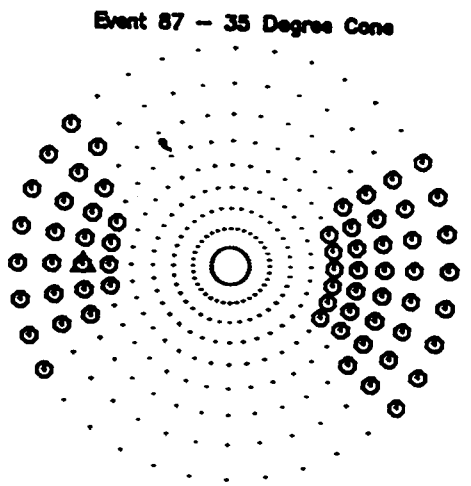

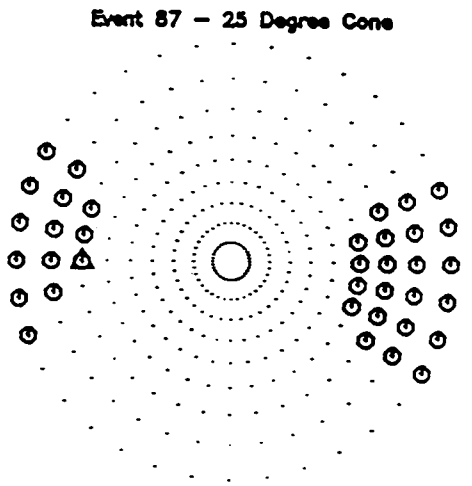

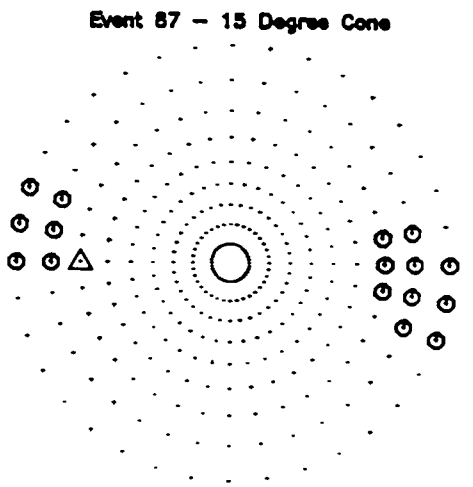

Figure 52. Event 87 - Central Virginia Seismic Zone (Deeper)

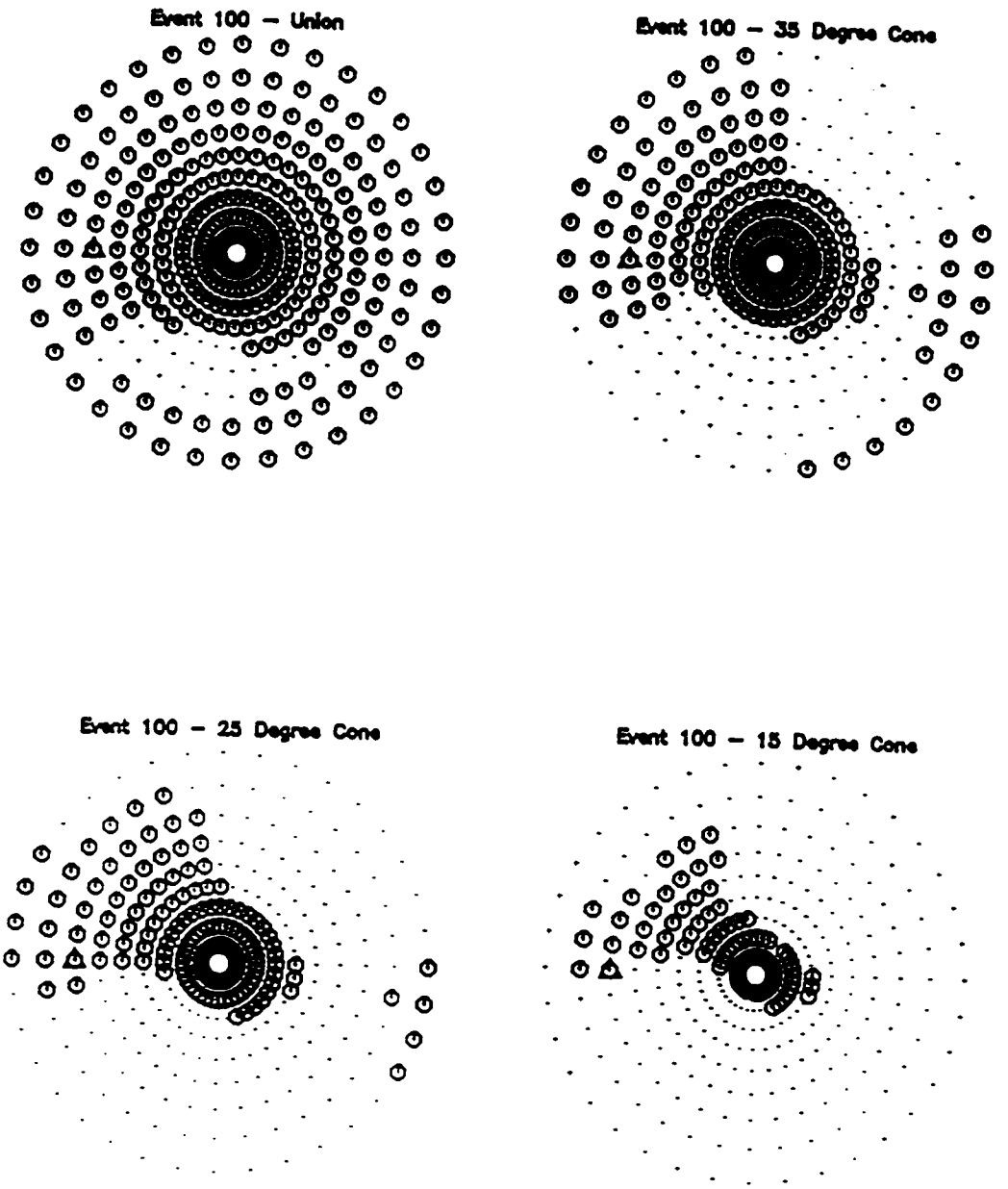

Figure 53. Event 100 - Central Virginia Seismic Zone (Deeper)

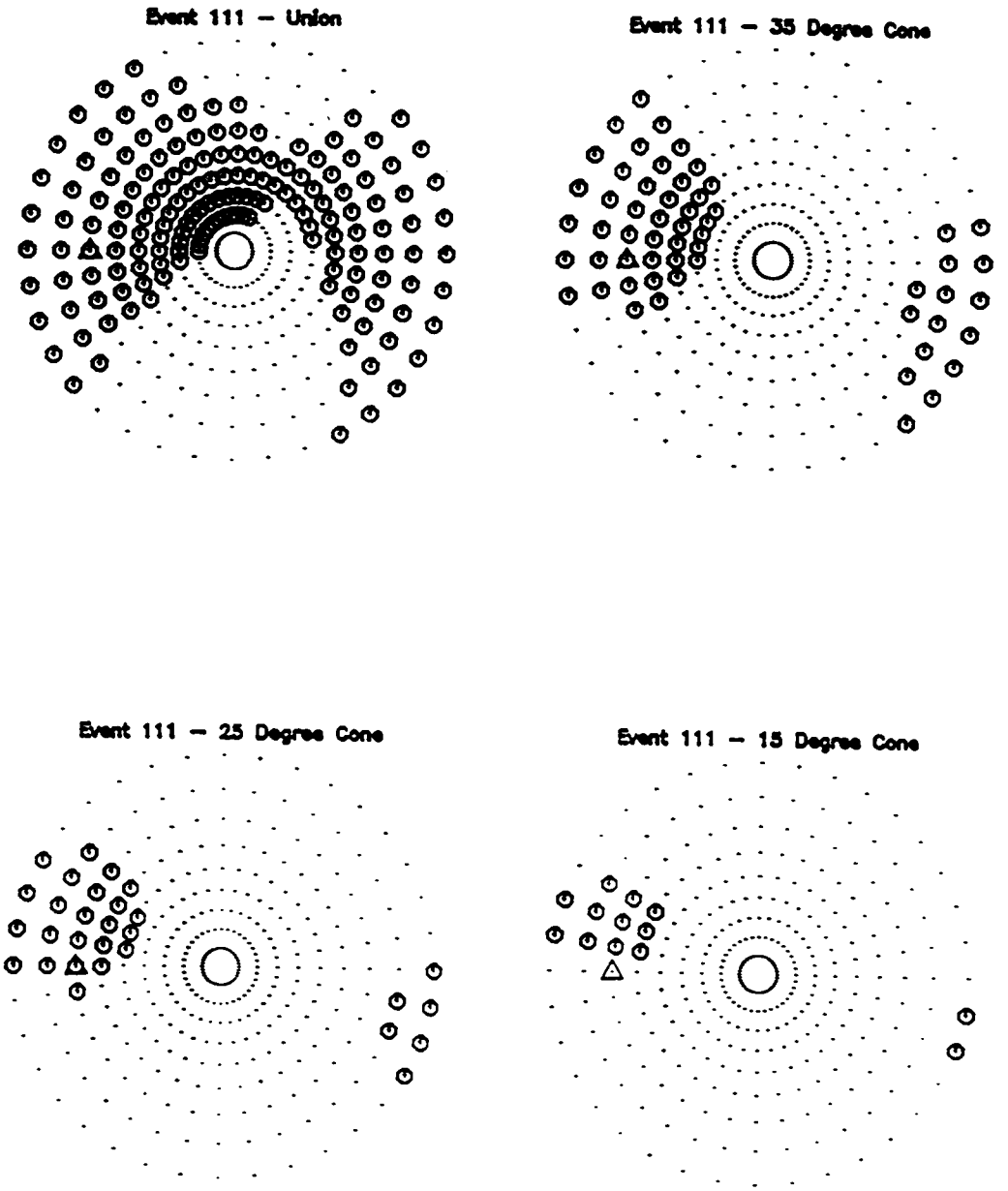

Figure 54. Event 111 - Central Virginia Seismic Zone (Deeper)

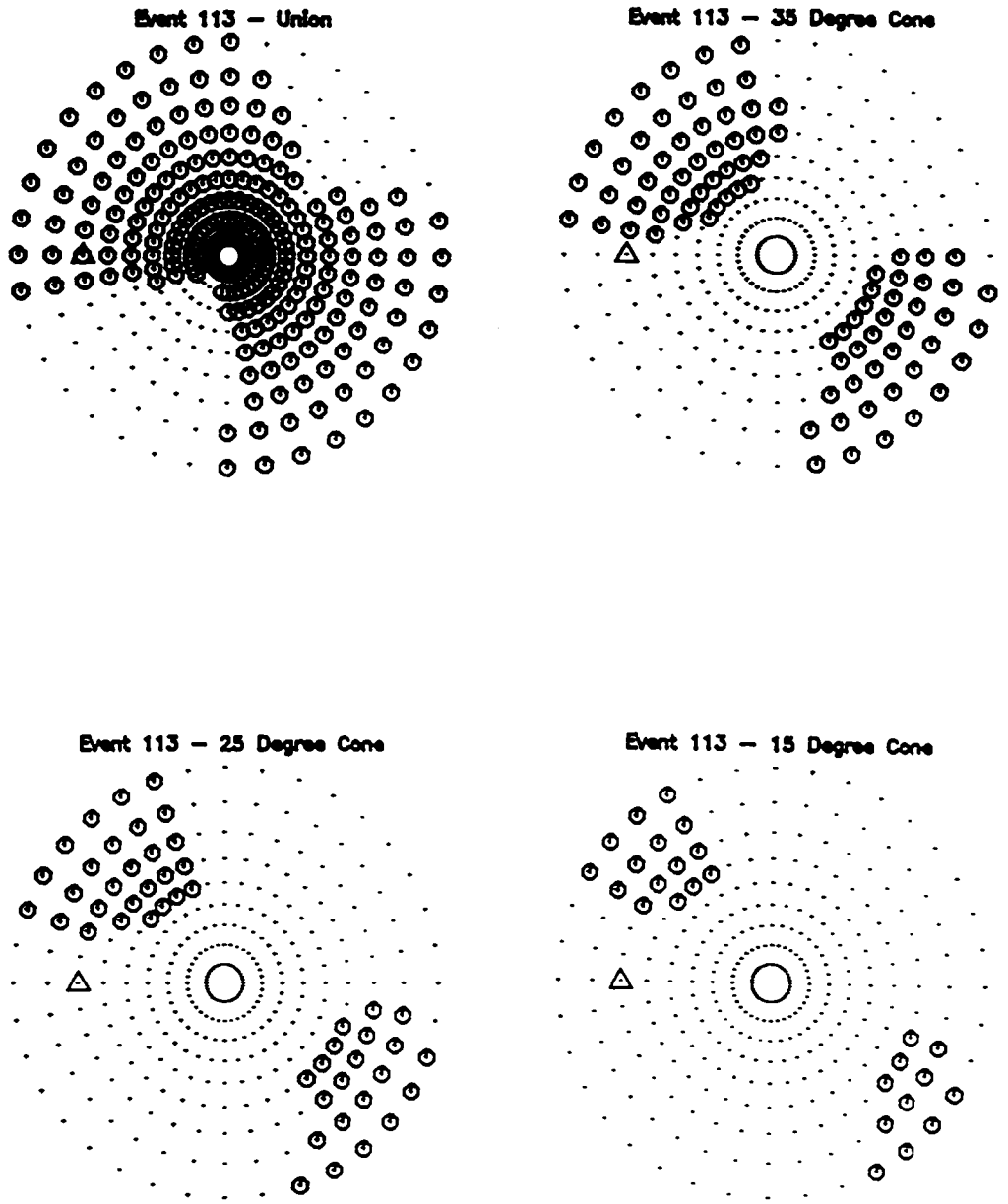

Figure 55. Event 113 - Central Virginia Seismic Zone (Deeper)

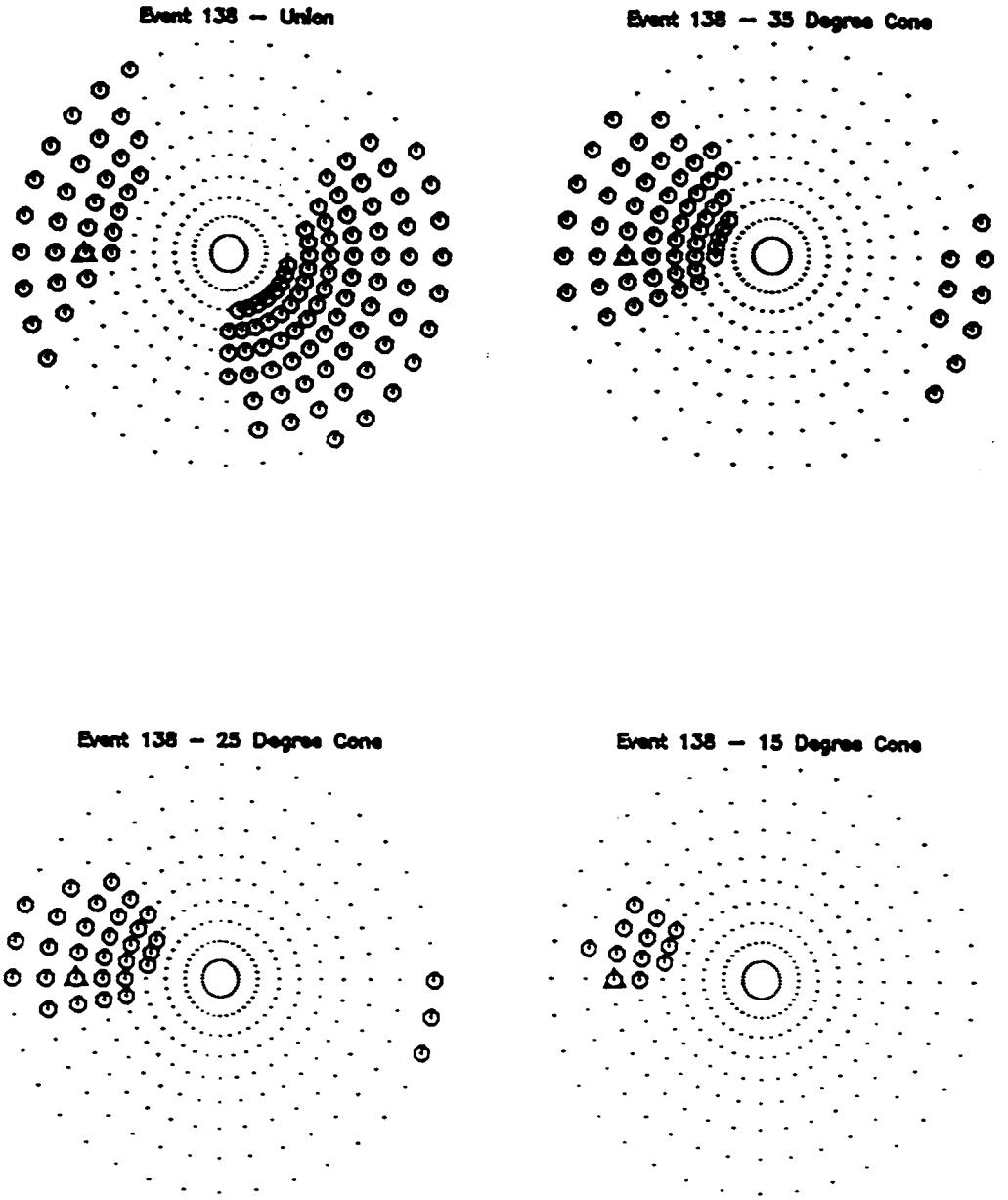

Figure 56. Event 138 - Central Virginia Seismic Zone (Deeper)

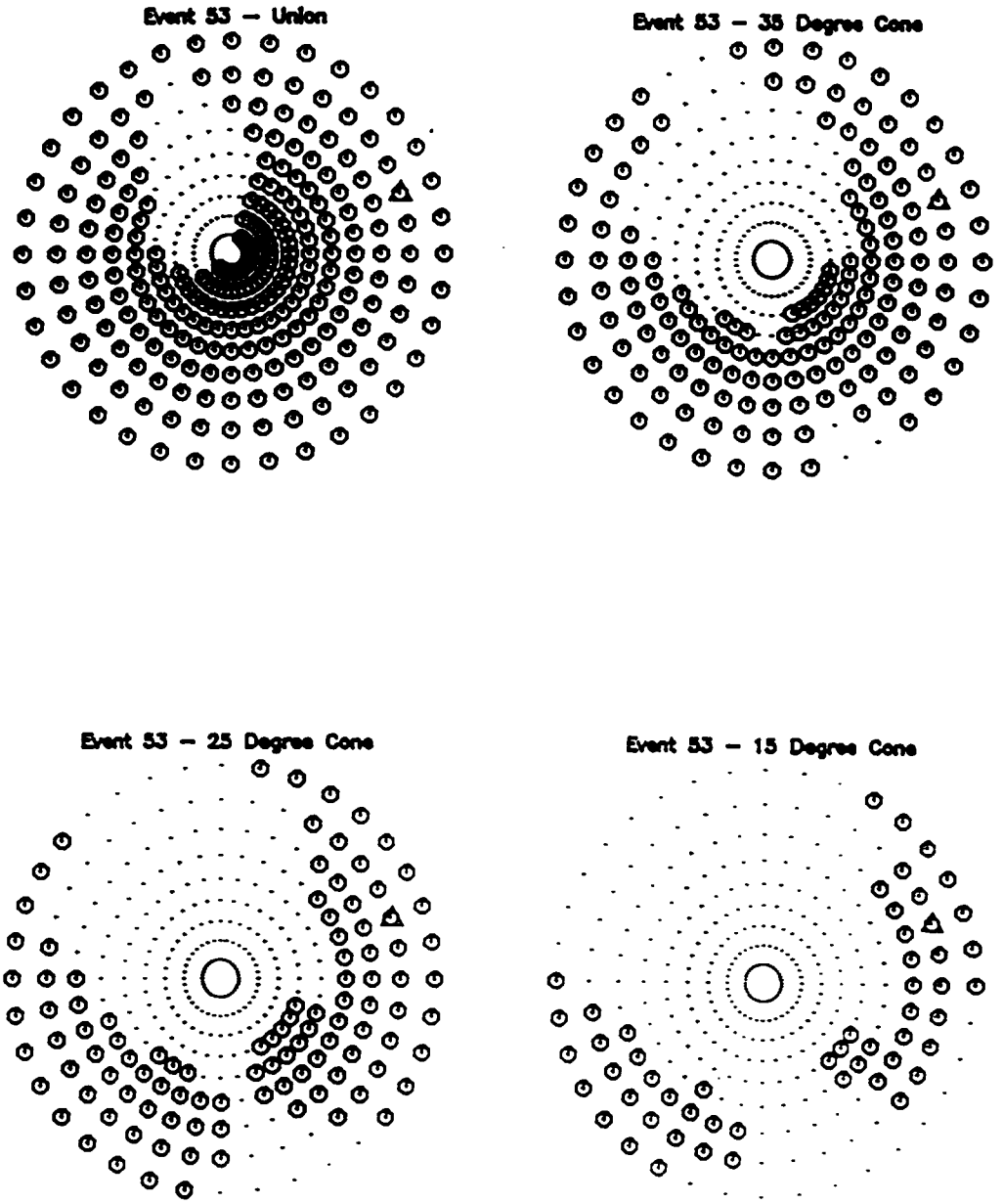

Figure 57. Event 53 - Central Virginia Seismic Zone (Shallow)

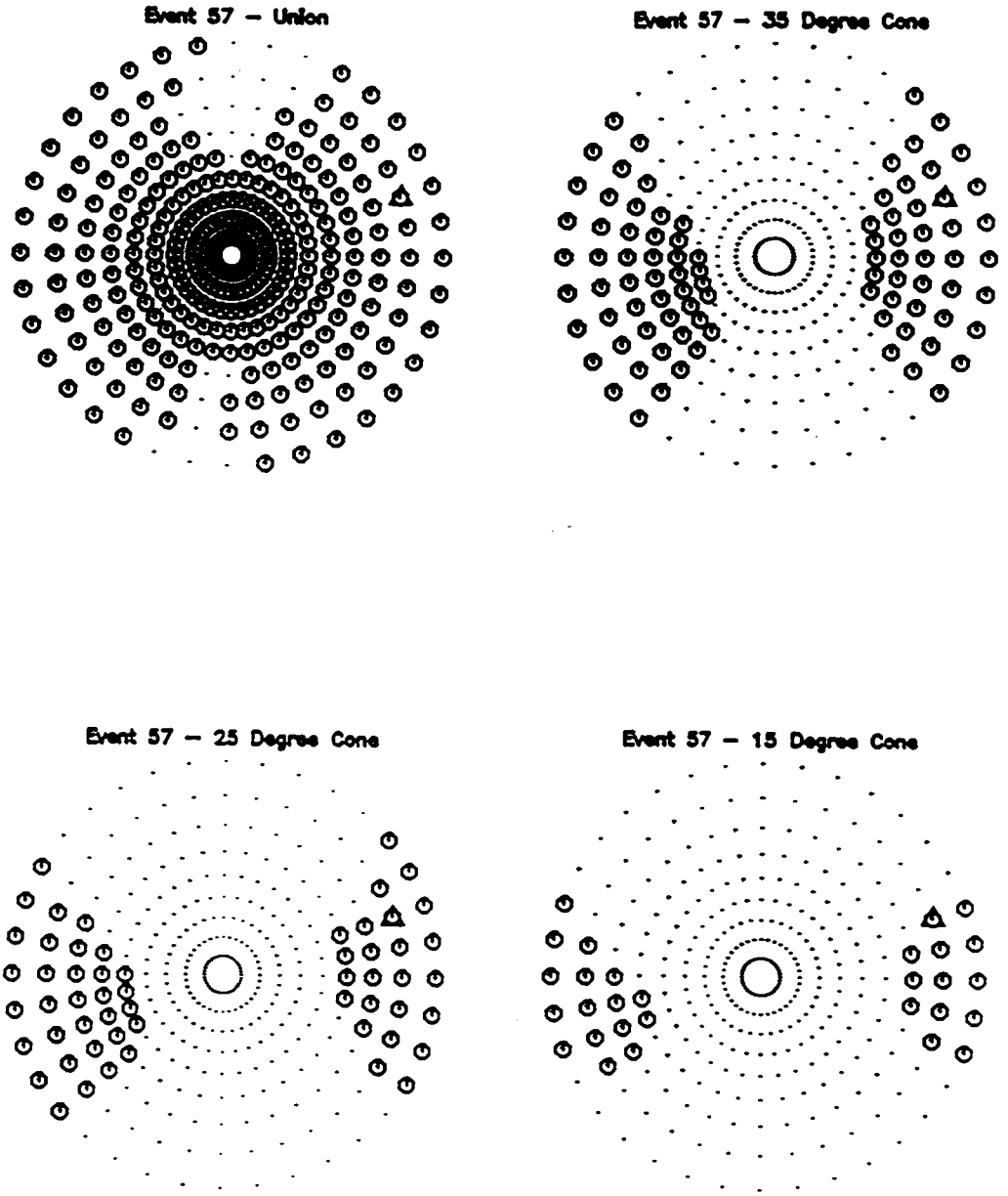

Figure 58. Event 57 - Central Virginia Seismic Zone (Shallow)

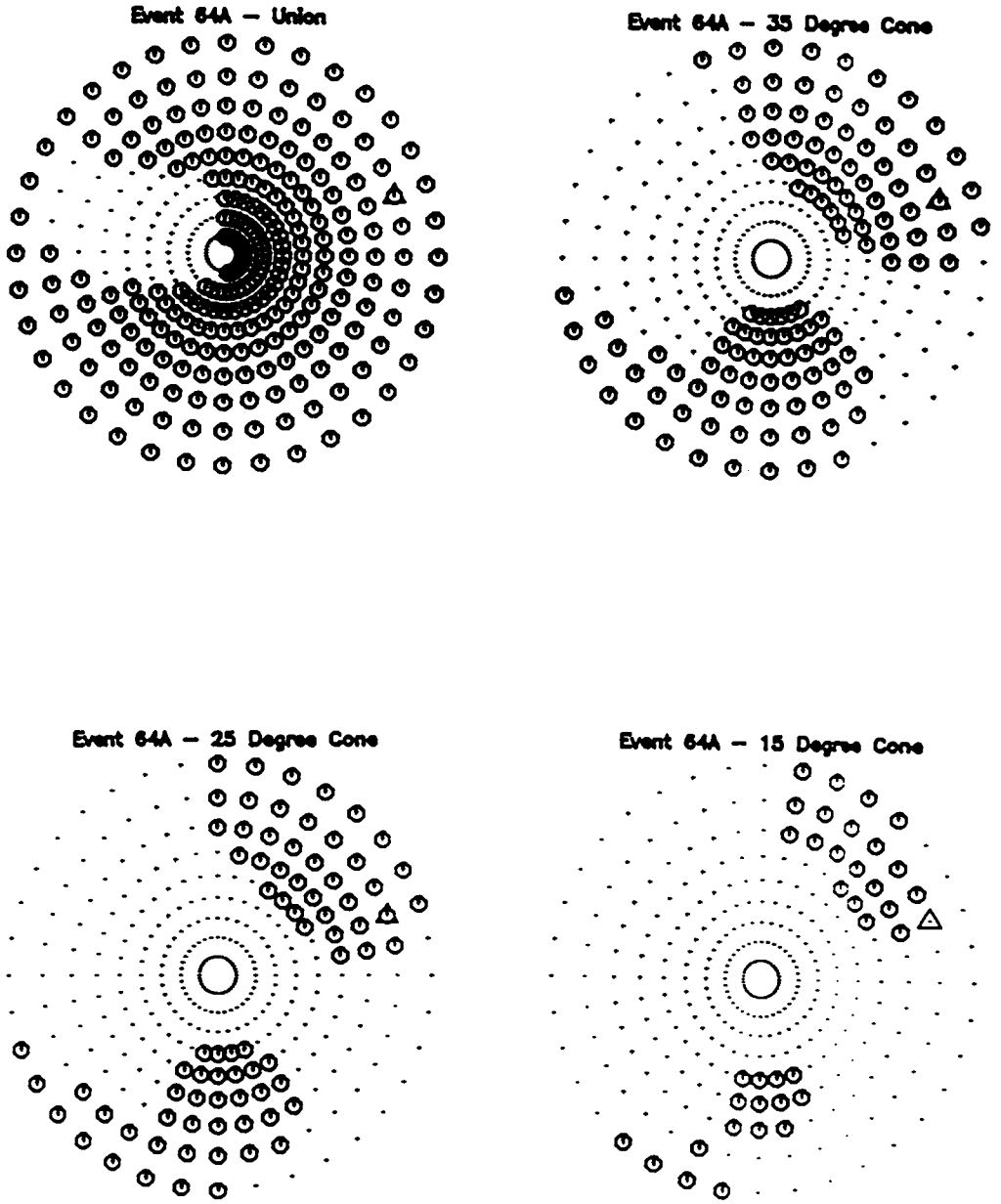

Figure 59. Event 64A - Central Virginia Seismic Zone (Shallow)

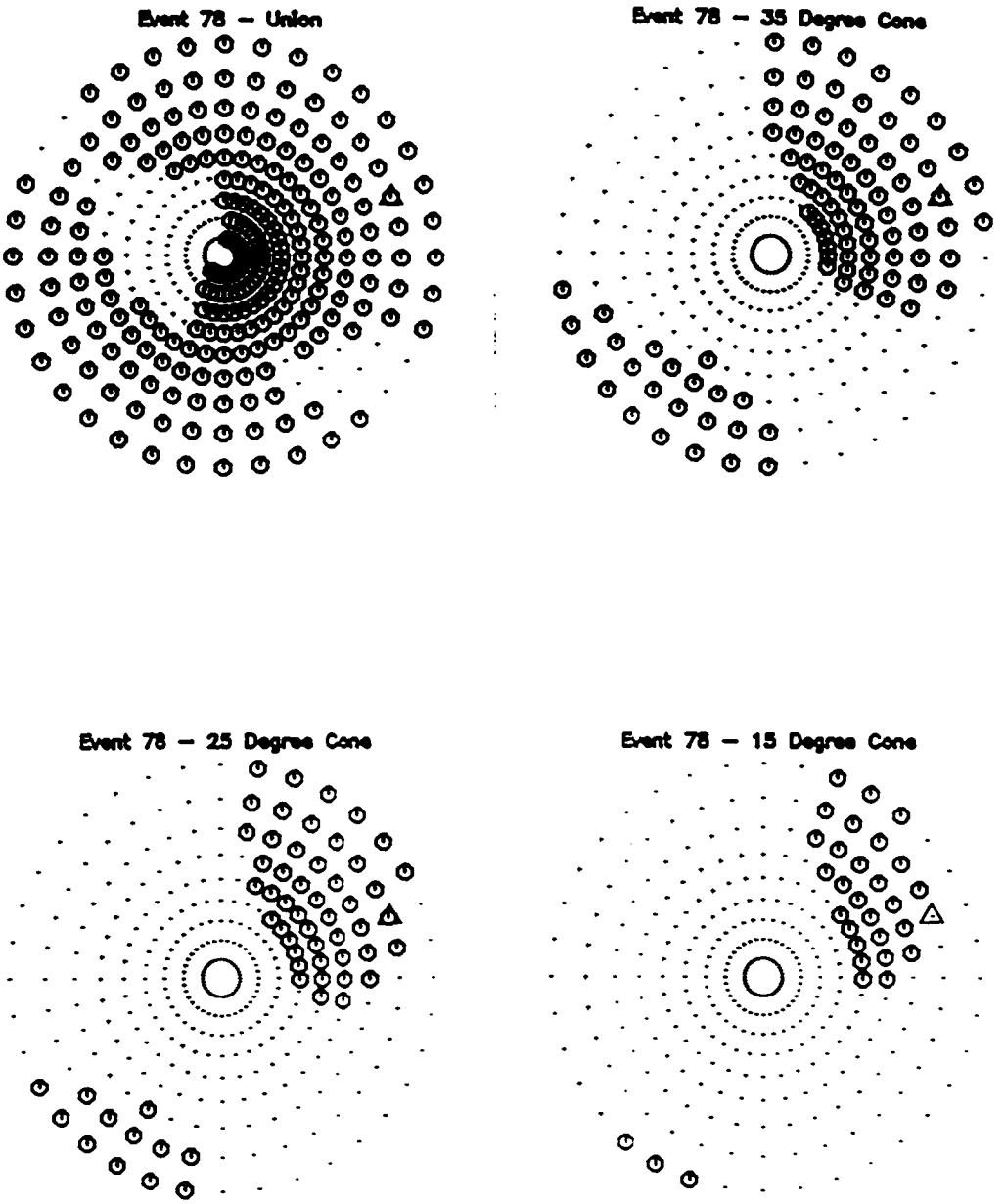

Figure 60. Event 78 - Central Virginia Seismic Zone (Shallow)

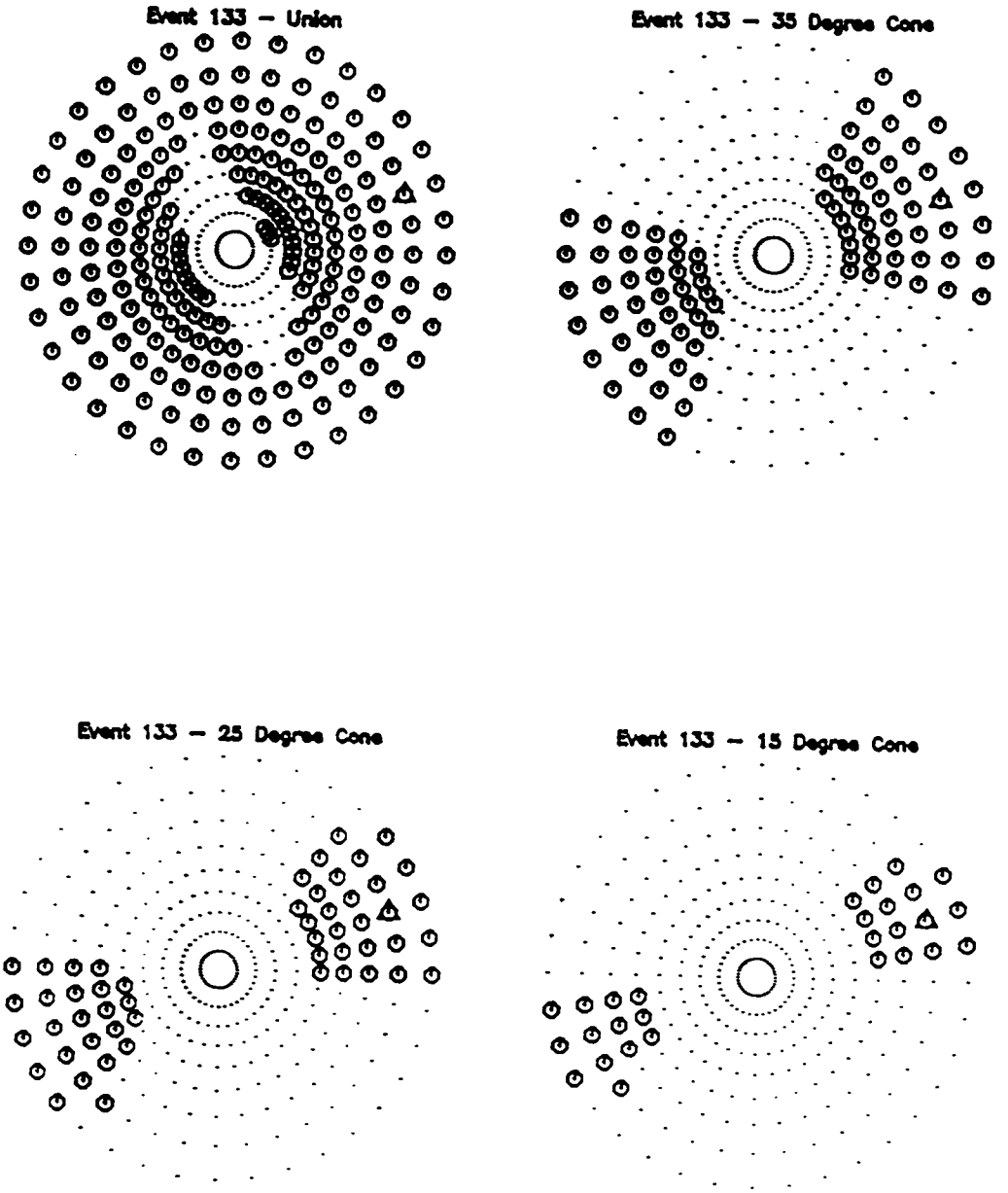

Figure 61. Event 133 - Central Virginia Seismic Zone (Shallow)

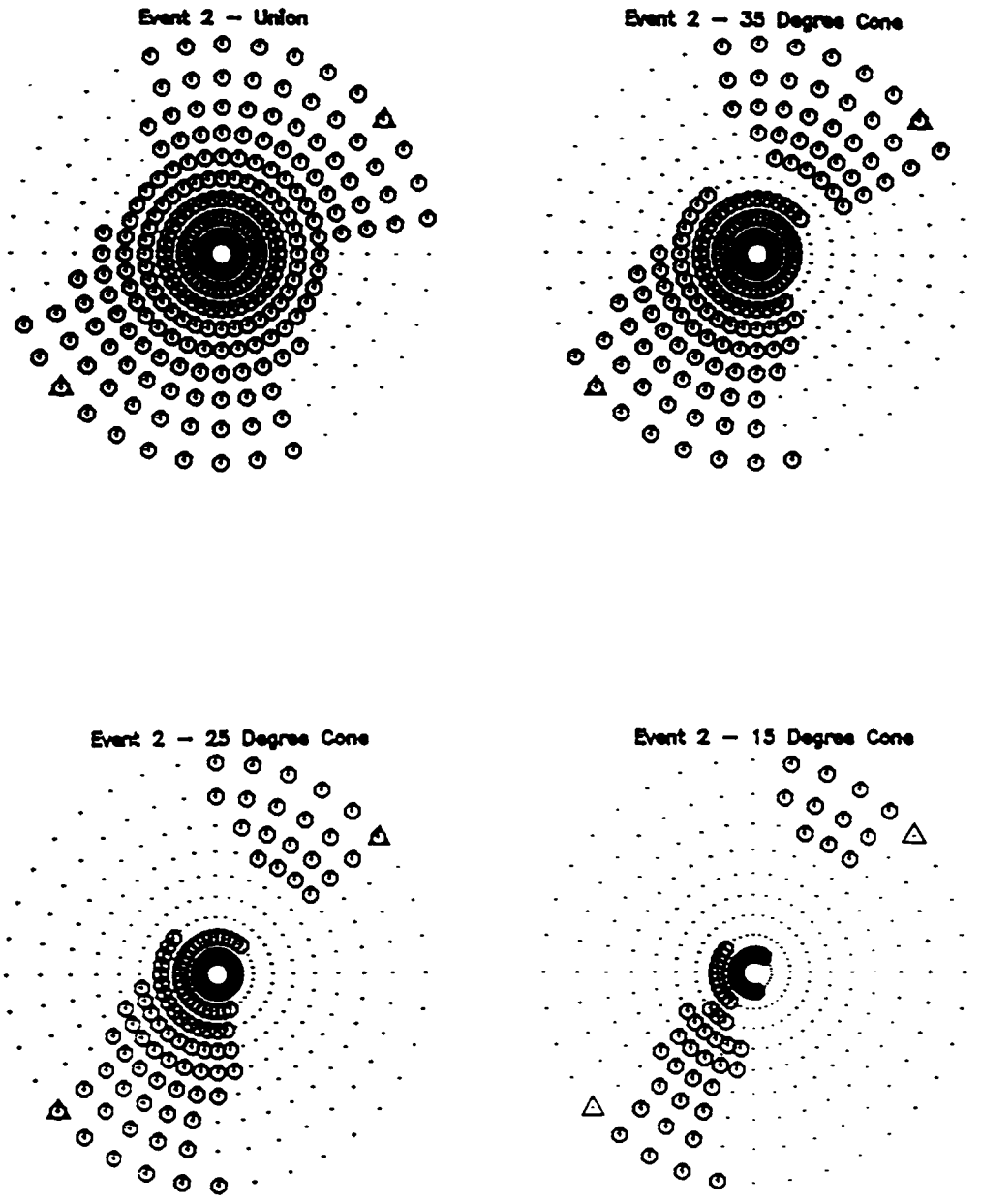

Figure 62. Event 2 - Eastern Tennessee Seismic Zone

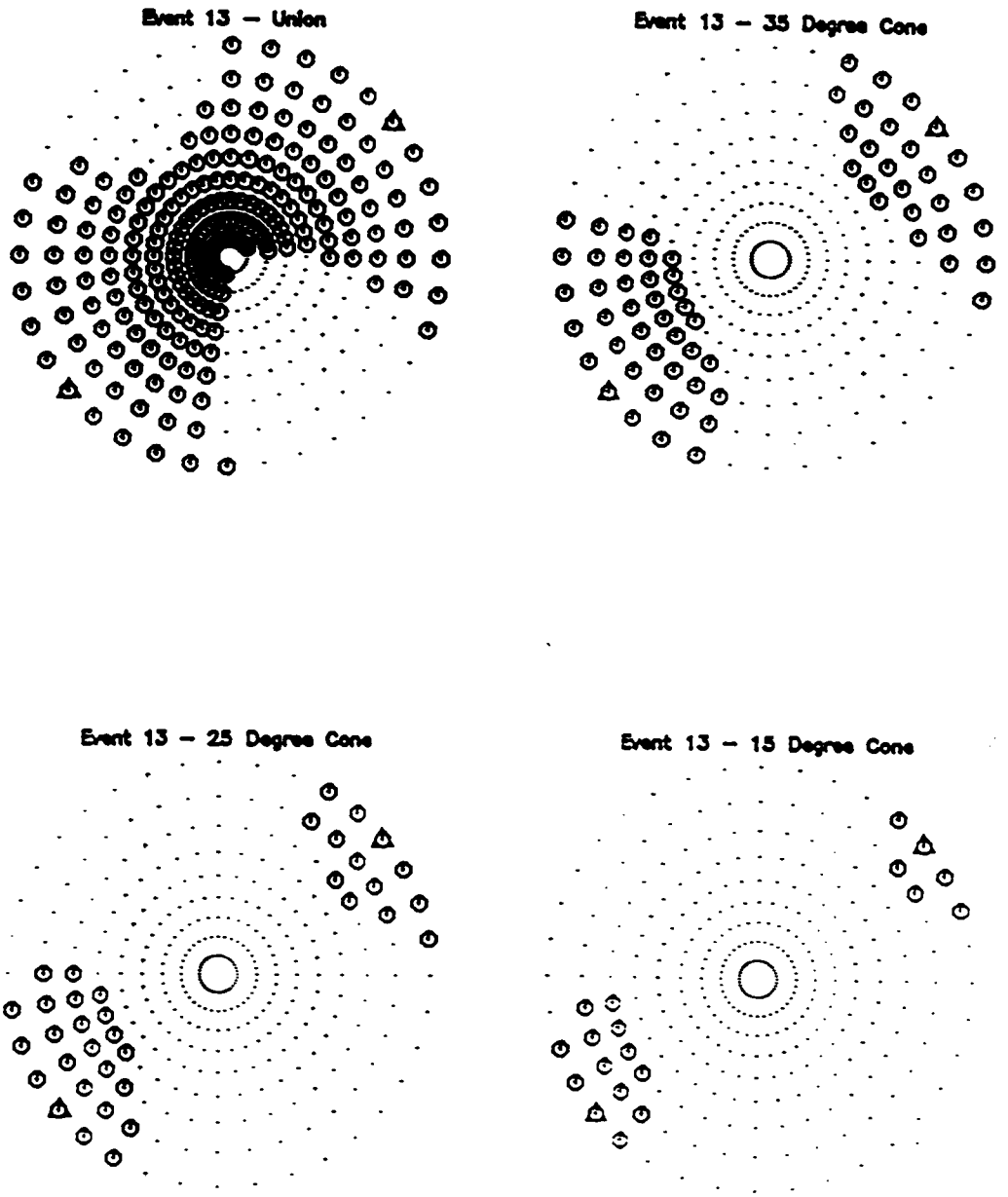

Figure 63. Event 13 - Eastern Tennessee Seismic Zone

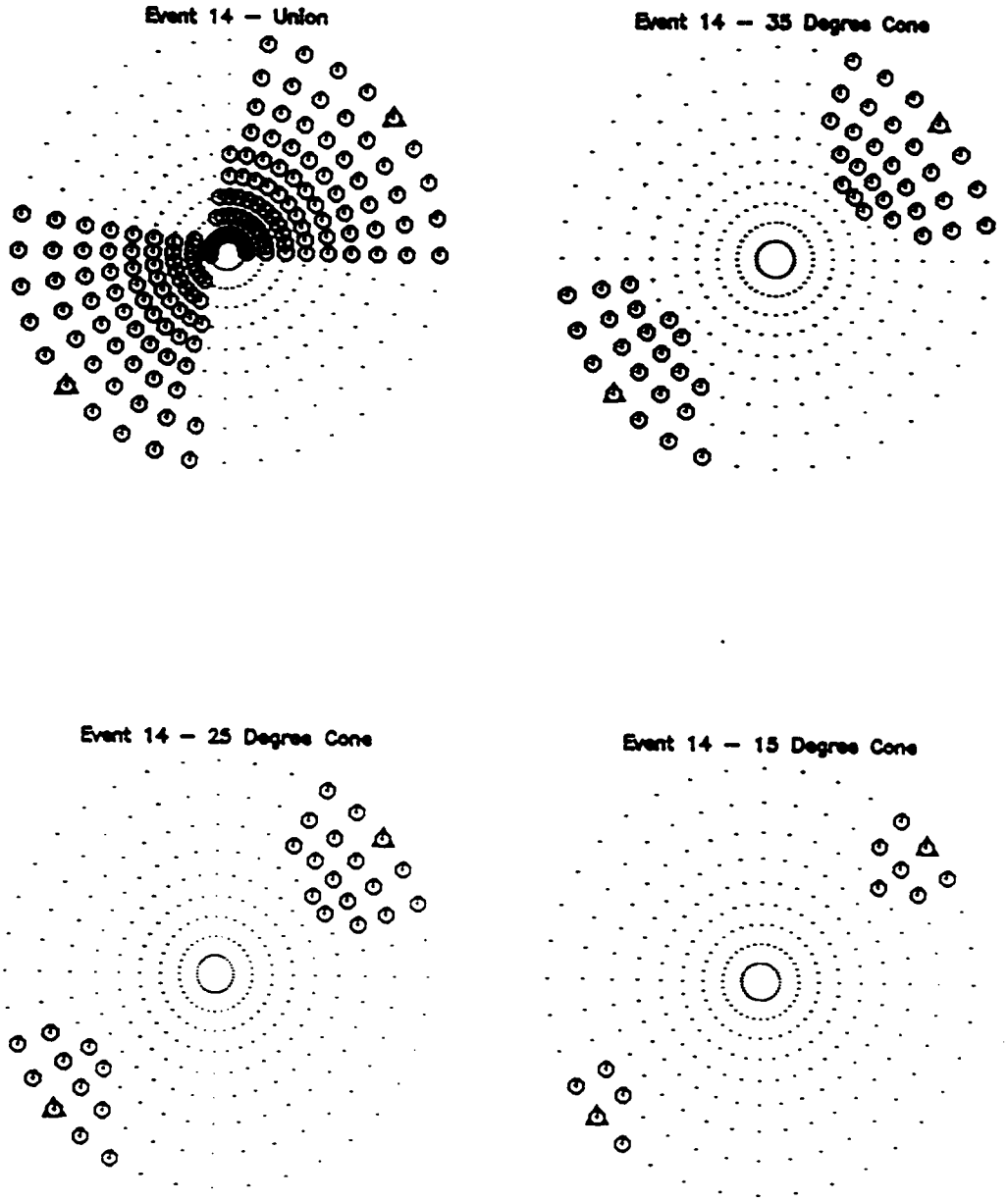

Figure 64. Event 14 - Eastern Tennessee Seismic Zone

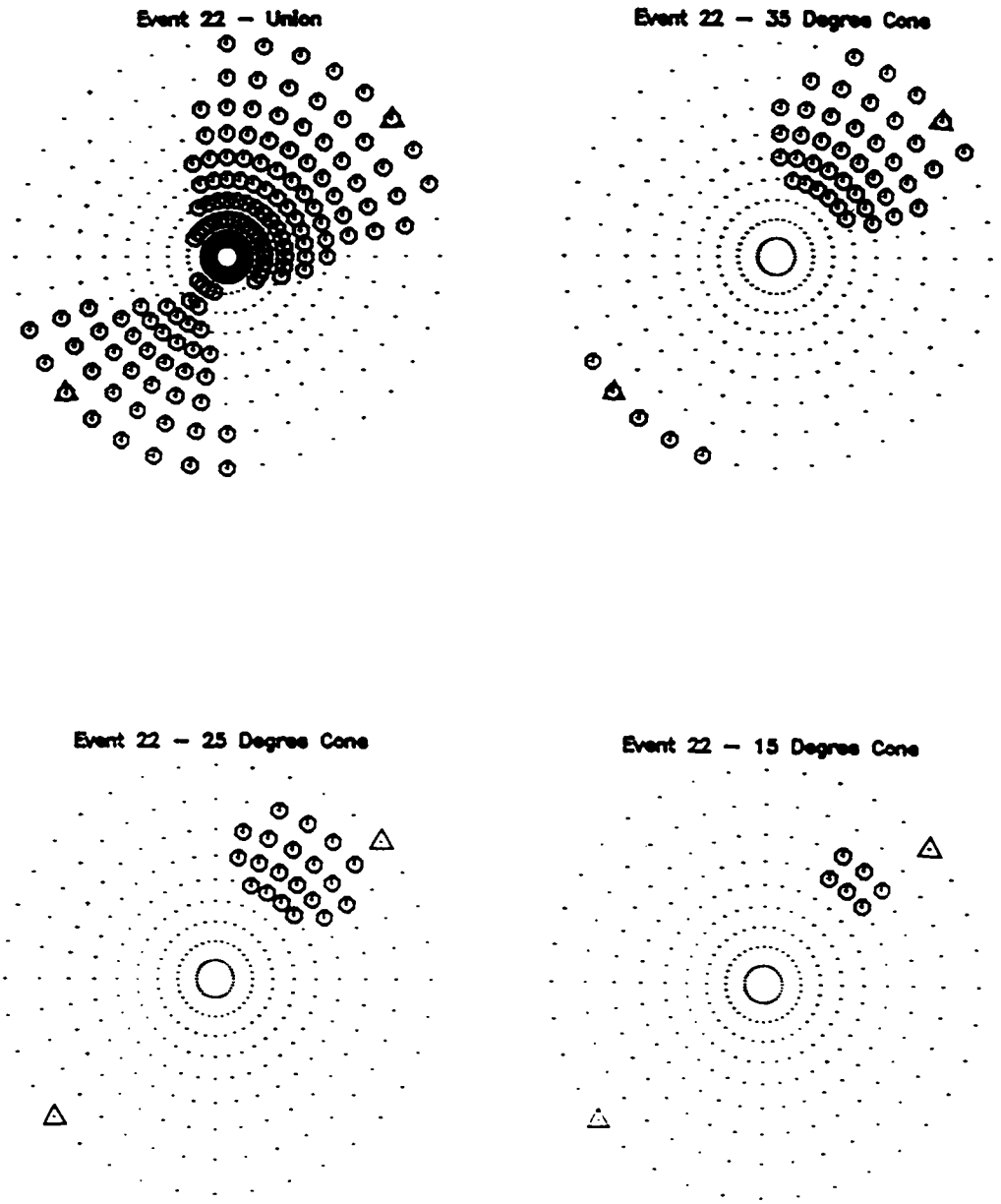

Figure 65. Event 22 - Eastern Tennessee Seismic Zone

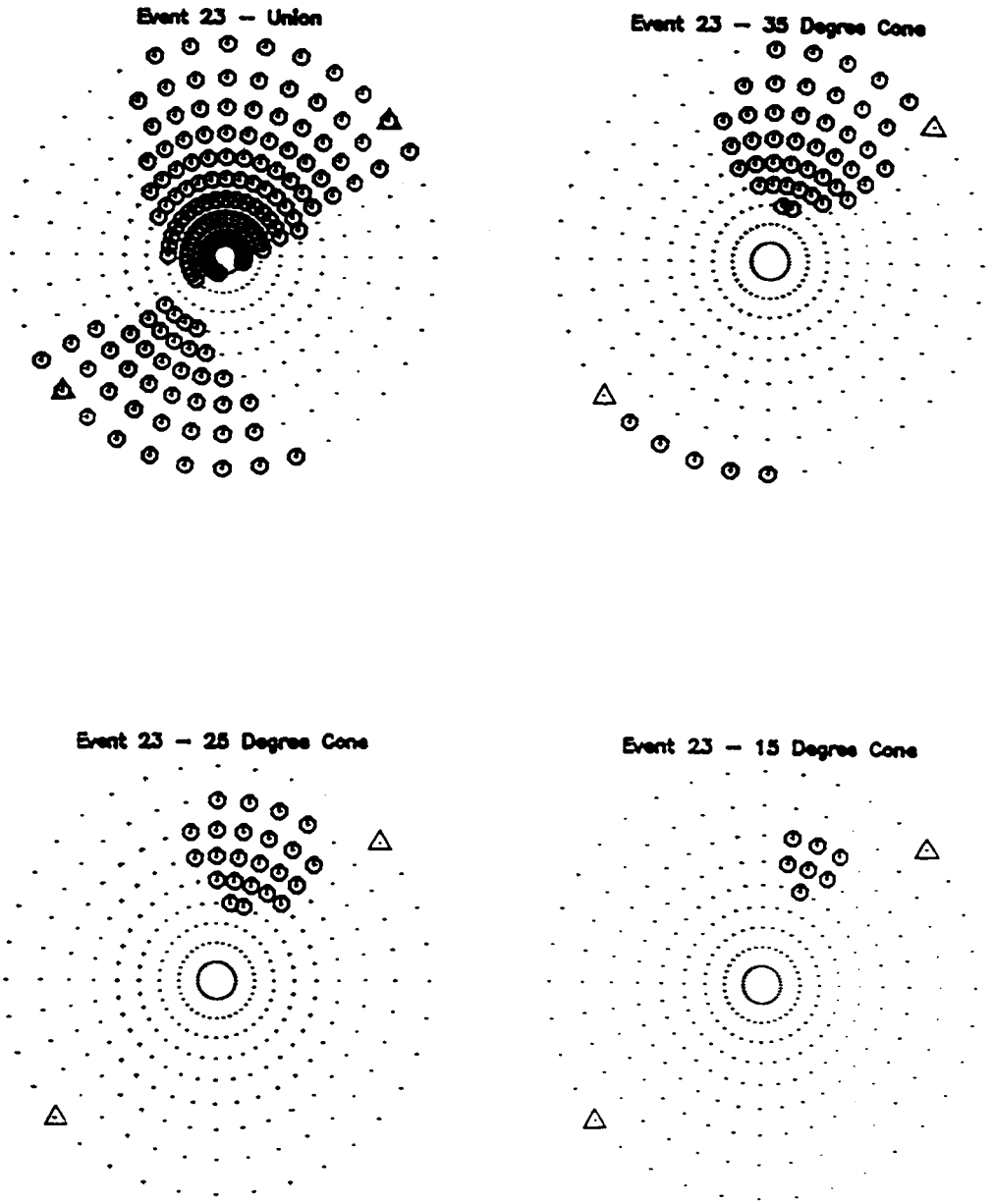

Figure 66. Event 23 - Eastern Tennessee Seismic Zone

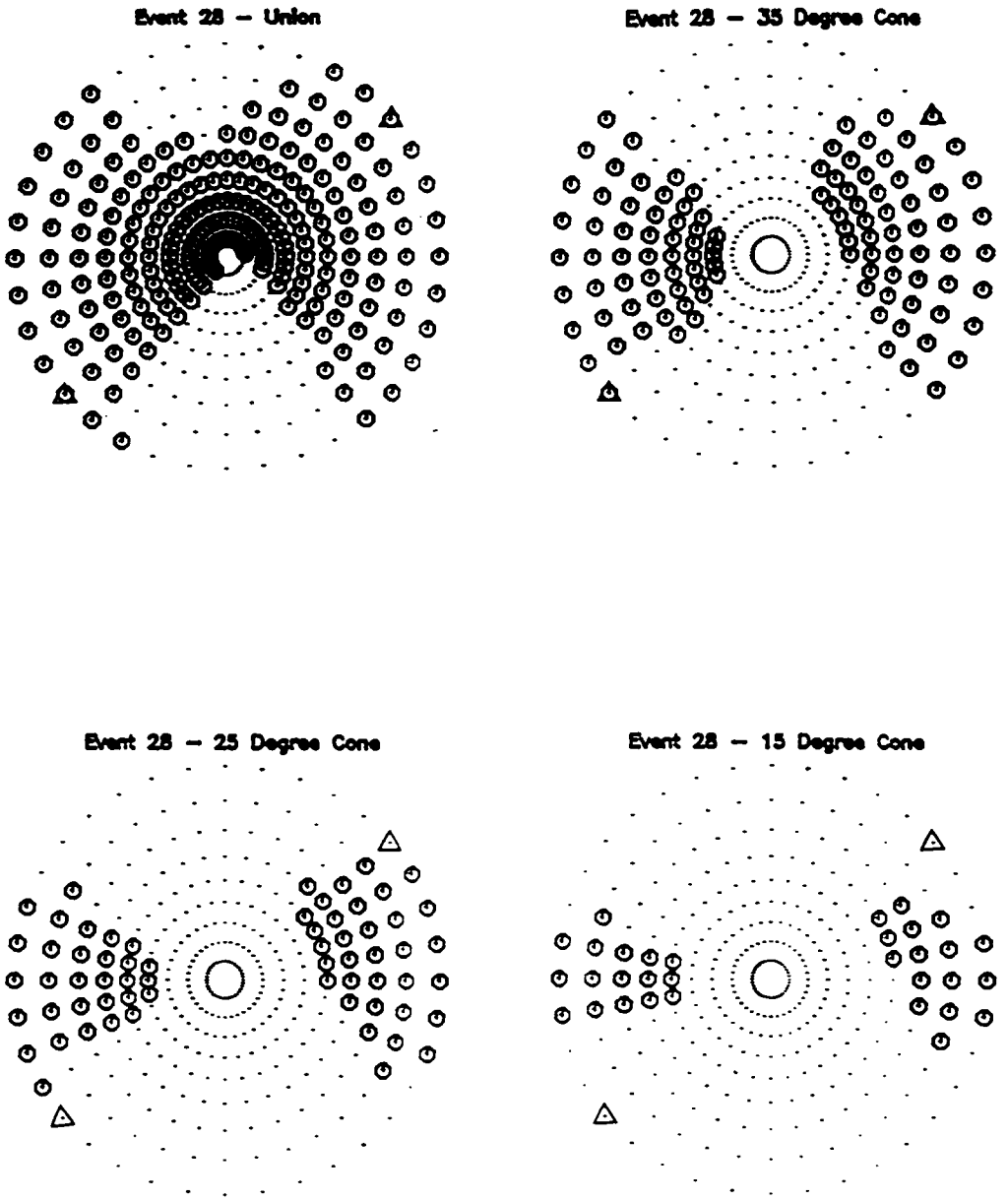

Figure 67. Event 28 - Eastern Tennessee Seismic Zone

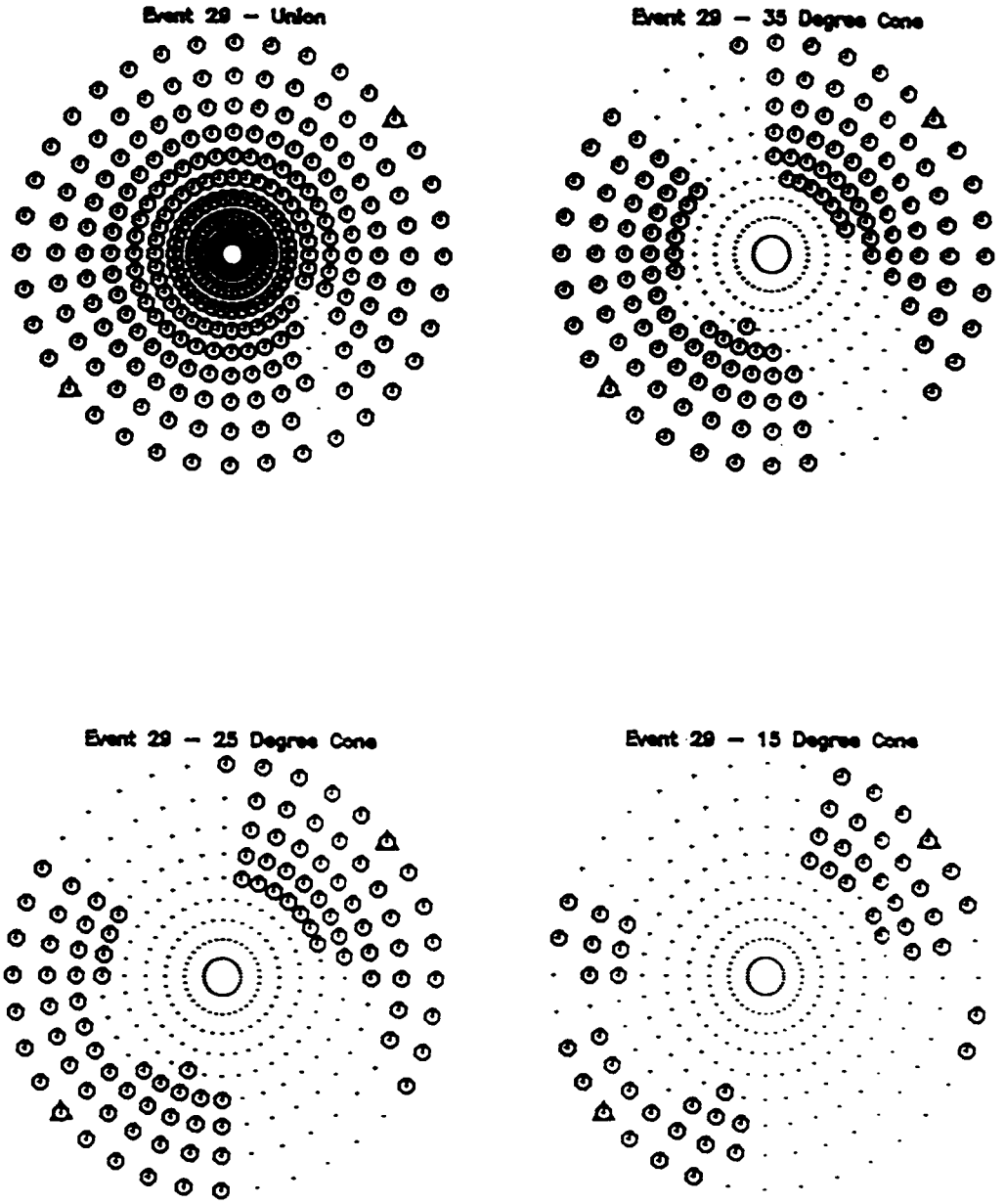

Figure 68. Event 29 - Eastern Tennessee Seismic Zone

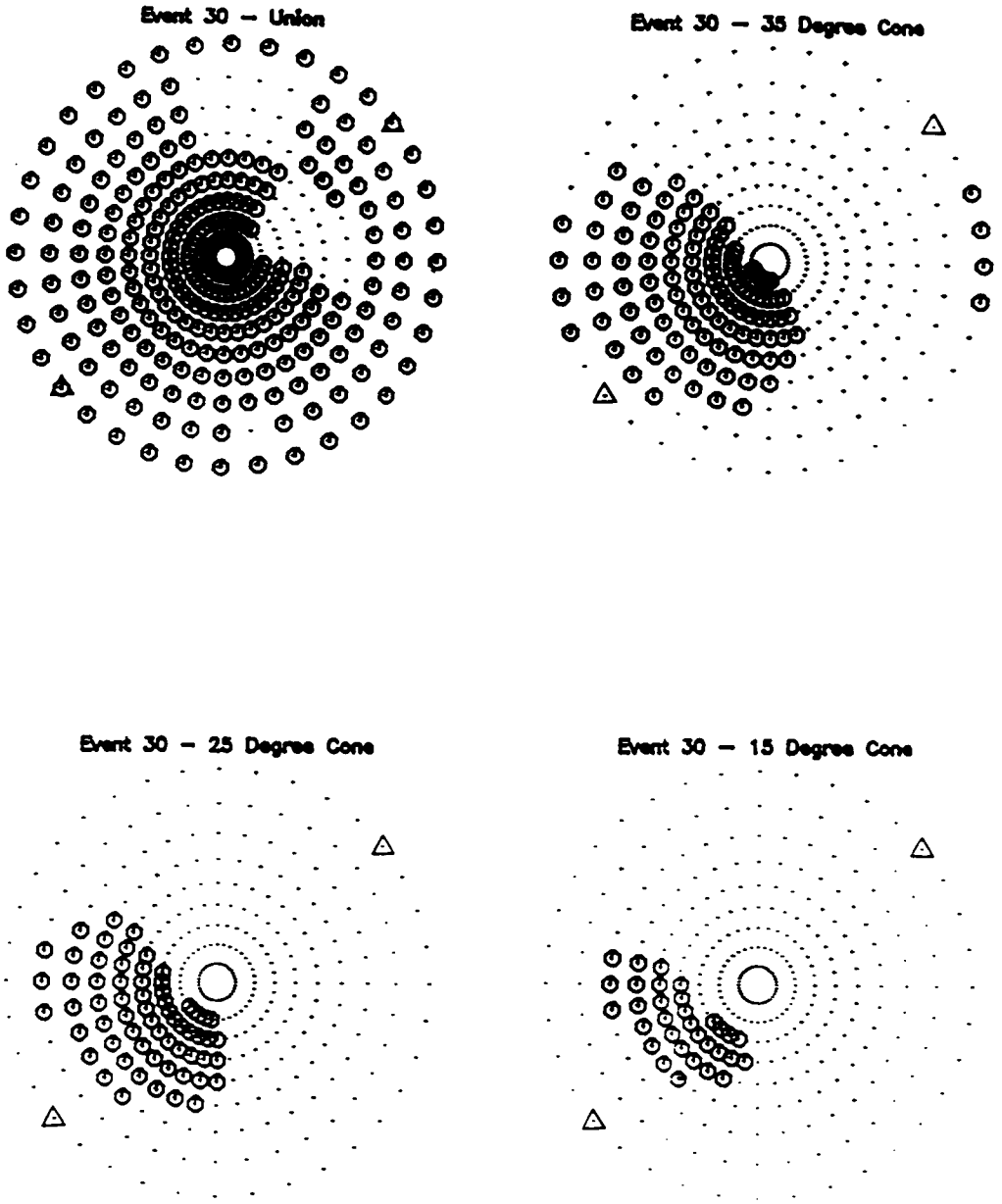

Figure 69. Event 30 - Eastern Tennessee Seismic Zone

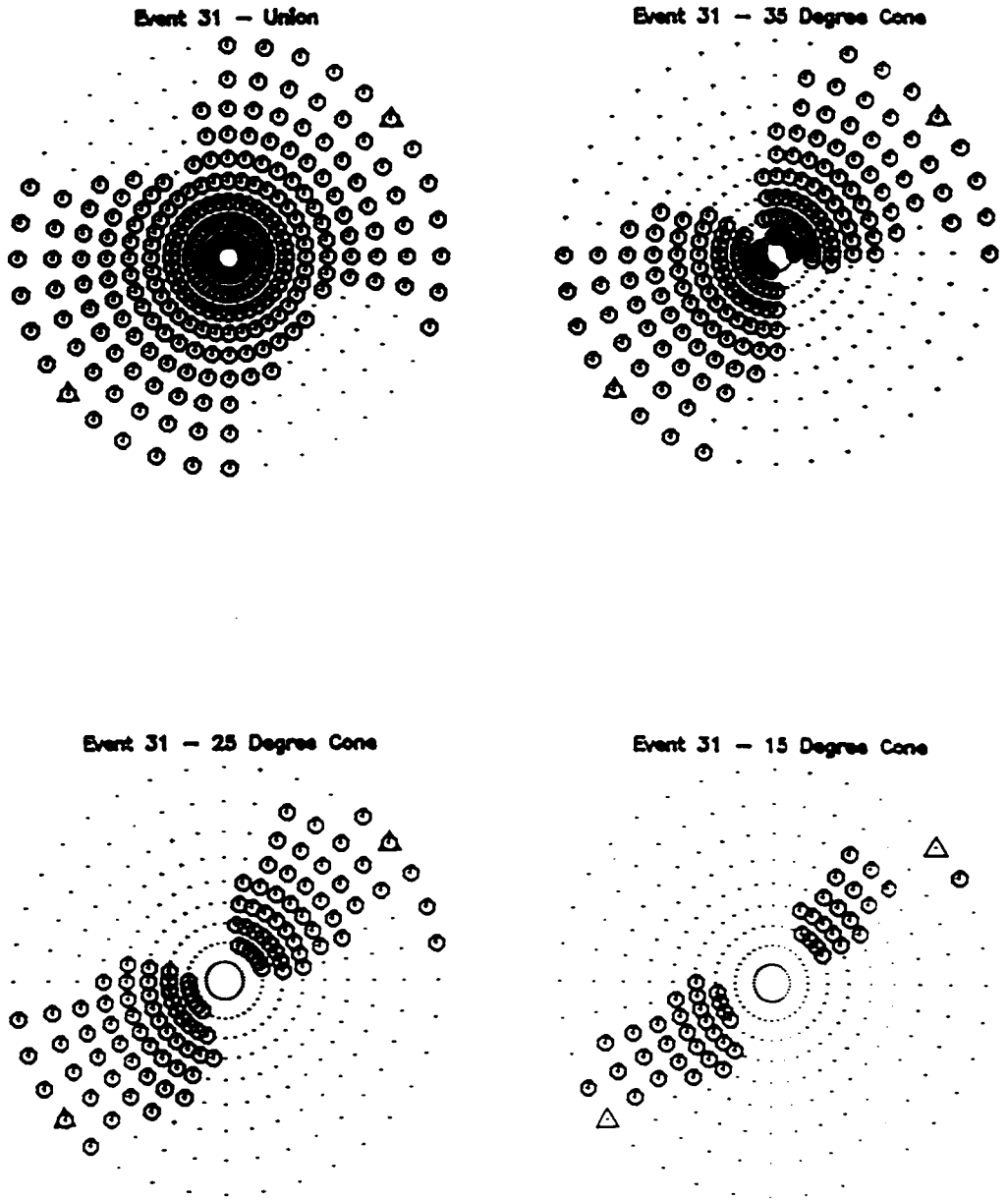

Figure 70. Event 31 - Eastern Tennessee Seismic Zone

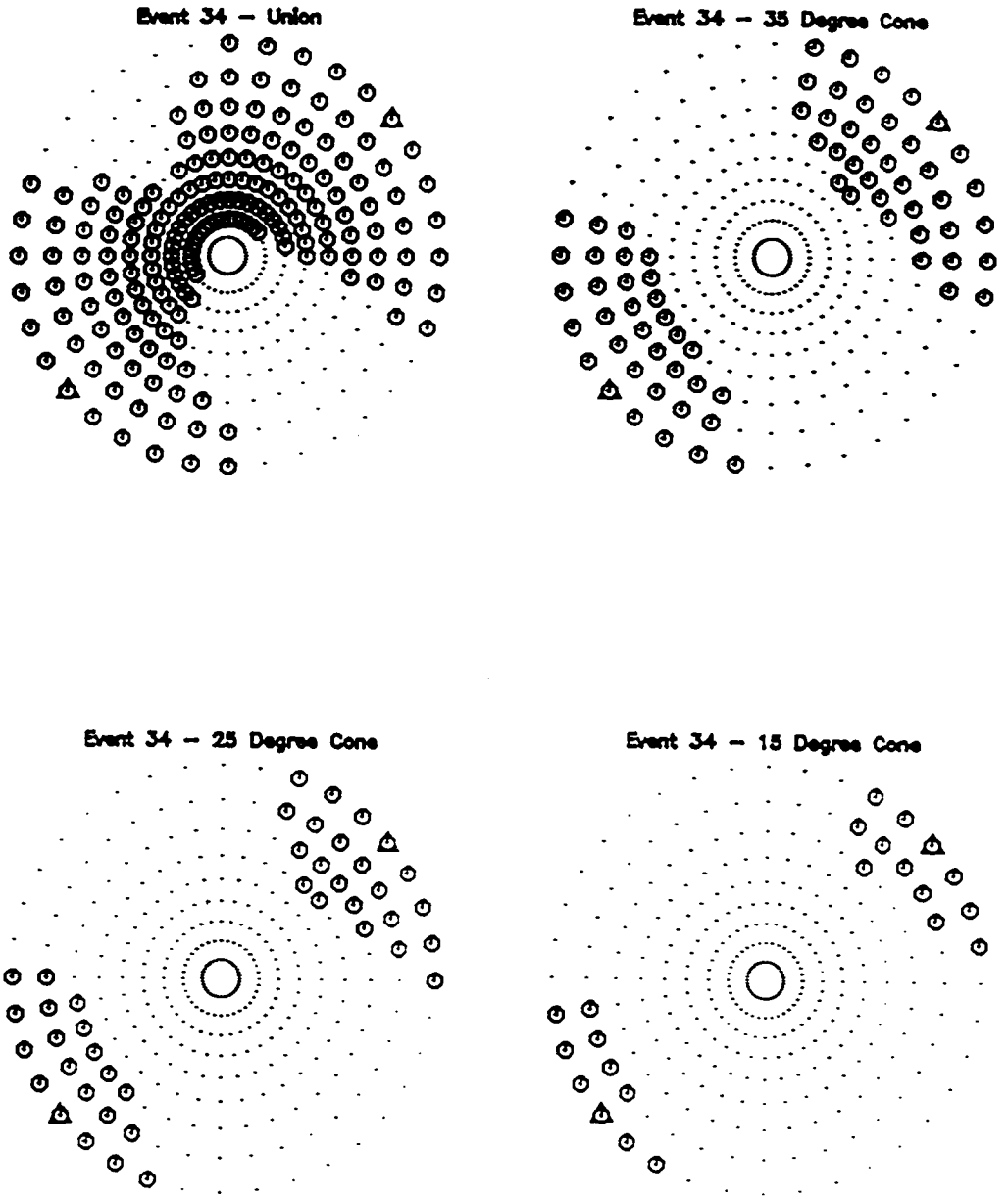

Figure 71. Event 34 - Eastern Tennessee Seismic Zone

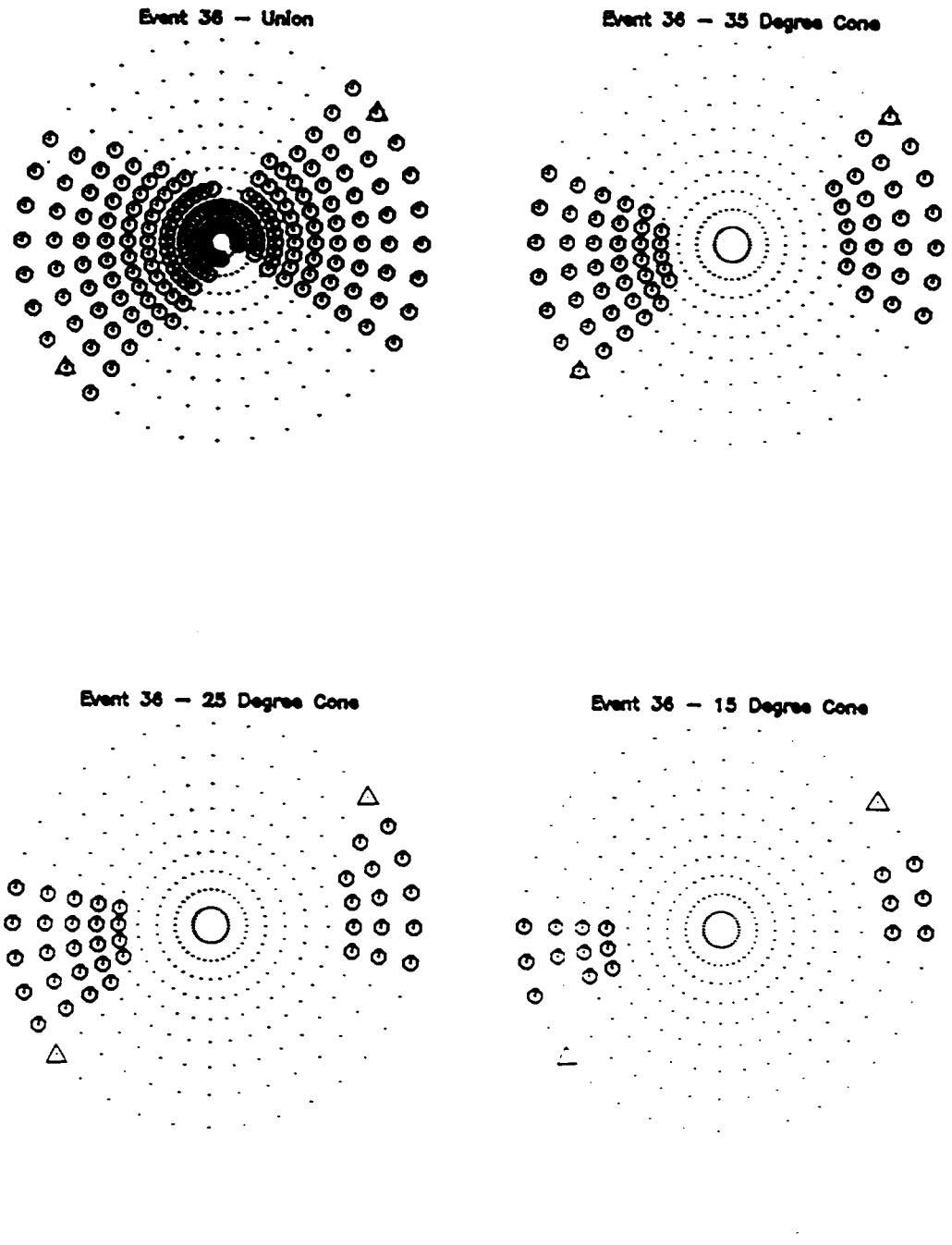

Figure 72. Event 36 - Eastern Tennessee Seismic Zone

The vita has been removed from the scanned document